

# U. S. Army Communications- Electronics Command

## Night Vision & Electronic Sensors Directorate

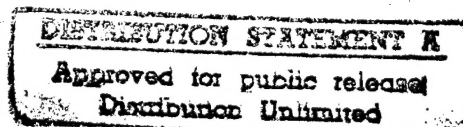
**Title:** Nanosecond and Subnanosecond Investigation  
of Intrinsic Optical Limiting Mechanisms in  
Photorefractive and Semiconductor Materials

**Author(s):** A. L. Smirl and T. F. Boggess

**Address:** University of Iowa  
Center for Laser Science and Engineering  
144 IATL  
Iowa City, IA 52242-1000

**Type of Report (Final, Interim, etc.):** Final

**Date:** ~~March 1996~~



**Contract Number**

DAAB07-89-C-F412

**Report Number**

NV-96-C07



19960501 154

Fort Belvoir, Virginia 22060-5806

# DISCLAIMER NOTICE



**THIS DOCUMENT IS BEST QUALITY AVAILABLE. THE COPY FURNISHED TO DTIC CONTAINED A SIGNIFICANT NUMBER OF PAGES WHICH DO NOT REPRODUCE LEGIBLY.**

## REPORT DOCUMENTATION PAGE

Form Approved  
OMB No. 0704-0188

1a. REPORT SECURITY CLASSIFICATION Unclassified			1b. RESTRICTIVE MARKINGS none		
2a. SECURITY CLASSIFICATION AUTHORITY N/A			3. DISTRIBUTION / AVAILABILITY OF REPORT Approved for Public Release Distribution Unlimited		
2b. DECLASSIFICATION / DOWNGRADING SCHEDULE N/A					
4. PERFORMING ORGANIZATION REPORT NUMBER(S)			5. MONITORING ORGANIZATION REPORT NUMBER(S) NV-96-C07		
6a. NAME OF PERFORMING ORGANIZATION University of Iowa		6b. OFFICE SYMBOL (If applicable)	7a. NAME OF MONITORING ORGANIZATION U. S. Army CECOM NVESD		
6c. ADDRESS (City, State, and ZIP Code) 100 IATL Iowa City, IA 52242-1000			7b. ADDRESS (City, State, and ZIP Code) Ft. Belvoir, VA 22060-5677		
8a. NAME OF FUNDING / SPONSORING ORGANIZATION ARPA		8b. OFFICE SYMBOL (If applicable)	9. PROCUREMENT INSTRUMENT IDENTIFICATION NUMBER DAAB07-89-C-F412		
8c. ADDRESS (City, State, and ZIP Code) 3701 N. Fairfax Dr. Arlington, VA 22203-1714			10. SOURCE OF FUNDING NUMBERS		
PROGRAM ELEMENT NO. 62 301 E		PROJECT NO.	TASK NO. DO	WORK UNIT ACCESSION NO.	
11. TITLE (Include Security Classification) Nanosecond and Subnanosecond Investigations of Intrinsic Optical Limiting Mechanisms in Photorefractive and Semiconducting Materials (U)					
12. PERSONAL AUTHOR(S) Smirl, A. L., Boggess, T. F.					
13a. TYPE OF REPORT Final		13b. TIME COVERED FROM 3/31/89 TO 9/14/95		14. DATE OF REPORT (Year, Month, Day) 4/15/96	
15. PAGE COUNT 117					
16. SUPPLEMENTARY NOTATION					
17. COSATI CODES			18. SUBJECT TERMS (Continue on reverse if necessary and identify by block number)		
FIELD	GROUP	SUB-GROUP			
20	5				
20	6				
19. ABSTRACT (Continue on reverse if necessary and identify by block number) As a part of the ARPA Eye & Sensor Protection Program, this project has been focused on the exploration of a variety of optical nonlinearities in materials, including semiconductors, organometallic compounds, and photorefractive media, that have potential applications in optical limiting devices. Much of the progress on this project was previously reported in an Interim Final Report (Report # NV-93-C08). This report specifically summarizes progress made on the study of optical nonlinearities in GaP and their applications to optical limiting - research associated with the dissertation work of an AASERT student, funding for whom extended the performance period of this contract from 31 March 1993 to 14 September 1995. These studies have revealed that the dominant nonlinearity responsible for optical limiting at 532 nm in GaP (at fluences below the surface damage threshold of ~ 100 mJ/cm <sup>2</sup> ) is nonlinear refraction arising from band filling effects caused by holes in the valence band. A smaller contribution is found to arise from the free-carrier Drude effect. A per carrier index of $-3.1 \times 10^{-22}$ cm <sup>3</sup> is measured, which is within a factor of three of that predicted by theory. An unusually large two-photon absorption coefficient is measured in this material (~20 cm/GW; roughly an order of magnitude larger than predicted by scaling laws), which may be attributed to transitions to a higher lying conduction band with the fundamental conduction band providing a near resonant intermediate state. Also included in this report are reprints of manuscripts from the broader program which were not included in the Interim Final Report.					
20. DISTRIBUTION / AVAILABILITY OF ABSTRACT <input checked="" type="checkbox"/> UNCLASSIFIED/UNLIMITED <input type="checkbox"/> SAME AS RPT. <input type="checkbox"/> DTIC USERS			21. ABSTRACT SECURITY CLASSIFICATION U		
22a. NAME OF RESPONSIBLE INDIVIDUAL Bvong H. Ahn			22b. TELEPHONE (Include Area Code) (703) 704-2031		22c. OFFICE SYMBOL AMSEL-RD-NV-ST-AL

## Final Report

### NANOSECOND and SUB-NANOSECOND INVESTIGATIONS of INTRINSIC OPTICAL-LIMITING MECHANISMS in PHOTOREFRACTIVE and SEMICONDUCTING MATERIALS

DAAB07-89-C-F412

April 15, 1996

ARPA/NVESD

Department of Physics & Astronomy  
University of Iowa  
100 IATL  
Iowa City, Iowa 52242

(319) 335-3520  
FAX (319) 353-1115  
e-mail: thomas-boggess@uiowa.edu

Arthur L. Smirl, Professor and Endowed Chair  
and  
Thomas F. Boggess, Associate Professor

The views, opinions, and/or findings contained in this report are those of the author(s) and should not be construed as an official Department of the Army position, policy, or decision, unless designated by other documentation.

The Contractor, The University of Iowa, hereby certifies that, to the best of its knowledge and belief, the technical data delivered herewith under Contract No. DAAB07-89-C-F412 is complete, accurate, and complies with all requirements of the contract.



April 15, 1996  
Thomas F. Boggess  
Associate Professor  
Department of Physics and Astronomy and  
Department of Electrical & Computer Engineering  
University of Iowa



## Table of Contents

EXECUTIVE SUMMARY .....	3
CONTRACT INFORMATION .....	4
PROJECT DESCRIPTION AND SUMMARY.....	4
PRIMARY CONCLUSIONS FROM AASERT PROGRAM.....	8
RECOMMENDATIONS .....	10
PUBLICATIONS .....	11
APPENDIX A.....	12
APPENDIX B .....	23
APPENDIX C .....	36
APPENDIX D .....	44
APPENDIX E .....	52
APPENDIX F .....	56
APPENDIX G.....	60
APPENDIX H.....	64
APPENDIX I.....	68
APPENDIX J.....	72
APPENDIX K.....	79
APPENDIX L.....	89
APPENDIX M.....	98
APPENDIX N.....	105
APPENDIX O.....	111

## Executive Summary

The objective of our project has been to explore the fundamental physics underlying optical nonlinearities in a variety of materials that have potential application to eye and sensor protection and to demonstrate simple devices based on these materials. We have previously reported, in an Interim Final Report (Report Number NV-93-C08, 28 June 1993) for the Parent Contract, a summary of our results, primary conclusions, and recommendations for future directions in optical limiting. Research on the Parent Contract included studies of optical nonlinearities in bulk GaAs, Si, and GaP, spatial solitons, photorefractive materials, and organometallic compounds, and the application of such nonlinearities to simple optical limiting devices. Research continued on the program under AASERT funding, which provided support for one graduate student through September 1995. We have previously reported in the Interim Final Report the results of research performed by the AASERT student on low-f-number ( $f/5$ ) optical limiters based on GaP. In this report, we focus on progress made by the AASERT student toward understanding the fundamental nature of the optical nonlinearities in GaP that lead to optical limiting. We have also included as Appendices in this Report copies of publications not included in the Interim Final Report.

The focus of the research under the AASERT funding was optical nonlinearities and optical limiting in GaP at 532 nm. These studies have revealed that the dominant nonlinearity responsible for optical limiting at 532 nm in GaP (at fluences below the threshold for surface damage,  $\sim 100 \text{ mJ/cm}^2$ ) is nonlinear refraction arising from linearly generated carriers. More specifically, we find that this nonlinear refraction is primarily associated with band filling effects caused by holes in the valence band. A smaller contribution is found to arise from the free-carrier Drude effect. We measure a per carrier index of  $-3.1 \times 10^{-22} \text{ cm}^3$ , which is within a factor of three of that predicted by theory. Although we demonstrate that it has no significant impact on the GaP limiter, we measure an unusually large two-photon absorption coefficient in this material ( $\sim 20 \text{ cm/GW}$ ; roughly an order of magnitude larger than predicted by scaling laws), and we attribute the effect to transitions to a higher lying conduction band with the fundamental conduction band providing a near resonant intermediate state.

**NANOSECOND and SUB-NANOSECOND INVESTIGATIONS  
of INTRINSIC OPTICAL-LIMITING MECHANISMS in  
PHOTOREFRACTIVE and SEMICONDUCTING MATERIALS  
DAAB07-89-C-F412**

**Contract Information**

This contract, which had an original total cost of \$775,560, began 31 March 1989 and was scheduled to end 30 March 1993. In March of 1992, a proposal for a Department of Defense Augmentation Award for Science and Engineering Research Training (AASERT) was selected for funding. The purpose of this award was to provide funding for one additional Ph. D. student on the Parent Contract. Funding for the AASERT award, which had a 15 September 1992 start date, totaled \$84,132, and the award was for a three year period. The AASERT award extended the performance period of the parent contract from 31 March 1993 to 14 September 1995. It must be emphasized, however, that during this extended period, the level of effort on the contract was greatly reduced; while the parent contract provided support for two students, one post doc, and significant faculty time, the AASERT award provided funding for only one student per year. Hence, as of 30 March 1993 the bulk of the research on this contract was completed, and the work was summarized in an Interim Final Report dated 28 June 1993, Report Number NV-93-C08. The AASERT program provided the support required for one student (Steven J. Rychnovsky, currently at the Naval Research Laboratory) to complete his Ph.D. dissertation and provided an apprentice laboratory experience for another student (Scott A. Anson) who is currently working toward his Ph.D. in Electrical Engineering.

**Project Description and Summary**

The objective of our project has been to explore the fundamental physics underlying optical nonlinearities in a variety of materials that have potential application to eye and sensor

protection and to demonstrate simple proof of principle devices based on these materials. The direction of these studies was determined by the overall program goal, which was to implement optical limiting devices capable of providing limiting levels of  $0.1 \mu\text{J}/\text{cm}^2$ , high linear throughput ( $> 70\%$ ), and a large dynamic range ( $> 60 \text{ dB}$ ) for 10 ns pulses throughout the spectral range of 400-700 nm. In addition, to preserve field of view, the devices must be based on low  $f/\#$  configurations. While these criteria may be easily satisfied individually in various materials, the requirement that they be simultaneously satisfied in a given device places extreme performance demands on the nonlinear element in the device. To our knowledge, no single material or combination of materials in any device has yet completely satisfied all of the program goals. Nevertheless, progress has been made on many fronts leading to an improved understanding of material properties that govern optical limiting devices and to the demonstration of optical limiters that satisfy many (though not all) of the program requirements.

We have previously reported in the Interim Final Report the use of the indirect band-gap semiconductor GaP in low-f-number optical limiting devices utilizing an intermediate focal plane and restrictive aperture. These studies revealed that GaP could provide eye-safe optical limiting ( $< 0.5 \mu\text{J}/\text{cm}^2$ ) for 532 nm,  $\sim 100$  ps pulses for input energies ranging from  $\sim 50$  nJ to  $> 1$  mJ in an  $f/5$  configuration. The attractive feature of this material for optical limiting is that it relies predominantly on fluence dependent nonlinearities - i.e., nonlinearities that are essentially pulse width independent. The nonlinearities originate primarily with linearly generated carriers. The limiting below the surface damage threshold of  $\sim 100 \text{ mJ}/\text{cm}^2$  is dominated by nonlinear refraction associated with linearly generated carriers, while above this level the GaP surface damages, and laser-induced melting (a process that again is only weakly dependent on pulse width) contributes strongly to the limiter performance. We further demonstrated that the limiter performance could be enhanced significantly by using a  $f/4$  input and  $f/5$  output. This configuration allows the restrictive system aperture to clip the ring arising from transmitted high-spatial frequency components that are unattenuated in the

intermediate focal plane of the device. The details of the GaP optical limiter will not be repeated here. Rather, the focus of this report will be the work performed by the AASERT student on the fundamental aspects of the nonlinear optical interactions in GaP that initiate optical limiting.

The measurements of carrier related optical nonlinearities in GaP were conducted using open and restricted aperture Z-scans and pump-probe transmission measurements. Pulses of 25 and 95 ps at 532 nm, obtained from a mode-locked and frequency doubled Nd:YAG laser were used for these studies. Open aperture Z-scans revealed a strongly pulsewidth dependent signal, with significantly more nonlinear absorption arising with the shorter duration (25 ps) excitation pulses. Analysis of these data provided a two-photon absorption (TPA) coefficient of 20 cm/GW and a free-carrier related absorption cross section of  $1.3 \times 10^{-18}$  cm<sup>2</sup>. This measurement was supported by pump-probe measurements, which revealed an ultrafast induced absorption, typical of TPA, and a long-lived induced absorption that we associate with carrier-induced effects.

A careful analysis of the TPA revealed that the TPA coefficient in GaP at 532 nm is anomalously large, exceeding the predicted value based on band-gap scaling laws by a factor of 9. A subsequent investigation of all possible optically-coupled states at 532 nm in GaP revealed that this behavior may be a consequence of a Coulomb-enhanced TPA transition to a higher lying conduction band near  $k=0$ , with the fundamental conduction band edge providing enhancement of the process by acting as a resonant intermediate state. Verification of this result would require subsequent experiments using a tunable visible source. Although this enhanced TPA was clearly not sufficient in this particular case to provide significant TPA-related optical limiting even for ps pulses (see discussion below), the mechanism for TPA enhancement is intriguing and should not be discarded as engineered nonlinear optical materials are considered for future optical limiting applications.

Restricted aperture Z-scans exhibited a nearly pulsewidth independent response that was significantly larger than the open aperture response. Four conclusions may be drawn from this

result: 1) the magnitude of the signal indicates that the refractive nonlinearity is significantly more effective than the absorptive nonlinearity (e.g., at 110 nJ of input and 95 ps pulse, a 3% change in transmission is obtained in the open aperture arrangement while a 40% change is obtained with the restrictive aperture), 2) the nonlinearity giving rise to the refractive response is largely fluence dependent, 3) as such, the TPA observed in the open-aperture measurement is not significantly influencing the number of carrier generated, i.e., the carrier generation is dominated by linear absorption, and 4) an optical limiter composed with GaP will have a response dominated by an essentially fluence dependent nonlinear refraction at 532 nm. A fit to the restricted aperture Z-scan provided a value of  $-3.1 \times 10^{-22} \text{cm}^3$  for the index change per photogenerated pair. This value is within a factor of 3 of that obtained using a simple Drude-Lorentz model for the refractive index.

A more complete analysis of the carrier-related refractive index in GaP at 532 nm revealed that the index change is primarily associated with band filling by holes in the valence band. A smaller contribution arises from the Drude contribution. GaP is an indirect band gap semiconductor with a conduction band minimum at 2.26 eV near the X-point and a direct minimum at 2.78 eV at the  $\Gamma$  point. As such, excitation at 532 nm (2.34 eV) results in indirect absorption in which holes are created at zone center and electrons are promoted to the X-valleys. This results in the creation of a free electron and free hole, which may be thought of a zero-frequency oscillators providing a negative contribution to the refractive index at all frequencies (Drude contribution), and the partial destruction of an oscillator resonant at the *direct* band gap energy of 2.78 eV by the presence of a hole at the zone center (band filling contribution). The electron does not contribute to this blocking since it resides in the X-valley. These electrons do of course contribute to the index change by blocking states that were previously available for *indirect* transitions at the fundamental band edge, but phonon participation in this process greatly reduces its importance. Thus band filling provided by electrons in this system is much less than that provided by holes. The index change provided by the holes is also negative for frequencies below the direct gap, i.e., those relevant to the

optical limiter studied in this program. Hence the band filling associated with holes complements, rather than competes with the Drude effect. Theoretical estimates of the two effects indicate that for 532 nm, the band filling contribution dominates, with an index change per carrier pair of  $-7.9 \times 10^{-22} \text{ cm}^3$  for band filling and  $-1.8 \times 10^{-22} \text{ cm}^3$  for holes.

We have also considered the possible contributions of plasma screening and band gap renormalization to the carrier-induced index. The former results in a decrease in index at photon energies below the gap, while the latter provides an increase in index at these photon energies. Both of these processes result in index changes that, at low densities, are highly nonlinear in density. Experimentally we do not observe such a nonlinear dependence, but instead observe a simple linear dependence as would be expected from band filling under nondegenerate conditions. Hence, we attribute the nonlinear refraction to band filling and the Drude contribution. We note, however, that this conclusion seems to contradict results from simple plasma theory models, which predict significant contributions from many body effects. The apparent discrepancy may be associated with the tendency of band gap renormalization to offset plasma screening or it may indicate that the simple plasma models strongly overestimate the many-body effects. Significantly more experimentation is required to resolve this problem.

A detailed discussion of the measurements and theory of optical nonlinearities and optical limiting in GaP may be found in the dissertation of the AASERT student: Steven J. Rychnovsky, "Optical Nonlinearities and Optical Limiting in Gallium Phosphide at 532 Nanometers," Ph. D. Dissertation, University of Iowa (1994).

### **Primary Conclusions from AASERT Program**

We summarize below the key conclusions that have arisen from the studies performed by the AASERT student. A portion of this list was included in the Interim Final Report but is repeated here for completeness.

- Nonlinearities associated with linearly generated carriers in semiconductors such as GaP can provide eye-safe limiting levels for a wide range of pulse durations, but only over a very limited bandwidth. It is possible that the bandwidth might be improved by incorporating deep levels into the GaP and utilizing impurity to conduction band and valence band to impurity transitions for broad band absorption. Substantial experimental and theoretical investigations would be required to determine the potential for this approach.
- In the low  $f/\#$  limiters ( $f/5$ ) that are required for practical applications, damage to the nonlinear element itself should not necessarily be used to determine the dynamic range of the device. For example, the GaP limiter continues to limit far above the GaP damage threshold, and the small spot size associated with the low  $f/\#$  configuration ensures that the damaged spot does not significantly degrade the imaging performance of the optical system.
- We have demonstrated an improved limiter response in an  $f4/f5$  input/output configuration. Such a geometry takes advantage of the fact that in the nonlinear medium, light is preferentially blocked in the center of the focused spot, resulting in a ring-like far field pattern. The larger output  $f/\#$  can be used to block much of this ring, thereby reducing the limiter throughput.
- We have determined that the dominant optical nonlinearity in GaP at fluences below the damage threshold is nonlinear refraction arising from band filling associated with holes in the valence band and that the index change per photogenerated carrier pair is  $-3.1 \times 10^{-22} \text{cm}^3$ . Although the effects of plasma screening and band gap renormalization were expected, we see no experimental evidence indicating that they significantly contribute to the index at the wavelength of interest.



- We have measured an anomalously large TPA coefficient (20 cm/GW) in GaP and tentatively attribute it to enhancement associated with transitions to a higher lying conduction band with the fundamental conduction band serving as a near resonant intermediate state.

## **Recommendations**

Semiconductors remain interesting as nonlinear optical elements in optical limiting devices because of the variety of nonlinear mechanisms available, the numerous material systems available, the wealth of knowledge that currently exists for these materials, and most importantly, the current ability to engineer materials using sophisticated growth techniques, such as molecular beam epitaxy. The disadvantage of these materials is that they (like all materials currently available) do not have nonresonant nonlinearities sufficiently large to be used in eye safe limiters. This restricts the nonlinearities of interest to resonant nonlinearities in which carriers are generated. Given existing TPA coefficients, TPA generation of carriers can result in significant optical limiting only for subnanosecond pulses. On the other hand, this mechanism provides a means of broad band operation, since TPA is a relatively slowly varying function of photon energy. Optical limiting with semiconductors for nanosecond and longer pulses is likely to require linear generation of carriers. For intrinsic semiconductors, this results in narrow band operation, as for GaP. Thus there exists an incompatibility between large bandwidth and pulsewidth independent operation. Novel concepts based on materials engineering should be explored to attempt to overcome this problem. This research might focus on broadening the absorption edge, enhancing the carrier induced refraction, and/or enhancing TPA. Such manipulation might be achieved, e.g., through engineering of material resonances in superlattices or superlattice quantum wells and/or through controlled doping of the material.

## **Publications**

A large body of detailed additional information regarding progress on this contract has been communicated in numerous publications which are included as appendices in this report. These Appendices exclude the manuscripts contained in the Interim Final Report. Appendices A-E describe measurements of optical nonlinearities in bulk semiconductors and their application to optical limiting. Appendices F-H contain information regarding our studies of the photorefractive effect in semiconductors for potential application to optical limiting. Appendices I-K describe studies of spatial dark soliton propagation in bulk semiconductors. Finally, our investigations of optical limiting and optical nonlinearities in organometallic compounds are summarized in Appendices L-O.

## **Appendix A**

### **Comparison Between Single-Beam and Multiple-Beam Optical Limiters in Semiconductors**

SPIE, Vol. 1307, pp. 242-250 (1990)

*Reprinted from*

# Electro-Optical Materials for Switches, Coatings, Sensor Optics, and Detectors

16–20 April 1990  
Orlando, Florida



Volume 1307

## Comparison between single-beam and multiple-beam optical limiters in semiconductors

J. Dubard, Arthur L. Smirl, Thomas F. Boggess, A. G. Cui, and Steven R. Skinner

Center for Laser Science and Engineering  
Departments of Electrical and Computer Engineering and of Physics and Astronomy  
The University of Iowa  
124 AMRF, Oakdale Campus, Iowa City, Iowa 52242  
(319) 335-4580

### ABSTRACT

We report our investigations of multiple-beam optical limiter configurations using GaAs and Si as the nonlinear optical material. Three distinct multiple-beam geometries are discussed. One of these, in which two beams interfere within the semiconductor, takes advantage of transient energy transfer and photorefractive beam coupling to deplete the signal beam. The other two configurations exploit the absorptive and refractive index changes induced in the semiconductor by a strong control beam that arrives at the sample before the signal. For one of these configurations, nonlinear absorption and induced defocusing are used to attenuate the signal; in the other, nonlinear absorption and induced deflection are used. We discuss the relative merits of each configuration and compare them to single beam results obtained under identical experimental conditions.

### 1. INTRODUCTION

To date, the vast majority of optical limiters (OL's) reported in the literature have been based on single-beam geometries, such as that shown schematically in Fig. 1, that use a nonlinear optical material placed at an intermediate focal plane in an optical system. At low intensities the material responds linearly, but at high excitation levels either nonlinear absorption, nonlinear refraction, or both effectively limit the throughput of the OL at a fixed level. Multiple-beam geometries offer several potential advantages over such single beam configurations. For example, multiple beam configurations allow access to a number of grating related phenomena, such as photorefractive energy transfer, polarization rotation, and free-carrier transient energy transfer (TET), that are inherently absent in single beam configurations (with the exception of OL's that utilize photorefractive beam fanning). Alternatively, by arranging the device such that the signal beam arrives at the sample coincident in space but delayed in time relative to a strong control beam, two-beam geometries can be used to take full advantage of optical nonlinearities, such as free-carrier absorption and free-carrier defocusing, that depend on the accumulated carrier density. Furthermore, by offsetting the signal beam relative to the control beam axis, induced beam deflection can also be realized with two-beam techniques.

Recently, a multiple-beam OL that utilizes photorefractive energy transfer from a signal beam into a control beam was demonstrated.<sup>1</sup> In this device, which is called a "coherent beam excisor", a small portion (a few percent) of the input signal is split off and is recombined with the signal at a small angle within a high-gain photorefractive material such as BaTiO<sub>3</sub>. For an incoherent image, no interaction occurs between the two beams, and the overall effect of the device is simply a slight attenuation associated with splitting the input. If, however, a coherent optical signal impinges on the device, the two beams interfere within the photorefractive material and write a grating. The grating results in energy transfer between the two beams. By properly choosing the orientation of the photorefractive crystal, energy can be transferred out of the strong beam and into the weak beam with high efficiency, thereby protecting any subsequent optical components. The advantages of this technique are that it has a high throughput, it discriminates against coherent signals, and it does not require an intermediate focal plane or spatial filtering. On the other hand, a major disadvantage of this device is that the photorefractive response time in materials such

as  $\text{BaTiO}_3$  is typically too long for this device to be effective against short-pulsed (ns) signals.

Here, we report our progress in investigating various multiple-beam OL geometries using inherently fast optical nonlinearities in semiconductors. Such OL's are potentially suitable for limiting ns or even ps optical signals. For each multiple-beam measurement we compare our results to a single beam measurement conducted with identical experimental conditions (focused spot size, collection geometry, etc.). Three different two-beam configurations will be described: (A) one in which a strong signal beam and a weak copolarized control beam are spatially and temporally coincident in the nonlinear material, (B) one in which a weak signal beam is spatially coincident but temporally delayed with respect to an intense control pulse, and (C) one in which a weak signal is temporally delayed and spatially offset with respect to an intense control pulse. In each case, the transmission of the signal through an aperture is measured as the total fluence is increased. These configurations, which are described in detail below, are designed to study the relative merits of (A) transient energy transfer and photorefractive beam coupling, (B) control-induced lensing and absorption, and (C) control-induced beam deflection for dynamic attenuation of the signal beam. In each case we compare the degradation in OL throughput to the improvement in reduced output energy relative to the single beam configuration.

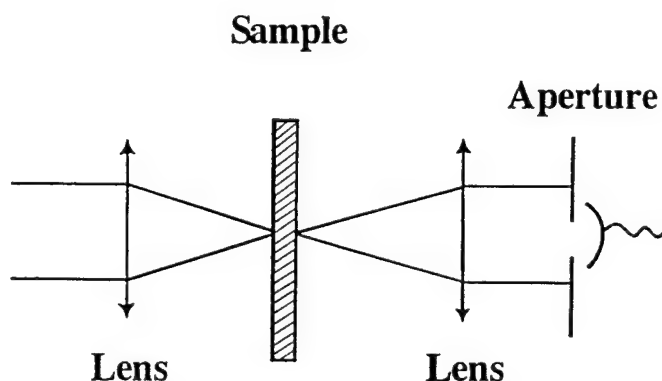


Fig.1: Single-beam Optical Power Limiter geometry.

To ensure an accurate comparison of the various configurations, we used two well-characterized semiconductor samples, a 1-mm-thick Si wafer and a 3-mm-thick sample of undoped semi-insulating GaAs, to provide the limiting action. Measurements were conducted with short pulses at  $1.06\ \mu\text{m}$ . These two materials respond quite differently to such excitation.<sup>2,3</sup> At this wavelength and at low fluences, the optical excitation induces indirect optical transitions from the valence band to the X-valleys in the conduction band of Si. As the fluence increases and the accumulated carrier density rises, free-carrier absorption, which is the dominant nonlinear absorption mechanism in Si, becomes significant. The negative index change associated with the photogenerated carriers, together with a nonuniform beam profile, results in self-defocusing for the single-beam case<sup>4</sup> and either induced defocusing or beam deflection in the multiple-beam configurations. Furthermore, for configurations in which two beams interfere to write a grating in the Si, this same refractive index change results in transient energy transfer from the strong beam into the weak beam.

The absorption mechanisms are dramatically different in the semi-insulating GaAs sample. At low excitation levels, the optical field induces transitions from the EL2 defect level to the conduction band (cross section  $\sigma_e$ ) and from the valence band to the ionized EL2<sup>+</sup> level (cross section  $\sigma_p$ ). In the dark, the EL2 population in our sample is much greater than the EL2<sup>+</sup> population. Furthermore, we know from our previous picosecond pump-probe measurements that  $\sigma_p \approx 0.8\sigma_e$ . As carriers are excited from EL2 to the conduction band, more EL2<sup>+</sup> are available for transitions from the valence band. Since the cross section for the latter process is smaller, this results in a weak bleaching of the overall defect absorption

and an increase in signal transmission. For short pulse excitation, however, this bleaching effect is insignificant compared to two-photon absorption, even at very low fluences. Free-carrier absorption associated with both linearly and two-photon generated carriers also increases the overall absorption. As with Si, these free carriers can be exploited in limiter configurations that are designed to utilize refractive index changes, including those based on transient energy transfer. In contrast with Si, in GaAs there is also an instantaneous contribution to the change in index arising from TPA. An additional mechanism, that is not present in Si but that can be accessed in GaAs, is the photorefractive effect.<sup>5</sup> When two beams interfere in GaAs, the photogenerated electrons diffuse from the peaks of the gratings to the troughs leaving behind excess positive charge. For a properly oriented crystal, the resulting space charge field creates a refractive index change through the electrooptic effect, and beam coupling results. The direction of energy transfer is determined by the crystal orientation and the sign of the dominant charge carrier in a given sample. We emphasize, however, that the saturated photorefractive gain in GaAs at  $1.06\mu\text{m}$  is small compared to that in  $\text{BaTiO}_3$  at visible wavelengths. Nevertheless, the saturation fluence for GaAs ( $\sim 1\text{ mJ/cm}^2$ ) is much less than for  $\text{BaTiO}_3$  ( $\sim 100\text{ mJ/cm}^2$ ), so that at low fluences (such as might be expected for short-pulse excitation) the photorefractive gain in GaAs can exceed that of  $\text{BaTiO}_3$ .

In the next section, we describe our experiments in detail, discuss our results, and compare the relative merits of the single- and multiple-beam geometries. We also discuss the relative merits of Si and GaAs for each configuration. Our concluding remarks are contained in Section III.

## 2. EXPERIMENTAL DETAILS AND RESULTS

### 2.1 Experimental Apparatus

All measurements reported here were performed with an actively and passively mode-locked Nd:YAG laser, which operated at a repetition rate of 5 Hz and produced 30-ps (FWHM) pulses at  $1.064\mu\text{m}$ . The laser operated in a  $\text{TEM}_{00}$  mode, and pinhole scans of the beam profile at the sample were used to measure the spot size. These scans also verified that the beam profiles at the sample were Gaussian. Second harmonic techniques were used to measure the duration of each laser pulse, and computer controlled data acquisition was used to accept data only for pulses with durations within a narrow predetermined window. Similar windows were placed on the energy for each pulse. For each configuration, a single pulse was split into two, a signal which was the primary beam of interest and a control that was used to dynamically attenuate the signal. The transmitted signal was measured through an aperture that was set to clip the linearly transmitted signal at the  $e^{-1}$  point in intensity. In each case, the fluence dependence of the transmitted signal was compared to that obtained in a single beam configuration with identical focusing and collection optics.

### 2.2 Grating Related Phenomena

The first configuration that we investigated is illustrated in Fig. 2. For this configuration, the copolarized control and signal were both spatially and temporally coincident in the GaAs sample and the control beam fluence was less than the signal fluence. In this configuration, the two pulses interfere to write a grating in the sample and transient energy transfer, which is always from the strong beam into the weak beam, will deplete the signal. We chose the GaAs for this study, since we knew from our previous work that TET is much stronger in the 3-mm-thick GaAs than in the 1-mm-thick Si for a given fluence. Furthermore, GaAs is photorefractive, whereas Si is not. Therefore, by properly orienting the GaAs crystal, we can use photorefractive beam coupling from the signal into the control beam to deplete the signal. Thus, when we use GaAs in this configuration, nonlinear absorption, defocusing, photorefractive and transient energy transfer all contribute to the depletion of the transmitted signal beam.

The results of this measurement are represented by the triangles in Fig. 3, where we plot the energy transmitted through the aperture as a function of incident fluence. For this measurement the signal was 25 times more intense than the control beam, and both beams were collimated with a beam diameter of

2 mm ( $\text{FWe}^{-1}$ ). The results of the equivalent single beam measurement are represented by the circles. Clearly, we obtain only a modest improvement in the limiting action in this two-beam-coupling geometry. We measure a 20% reduction in the maximum fluence transmitted by the aperture at a cost of a 4% reduction in linear transmission. In the fluence range for which any significant improvement of the limiter performance was measured, our previous work<sup>5</sup> indicates the energy transfer is dominated by TET rather than photorefractive effects. Note that the maximum signal attenuation that can be achieved with TET is  $<50\%$ .

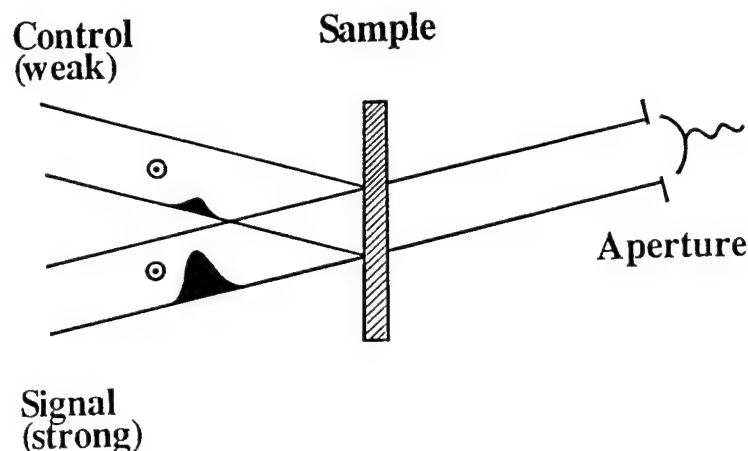


Fig.2: Two-beam coupling OL geometry. Control-to-signal fluence ratio 1/25, 0 delay. Sample oriented for control beam photorefractive and TET gain.

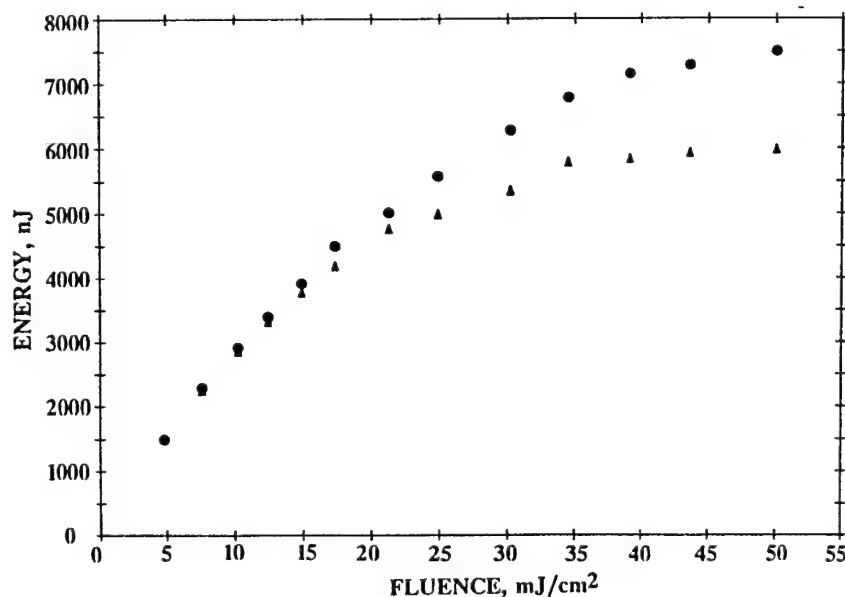


Fig.3: Single-beam (circle) and two-beam coupling (triangle) limiting curves. Linear transmission of the two-beam device is 96% compared to the single-beam device.

We found that we could continue to trade linear transmission for optical limiting with increasing control-to-signal ratio, but with decreasing efficiency. For a ratio of 1/1, the maximum transmitted fluence was reduced to  $\sim 50\%$  of its single beam value with a corresponding 50% reduction in linear transmission. For



equal control and signal pulses, there is no transient energy transfer, and photorefractive energy transfer is the most obvious mechanism which distinguishes the two-beam and single-beam techniques. In the case of equal signal and control pulses, the same result could have been obtained by placing a linear 50% transmitting filter in front of the detector. This indicates that photorefractive beam coupling is insignificant for this configuration at the fluences of interest. If the control-to-signal ratio is further increased to a value above unity (i.e., signal weaker than control), transient energy transfer, which is always from strong to weak beam, begins to work against limiting action for the signal. In this case, it is advantageous to "turn off" the grating effects by arranging the signal polarization orthogonal to the control polarization. When the control and signal are temporally coincident, the latter geometry produces a limiting action on the probe exactly equivalent to placing a filter in the signal beam with a transmission equal to the control-to-signal ratio.

### 2.3. Induced Absorption and Defocusing

Next, we investigated the effects of arranging a weak signal to arrive approximately one pulse width behind an intense control pulse. The advantage of this technique is that the signal "sees" all of the carriers generated by the control pulse; the disadvantage is that the signal does not experience the TPA or the instantaneous index changes induced by the stronger control pulse. Another disadvantage is that, since the control beam should be more intense than the signal, the throughput for this system is necessarily low. For this configuration, the signal was symmetrically focused with respect to the control beam, and the two pulses were recombined at an angle of  $2^\circ$  at the sample surface. Both pulses were focused with a 50-cm lens to the same spot size ( $\approx 100 \mu\text{m FWe}^{-1}$ ), and an optical delay line was used to allow the signal to arrive at the sample 100 ps after the control. The signal was recollimated with a 30-cm lens and then transmitted through an aperture, which was again set to clip the linearly transmitted signal beam at the  $e^{-1}$  point. The control-to-signal fluence ratio was 25/1. The optical configuration is shown schematically in Fig. 4.

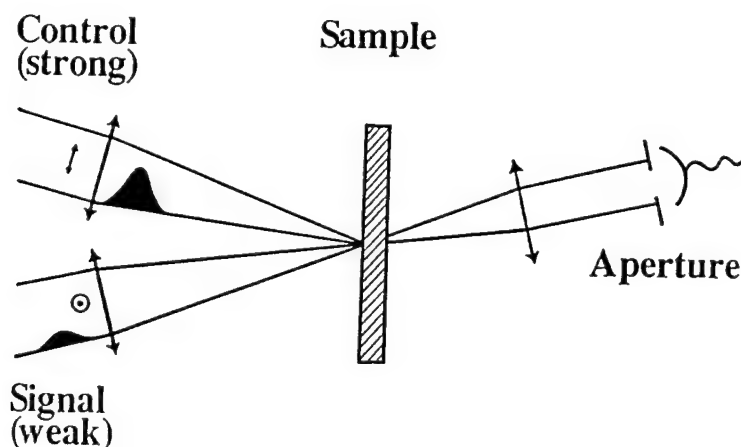


Fig.4: Control-induced absorption and defocusing OL geometry. Control-to-signal fluence ratio 25/1. Delay -100ps.

In Fig. 5, the squares represent the results of measuring the energy transmitted through the aperture as a function of total fluence incident on the 1-mm-thick Si wafer. The open triangles represent the single beam measurement, and the closed triangles are those same results divided by the control-to-signal beam ratio of 25. The latter is equivalent to placing a 4% linearly transmitting filter in front of the sensor. A comparison of this curve with the multiple-beam results, therefore, directly illustrates the enhancement of the optical nonlinearities obtained in the multiple-beam case. There are clearly several differences between the single-beam and multiple beam results. First, notice that the limiting action starts earlier (15

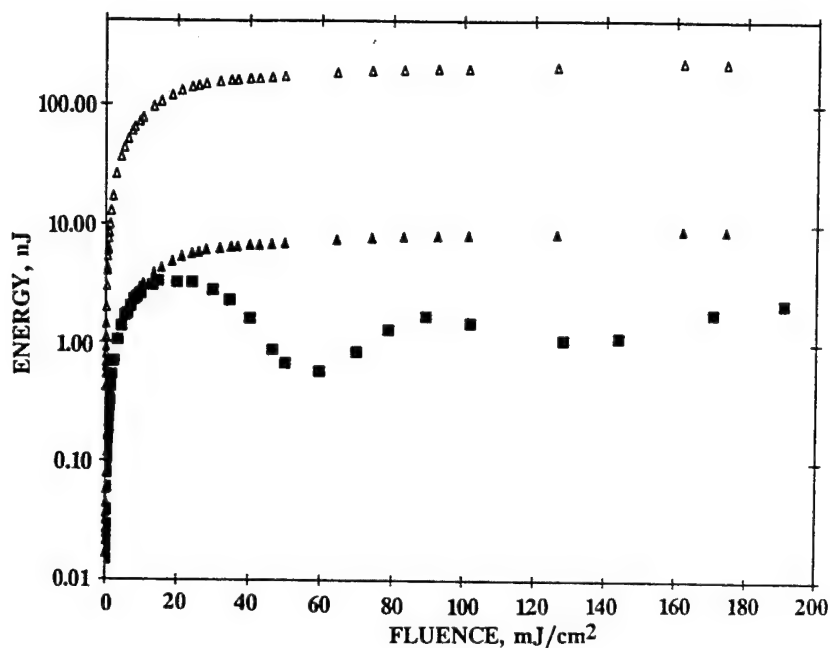


Fig.5: Single-beam (open triangle) and control-induced absorption and defocusing (square) limiting curves in Si. (triangle) Single-beam data reduced by the linear transmission of the two-beam device (4%).

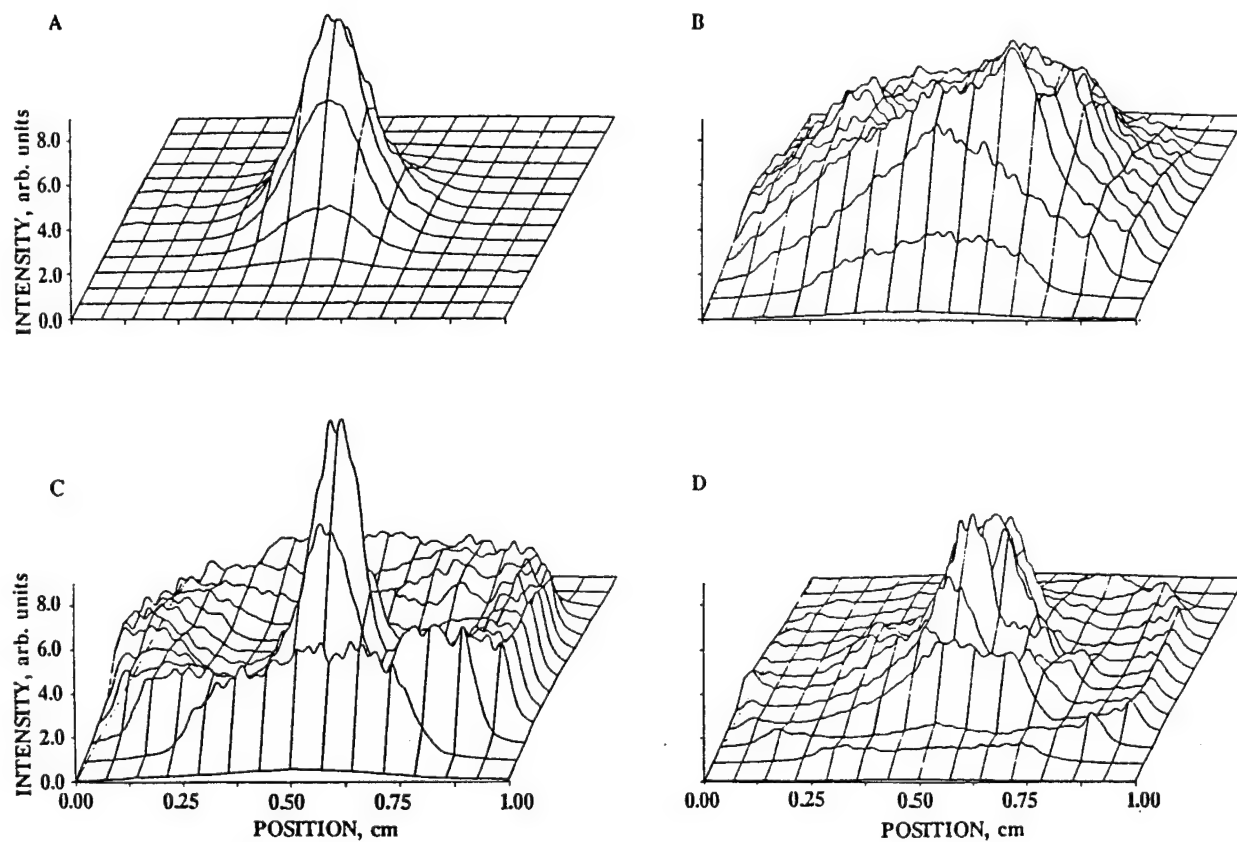


Fig.6: Spatial profile of the transmitted signal beam at the aperture position for a control beam fluence of 20 mJ/cm<sup>2</sup> (A), 50 mJ/cm<sup>2</sup> (B), 80 mJ/cm<sup>2</sup> (C), 125 mJ/cm<sup>2</sup> (D) in Si.

instead of  $30 \text{ mJ/cm}^2$ ) and that the transition from the linear to nonlinear regime is sharper. At  $20 \text{ mJ/cm}^2$  the measured signal for the multiple-beam configuration is 2 times smaller than the normalized value for the equivalent single-beam configuration. Further improvements are achieved at higher fluences, and a maximum improvement by a factor 12 is obtained near  $50 \text{ mJ/cm}^2$ .

The other feature that is clearly evident in Fig. 5 is the oscillatory behavior of the transmitted energy with increasing input fluences. The nature of these oscillations has been investigated by measuring the spatial profile of the signal beam at the aperture plane using an Optical Multichannel Analyzer. We find that these oscillations are a manifestation of control-beam-induced defocusing of the signal beam. The spatially Gaussian carrier density profile produced by the control beam acts as a negative Gaussian lens with an effective focal length that is fluence dependent. Diffraction of the signal by this Gaussian lens results in a ring pattern in the far field. The oscillations with fluence correspond to successive rings moving away from the beam axis. The peaks and the valleys correspond, respectively, to the states where the ring is transmitted through and blocked by the aperture. This is illustrated in Fig. 6, where we show the spatial profiles measured in the plane of the aperture for several different fluences. This behavior was not evident in either the single beam data or the zero-delay data because of the temporal averaging of the defocusing over the pulse profile that occurs in these measurements.

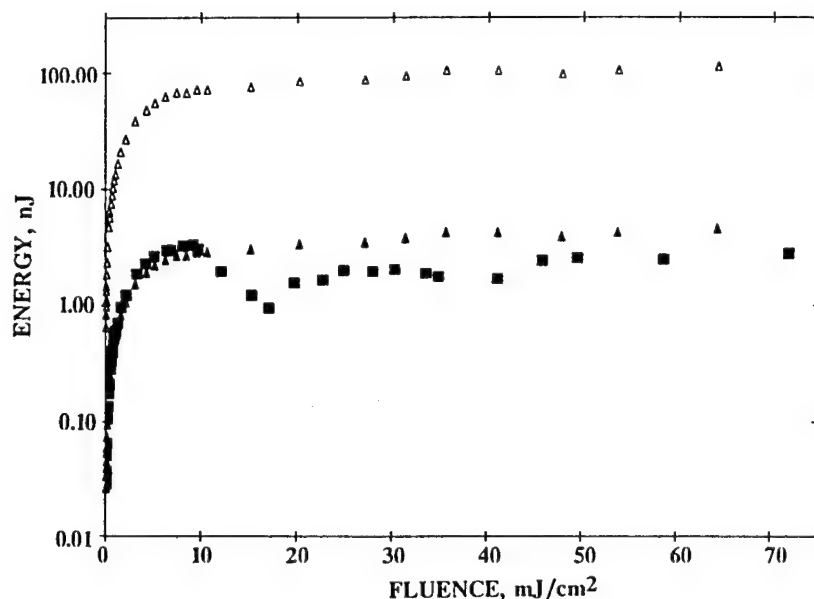


Fig.7: Single-beam (open triangle) and control-induced absorption and defocusing (square) limiting curves in GaAs. (triangle) Single-beam data reduced by the linear transmission of the two-beam device (4%).

Although similar behavior is observed in GaAs, the limiting action is not improved as dramatically as in Si. The results of the measurement made with GaAs is shown in Fig. 7. The difference in OL performance for the two semiconductors lies in the nature of the nonlinear absorption processes in these two materials. For 30 psec pulses and the fluences of interest here, the nonlinear absorption in GaAs is dominated by two-photon absorption, whereas free-carrier absorption is the dominant in Si. Since TPA depends on the instantaneous intensity in the sample, the present configuration does not access this strong absorptive nonlinearity in GaAs. Although the refractive nonlinearity associated with TPA-generated free carriers is fully accessed, the instantaneous refractive nonlinearity associated with TPA is also absent here. On the other hand, since free-carrier absorption depends only on the time integrated intensity or the fluence, this configuration takes full advantage of all optical nonlinearities in Si.

## 2.4 Induced Absorption and Beam Deflection

The final configuration investigated uses the control-beam-induced deflection and absorption of a weak signal beam as a limiting process. The experimental configuration, which is shown schematically in Fig. 8, is similar to that used for photothermal deflection spectroscopy.<sup>6</sup> Here, the signal spot size is considerably smaller than the control spot, and the signal propagates to one side of the control beam axis as illustrated in Fig. 8. Again, the signal is arranged to arrive 100 ps after the control pulse. For this configuration, the signal experiences a quasi-linear, control-induced variation of the refractive index along one of its spatial axes. The nonlinear medium then behaves much like a prism, deflecting the signal beam in a direction that depends on the sign of the nonlinear refractive index and with an angle that depends on the amplitude of the change in the refractive index of the medium. The angle of deflection is also a function of the slope of the index variation. For a Gaussian-like refractive index profile, the slope is maximum at the inflection point. This has been verified experimentally, and the measurements reported here have been performed in this configuration.

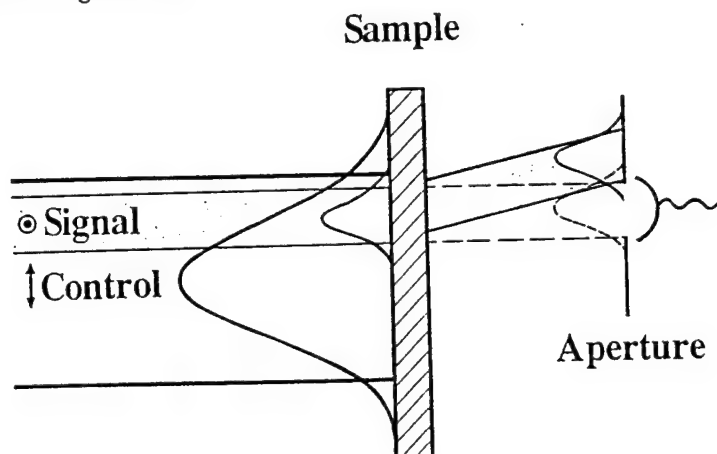


Fig.8: Control-induced absorption and deflection OL geometry. Control-to-signal fluence ratio 20/1, control-to-signal beam size ratio 3/1, delay -100ps.

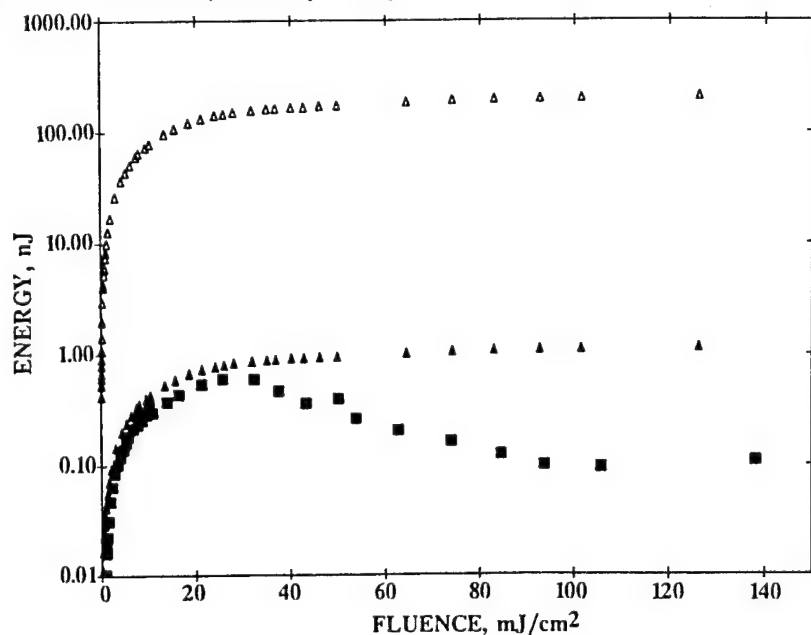


Fig.9: Single-beam (open triangle) and control-induced absorption and deflection (square) limiting curves in Si. (triangle) Single-beam data reduced by the linear transmission of the two-beam device (0.055%).

Fig. 9 illustrates the results obtained in Si for a control-to-signal beam radius ratio of 3/1 and a control-to-signal fluence ratio of 20/1. With these parameters the linear transmission of the device is 180 times lower than the transmission of the single-beam optical limiter. Taking this into account, the results show an improvement of about 40% at a fluence of 20 mJ/cm<sup>2</sup>. At still higher fluences, an improvement by up to one order of magnitude is measured. Similar results are obtained with GaAs. Again, however, the improvement over the single beam result is less dramatic in GaAs for reasons described above.

### 3. CONCLUSIONS

In summary, transient energy transfer in the "zero-delay" two-beam configuration gives a small improvement in the limiting performance when the control is weak compared to the signal and the signal and control pulses have parallel polarizations. The improvement, however, probably does not justify the additional complexity of this approach. We find that the two-beam time-delayed configurations offer substantial improvements in the limiting performance when compared to single-beam configurations. The price paid for this improvement, however, is a substantial reduction in the system throughput.

### 4. ACKNOWLEDGEMENTS

This research was supported by the Defense Advanced Research Projects Agency (contract DAAB07-89-F412).

### 5. REFERENCES

1. S. W. McCahon and M. B. Klein, "Coherent Beam Excisors Using the Photorefractive Effect in BaTiO<sub>3</sub>," Proc. SPIE, Vol. 1105, pp. 119-124, 1989.
2. Thomas F. Boggess, Klaus Bohnert, Kamjou Mansour, Steven C. Moss, Ian W. Boyd, and Arthur L. Smirl, "Simultaneous Measurement of the Two-Photon Coefficient and Free-Carrier Cross Section Above the Bandgap of Crystalline Silicon," IEEE J. Quantum Electron., Vol. QE-22, pp.360-368, 1986.
3. George C. Valley, Thomas F. Boggess, J. Dubard, and Arthur L. Smirl, "Picosecond Pump-Probe Technique to Measure Deep-Level, Free-Carrier, and Two-Photon Cross Sections in GaAs," J. Appl. Phys., Vol. 66, pp. 2407-2413, 1989.
4. Thomas F. Boggess, Steven C. Moss, Ian W. Boyd, and Arthur L. Smirl, "Nonlinear Energy Regulation by Nonlinear Refraction and Absorption in Silicon," Opt. Lett., Vol. 9, pp. 291-293, 1984.
5. George C. Valley, Arthur L. Smirl, M. B. Klein, K. Bohnert, and Thomas F. Boggess, "Picosecond Photorefractive Beam Coupling in GaAs," Opt. Lett., Vol. 11, pp. 647-649, 1986.
6. A. C. Boccara, D. Fournier, Warren Jackson, and Nabil M. Amer. "Sensitive Photothermal Deflection Technique for Measuring Absorption in Optically Thin Media," Opt. Lett., Vol. 5, pp. 377-379, 1980.

## **Appendix B**

### **Single and Multiple Beam Nonlinear Absorption and Refraction Measurements in Semiconductors**

SPIE, Vol. 1307, pp.251-261 (1990)

*Reprinted from*

# Electro-Optical Materials for Switches, Coatings, Sensor Optics, and Detectors

16–20 April 1990  
Orlando, Florida



Volume 1307

# Single and multiple beam nonlinear absorption and refraction measurements in semiconductors

Arthur L. Smirl, Thomas F. Boggess, J. Dubard, and A. G. Cui

Center for Laser Science and Engineering  
Departments of Electrical and Computer Engineering and of Physics and Astronomy  
The University of Iowa  
124 AMRF, Oakdale Campus, Iowa City, IA 52242

## ABSTRACT

We describe picosecond single- and multiple-beam measurements of the nonlinear absorption and refraction in a variety of semiconductors. Single-beam and pump-probe transmission measurements are used to isolate instantaneous nonlinearities from cumulative processes. These techniques, together with a simple rate equation model, have allowed us to extract information regarding mid-gap levels and to measure both the two-photon absorption coefficients and the free carrier absorption cross sections in these samples. Our model, together with Z-scan and beam deflection measurements of the nonlinear refraction, has provided the change in index due to each photogenerated electron-hole pair.

## 1. INTRODUCTION

The large optical nonlinearities and fast response times present in semiconductors make these materials particularly attractive for use in nonlinear-optical devices. A specific class of such devices of current interest to us is the passive optical limiter. The overall limiting action in passive optical limiters may be a consequence of several intrinsic nonlinearities induced by the incident radiation. For example, the limiter may operate using both nonlinear absorption (e.g., two-photon absorption and/or absorption associated with photogenerated free carriers) and nonlinear refraction<sup>1,2</sup>. In a semiconductor these two processes can occur simultaneously since the band-to-band absorption of incident light generates spatially localized carriers in the conduction and valence bands which modify the refractive index of the material. Once generated, the carriers can enhance the limiting action further by introducing free carrier absorption.

In addition to the rich variety of intrinsic nonlinearities present in semiconductors, the response of these materials can be influenced by impurity levels, either through the controlled introduction of dopants or through native defect levels (such as EL2 in GaAs). Mid-gap levels, such as EL2 or Cr in GaAs and V and Fe in CdTe and InP, respectively, provide a channel for band-to-band absorption (two-photon stepwise absorption) by single-photon ionization to produce an electron in the conduction band followed by single-photon neutralization to produce a hole in the valence band. If these two processes have different cross sections, an absorptive nonlinearity results. Shallow impurity levels, such as Si in GaAs, are largely ionized at room temperature, and scattering processes in the semiconductor are enhanced through ionized impurity scattering. This, in principle, may result in enhanced free carrier absorption and refraction, since such scattering provides momentum necessary for intraband transitions.

Since the role of both intrinsic and extrinsic nonlinearities in semiconductors is clearly important to the performance of passive optical limiters and other nonlinear-optical devices, a fundamental understanding of the type, magnitude, speed, and origin of these phenomena is necessary to optimize the design of a given device. We have recently applied single-beam and pump-probe transmission measurements to isolate and measure various nonlinear absorption mechanisms and Z-scans, beam deflection, two-beam coupling, and four-wave mixing techniques to measure nonlinear refraction in a variety of doped and undoped semiconductors. These include GaAs:EL2, GaAs:Si, GaAs:Cr, CdTe:V, CdTe (undoped), InP:Fe, and Si. In this paper, we present a brief comparison of the techniques, emphasizing the relative merits of each, and we focus our discussion of specific results on our measurements in GaAs. We will describe the



influence of the EL2 mid-gap level on the nonlinear transmission properties of undoped GaAs and briefly describe preliminary results for GaAs:Si that indicate an enhancement of the free-carrier absorption cross section relative to undoped GaAs.

## 2. EXPERIMENTAL APPARATUS

All measurements were performed with an actively and passively mode-locked Nd:YAG laser operating at  $1.06\text{ }\mu\text{m}$ . The laser produced  $\sim 30\text{ ps}$  (FWHM) pulses in a  $\text{TEM}_{00}$  mode. The actual duration of each pulse was determined using second harmonic techniques, and only pulses with durations within a narrow predetermined window were accepted. We emphasize that picosecond excitation allows us to neglect recombination and diffusion during our measurements. This greatly simplifies the analysis of our data. Furthermore, the use of such pulses allows us to isolate and accurately measure both cumulative (e.g., free-carrier absorption) and instantaneous (e.g., two-photon absorption) nonlinearities. Pinhole scans of the beam profile at the sample location were used to determine the spot size and to ensure that the beam profiles remained Gaussian after propagation to the samples.

## 3. NONLINEAR ABSORPTION

Two distinct and complimentary techniques were used to isolate and measure the various nonlinear absorption processes. The first of these is a simple single-beam measurement in which the transmission of a single (pump) pulse is measured as a function of incident fluence. This technique is in principle sensitive to both instantaneous and cumulative nonlinearities, although as we show below, for the samples investigated, the sensitivity to instantaneous nonlinear absorption is greater. The second technique is a pump-and-probe technique in which a single pulse is split into two, a variable time delay is introduced into one optical path, and the two pulses are recombined at a small angle at the sample. The more intense pulse (pump) modifies the optical properties of the sample, and the weaker pulse (probe) interrogates those modifications. For the pump-probe experiments described here, the probe delay was fixed at approximately  $100\text{ ps}$  after the pump, so that the weak probe interrogated only cumulative effects introduced by the pump.

We begin our discussion of nonlinear absorption by considering the various absorption processes that are possible for a semiconductor that contains a deep impurity or defect level. To be specific in our discussion, we focus our attention on  $1.06\text{ }\mu\text{m}$  picosecond excitation of undoped semi-insulating GaAs, which contains the native mid-gap defect level EL2. The mid-gap level exists in both the neutral state and the singly-ionized  $\text{EL2}^+$  state. The density of the latter is nearly equal to the density  $N_A$  of ionized shallow acceptors (typically carbon) providing compensation. A single  $1.06\text{ }\mu\text{m}$  photon cannot directly create an electron-hole pair, but a single photon can ionize neutral EL2 to create an electron in the conduction band, or it can neutralize  $\text{EL2}^+$  to create a hole in the valence band. Since in the dark, the density of neutral EL2 typically greatly exceeds the density of  $\text{EL2}^+$ , the initial absorption arises primarily from the ionization of neutral EL2 to create electrons in the conduction band. As the excitation is increased, the ratio of ionized to neutral EL2 increases, and transitions from the valence band to ionized EL2 become significant. Since the latter have a smaller cross section for absorption<sup>3</sup>, this redistribution of charge in the mid-gap level results in a bleaching of the absorption. Steady state is reached when the products of the cross sections and their corresponding number densities become equal. We refer to the process of generating an electron-hole pair through sequential ionization and neutralization of the mid-gap level as *stepwise TPA*. At sufficiently high irradiances, TPA via *virtual* intermediate states is also possible. One consequence of each of these processes is the production of free electron-hole pairs that subsequently allow free-carrier absorption (FCA), which is yet another nonlinear absorption mechanism. Note that, unlike the linear and nonlinear absorption mechanisms mentioned above, FCA does not result in the generation of additional carriers.

In the absence of recombination and diffusion, all of these processes can be modeled with a simple set of rate equations for the electrons, holes, and ionized donors. These equations include ionization and

neutralization of the donors and two-photon absorption. The equations can be solved in a self-consistent manner with Maxwell's equations, which also allow for FCA. The equations are summarized as follows.

Material Equations:

$$\frac{dn}{dt} = \frac{\sigma_e}{h\nu} (N-N^+) I + \frac{\beta}{2h\nu} I^2, \quad (1)$$

$$\frac{dp}{dt} = \frac{\sigma_p}{h\nu} N^+ I + \frac{\beta}{2h\nu} I^2, \quad (2)$$

$$\frac{dN^+}{dt} = \frac{\sigma_e}{h\nu} (N-N^+) I - \frac{\sigma_p}{h\nu} N^+ I, \quad (3)$$

Maxwell's Equations:

pump beam:

$$\frac{dI}{dz} = -\sigma_e(N-N^+) I - \sigma_p N^+ I - \sigma_{fe} n I - \sigma_{fp} p I - \beta I^2, \quad (4)$$

probe beam:

$$\frac{dI_p}{dz} = -\sigma_e(N-N^+) I_p - \sigma_p N^+ I_p - \sigma_{fe} n I_p - \sigma_{fp} p I_p. \quad (5)$$

In these equations  $n$ ,  $p$ ,  $N$ , and  $N^+$  are the population densities of electrons, holes, total donors, and ionized donors, respectively. The absorption cross sections for free electrons, free holes, neutral-donor-to-free-electron transitions, and ionized-donor-to-free-hole transitions are  $\sigma_{fe}$ ,  $\sigma_{fp}$ ,  $\sigma_e$ , and  $\sigma_p$ , respectively. The irradiance for the single (pump) beam is  $I$ , and the probe irradiance for the two beam case is  $I_p$ . The two photon absorption coefficient is  $\beta$ ,  $h\nu$  is the photon energy, and propagation in the  $z$  direction is assumed. A key point here is that such a simple set of equations is made possible by the use of picosecond excitation, which justifies neglecting recombination and diffusion.

For fluences well below that required to saturate the mid-gap level [i.e.,  $F_s = h\nu/(\sigma_e + \sigma_p) \sim 2 \text{ mJ/cm}^2$  for GaAs:EL2] and below that which results in a significant number of TPA-generated free carriers ( $\sim 6 \text{ mJ/cm}^2$  for GaAs), the equations for the single beam case (pump only) can be solved, yielding a very simple approximate form for the inverse energy transmission,

$$T^{-1} \approx T_0^{-1} \left[ 1 + \frac{F}{2F_c} \right], \quad F < F_c, F_s. \quad (6)$$

A plot of inverse transmission versus fluence is clearly a straight line with a slope determined by the constant  $F_c$ , where

$$\frac{1}{F_c} \equiv \frac{1}{F_{FCA}} + \frac{1}{\sqrt{2\pi} I_{TPA} \tau} - \frac{1}{F_{SAT}}, \quad (7)$$

and

$$F_{FCA} \equiv \frac{2h\nu\alpha}{[\sigma_{fe}\sigma_e(N-N_A) + \sigma_{fp}\sigma_p N_A](1-R_1)(1-e^{-\alpha l})}, \quad (8)$$

$$F_{SAT} \equiv \frac{2h\nu\alpha}{(\sigma_e + \sigma_p)(\sigma_e - \sigma_p) \left( N_{ss}^+ - N_A \right) (1-R_1)(1-e^{-\alpha l})}, \quad (9)$$

$$I_{TPA} \equiv \frac{\alpha}{\beta(1-R_1)(1-e^{-\alpha l})}. \quad (10)$$

$F_{FCA}$  and  $F_{SAT}$  are critical fluences for free-carrier absorption and saturation of the mid-gap level, and  $I_{TPA}$  is a critical irradiance for two-photon absorption. The pulsewidth ( $HWe^{-1}I$ ) is  $\tau$ ,  $N_{ss}^+$  is the number density of ionized donors at steady state [ $N_{ss} = \sigma_e N / (\sigma_e + \sigma_p)$ ], and

$$\alpha = \sigma_e (N - N_A) + \sigma_p N_A, \quad (11)$$

$$F_s \equiv \frac{h\nu}{\sigma_e + \sigma_p}, \quad (12)$$

and the linear transmission is

$$T_0 = (1-R_1)(1-R_2) e^{-\alpha l}. \quad (13)$$

Using typical parameters for GaAs, we find that  $F_{FCA} \simeq 327 \text{ mJ/cm}^2$ ,  $\sqrt{2\pi} r I_{TPA} \simeq 17 \text{ mJ/cm}^2$  (for 30 ps pulses), and  $F_{SAT} \simeq 114 \text{ mJ/cm}^2$ . Hence, TPA largely determines the slope of the single beam inverse transmission at low fluences.

By contrast, the equations for a weak time-delayed probe (pump-probe case) can be solved for  $F < F_s$  to yield

$$T^{-1} \simeq T_0^{-1} \left[ 1 + 2 \left( \frac{r_{eff}}{r_{probe}} \right)^2 \frac{F}{F_{cp}} \right], \quad (14)$$

where

$$\left( \frac{1}{r_{eff}} \right)^2 = \left( \frac{1}{r_{pump}} \right)^2 + \left( \frac{1}{r_{probe}} \right)^2, \quad (15)$$

and now

$$\frac{1}{F_{cp}} = \frac{1}{F_{FCA}} - \frac{1}{F_{SAT}}. \quad (16)$$

The pump and probe beam radii ( $HWe^{-1}I$ ) are  $r_{pump}$  and  $r_{probe}$ , respectively. Thus, the inverse transmission in this fluence regime is again a straight line with a slope determined by  $F_{cp}$  and the spot

sizes of the pump and probe. Note that, since the probe is too weak to induce significant TPA and the pump is assumed to be sufficiently weak such that FCA associated with TPA-generated carriers is negligible,  $F_{cp}$  is independent of  $\beta$ . That is, TPA plays no significant role in the results for sufficiently low fluences. Again, for GaAs:EL2,  $F_{FCA} \approx 327 \text{ mJ/cm}^2$  and  $F_{SAT} \approx 114 \text{ mJ/cm}^2$ . This implies that, at the lowest fluences, saturation dominates the response. The slope of the inverse transmission versus fluence is negative in this case, and it can be used to extract the ratio of  $\sigma_e$  to  $\sigma_p$ .

As the fluence is increased, the mid-gap levels saturate and for  $F_s < F < F_{cp}$ ,  $F_{cp} \approx F_{FCA}$ , where now we have

$$F_{FCA} = \frac{2h\nu\alpha_{ss}}{\left[ \sigma_{fe}\sigma_e \left( N - N_{ss}^+ \right) + \sigma_{fp}\sigma_p N_{ss}^+ \right] (1-R_1)(1-e^{-\alpha l})} \quad (17)$$

Again using typical numbers for GaAs, we obtain  $F_{FCA} \approx 524 \text{ mJ/cm}^2$ . In the indicated regime, the slope of the inverse transmission yields the free carrier cross section ( $\sigma_{fe} + \sigma_{fp}$ ).

The above solutions neglect TPA-generated FCA. Since this process is important at fluences greater than  $6 \text{ mJ/cm}^2$  in GaAs, numerical solutions must be used to analyze the data in this regime. Fits to the data at these higher fluences provide confirmation of the parameters extracted at lower fluences. By fitting the data over an extended range of fluences, we can distinguish TPA, mid-gap saturation, and FCA.

Both single-beam and two-beam (pump-probe) transmission measurements were conducted, and the two techniques were used in the complimentary manner described above to separately measure instantaneous and cumulative absorption processes.

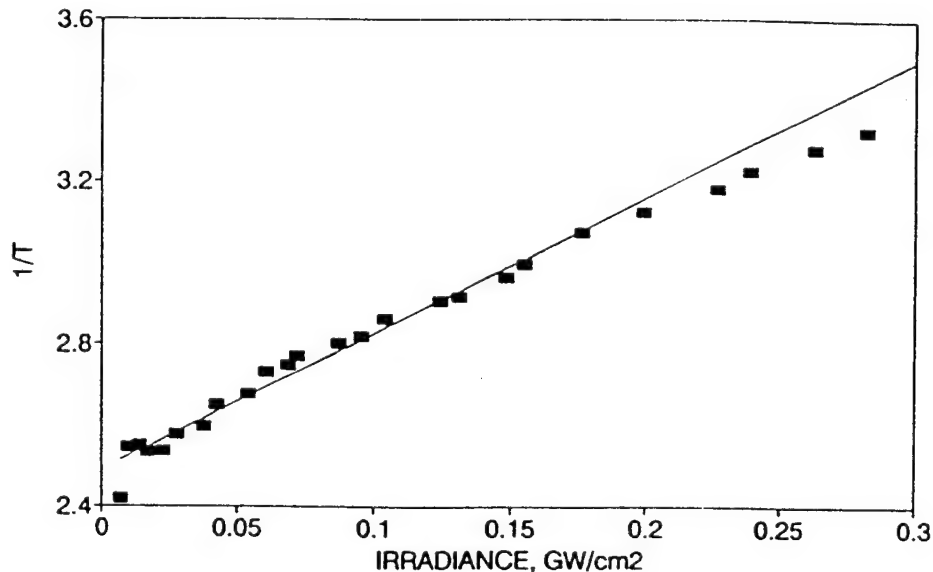


Fig. 1. Low irradiance single beam inverse transmission for undoped GaAs.

The results of the single beam transmission measurement for low irradiances (maximum fluence of approximately  $10 \text{ mJ/cm}^2$ ) are shown in Fig. 1. As expected from the above analysis, the data at the lowest irradiances lie on a straight line, the slope of which provides a value of  $\beta = 20 \text{ cm/GW}$ . The single pulse data are shown over a much wider fluence range in Fig. 2, demonstrating the deviation from the

straight line behavior as the fluence increases. Also shown in Fig. 2 are theoretical curves that illustrate the various contributions to the inverse transmission. The curves were generated by selectively turning on the different processes in our numerical model. Clearly, as expected, the nonlinear response for the single beam measurement is dominated by TPA. It is also clear that deep level saturation provides some degree of compensation for FCA.

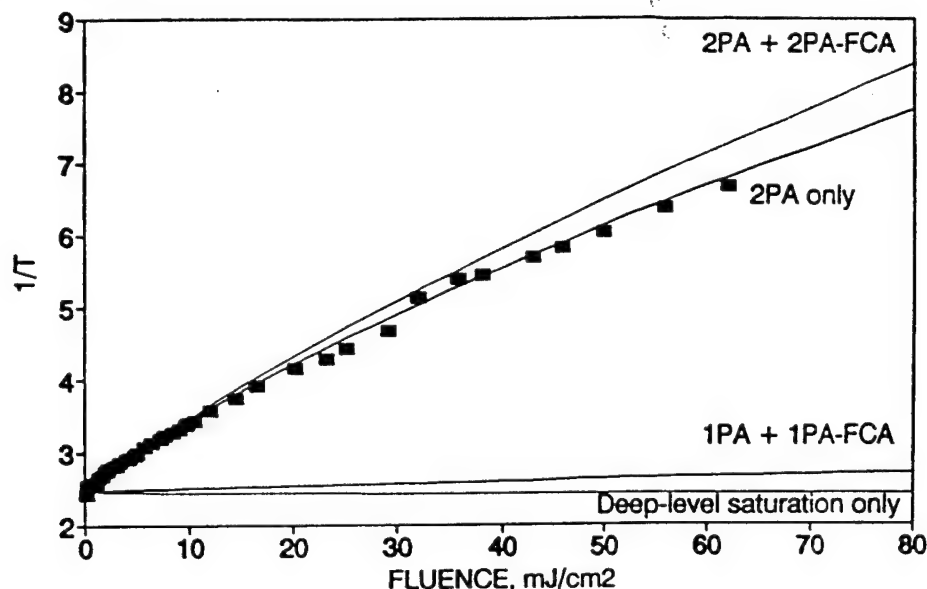


Fig. 2. Measured single-beam inverse transmission over a wide range of fluences for undoped GaAs. The curves represent the result of numerical solutions to the rate equation model with various processes active: 1PA + 1PA-FCA represents single photon absorption and single-photon-generated FCA, 2PA only indicates two photon absorption is the only nonlinear absorption mechanism, 2PA + 2PA-FCA indicates two-photon absorption plus two-photon-generated FCA.

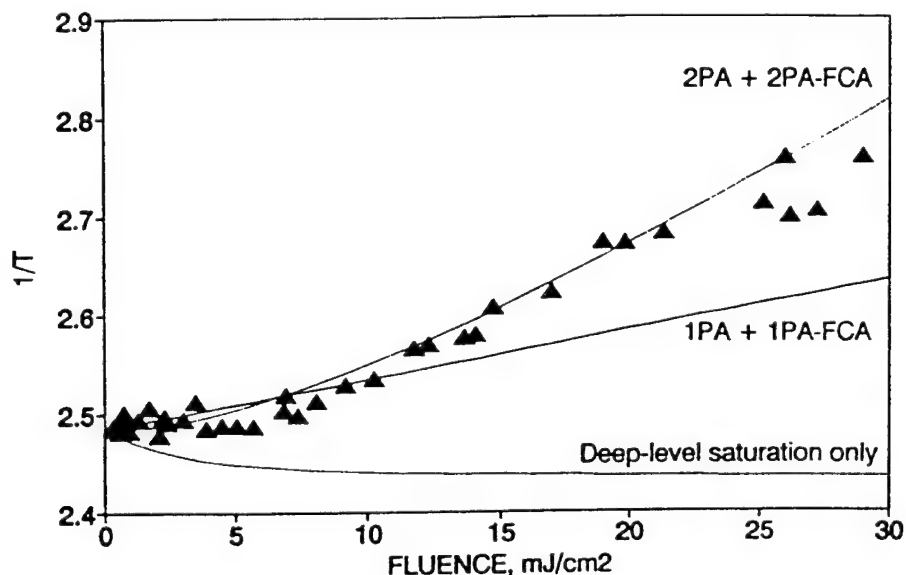


Fig. 3. Probe inverse transmission versus fluence for pump-probe measurement in undoped GaAs. Curves again represent the results of various nonlinear mechanisms active in the model.

By contrast, in Fig. 3 we show the data for the probe transmission in the pump-probe measurement. Again several theoretical curves are shown with various processes turned on in the model. It is clear that deep level saturation strongly influences the probe transmission at the lowest fluences, but single- and two-photon-generated free carriers dominate the absorption at the highest fluences. It is also apparent that the deep level saturation again largely compensates the single-photon-generated FCA, resulting in a flat response until fluences where two-photon-generated FCA becomes significant. Knowing  $\beta$  from the low irradiance single-pulse transmission measurement, the initial linear absorption coefficient, and from previous measurements<sup>3</sup> the values of  $\sigma_p$  and  $\sigma_e$ , a fit to the data in Fig. 3 yields the free carrier absorption cross section ( $\sigma_{fe} + \sigma_{fp}$ ).

In Fig. 4 we display the data and final fits for both the single-beam (pump) and the two-beam probe inverse transmission as a function of fluence. The final parameters, which were used to fit both sets of data, are  $\beta = 20 \text{ cm/GW}$ ,  $(\sigma_{fe} + \sigma_{fp}) = 9 \times 10^{-18} \text{ cm}^2$ ,  $\sigma_e = 1.2 \times 10^{-16} \text{ cm}^2$ , and  $\alpha = 0.92 \text{ cm}^{-1}$ .

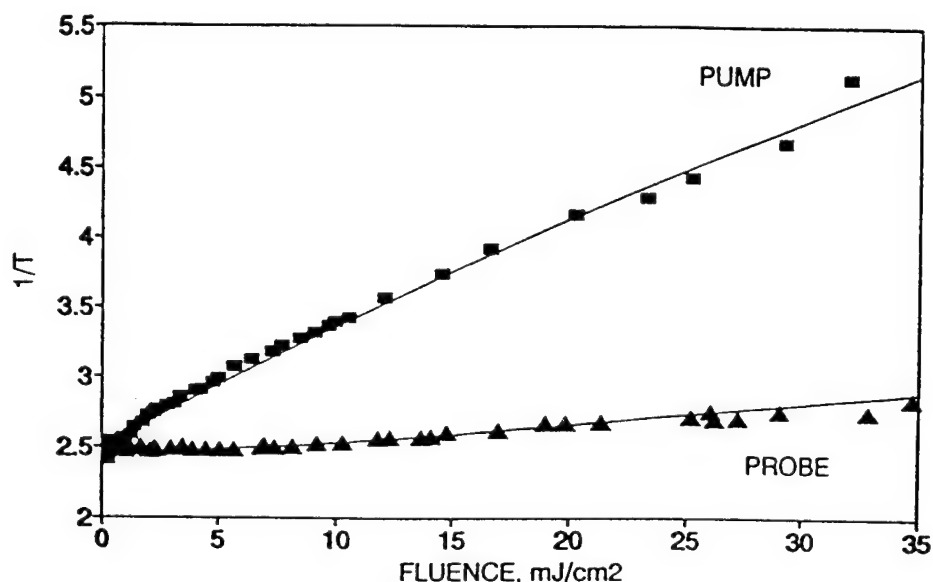


Fig. 4. Final numerical fits to single- and two-beam transmission measurements in undoped GaAs using parameters indicated in the text.

We have applied this technique to all of the doped and undoped semiconductors delineated in the introduction. Although we found the TPA coefficient to be independent of doping for a given semiconductor<sup>4</sup>, we have preliminary evidence that indicates that the FCA cross section may be enhanced in semiconductors with a high density of shallow impurity levels. This is illustrated in Fig. 5, where we show the inverse pump and probe transmissions versus fluence for the Si-doped GaAs sample. The fits to the data were obtained with the same TPA coefficient as for the undoped GaAs sample, but a free-carrier cross section twice as large ( $1.8 \times 10^{-17} \text{ cm}^2$ ) was required. For comparison, the theoretical curve obtained with a cross section of  $9 \times 10^{-18} \text{ cm}^2$  is also shown, indicating the sensitivity of the measurement to this parameter and the discrepancy between the doped and undoped GaAs responses. The doping density in this sample is on the order of  $10^{18} \text{ cm}^{-3}$ , and at room temperature these impurities are largely ionized. The ionized impurities provide additional scattering centers in the GaAs that can provide momentum necessary to promote carriers higher within the band<sup>5</sup>. Our results are consistent with such a process, but additional measurements on a set of samples with a range of doping densities will be required to confirm this result. Clearly a factor of two improvement in the free carrier cross section is attractive for optical limiter applications, but there is a trade off between this and the linear absorption in the sample. That is, the large number of carriers in the conduction band in the dark results in a high linear absorption coefficient ( $6.1 \text{ cm}^{-1}$  compared to  $0.92 \text{ cm}^{-1}$  in the undoped sample) and, therefore, either lower

transmission for equivalent thicknesses or a shorter interaction length for a transmission comparable to the undoped GaAs.

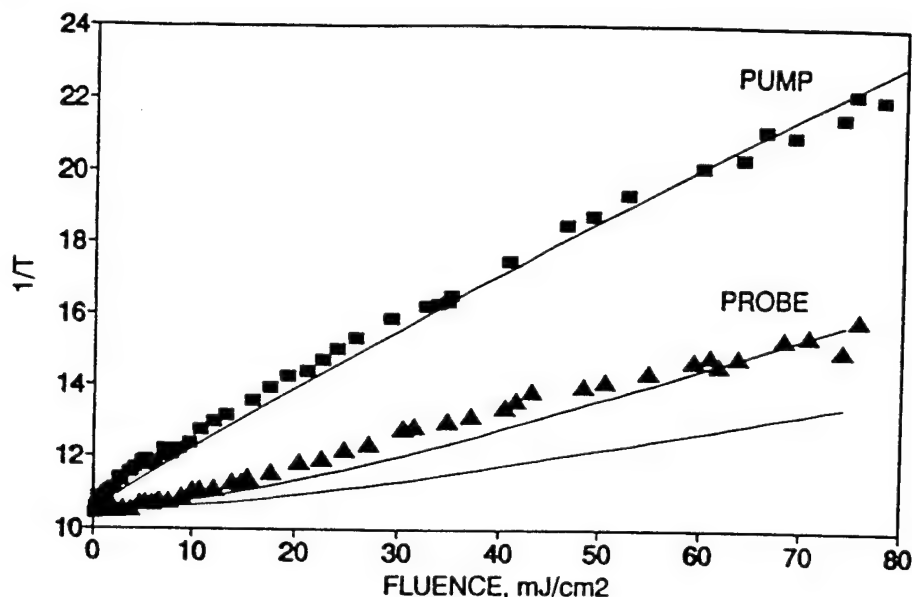


Fig. 5. Single- and two-pulse transmission measurements for GaAs:Si along with theoretical fits. The lower theoretical curve was obtained with the FCA cross section used for undoped GaAs, indicating the enhancement of this parameter measured for the doped sample.

#### 4. NONLINEAR REFRACTION MEASUREMENTS

Four distinct techniques for measuring nonlinear refraction have been analyzed. These include Z-scans<sup>6</sup>, beam deflection, two-beam coupling, and degenerate four-wave mixing. This work is still in progress, and we report here a comparison of the Z-scan and beam deflection techniques along with preliminary data on the undoped GaAs sample.

The most straightforward of the four techniques is the Z-scan, which is a single-beam technique in which the sample is translated through the intermediate focal plane of a lens as the sample transmission is measured. Optically induced lensing in the sample results in position-dependent changes in the beam divergence and, therefore, changes in the spot size at the detector. By measuring the transmission with and without an aperture in front of the detector, both the nonlinear absorption and nonlinear refraction can be determined. This technique has a sensitivity of  $\sim \lambda/200$ . The disadvantages of the technique are that it provides temporally and spatially averaged results, it is monochromatic, and the quality of the data is strongly dependent upon the flatness and parallelism of the sample. A typical Z-scan result for GaAs corrected for nonlinear absorption is shown in Fig. 6. The fact that the transmission initially increases as the sample is moved toward focus and then decreases after focus is a clear indication of a negative refractive nonlinearity. The magnitude of the nonlinearity is found measuring the ratio of the maximum transmission ( $T_p$ , peak transmission) and minimum transmission ( $T_v$  transmission at valley) and using<sup>6</sup>

$$\Delta T_{p-v} = T_p - T_v = 0.405(1-S)^{0.25} |\Delta\phi_0|, \quad (18)$$

where  $S$  is the linear transmission of the aperture, and the average on-axis phase distortion,  $\Delta\phi_0$ , is half the peak phase shift,  $0.5 \Delta\phi_p$ . The peak phase shift for a weakly absorbing material is  $\Delta\phi_p = 2\pi\Delta n l/\lambda$ , where  $l$  is the sample length and  $\Delta n$  is the peak change in index. For the undoped GaAs sample (GaAs:EL2), we measure a peak refractive index change of  $-1.9 \times 10^{-4}$  for a maximum fluence at focus of  $10 \text{ mJ/cm}^2$ . By using the model discussed above, we determined the accumulated on-axis carrier density

averaged over the sample length, which in turn allowed us to extract the change in index per electron-hole pair,  $n_{eh} = -8 \times 10^{-21} \text{ cm}^3$ . Similar measurements were conducted for undoped CdTe and Si, with  $n_{eh} = -6.8 \times 10^{-21}$  and  $-1.8 \times 10^{-21}$  for CdTe and Si, respectively.

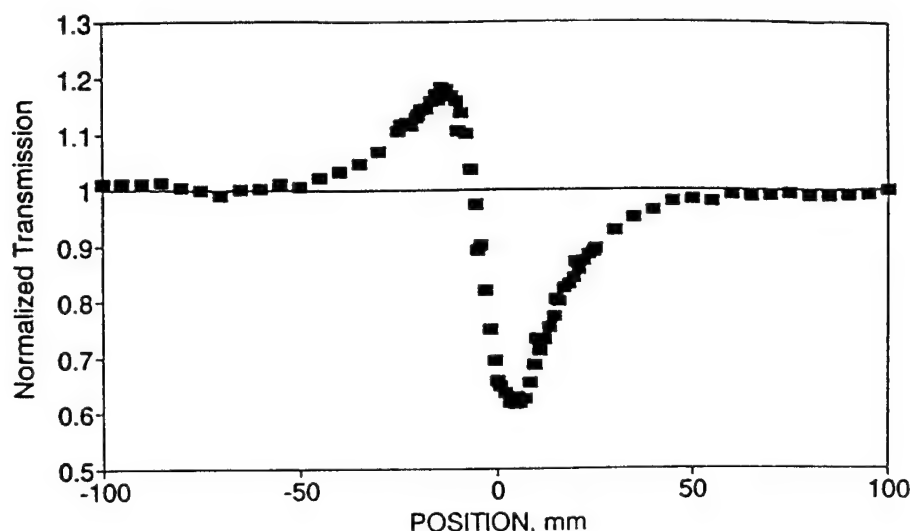


Fig. 6. Z-scan measurement for undoped GaAs.

A second technique that has been applied is that of pump-induced beam deflection<sup>7</sup>. For these measurements, a single pulse is split into a strong pump and a weak probe, the probe is time delayed by 100 ps relative to the pump, and the probe is arranged to propagate parallel to the pump. The optical system is configured such that the probe beam radius is small compared to the pump, and the probe beam is positioned at the inflection point in the Gaussian pump profile. The probe can be separated from the pump by either using crossed polarizations and an analyzer or by introducing a very small angle between the beams so that they can be spatially separated. At low excitation, the probe is linearly transmitted by the sample. At high excitation, however, the pump induces a Gaussian refractive index profile in the semiconductor that deflects the probe. A plot of the angle of deflection versus fluence can be used to extract the optically-induced change in refractive index. We have demonstrated a sensitivity of this technique of  $\lambda/50$  without optimization. The ultimate sensitivity should be comparable to Z-scans. The advantages of this technique are that it provides temporal, spatial, and spectral resolution, and it is less sensitive to sample quality, since the sample is stationary in the experiment. The disadvantage is that it is more complicated than the Z-scan. Results of a typical beam deflection measurement are demonstrated in Fig. 7, where we show data obtained with GaAs:EL2. The refractive index change is extracted using the simple relation

$$\sin \alpha \approx \sqrt{2} |\Delta n| / r_0, \quad (19)$$

for small deflections, where  $\alpha$  is the measured deflection angle and  $r_0$  is the radius ( $\text{HWe}^{-1/2}$ ) of the induced index profile.



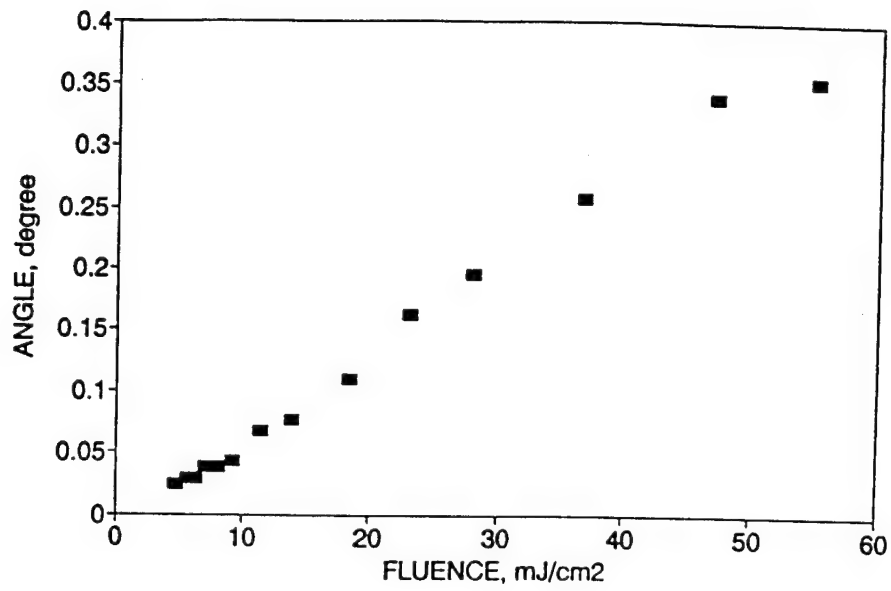


Fig. 7. Beam deflection versus fluence for undoped GaAs.

Table I: Material Parameters

Sample	$\alpha(\text{cm}^{-1})$	$\beta(\text{cm/GW})$	$\sigma(\text{cm}^2) \times 10^{-17}$	$n_{\text{eh}}(\text{cm}^3) \times 10^{-21}$
GaAs undoped	1	20	1	8
GaAs Cr-doped	1.9	22		
GaAs Si-doped	6.2	18	1.8	
CdTe undoped	0	17	2.2	6.8
InP Fe-doped	0.9	26		
Si	9.2	0.65	0.62	1.8

## 5. CONCLUSIONS

We have described our studies of nonlinear absorption and refraction in a variety of doped and undoped semiconductors using single- and multiple-beam picosecond techniques. Our results, to date, are summarized in Table I. Single-beam and pump-probe transmission measurements, together with a simple rate equation model, have allowed us to isolate and evaluate the TPA coefficient,  $\beta$ , and the FCA cross section ( $\sigma_{fe} + \sigma_{fp}$ ) in these samples. We have observed no dependence of  $\beta$  on doping, but we found a dramatic increase in the FCA cross section in a sample of highly Si-doped GaAs. This is consistent with increased scattering due to ionized impurities in the material. The change in index per electron-hole pair was measured in GaAs:EL2, undoped CdTe, and Si using Z-scans and beam deflection.

## 6. ACKNOWLEDGEMENTS

This research was sponsored by the Defense Advanced Research Projects Agency (contract #DAAB07-89-C-F412).

## 7. REFERENCES

1. Thomas F. Boggess, Steven C. Moss, Ian W. Boyd, and Arthur L. Smirl, "Nonlinear-Optical Energy Regulation by Nonlinear Refraction and Absorption in Silicon," *Opt. Lett.*, Vol. 9, pp. 291-293, 1984.
2. Thomas F. Boggess, Arthur L. Smirl, Steven C. Moss, Ian W. Boyd, and Eric W. Van Stryland, "Optical Limiting in GaAs," *IEEE J. Quantum Electron.*, Vol. QE-21, pp. 488-494, 1985.
3. George C. Valley, Thomas F. Boggess, J. Dubard, and Arthur L. Smirl, "Picosecond Pump-Probe Technique to Measure Deep-Level, Free-Carrier, and Two-Photon Cross Sections in GaAs," *J. Appl. Phys.*, Vol. 66, pp. 2407-2413, 1989.
4. W. Andreas Schroeder, Thomas S. Stark, Martin D. Dawson, and Arthur L. Smirl, "Two-Photon Absorption in GaAs and CdTe in the Presence of Mid-Gap States," unpublished.
5. H. Y. Fan, "Effects of Free Carriers on the Optical Properties," in *Semiconductors and Semimetals*, Vol. 3, pp. 406-418, Academic Press, New York, 1967.
6. M. Sheik-Bahae, A. A. Said, and E. W. Van Stryland, *Opt. Lett.*, Vol. 14, pp. 955-957, 1989.
7. A. C. Boccara, D. Fournier, Warren Jackson, and Nabil M. Amer, "Sensitive Photothermal Deflection Technique for Measuring Absorption in Optically Thin Media," *Opt. Lett.*, Vol. 5, pp. 377-379, 1980.

## **Appendix C**

### **Single-Beam and Multiple-Beam Optical Limiters Using Semiconductors**

Optical Engineering, Vol. 30, pp.629-635 (1991)

# Single-beam and multiple-beam optical limiters using semiconductors

Thomas F. Boggess

Arthur L. Smirl, MEMBER SPIE

J. Dubard

A. G. Cui

Steven R. Skinner

Center for Laser Science and Engineering

University of Iowa

124 AMRF, Oakdale Campus

Iowa City, Iowa 52242

**Abstract.** We report our investigations of single- and multiple-beam optical limiter configurations using GaAs and Si as the nonlinear optical materials. Three distinct multiple-beam geometries are discussed. One of these, in which two beams interfere within the semiconductor to produce a grating, takes advantage of transient energy transfer and photorefractive beam coupling to deplete the signal beam. The other two configurations exploit the whole-beam absorptive and refractive index changes induced in the semiconductor by a strong control beam that arrives at the sample before the signal. For one of the latter two configurations, nonlinear absorption and induced defocusing are used to attenuate the signal; in the other, nonlinear absorption and induced deflection are used. We discuss the relative merits of each configuration and compare them to single-beam results obtained under identical experimental conditions.

**Subject terms:** optical limiter; semiconductor; nonlinear absorption; nonlinear refraction.

*Optical Engineering* 30(5), 629-635 (May 1991).

## CONTENTS

1. Introduction
2. Experimental details
3. Coherent beam excisor
4. Control-induced defocusing and nonlinear absorption
5. Control-induced deflection and nonlinear absorption
6. Conclusions
7. Acknowledgments
8. References

## 1. INTRODUCTION

A passive optical limiter (OL) is a nonlinear optical device designed to protect sensitive optical components, such as detectors, from intense optical radiation. The desired response of an ideal OL is such that the low excitation transmission is linear, but at high excitation levels either nonlinear absorption, nonlinear refraction, or both effectively limit the throughput of the OL at a fixed level. The device should be designed such that this "clamped" output level is well below the damage threshold of even the most sensitive sensor; a goal of  $0.1 \mu\text{J}/\text{cm}^2$  would be appropriate for pulsed radiation. An ideal device will also provide a broadband response, function equally well for cw to subnanosecond inputs, possess a large dynamic range and low insertion loss, and maintain a wide field of view. At present, no single device demonstrating all of these properties has been realized. Nevertheless, devices have been demonstrated that satisfy some of these requirements. The most common design of these passive nonlinear optical limiters is based on the simple *single-beam geometry*<sup>1</sup> shown schematically in Fig. 1. Here, a nonlinear optical material is placed at an intermediate focal plane

in an optical system, and the nonlinearities are used to limit the maximum output energy density transmitted through an aperture below some given level. The threshold fluence or irradiance (measured at the nonlinear medium) required to achieve a clamped output is primarily determined by the magnitude of the nonlinearity in the material. Limitation on the strength of the nonlinearities in existing materials requires the use of an intermediate focal plane to achieve a clamped output for input fluences on the order of  $0.1 \mu\text{J}/\text{cm}^2$ . In other words, the enhancement of the optical energy density achieved at the focal plane relative to the input and output planes allows one to most effectively utilize a given nonlinearity.

*Multiple-beam* geometries offer several potential advantages over single-beam configurations. For example, multiple-beam configurations allow access to a number of grating-related phenomena, such as photorefractive energy transfer, polarization rotation, and free-carrier transient energy transfer (TET), that are inherently absent in single-beam configurations (with the exception of OLs that utilize photorefractive beam fanning). Alternatively, by arranging the device such that the signal pulse arrives at the sample coincident in space but delayed in time relative to a strong control pulse, two-beam geometries can be used to take full advantage of optical nonlinearities, such as free-carrier absorption and free-carrier defocusing, that depend on the accumulated carrier density. Furthermore, by offsetting the signal beam relative to the control beam axis, induced beam deflection can also be realized with two-beam techniques.

Recently, a multiple-beam OL that utilizes photorefractive energy transfer from a signal beam into a control beam was demonstrated.<sup>2</sup> In this device, which is called a "coherent beam excisor," a small portion (a few percent) of the input signal is split off and recombined with the signal at a small angle within a high-gain photorefractive material such as  $\text{BaTiO}_3$ . When a coherent optical signal impinges on the device, the two beams interfere within the photorefractive material and write a grating. The grating results in energy transfer between the two beams.

Paper 2934 received June 21, 1990; revised manuscript received Dec. 17, 1990; accepted for publication Dec. 17, 1990. This paper is a revision of a paper presented at the SPIE conference Electro-Optical Materials for Switchings, Coatings, Sensor Optics, and Detectors, April 1990, Orlando, Fla. The paper presented there appears (unrefereed) in SPIE Proc. Vol. 1307.  
© 1991 Society of Photo-Optical Instrumentation Engineers.

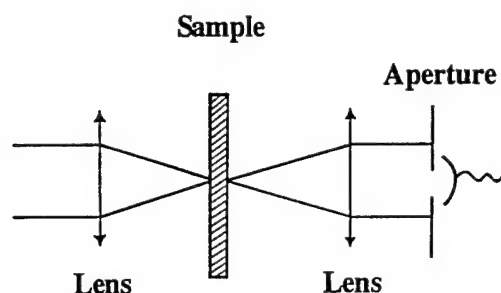


Fig. 1. Single-beam optical power limiter geometry.

By properly choosing the orientation of the photorefractive crystal, energy can be transferred out of the strong beam and into the weak beam with high efficiency, thereby protecting any subsequent optical components. The advantages of this technique are that it has a high throughput, it discriminates against coherent signals, and it does not require spatial filtering. On the other hand, existing high-gain photorefractive materials such as  $\text{BaTiO}_3$ , which are required for the device operation, are too insensitive for this device to be effective against short-pulsed signals.

Here, we report investigations of various multiple-beam OL geometries using optical nonlinearities in semiconductors. Such OLs are potentially suitable for limiting nanosecond or even picosecond optical signals. For each multiple-beam measurement we compare our results to a single-beam measurement conducted with identical experimental conditions (focused spot size, collection geometry, etc.). Three different two-beam configurations will be described: (a) a strong signal beam and a weak copolarized control beam are spatially and temporally coincident in the nonlinear material, (b) a weak signal beam is spatially coincident but temporally delayed with respect to an intense control pulse, and (c) a weak signal is temporally delayed and spatially offset with respect to an intense control pulse. In each case, the transmission of the signal through an aperture is measured as the total fluence is increased. These configurations, which are described in detail below, are designed to study the relative merits of (a) transient energy transfer<sup>3</sup> and photorefractive beam coupling, (b) control-induced lensing and absorption, and (c) control-induced beam deflection and absorption for dynamic attenuation of the signal beam. In each case, we compare the reduction in linear device transmission to the improvement in limiting threshold.

To ensure an accurate comparison of the various configurations, we used two well-characterized semiconductor samples, a 1 mm thick Si wafer and a 3 mm thick sample of undoped semi-insulating GaAs, to provide the limiting action. Measurements were conducted with picosecond pulses at 1.06  $\mu\text{m}$ . These two materials respond quite differently to such excitation.<sup>4,5</sup> At this wavelength and at low fluences, the optical excitation induces indirect optical transitions from the valence band to the X valleys in the conduction band of Si. As the fluence increases and the accumulated carrier density rises, free-carrier absorption, which is the dominant nonlinear absorption mechanism in Si, becomes significant. The negative index change associated with the photogenerated carriers, together with a nonuniform beam profile, results in self-defocusing for the single-beam case and either induced defocusing or beam deflection in the multiple-beam configurations. Furthermore, for configurations in which two beams interfere to write a grating in the Si, the free-carrier refractive nonlinearity results in transient energy transfer from the strong beam into the weak beam.

The absorption mechanisms are dramatically different in the undoped semi-insulating GaAs sample. Such material contains the native midgap antisite defect level EL2, which compensates the background acceptors (typically carbon). At low excitation levels, the optical field induces transitions from the EL2 defect level to the conduction band (cross section  $\sigma_e$ ) and from the valence band to the ionized EL2<sup>+</sup> level (cross section  $\sigma_p$ ). In the dark, the EL2 population in our sample is much greater than the EL2<sup>+</sup> population. Furthermore, we know from previous picosecond pump-probe measurements<sup>5</sup> that  $\sigma_p \approx 0.8\sigma_e$ . As carriers are excited from EL2 to the conduction band, more EL2<sup>+</sup> are available for transitions from the valence band. Since the cross section for the latter process is smaller, this results in a weak bleaching of the overall defect absorption and an increase in signal transmission. For short pulse excitation, however, this bleaching effect is insignificant compared to two-photon absorption (TPA), even at very low fluences. Free-carrier absorption associated with both linearly and two-photon generated carriers also increases the overall absorption. As with Si, these free carriers can be exploited in limiter configurations that are designed to utilize refractive index changes, including those based on transient energy transfer. In contrast to Si, in GaAs there is also a significant instantaneous contribution to the change in index arising from TPA.<sup>6</sup> An additional mechanism that is not present in Si but that can be accessed in GaAs is the photorefractive effect.<sup>7,8</sup> When two beams interfere in GaAs, the photogenerated electrons diffuse from the peaks of the gratings to the troughs, leaving behind excess positive charge. For a properly oriented crystal, the resulting space charge field creates a refractive index change through the electro-optic effect, and beam coupling results. The direction of energy transfer is determined by the crystal orientation and the sign of the dominant charge carrier in a given sample.

In the next section, we describe the laser system used for these studies and details of the measurements. The coherent excisor measurements in photorefractive GaAs are discussed in Sec. 3. In Sec. 4, we describe OLs based on control-induced lensing and absorption, and in Sec. 5 we discuss OLs that use control-induced beam deflection and absorption in GaAs and Si. The relative merits of each configuration and each material are discussed, and our concluding remarks are presented in Sec. 6.

## 2. EXPERIMENTAL DETAILS

All measurements reported here were performed with an actively and passively mode-locked Nd:YAG laser that operated at a repetition rate of 5 Hz and produced 30 ps (FWHM) pulses at 1.064  $\mu\text{m}$ . The laser operated in a TEM<sub>00</sub> mode, and pinhole scans of the beam profile at the sample were used to measure the spot size. These scans also verified that the beam profiles at the sample were Gaussian. Second harmonic techniques were used to measure the duration of each laser pulse, and computer-controlled data acquisition was used to accept data only for pulses with durations within a narrow predetermined window. Similar windows were placed on the energy for each pulse. For each configuration, a single pulse was split into two, a signal that was the primary beam of interest and a control that was used to dynamically attenuate the signal. The transmitted signal was measured through an aperture that was set to clip the linearly transmitted signal at the  $e^{-1}$  point in intensity. In each case, the fluence dependence of the transmitted signal was compared to that obtained in a single-beam configuration with identical focusing and collection optics.

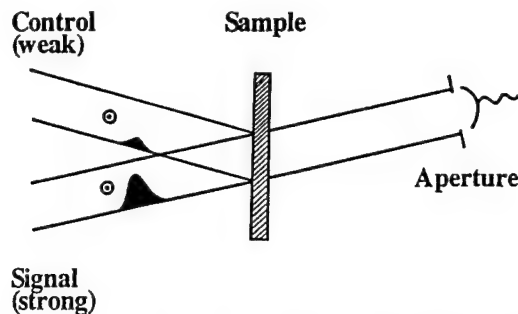


Fig. 2. Two-beam-coupling OL geometry. Control-to-signal fluence ratio 1/25, 0 delay. Sample oriented for control beam photorefractive and TET gain.

### 3. COHERENT BEAM EXCISOR

The first configuration that we investigated is illustrated in Fig. 2. For this geometry, the copolarized control and signal were both spatially and temporally coincident in the GaAs sample, and the control beam fluence was less than the signal fluence. In this configuration, the two pulses interfere to write a grating in the sample, and transient energy transfer, which is always from the strong beam into the weak beam, will deplete the signal. We chose the GaAs sample for this study, since we knew from our previous work that TET is much stronger in the 3 mm thick GaAs than in the 1 mm thick Si for a given fluence.<sup>9</sup> Furthermore, GaAs is photorefractive, whereas Si is not. Therefore, by properly orienting the GaAs crystal, we can in principle use photorefractive beam coupling from the signal into the control beam to deplete the signal. Thus, when we use GaAs in this configuration, nonlinear absorption, defocusing, photorefractive, and transient energy transfer can all contribute to the depletion of the transmitted signal beam.

The results of this measurement are represented by the triangles in Fig. 3, where we plot the energy transmitted through the aperture as a function of incident fluence. For this measurement the signal was 25 times more intense than the control beam, and both beams were collimated with a beam diameter of 2 mm ( $\text{FWe}^{-1}$ ). This specific geometry, which does not take advantage of an intermediate focal plane, was used to make contact with our previous measurements.<sup>8</sup> Clearly, the limiting threshold would be reduced in an intermediate focal plane configuration. The results of the equivalent single-beam measurement are represented by the circles. Comparison with the two-beam results shows that we obtain only a modest improvement in the limiting action in this two-beam-coupling geometry. We measure a 20% reduction in the maximum fluence transmitted by the aperture at a cost of a 4% reduction in linear transmission.

We found that we could continue to trade linear transmission for a reduction in threshold with increasing control-to-signal ratio, but with decreasing efficiency. For a ratio of 1/1, the maximum transmitted fluence was reduced to  $\sim 50\%$  of its single-beam value with a corresponding 50% reduction in linear transmission. For equal control and signal pulses, there is no transient energy transfer, and photorefractive energy transfer is the most obvious mechanism that distinguishes the two-beam and single-beam techniques. In the case of equal signal and control pulses, the same result could have been obtained by placing a linear 50% transmitting filter in front of the detector. This, together with the fact that the limiter performance was independent of crystal orientation, indicates that photorefractive beam coupling is insignificant for this configuration at the fluences of interest.

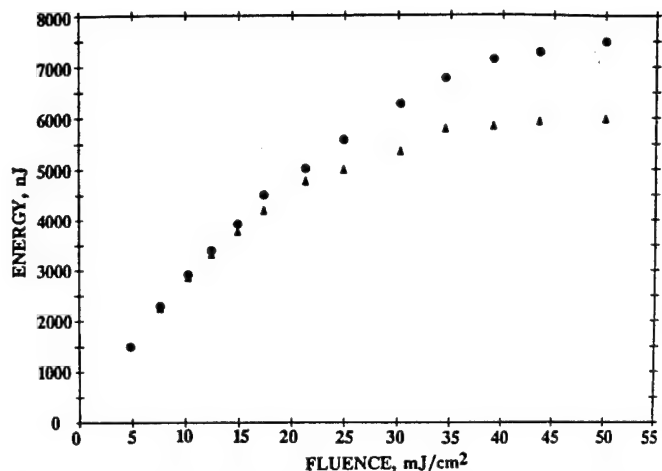


Fig. 3. Single-beam (circle) and two-beam coupling (triangle) limiting curves. Linear transmission of the two-beam device is 96% compared to the single-beam device.

This is consistent with our previous studies<sup>8</sup> of TET and photorefractive beam coupling in GaAs. If the control-to-signal ratio is further increased to a value above unity (i.e., signal weaker than control), transient energy transfer, which is always from strong to weak beam, begins to work against limiting action for the signal. In this case, it is advantageous to "turn off" the grating effects by arranging the signal polarization orthogonal to the control polarization. When the control and signal are temporally coincident, the latter geometry produces a limiting action on the probe exactly equivalent to placing a filter in the signal beam with a transmission equal to the signal-to-control ratio. The dominance of TET in the excisor operation indicates that the maximum improvement in attenuation that can be achieved with this two-beam geometry is 50%, since again the energy transfer is always from the weak to the strong beam.

### 4. CONTROL-INDUCED DEFOCUSING AND NONLINEAR ABSORPTION

Next, we investigated the effects of arranging a weak signal to arrive approximately one pulse width behind an intense control pulse. The advantage of this technique is that the signal "sees" all of the carriers generated by the control pulse; the disadvantage is that the signal does not experience the TPA or the instantaneous index changes induced by the stronger control pulse. Another disadvantage is that, since the control beam should be more intense than the signal, the throughput for this system is necessarily low. For this configuration the two pulses were recombined at an angle of  $2^\circ$  at the sample surface. Both pulses were focused with a 50 cm lens to the same spot ( $\approx 100 \mu\text{m FWe}^{-1}$ ), and an optical delay line was used to allow the signal to arrive at the sample 100 ps after the control. The signal was recollimated with a 30 cm lens and then transmitted through an aperture, which was again set to clip the linearly transmitted signal beam at the  $e^{-1}$  point. The control-to-signal fluence ratio was 25/1. The optical configuration is shown schematically in Fig. 4.

In Fig. 5, the squares represent the results of measuring the energy transmitted through the aperture as a function of total fluence incident on the 1 mm thick Si wafer. The open triangles represent the single-beam measurement, and the closed triangles are those same results divided by the control-to-signal beam ratio of 25. The latter is equivalent to placing a 4% linearly transmitting filter in front of the detector. A comparison of this curve

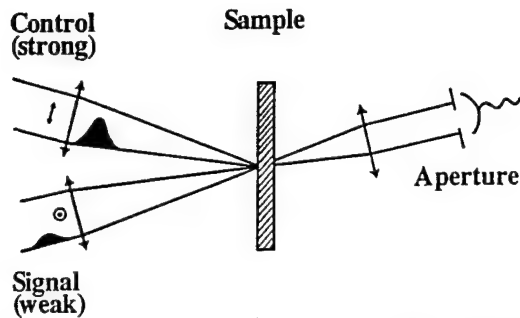


Fig. 4. Control-induced absorption and defocusing OL geometry. Control-to-signal fluence ratio 25/1. Delay -100 ps.

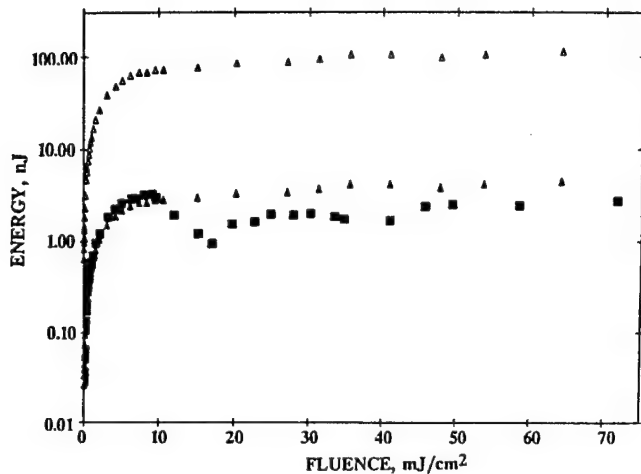


Fig. 5. Single-beam (open triangle) and control-induced absorption and defocusing (square) limiting curves in Si. Closed triangle indicates single-beam data reduced by the linear transmission of the two-beam device (4%).

with the multiple-beam results, therefore, directly illustrates the enhancement of the optical nonlinearities obtained in the multiple-beam case. There are clearly several differences between the single-beam and multiple-beam results. Notice that the maximum output energy is achieved at a lower fluence (15 instead of 30  $\text{mJ}/\text{cm}^2$ ) in the two-beam case. At 20  $\text{mJ}/\text{cm}^2$  the measured signal for the multiple-beam configuration is a factor of two smaller than the normalized value for the equivalent single-beam configuration. Although further reduction in the output for the two-beam geometry is realized at higher fluences (a maximum reduction of a factor of 12 is obtained near 50  $\text{mJ}/\text{cm}^2$ ), this is irrelevant since the device performance is characterized by its maximum output energy.

The other feature that is clearly evident in Fig. 5 is the oscillatory behavior of the transmitted energy with increasing input fluences. The nature of these oscillations has been investigated by measuring the spatial profile of the signal beam at the aperture plane using a vidicon and an optical multichannel analyzer. We find that these oscillations are a manifestation of control-beam-induced defocusing of the signal beam. The spatially Gaussian carrier density profile produced by the control beam acts as a negative Gaussian lens with an effective focal length that is fluence dependent. Diffraction of the signal by this Gaussian lens results in a fluence-dependent ring pattern in the far field. The oscillations with fluence correspond to successive rings moving away from the beam axis. The peaks and the valleys correspond,

respectively, to the states where the ring is transmitted through and blocked by the aperture. This is illustrated in Fig. 6, which shows the spatial profiles measured in the plane of the aperture for several different fluences. This behavior was not evident in either the single-beam data or the zero-delay data. The reason for this is that in these latter geometries the probe "sees" an evolving lens produced by the accumulation of carriers. Our measurements are only sensitive to the time-integrated signal pulse. The temporal averaging, therefore, obscures the oscillations. In contrast, for the present measurement, the optically induced lens is completely formed and static (on a ps time scale) when the signal arrives.

Although similar behavior is observed for GaAs, in contrast with Si, the performance is not improved at all. The results of the measurement made with GaAs are shown in Fig. 7. It is clear that the device response is, in fact, degraded for this geometry. The difference in OL performance for the two semiconductors lies in the nature of the nonlinear absorption processes in these two materials. For 30 ps pulses and the fluences of interest here, the nonlinear absorption in GaAs is dominated by two-photon absorption, whereas free-carrier absorption is dominant in Si. Since TPA depends on the instantaneous intensity in the sample, in the present time-delayed configuration the signal does not experience the strong control-induced TPA in GaAs. Although the refractive nonlinearity associated with TPA-generated free carriers is fully accessed by the signal, the signal does not see the instantaneous refractive index change ( $n_2$ ) generated by the control. On the other hand, since the Si device operates through strictly fluence dependent or cumulative effects, this configuration takes full advantage of all optical nonlinearities in Si.

## 5. CONTROL-INDUCED DEFLECTION AND NONLINEAR ABSORPTION

The final configuration investigated uses the control-beam-induced deflection and absorption of a weak signal beam as a limiting process. The experimental configuration, which is shown schematically in Fig. 8, is similar to that used for photothermal deflection spectroscopy.<sup>10</sup> Here, the signal spot size is considerably smaller than the control spot, and the signal propagates to one side of the control beam axis. Again, the signal is arranged to arrive 100 ps after the control pulse. For this configuration, the signal experiences a quasi-linear, control-induced variation of the refractive index along one of its spatial axes. The nonlinear medium then behaves much like a prism, deflecting the signal beam in a direction that depends on the sign of the nonlinear refractive index and with an angle that depends on the amplitude of the change in the refractive index of the medium. The angle of deflection is also a function of the slope of the index variation, with maximum deflection expected at the inflection point in the profile. This has been verified experimentally, and the measurements reported here have been performed in this configuration.

Figure 9 illustrates the results obtained in Si for a control-to-signal beam radius ratio of 3/1 and a control-to-signal fluence ratio of 20/1. With these parameters the linear transmission of the device is 180 times lower than the transmission of the single-beam optical limiter. Taking this into account, the results show an improvement of about 40% at a fluence of 20  $\text{mJ}/\text{cm}^2$ . At still higher fluences, a reduction in output energy of up to one order of magnitude is measured relative to the single-beam case.



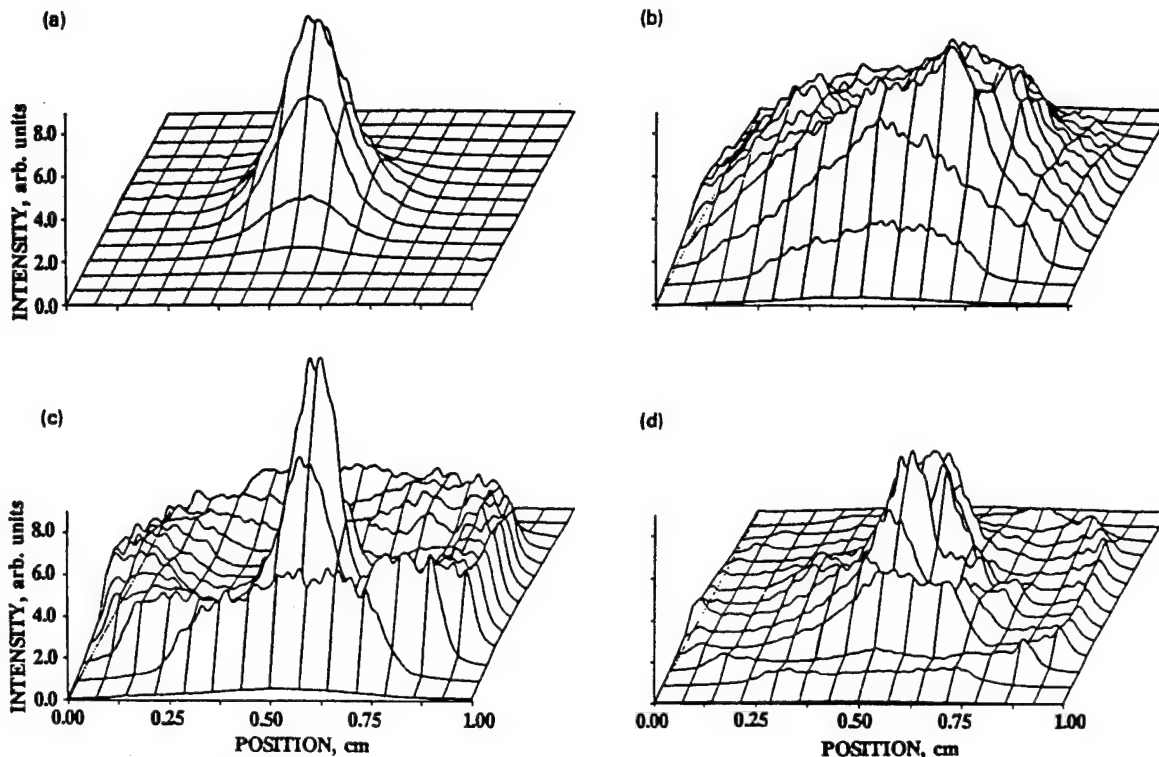


Fig. 6. Spatial profile of the transmitted signal beam at the aperture position for a control beam fluence of (a) 20 mJ/cm<sup>2</sup>, (b) 50 mJ/cm<sup>2</sup>, (c) 80 mJ/cm<sup>2</sup>, and (d) 125 mJ/cm<sup>2</sup> in Si.

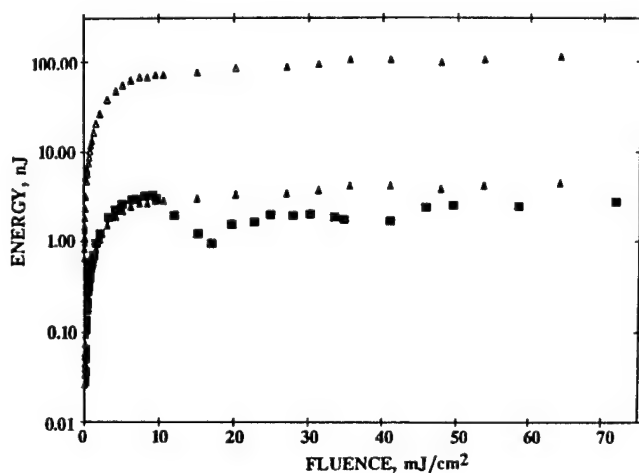


Fig. 7. Single-beam (open triangle) and control-induced absorption and defocusing (square) limiting curves in GaAs. Closed triangle indicates single-beam data reduced by the linear transmission of the two-beam device (4%).

Again, no significant improvement in device performance was observed using GaAs, for reasons discussed in the previous section.

## 6. CONCLUSIONS

In summary, it is clear that an efficient coherent excisor OL cannot be realized using transient energy transfer alone, since this effect always transfers energy from the strong to the weak beam, therefore providing at most an attenuation factor of 2. Nevertheless, when used in conjunction with the other nonlinearities already active for a single beam OL, transient energy

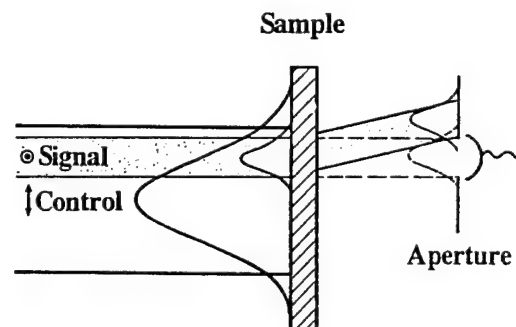


Fig. 8. Control-induced absorption and defocusing OL geometry. Control-to-signal fluence ratio 20/1, control-to-signal beam size ratio 3/1, delay - 100 ps.

transfer gives a modest improvement in the limiting performance. The improvement, however, comes at the expense of additional complexity in the device design. We believe the most promising coherent excisors will continue to rely on photorefractive beam coupling because of the asymmetric gain that is possible using the photorefractive effect (i.e., nearly all of one beam can be transferred into the other). For example, a two-beam-coupling gain length product  $\Gamma l$  of 15 is completely feasible in, e.g., 1 cm of BaTiO<sub>3</sub>. Since the transmission of the coherent excisor is  $T = 1/[1 + m \exp(\Gamma l)]$ , where  $m$  is the ratio of the control to signal beam intensity, it is possible to achieve 45 dB attenuation with  $m = 0.01$ . Thus, for a 1 mJ/cm<sup>2</sup> input, the output of such a device will be less than 0.1  $\mu$ J/cm<sup>2</sup>. On the other hand, there is a fundamental problem with existing high-gain photorefractive materials like BaTiO<sub>3</sub>, i.e., their low sensitivities. For example, to achieve a  $\Gamma l$  of 15 in BaTiO<sub>3</sub>, we must achieve saturation, which occurs at approximately 100



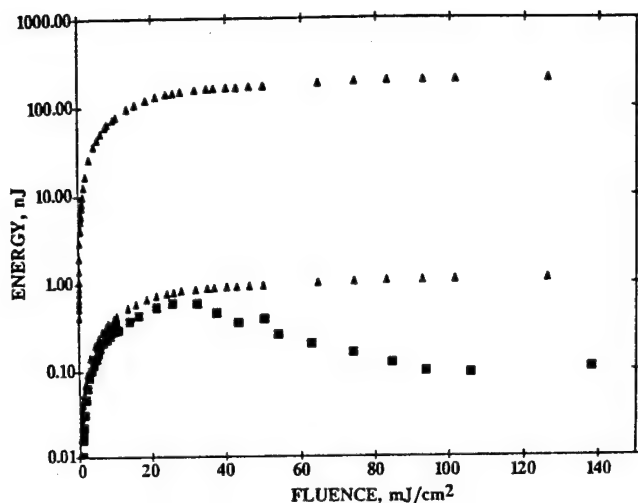


Fig. 9. Single-beam (open triangle) and control-induced absorption and deflection (square) limiting curves in Si. Closed triangle indicates single-beam data reduced by the linear transmission of the two-beam device (0.055%).

mJ/cm<sup>2</sup>. By contrast, photorefractive semiconductors like GaAs are much more sensitive than BaTiO<sub>3</sub> (saturation fluence  $\sim 1$  mJ/cm<sup>2</sup>), but the gain is too low to provide significant attenuation ( $\Gamma$  at saturation is  $\sim 0.4$  in our 3 mm crystal). The potential for the coherent excisor configuration for optical limiting clearly rests with the development and/or identification of more sensitive high-gain photorefractive materials.

We find that the two-beam time-delayed configurations can offer improvements in both the threshold and output fluences when compared to single-beam configurations. The price paid for this improvement, however, is increased complexity in the optical system and a substantial reduction in the system throughput.

The limited success of the multiple beam configurations led us to reconsider the properties of single-beam intermediate focal plane limiters based on GaAs and Si. In an f250 optical system, we achieved a clamped output for a (threshold) fluence at the intermediate focal plane of 20 mJ/cm<sup>2</sup> for GaAs using 30 ps pulses at 1.06  $\mu$ m. Since the nonlinearities in GaAs are dominated by two-photon absorption for these optical pulses, it is more appropriate to discuss threshold in terms of irradiance, which has a corresponding value of 630 MW/cm<sup>2</sup>. For 1:1 imaging, the clamped output fluence is 3.2  $\mu$ J/cm<sup>2</sup>. Keeping in mind our goal of a clamped output fluence of 0.1  $\mu$ J/cm<sup>2</sup>, we recognize that this performance can be achieved if we design our optical system such that we achieve threshold (630 MW/cm<sup>2</sup>) for an input fluence of 0.1  $\mu$ J/cm<sup>2</sup>. Note that this is a worst case scenario, since the system transmission will always be less than unity at threshold. If we assume that we completely fill a 1 in. input optic, this leads to a requirement that  $(f\#)^2\tau < 10^{-8}$  s, where  $\tau$  is the input pulse duration. Furthermore, we recognize that an  $f\#$  of less than 30 would result in a Rayleigh range less than our sample lengths. Requiring an  $f\#$  greater than 30 leads to a maximum pulse duration of 38 ps for limiting at the 0.1  $\mu$ J/cm<sup>2</sup> level for GaAs. This is a significant restriction for limiters based on GaAs.

On the other hand, the nonlinearities in Si are fluence dependent rather than irradiance dependent. The threshold in the silicon limiter is less than 40 mJ/cm<sup>2</sup>, and the clamped output fluence (again using 1:1 imaging) is 6.4  $\mu$ J/cm<sup>2</sup>. Using the same approach as described above for GaAs, we find that we can achieve the threshold fluence for an input of 0.1  $\mu$ J/cm<sup>2</sup> with

an f30 system. In contrast with the GaAs limiter, the performance of the Si limiter should be nearly independent of pulse width up to input pulse durations of  $\sim 100$  ns, at which point diffusion of carriers out of the beam could become significant. The limiting threshold and single-shot melting threshold<sup>11</sup> ( $\sim 2$  J/cm<sup>2</sup>) indicate a dynamic range of this device of nearly 20 dB. With good antireflection coatings on each Si surface, a low fluence (linear) transmission of  $> 40\%$  can be expected (for 1 mm thick samples). The major disadvantage of Si limiters, unlike two-photon absorbers such as GaAs, is that they are narrow band, since they function well only for photon energies near the indirect band-gap energy ( $E_g = 1.1$  eV) where the linear absorbance is low. A similar performance is anticipated for other indirect band gap semiconductors. Thus, AlGaAs with high Al concentrations might be an appropriate material for optical limiting of visible radiation over a narrow bandwidth. Ideally, one would like to identify a nonlinear material that has a response that is broadband, like that of the two-photon absorbers, but is also pulse-width independent, like that of Si.

## 7. ACKNOWLEDGMENTS

This research was supported by the Defense Advanced Research Projects Agency.

## 8. REFERENCES

1. See, e.g., M. J. Soileau, W. E. Williams, and E. W. Van Stryland, "Optical power limiter with picosecond response time," *IEEE J. Quantum Electron.* QE-19, 731-735 (1983); T. F. Boggess, S. C. Moss, I. W. Boyd, and A. L. Smirl, "Nonlinear energy regulation by nonlinear refraction and absorption in silicon," *Opt. Lett.* 9, 291-293 (1984); T. F. Boggess, A. L. Smirl, S. C. Moss, I. W. Boyd, and E. W. Van Stryland, "Optical limiting in GaAs," *IEEE J. Quantum Electron.* QE-21, 488-494 (1985).
2. S. W. McCahon and M. B. Klein, "Coherent beam excisors using the photorefractive effect in BaTiO<sub>3</sub>," in *Materials for Optical Switches, Isolators, and Limiters*, M. J. Soileau, ed., Proc. SPIE 1105, 119-124 (1989).
3. V. L. Vinetskii, N. V. Kukhtarev, and M. S. Soskin, "Transformation of intensities and phases of light beams by transient 'undisplaced' holographic grating," *Sov. J. Quantum Electron.* 7, 230-233 (1977).
4. T. F. Boggess, K. Bohnert, K. Mansour, S. C. Moss, I. W. Boyd, and A. L. Smirl, "Simultaneous measurement of the two-photon coefficient and free-carrier cross section above the band gap of crystalline silicon," *IEEE J. Quantum Electron.* QE-22, 360-368 (1986).
5. G. C. Valley, T. F. Boggess, J. Dubard, and A. L. Smirl, "Picosecond pump-probe technique to measure deep-level, free-carrier, and two-photon cross sections in GaAs," *J. Appl. Phys.* 66, 2407-2413 (1989).
6. M. Sheik-Bahae, D. J. Hagan, and E. W. Van Stryland, "Dispersion and band-gap scaling of the electronic Kerr effect in solids associated with two-photon absorption," *Phys. Rev. Lett.* 65, 96-99 (1990).
7. M. B. Klein, "Beam coupling in undoped GaAs at 1.06  $\mu$ m using the photorefractive effect," *Opt. Lett.* 9, 350-352 (1984).
8. G. C. Valley, A. L. Smirl, M. B. Klein, K. Bohnert, and T. F. Boggess, "Picosecond photorefractive beam coupling in GaAs," *Opt. Lett.* 11, 647-649 (1986).
9. J. Dubard, A. L. Smirl, A. G. Cui, G. C. Valley, and T. F. Boggess, "Beam amplification by transient energy transfer in GaAs and Si," *Phys. Status Solidi B* 150, 913-919 (1989).
10. A. C. Boccara, D. Fournier, W. Jackson, and N. M. Amer, "Sensitive photothermal deflection technique for measuring absorption in optically thin media," *Opt. Lett.* 5, 377-379 (1980).
11. I. W. Boyd, S. C. Moss, T. F. Boggess, and A. L. Smirl, "Various phase transitions and changes in surface morphology of crystalline silicon induced by 4-260-ps pulses of 1- $\mu$ m radiation," *Appl. Phys. Lett.* 45, 80-82 (1984).

**Thomas F. Boggess** graduated from Lamar University in Beaumont, Texas, with a BS degree in physics in 1978. He received the MS and Ph.D. degrees in physics from North Texas State University in Denton, Texas, in 1980 and 1982, respectively. From 1982 to 1985 he was a postdoctoral research scientist at North Texas State University, and in 1985 he joined the faculty as an assistant professor. In 1987 Boggess became a member of the technical staff at Hughes Research Laboratories in Malibu, Calif., where he was responsible for developing ultrafast laser facilities and research programs utilizing those facilities. Since 1989 he has been with the Center for Laser Science and Engineering at the University of Iowa in Iowa City. He is also a member of the Department of Electrical and Computer Engineering at the University. His current research interests include the study of ultrafast carrier dynamics and optical nonlinearities in strained semiconductor microstructures and optical limiters and switches based on semiconductors and organometallic compounds. Boggess is a member of the OSA and APS, and is a senior member of IEEE.

**Arthur L. Smirl:** Biography and photograph unavailable.

**J. Dubard:** Biography and photograph unavailable.



**A. G. Cui** received the BS degree in Laser Technology from Tianjin University in 1980 and the MS degree in optics from Huazhong University of Science & Technology, China, in 1983. He worked in the Department of Physics of Tianjin University from 1983 to 1985. Since 1987, he has been working toward the Ph.D. degree in physics at the Center for Applied Quantum Electronics at the University of North Texas and the Center for Laser Science & Engineering at the University of Iowa. He expects to receive his Ph.D. degree from the University of North Texas in 1991. His current research interests include nonlinear optical properties of semiconductors, picosecond spectroscopy, and nonlinear optical devices.

**Steven R. Skinner** received the BS and MS degrees in electrical and computer engineering from the University of Iowa in 1985 and 1989, respectively. He was a design engineer for Electronic Technology Corp., Cedar Rapids, Iowa, from 1985 to 1987. He is currently working toward a Ph.D. degree at the center for Laser Science and Engineering at the University of Iowa. His interests include ultrafast nonlinear optics and solitary wave propagation phenomena.

## **Appendix D**

### **Optical Nonlinearities and Optical Limiting in GaP at 532 nm**

SPIE, Vol. 1692, pp. 191-196 (1992)



*Reprinted from*

# ***Nonlinear and Electro-Optic Materials for Optical Switching***

23–24 April 1992  
Orlando, Florida



**Volume 1692**

## Optical nonlinearities and optical limiting in GaP at 532 nm

S.J. Rychnovsky, G.R. Allan, C.H. Venzke, Arthur L. Smirl, and Thomas F. Boggess

Center for Laser Science and Engineering  
The University of Iowa  
124 AMRF, Oakdale Campus, Iowa City, Iowa 52242

### ABSTRACT

We demonstrate a proof-of-principle, GaP optical energy limiter for 532 nm, 25 ps, pulsed radiation that exhibits an output limiting level of less than  $1 \mu\text{J}/\text{cm}^2$ . Optical limiting at this level is significant for use in systems designed to protect the human eye from laser radiation damage. The device employs a standard configuration that is realized by placing the GaP at the intermediate focal plane of a 1-to-1 inverting telescope, which is followed by an aperture set to clip the linearly transmitted beam at the  $1/e$  point of the irradiance profile. The linear (indirect) absorption in GaP at this wavelength results in the optical generation of very large densities of free carriers. We therefore anticipate the performance of this device to be highly dependent on free carrier nonlinearities. This is confirmed by performing both two beam and single beam measurements on the material itself in order to determine both the absorptive and refractive parameters at this wavelength. We find that the free carrier absorption cross section is  $\approx 2 \times 10^{-18} \text{ cm}^2$ , and the change in index per photogenerated electron hole pair is  $\approx -2.4 \times 10^{-22} \text{ cm}^3$ .

### 1. INTRODUCTION

It is well known that the optical nonlinearities inherent to semiconductor materials show promise for use in optical limiters for sensor protection. To date, much of the limiting related research on these materials has utilized two photon absorption (TPA)<sup>1-2</sup> in semiconductors with a band gap energy greater than the photon energy of the optical source. This allows high transmission at low intensities, yet at high intensities, processes associated with TPA limit the throughput of the device. These processes can include TPA, two-photon-generated-free-carrier absorption, and defocusing caused by an induced change in refractive index. One of the primary advantages of a device based on such two photon effects is the potentially large bandwidth over which it may be used. In principle, such a device could possess a bandwidth on the order of  $E_g/2 < h\nu < E_g$ , which for wide gap semiconductors can be hundreds of nanometers. The principal disadvantage of these devices is their reliance on the intensity dependent TPA process. As a result, they may only be practical for protection against short pulse laser sources.

In order to provide optical limiting over a range of pulse widths, it would be advantageous to have a device with a response that is fluence dependent rather than intensity dependent. The potential for such a device was demonstrated in Si at  $1.06 \mu\text{m}$  by Boggess et. al.<sup>3</sup> In this case, linear indirect absorption was used to excite large numbers of free carriers that subsequently lead to optical nonlinearities. Since the number of carriers generated is fluence dependent (provided the timescales of interest are long compared to carrier recombination and diffusion times), this technique could be used for optical limiting over a wide range of pulse widths. Furthermore, because Si is an indirect gap semiconductor, the free carrier lifetime is long. This enhances both the maximum carrier density that can be achieved and the fluence dependent nature of the device, as the corresponding optical nonlinearities will be long-lived as well. A drawback of this technique is that the absorption process itself is strongly frequency dependent, hence the device is narrowband, unlike the case of TPA. Therefore, the price paid for enhancing the fluence dependent nature of the device is that there will be a corresponding decrease in bandwidth.

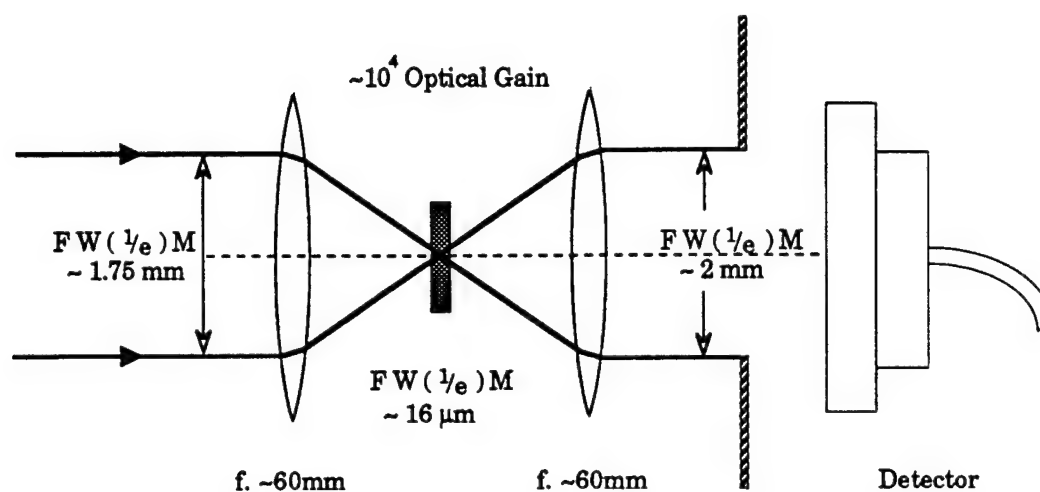


Figure 1: Intermediate focal plane geometry used to demonstrate optical limiting in GaP.

Although the concept of an optical limiter based on single photon generation can be demonstrated in Si, a practical device for eye protection will of course have to be based on a visible band gap semiconductor. In this work we demonstrate optical limiting in such a semiconductor, specifically GaP, an indirect gap semiconductor that is transparent over the red half of the visible spectrum. We further quantify the nonlinear optical parameters in this material so as to assess the contributions of the various mechanisms to the optical limiting. This information will be necessary as a guide to future optical limiting research in this material as well as in the optimization of actual device designs.

## 2. DEMONSTRATION OF OPTICAL LIMITING IN GaP

In order to demonstrate that GaP does indeed have potential as an optical limiting material, we constructed a simple proof-of-principle device based on GaP as illustrated in Figure 1. The intermediate focal plane geometry shown in this figure is a commonly used arrangement for demonstrating optical limiting performance and it is conceptually similar to what may well be used in actual optical limiting devices. In this configuration, the nonlinear material is placed at the intermediate focal plane to take advantage of the high optical gain provided by the input lens. This causes the nonlinearities to be induced at much lower input fluences than if the material were illuminated directly by the beam, thus causing the overall throughput to limit at a much lower level than would occur for the case of direct illumination. Furthermore, if the limiting material exhibits nonlinear refraction, the intensity gradients near focus can induce a lens in the material leading to defocusing in the far field. In the case of semiconductors, this contribution to the limiting can be the dominant mechanism. Our specific experimental arrangement consists of a pair of bi-convex lenses, each with a nominal focal length of 60 mm, which are separated by two focal lengths so as to provide unity system gain. For our input beam parameters this system provides an optical gain at the intermediate focal plane of

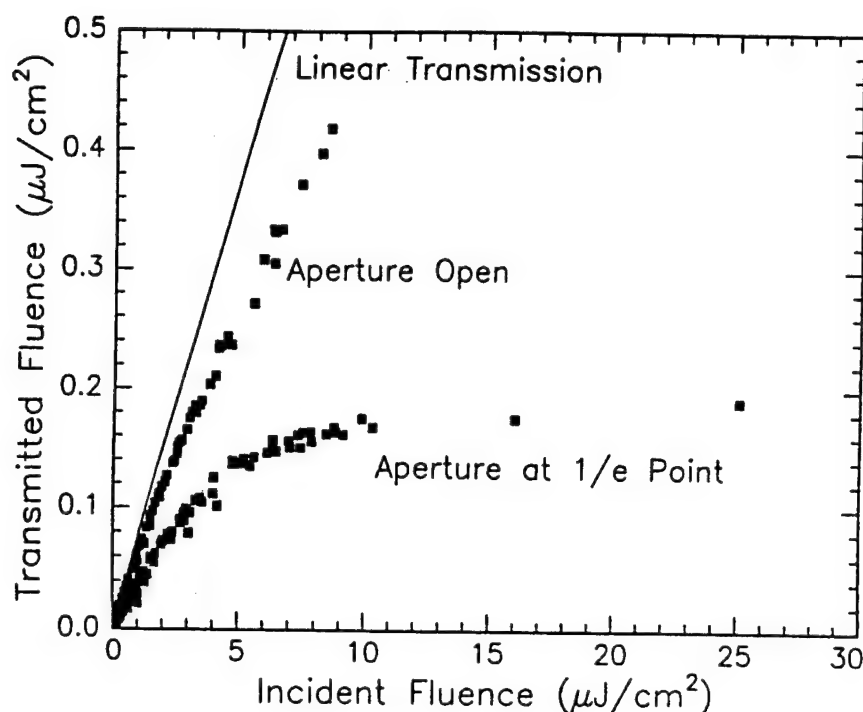


Figure 2: Optical limiting in GaP. A comparison of the aperture closed vs. aperture open cases indicates the limiting is primarily the result of a refractive nonlinearity.

$> 10^4$ . An aperture is located 8.5 cm beyond the second lens and its diameter is adjusted so as to clip the beam at a radius at which the intensity is  $1/e$  of its peak value (when operated in the linear regime). The system is illuminated by a pulsed beam at 532 nm from a frequency doubled Nd:YAG laser operating at a 1 Hz repetition rate. This wavelength will generate carriers via indirect absorption, yet the photon energy is insufficient for direct band-to-band transitions. The laser pulses are nearly Gaussian in both time and space with a time duration of 25 picoseconds (FWHM) and a spatial width of  $16 \mu\text{m}$  (FW1/eM) at the sample site. The GaP sample (100 microns thick) was mounted at the intermediate focal plane of this optical system.

In addition to optical limiting from free carrier absorption, limiting in this arrangement should result from the defocusing which arises from an induced negative index change in the GaP. At our 532 nm wavelength, we anticipate two dominant contributions to the refractive index change in this material. The first of these is the index change associated with any free carriers generated via linear absorption. Based on a simple Drude type model we expect this free carrier component to provide a negative index change. In addition to this contribution, a second contribution should arise as the result of band filling. Although our photon energy is above the indirect band gap, it is still below the strong resonance associated with the direct band gap. As a result, interband absorption at this wavelength should provide an additional negative index change as would be predicted by a Lorentz type model.

The experimental results are given in Figure 2 both for the case of the aperture completely open, as well as for the case of the aperture closed to the  $1/e$  point as discussed above. A straight line indicating linear transmission of the system is also provided for reference. Notice that the arrangement using the restricted aperture provides an optical limiting level of  $0.2 \mu\text{J}/\text{cm}^2$ . When the aperture is opened there is only a minor deviation from the linear response, indicating that nonlinear absorption contributes little to

the optical limiting. In fact, by comparing the two cases (aperture open vs. aperture partially open) it is clear that the primary optical limiting action is due to severe clipping of the beam by the aperture at the higher fluences. We attribute this to defocusing which arises from an induced negative change in the index of refraction as discussed above. Because self-focusing can also give this type of response, we performed z-scan<sup>4</sup> measurements to confirm that the sign of the index change is indeed negative.

In order to estimate the dynamic range, the input fluence was increased until single shot damage occurred. We found that at input fluences on the order of  $30 \mu\text{J}/\text{cm}^2$  damage occurred which reduced the linear transmission. (Here we define damage to be an irreversible reduction in linear transmission of at least 10%.) No attempt was made to assess how this damage would affect the image quality. Therefore, as a worst case, we can quantify the "clamping range" of such a device as  $3\text{--}30 \mu\text{J}/\text{cm}^2$  at the input to the limiter, yielding a dynamic range of approximately 10 dB. We emphasize, however, that the device continues to limit far beyond the  $30 \mu\text{J}/\text{cm}^2$  level, i.e., it is fail safe over the fluence range of our experimental setup.

### 3. MEASUREMENT OF NONLINEAR PARAMETERS

Although this proof of principle demonstration indicates that GaP holds promise as a material for use in optical limiters, it will be necessary to better quantify the relative contributions of the various nonlinear mechanisms before a practical device can be considered. Therefore, we have initiated a study of the salient nonlinear absorptive and refractive properties of GaP at 532 nm. For preliminary measurements we have configured two experimental arrangements, a pump-probe setup for quantitative measurements of absorptive parameters and a defocusing arrangement to determine the index change per optically generated free carrier pair, ( $n_{eh}$ ). Furthermore, we have obtained a well characterized wafer of GaP in order to minimize any experimental errors related to unknown material parameters. This sample is LED substrate material which is sulfur doped to yield a carrier density of  $10^{18} \text{ cm}^{-3}$ . The linear absorption coefficient of this antireflection-coated sample was measured to be  $118 \text{ cm}^{-1}$  at 532 nm, and the sample was polished to a thickness of  $140 \mu\text{m}$  which yields a linear transmission of approximately 20%.

In the pump-probe arrangement, a strong pump beam is used to excite a volume within the crystal and the resulting change in transmission is then measured with a much weaker probe beam. By varying the position of a delay stage in the probe beam path, it is then possible to measure the induced absorption as a function of time delay, and in this way the nonlinear absorptive dynamics of the crystal are determined. It is important to note that this measurement is carefully configured such that all of the transmitted probe energy is detected. Hence, it is insensitive to any induced refractive index change, i.e., only absorptive changes are measured. Such measurements reveal an induced absorption that is essentially constant on a nanosecond time scale. We attribute this to free carrier absorption, and by modelling these data we extract a free carrier absorption cross section of  $\sigma = 2 \times 10^{-18} \text{ cm}^2$ .

With the absorptive nonlinearity characterized, we next quantified the refractive parameters using a single beam defocusing arrangement. Here, a best form lens with a 240 mm focal length was used to focus the incident Gaussian beam to a  $28 \mu\text{m}$  spot (FW1/eM) on the sample of GaP. A limiting aperture with a diameter of 4.1 mm was then placed 45 cm behind the sample. This aperture causes the overall transmission to be sensitive to defocusing. The output fluence was then measured as a function of incident fluence. In order to model this experiment, a Fresnel type propagation code was used in conjunction with a system of rate equations. For the purposes of modelling, we have assumed that no defocusing occurs within the sample, an assumption that is justified by the small sample thickness and focusing conditions of the beam (thin limiter configuration). Because we have determined the absorptive parameters from the pump-probe experiment above, the only unknown parameter in this modelling is the induced index change. Therefore, by fitting the experimental curve using this model, we are able to extract a value for the induced index change.



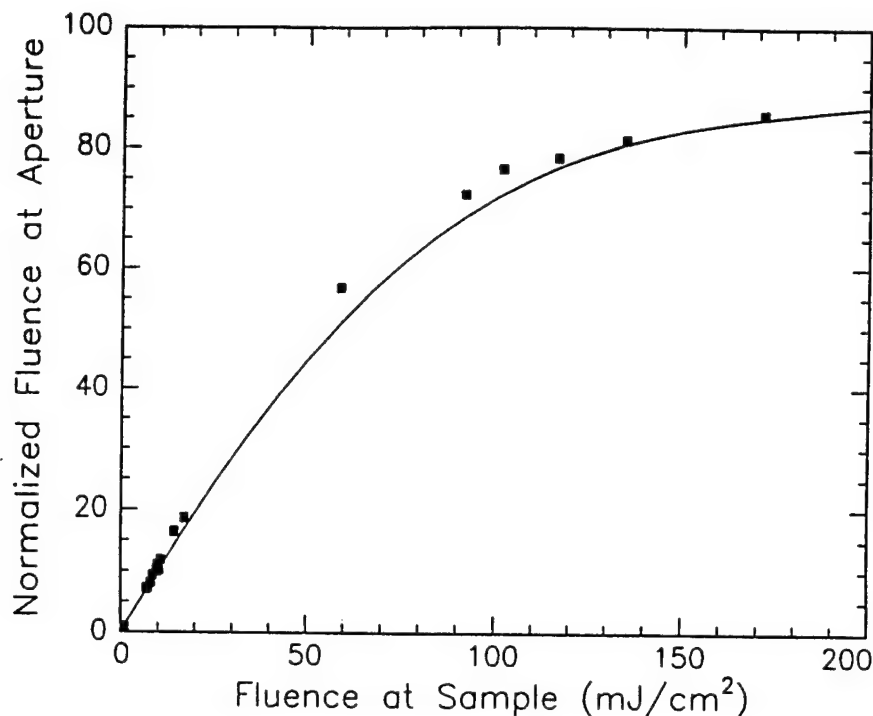


Figure 3: Normalized output fluence vs input fluence for the experimental defocusing arrangement. The numerical fit shown (solid line) was used to extract a value for  $n_{eh}$  of  $-2.4 \times 10^{-22} \text{ cm}^3$ .

The results of such an experiment and the corresponding theoretical fit are given in Figure 3. By attributing the induced index change entirely to the carrier generation process, the index change per free carrier pair was determined to be  $n_{eh} = -2.4 \times 10^{-22} \text{ cm}^3$ . This fit is given by the solid line in Figure 4. Although bound electronic effects ( $n_2$ ) could also be contributing to the index change, we expect their contribution to be relatively small. Experiments with different pulse widths are currently underway to verify this.

#### 4. CONCLUSIONS

By using a simple optical system that utilizes an intermediate focal plane, we have demonstrated a proof-of-principle optical limiter based on GaP. This material functions as an optical limiter in the visible spectrum, near the peak of the human eye response. We anticipate that this material should give a response that is primarily fluence dependent, an advantage over TPA based devices. Also important is the fact that it limits the throughput fluence to levels well below  $1 \mu\text{J}/\text{cm}^2$ . As a result of the promising potential of this material we were motivated to measure the nonlinear optical parameters relevant to optical limiting at this wavelength. Using two simple experiments we have measured the free carrier cross section and the index change per carrier pair.

Although GaP appears to be a promising semiconductor material for use in a practical eye safe optical limiter, there are significant systems issues which must yet be addressed. A primary concern for this material is the potential for extending the operating bandwidth so that the device will provide optical limiting over a significant portion of the visible spectrum. One technique that shows promise here is the use of dopants so as to extend the spectral range of linear absorption. In addition to the bandwidth requirement, it will

also be necessary to extend the dynamic range of the limiter. This may be possible by using this material in a self-protecting mode or in conjunction with other optical limiting materials in hybrid configurations. Finally, it will be necessary to demonstrate optical limiting performance in a practical direct view system with a low  $f/\#$  using near plane wave illumination. This work is currently underway in our laboratory using an  $f/4$  system with matched achromatic lenses that are overfilled by our Gaussian input.

## 5. ACKNOWLEDGEMENTS

This research was supported by the Defense Advanced Research Projects Agency and the U.S. Army Center for Night Vision and Electro-Optics (contract DAAB07-F412).

## 6. REFERENCES

1. T.F. Boggess, A.L. Smirl, S.C. Moss, I.W. Boyd, and E.W. Van Stryland, "Optical Limiting in GaAs", IEEE J. Quantum Electron. QE-21, 488-494 (1985)
2. E.W. Van Stryland, Y.Y. Wu, D.J. Hagan, M.J. Soileau, and K. Mansour, "Optical Limiting in Semiconductors", J. Opt. Soc. Am. B, Vol. 5, No. 9, 1980 (1988)
3. T.F. Boggess, S.C. Moss, I.W. Boyd, and A.L. Smirl, "Nonlinear Energy Regulation by Nonlinear Refraction and Absorption in Silicon", Opt. Lett. 9, 291-293 (1984)
4. M. Sheik-bahae, A.A. Said, and E.W. Van Stryland, "High-Sensitivity, Single-Beam  $n_2$  Measurements", Opt. Lett. 14, 955-957 (1989)

## **Appendix E**

### **Picosecond Measurements of Absorptive and Refractive Optical Nonlinearities in GaP at 532 nm**

Optics Letters, Vol. 19, pp.527-529 (1994)

# Picosecond measurements of absorptive and refractive optical nonlinearities in GaP at 532 nm

Steve Rychnovsky, G. R. Allan, C. H. Venzke, and Thomas F. Boggess

Center for Laser Science and Engineering, Department of Physics and Astronomy, University of Iowa, Iowa City, Iowa 52242

Received September 27, 1993

Picosecond time-resolved pump-probe and Z-scan measurements are used to investigate the nonlinear refraction and absorption associated with intense picosecond excitation above the indirect band edge of GaP. The pump-probe results reveal both an instantaneous absorption feature, which is consistent with two-photon absorption, and a long-lived feature that is associated with the generation of free carriers by linear indirect absorption. Z scans conducted with pulses of 25- and 95-ps duration indicate that, for these pulse widths, the nonlinear refraction in GaP is dominated by the linear generation of free carriers and that the role of the electronic Kerr effect is negligible. The measured free-carrier refraction is compared with the value predicted from a simple model based on band filling. This model predicts that the primary contribution to the index change at the applied optical frequency arises from holes blocking direct transitions near the zone center and that similar blocking of indirect transitions has a negligible effect on the index.

GaP is an indirect gap semiconductor that has been widely studied for applications such as light-emitting diodes and acousto-optic cells, although its nonlinear optical properties have attracted little attention. Recently we demonstrated<sup>1</sup> that optical nonlinearities in GaP can be used to construct optical limiters for 532-nm pulses. The optimization and the determination of the operational limitations of such devices are intimately linked to our knowledge of the origin and magnitude of the contributing optical nonlinearities. In this Letter we describe the use of picosecond techniques to quantify both the absorptive and refractive nonlinearities in GaP at 532 nm. By using time-resolved pump-probe measurements and Z scans with various excitation pulse durations, we have isolated instantaneous, irradiance-dependent absorptive and refractive processes associated with the third-order susceptibility from fluence-dependent processes associated with carriers generated by single-photon absorption.

All measurements were performed at 532 nm and at room temperature with a frequency-doubled, actively/passively mode-locked Nd:YAG laser operated in the TEM<sub>00</sub> mode at a 1-Hz repetition rate. The temporal width of the output pulses was varied between 25 and 95 ps by means of interchangeable output coupling étalons. Pump-probe measurements were conducted on a 117- $\mu\text{m}$ -thick GaP sample, and Z scans were conducted on a 135- $\mu\text{m}$ -thick sample, both of which were polished and antireflection coated on both surfaces. These samples were cut from the same wafer of undoped, single-crystal GaP, which had a linear indirect absorption coefficient of 100 cm<sup>-1</sup> at 532 nm. Since GaP has<sup>2</sup> an indirect band gap at 550 nm near the X point and a direct gap at 445 nm, this absorption is associated with phonon-assisted transitions from the valence band to the X valleys.

To measure the dynamics of the absorptive nonlinearities, we used a standard two-beam, cross-polarized pump-probe technique. The normalized

change in probe transmission versus delay is shown in Fig. 1 for 25-ps (FWHM) pulses and various fluences. Two distinct features are observed in the data: a weak induced absorption that is essentially constant on a nanosecond time scale and a more pronounced induced absorption that occurs only near zero delay. While the long-lived signal is found to depend directly on the carrier density generated by linear indirect absorption, the induced absorption near zero delay scales linearly with irradiance and follows the temporal cross correlation of the pump and probe pulses, behavior that is consistent with two-photon absorption. Although one might expect such a mechanism to be dominated by the linear indirect absorption, we note that, in fact, two-photon absorption was previously observed in similar situations with optical excitation above the indirect band edge in both Si<sup>3,4</sup> and diamond.<sup>5</sup>

To quantify the nonlinear absorption, we fitted the data in Fig. 1, using a rate-equation model in which we keep the linear absorption coefficient fixed and characterize the irradiance-dependent absorption process by a two-photon absorption coefficient and the carrier-related absorption by an effective free-carrier

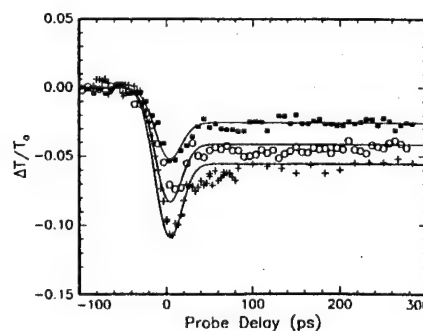


Fig. 1. Normalized change in probe transmission obtained from pump-probe measurements in GaP using 25-ps, 532-nm pulses with excitation fluences of 17 (■), 28 (○), and 38 (+) mJ/cm<sup>2</sup>. The solid curves are the results of numerical simulations as described in the text.

cross section. The latter characterization assumes that the weak, carrier-related absorption, which in principle includes contributions from free-carrier absorption, band filling, band-gap renormalization, and screening, is linearly proportional to the carrier density. Although this is clearly an approximation, we emphasize that all the data reported here can be well fitted by this simple model. Treating the irradiance-dependent component as two-photon absorption, we obtain fits to the data in Fig. 1, using a two-photon absorption coefficient ( $\beta_{\perp}$ ) of 7 cm/GW and an effective free-carrier absorption cross section ( $\sigma_{fc}$ ) of  $0.8 \times 10^{-18}$  cm<sup>2</sup>. The same parameters provide good fits to data obtained by repeating the experiment with 45-ps pulses, confirming the irradiance dependence of the signal near zero delay and the carrier density dependence of the long-lived signal.

We also performed linearly polarized, single-beam transmission experiments, using the arrangements shown in the insets of Fig. 2 to verify the above measurements and to provide complementary information. A 100-mm focal-length input lens and a 3.2-mm-diameter input aperture were used for each measurement. These configurations, which provide information regarding both nonlinear absorption and refraction, are identical in form to a Z scan,<sup>6</sup> except that, instead of a Gaussian beam input, we use a beam that more closely resembles a top-hat function. This geometry is analogous to that recently described by Zhao and Palffy-Muhoray<sup>7</sup> and, with the output aperture in place [Fig. 2(b)], is similar to standard optical limiter configurations. We analyze the results of these measurements numerically, using the approach described in Ref. 8 modified to include the top-hat beam profile, two-photon absorption, and a finite detection aperture. Over the range of fluences used, we assume that carrier-related refraction is linearly proportional to the carrier density.

We measured the single-beam absorption by opening the output aperture to eliminate the sensitivity of the measurement to refractive nonlinearities. The results for pulse widths of 25 and 95 ps and an input energy of 110 nJ are shown in Fig. 2(a). The differing results for the two pulse widths are a consequence of the irradiance-dependent absorption, which was observed near zero delay in the pump-probe measurements. We obtained best fits to the data by using  $1.1 \times 10^{-18}$  cm<sup>2</sup> for  $\sigma_{fc}$ , in reasonable agreement with the value extracted from the two-beam measurement, and 19 cm/GW for the two-photon absorption coefficient ( $\beta_{\parallel}$ ). Note that, owing to the tensor nature of  $\chi^{(3)}$  in zinc-blende semiconductors,<sup>9</sup> we expect  $\beta_{\parallel}$  to differ from  $\beta_{\perp}$ . The value of  $\beta_{\parallel}$  is considerably larger than that measured in materials with similar band gaps<sup>10</sup> and is an order of magnitude larger than the value of 2.1 cm/GW predicted by the well-known scaling law<sup>10,11</sup> for two-photon absorption near  $k = 0$ . Examination of the band structure<sup>2</sup> of GaP reveals that at 532 nm a broad range of states far from  $k = 0$  may be resonantly coupled by two photons, which might explain the surprisingly large irradiance-dependent absorption component.

We investigate the refractive nonlinearities by repeating the above Z scans at the same energy and

pulse widths but with a 1.6-mm-diameter output aperture placed two focal lengths beyond the input lens, as illustrated in the inset of Fig. 2(b). The results, shown in Fig. 2(b), are indicative of strong self-defocusing associated with a negative change in refractive index.<sup>6</sup> A comparison of the data in Figs. 2(a) and 2(b) shows that the absorptive nonlinearity is completely dominated by the refractive nonlinearity for the restricted aperture configuration, indicating that the refractive nonlinearity is the process that primarily determines the response of a GaP optical limiter for these excitation conditions. In addition, the data obtained with the restricted output aperture are nearly identical for the two pulse widths, indicating that the Z-scan (and hence optical limiter) response is dominated by the fluence-dependent self-defocusing associated with linearly generated carriers and that nonlinear refraction associated with the instantaneous electronic Kerr effect or with any two-photon-generated free carriers is negligible.

Using the measured absorptive parameters from Fig. 2(a), we numerically fitted the data in Fig. 2(b) with an index change per photogenerated free-carrier pair of  $-3.1 \times 10^{-22}$  cm<sup>3</sup>. Analogously to Miller *et al.*,<sup>12</sup> we attribute this index change to blocking and plasma effects associated with free carriers and neglect any effects that are due to screening or renormalization. Based on these assumptions, the index change can be separated into three distinct components associated with (1) the creation of free-carrier intraband transitions, (2) the blocking of direct interband transitions, and (3) the blocking of indirect interband transitions. The first component arises

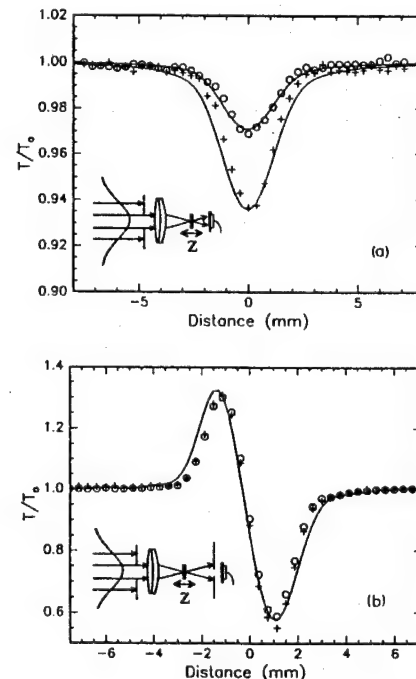


Fig. 2. (a) Open and (b) restricted Z-scan results for 25-ps (+) and 95-ps (O) pulses at 532 nm. In each case the input energy was 110 nJ. The insets schematically illustrate the experimental configurations, and the solid curves are the results of numerical simulations as described in the text.

when carriers that have been photogenerated undergo subsequent transitions within the band in response to the optical field. Because these carriers are not bound, they act as zero-frequency oscillators producing a negative change in index at all frequencies. The direct interband component arises from the creation of holes at the  $\Gamma$  point, which block oscillators associated with interband transitions across the 2.8-eV direct gap. For this process, oscillators with resonance frequencies above the optical frequency are removed, thereby providing a negative change in index at the optical frequency. Electrons do not contribute to this process, since they scatter to the more energetically favorable indirect valleys located near the X points on a time scale that is short compared with the excitation-pulse duration. Finally, these electrons and holes provide blocking of indirect interband transitions. In this case, because the band edge is at 2.27 eV, most of the states that are blocked have resonance frequencies below the optical frequency, so this blocking leads to a positive change in index at the optical frequency. We now address the magnitude of the contributions arising from each of these mechanisms.

The intraband contribution may be readily determined by application of the Drude model to the free electrons and holes. With  $m_{lh} = 0.17m_0$  and  $m_{hh} = 0.67m_0$  for the light- and heavy-hole masses, respectively, and  $m_e = 0.3m_0$  for the conductivity electronic effective mass,<sup>2</sup> this model gives an intraband index change per carrier of  $-1.6 \times 10^{-22} \text{ cm}^3$ . In obtaining this value we have used the fact that the electron density is equal to the hole density and the ratio of the light-hole to heavy-hole densities is equal to the ratio of the respective densities of states.

One estimates the interband contribution arising from blocking of direct transitions near  $k = 0$  by calculating the change in absorption that is due to blocking of direct gap transitions and then using a Kramers-Kronig transformation to compute the corresponding index change. Our treatment uses the equation for the change in absorption given by Miller *et al.*,<sup>13</sup> except that we neglect the change that is due to filling of the conduction band at the  $\Gamma$  point as discussed above. Using the Kane  $P$  parameter of  $2 \times 10^{-19} \text{ esu}$ , typical of zinc-blende semiconductors,<sup>10</sup> gives an index change per free carrier of  $-2.4 \times 10^{-22} \text{ cm}^3$ .

In principle, we can determine the change in index associated with blocking indirect transitions by using a procedure similar to that applied for the direct transitions. The change in the absorption profile in this case is difficult to analyze, however, because of the added complication of phonon-assisted transitions. Rather than attempting to model this process analytically, we use the following argument to estimate its contribution to the index change and demonstrate that we may neglect it. For sufficiently intense optical pumping at 2.33 eV, states near the indirect band edge will be filled, up to and including all optically coupled states, thereby completely saturating the absorption up to 2.33 eV. Assuming a zero temperature distribution, we find that a carrier density of  $5 \times 10^{19} \text{ cm}^{-3}$  is necessary for this satu-

ration. We simulate the effect of this state blocking by removing all absorption below 2.33 eV in the linear absorption spectrum and then performing a Kramers-Kronig analysis, which yields an index change per free-carrier pair of  $+0.2 \times 10^{-22} \text{ cm}^3$ . Since this saturation of the indirect absorption results in the blocking of oscillators below the optical frequency, as expected, this process yields a positive index change. Since this term is an order of magnitude smaller than the other contributions, effects that are due to blocking of the indirect absorption can be neglected. We note that these results and conclusions are in contrast to those recently reported by Ji *et al.*<sup>14</sup> They measured a similar negative index change per free carrier, using nanosecond pulses at 2.33 eV, but they attributed this change to saturation of the indirect absorption while neglecting the two effects that we believe to be dominant.

Summing the intraband and direct interband contributions and neglecting the contribution from the indirect transitions, we calculate the total index change per free carrier to be  $-4 \times 10^{-22} \text{ cm}^3$ , which is in good agreement with our measured result. We emphasize, however, that such agreement should be considered somewhat fortuitous given the simple models used and the neglect of such mechanisms as band-gap renormalization and screening.

We gratefully acknowledge the support of the Advanced Research Projects Agency and the U.S. Army Night Vision and Electronic Sensors Directorate.

## References

1. S. J. Rychnovsky, G. R. Allan, C. H. Venzke, A. L. Smirl, and T. F. Boggess, *Proc. Soc. Photo-Opt. Instrum. Eng.* **1692**, 191 (1992).
2. O. Madelung, ed., *Data in Science and Technology: Semiconductors—Group IV Elements and III-V Compounds* (Springer-Verlag, New York, 1991), p. 91.
3. T. F. Boggess, Jr., K. M. Bohnert, K. Mansour, S. C. Moss, I. W. Boyd, and A. L. Smirl, *IEEE J. Quantum Electron.* **QE-22**, 360 (1986).
4. D. H. Reitze, T. R. Zhang, W. M. Wood, and M. C. Downer, *J. Opt. Soc. Am. B* **7**, 84 (1990).
5. J. I. Dadap, G. B. Focht, D. H. Reitze, and M. C. Downer, *Opt. Lett.* **16**, 499 (1991).
6. M. Sheik-Bahae, A. A. Said, and E. W. Van Stryland, *Opt. Lett.* **14**, 955 (1989).
7. W. Zhao and P. Pallfy-Muhoray, *Appl. Phys. Lett.* **63**, 1613 (1993).
8. T. F. Boggess, K. Bohnert, D. P. Norwood, C. D. Mire, and A. L. Smirl, *Opt. Commun.* **64**, 387 (1987).
9. M. D. Dvorak, W. A. Schroeder, D. R. Andersen, and A. L. Smirl, "Measurement of the anisotropy of two-photon absorption in zinc blende semiconductors," *IEEE J. Quantum Electron.* (to be published).
10. E. W. Van Stryland, H. Vanherzelle, M. A. Woodall, M. J. Soileau, A. L. Smirl, S. Guha, and T. F. Boggess, *Opt. Eng.* **24**, 613 (1985).
11. B. S. Wherrett, *J. Opt. Soc. Am. B* **1**, 67 (1984).
12. A. Miller, D. A. B. Miller, and S. D. Smith, *Adv. Phys.* **30**, 697 (1981).
13. D. A. B. Miller, C. T. Seaton, M. E. Prise, and S. D. Smith, *Phys. Rev. Lett.* **47**, 197 (1981).
14. W. Ji, S. H. Tang, and A. K. Kukaswadia, *J. Appl. Phys.* **73**, 8455 (1993).

## **Appendix F**

### **Picosecond Time-Resolved Measurements of Photorefractive Grating Dynamics in Zincblende Semiconductors**

Springer Series in Chemical Physics, Vol. 53, Ultrafast Phenomena VII, pp. 324-326  
(1990)

# Picosecond Time-Resolved Measurements of Photorefractive Grating Dynamics in Zincblende Semiconductors

*A.L. Smirl<sup>1</sup>, M.D. Dawson<sup>1</sup>, W.A. Schroeder<sup>1</sup>, T.S. Stark<sup>1</sup>, T.F. Boggess<sup>1</sup>, and G.C. Valley<sup>2</sup>*

<sup>1</sup>Center for Laser Science and Engineering, 124 AMRF Oakdale Campus,  
Iowa City, IA 52242, USA

<sup>2</sup>Hughes Research Laboratories, 3011 Malibu Canyon Road,  
Malibu, CA 90265, USA

**Abstract.** The ultrafast evolution of photorefractive gratings in GaAs:EL2 and CdTe:V is separated from that of several co-existing gratings by a novel time-resolved polarization-rotation technique.

## 1. Introduction

We describe a novel nondegenerate, polarization-sensitive, transient-grating technique, which we use to isolate, to probe the symmetry of, and to time resolve (with resolution  $< 5$ -ps) the individual dynamics of several co-existing gratings written in GaAs:EL2 and CdTe:V. Specifically, we utilize optically-induced anisotropy to allow the first temporal resolution of the formation and decay of photorefractive gratings in these semiconductors on picosecond timescales. The measurements allow us to identify various contributions to the photorefractive effect, including the first direct evidence of a photorefractive grating arising from the Demmer field associated with free electron hole pairs. The technique also allows the instantaneous electronic and the cumulative free-carrier gratings (which normally obscure the weaker photorefractive grating) to be simultaneously monitored. Measurements were conducted with a unique, amplified, Styryl 13 dye laser system that was developed for these studies.

## 2. Experimental Results and Discussion

As illustrated schematically in Fig. 1, the gratings were written by two 1-psec pulses at 960 nm with fluences of between  $6 \mu\text{J}/\text{cm}^2$  and  $3 \text{ mJ}/\text{cm}^2$ . The writing beams were s-polarized and had equal fluences to eliminate transient energy transfer between the two beams. The pulses were produced by a Styryl 13 dye laser (synchronously pumped by the frequency-doubled, fiber-grating-compressed output of a mode-locked Nd:YAG laser) followed by a three-stage amplifier (which was pumped by the frequency-doubled output from a 10 Hz regenerative



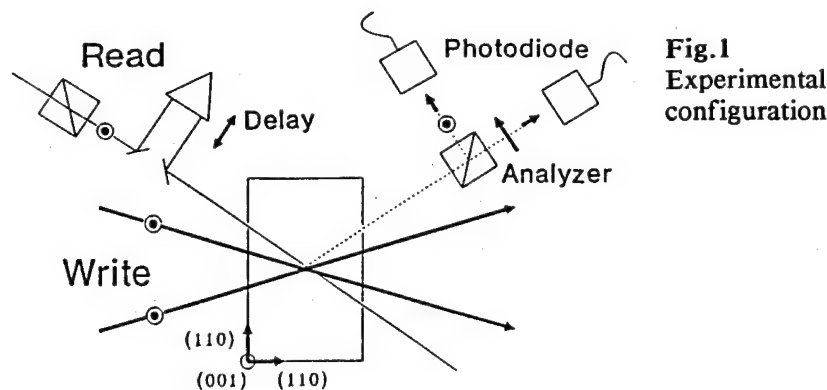


Fig.1  
Experimental  
configuration

amplifier). The s-polarized "readout" beam was generated by Raman-shifting a fraction of the 960 nm radiation in benzene to produce a  $1.06 \mu\text{m}$  pulse with a measured duration  $< 5\text{-ps}$ . A frequency-shifted probe is necessary in the Bragg regime to allow separation of the diffracted signal from the transmitted pump beams. Furthermore, since backward readout configurations are limited in temporal resolution by the sample thickness, a forward traveling probe was used. The diffracted signal was measured as a function of time delay, pump fluence, crystal orientation, and analyzer angle. The "photorefractive-cut" samples were oriented with the (100) crystallographic axis orthogonal to the grating wave vector, which for zincblende symmetry dictates that only the photorefractive grating will rotate by  $90^\circ$  the polarization of the diffracted probe. Consequently, the photorefractive contribution can be isolated from stronger free-carrier and bound-electronic gratings by an analyzer oriented to transmit p-polarization.

Representative measurements of the photorefractive and non-photorefractive gratings, recorded for three similar fluences (in  $\text{mJ}/\text{cm}^2$ ) in a 3.17 mm-thick GaAs:EL2 crystal, are displayed in Fig. 2. The non-photorefractive signal, which was obtained by measuring the s-polarized component of the diffracted probe, displays three distinct features, all of which were independent of crystal orientation. The initial peak, which is symmetric about zero delay and has a  $\chi^3$  power law dependence, is associated with the instantaneous electronic index change ( $n_2$ ). This peak is superposed on a broader feature arising from the accumulation and partial decay (by ambipolar diffusion) of a free-carrier grating, which for fluences above  $0.25 \text{ mJ}/\text{cm}^2$  is primarily an electron-hole grating produced by two-photon and step-wise (through EL2 midgap levels) two-photon absorption. The feature has a fifth-order ( $\chi^1\chi^3$ ) power law dependence so that it dominates the lower order  $\chi^3$  instantaneous electronic index change at fluences above  $\sim 2 \text{ mJ}/\text{cm}^2$ . The free carrier grating is prevented from decaying completely by the space-charge field associated with the ionized EL2. This is manifested in a much weaker signal, that is observed to persist for delays greater

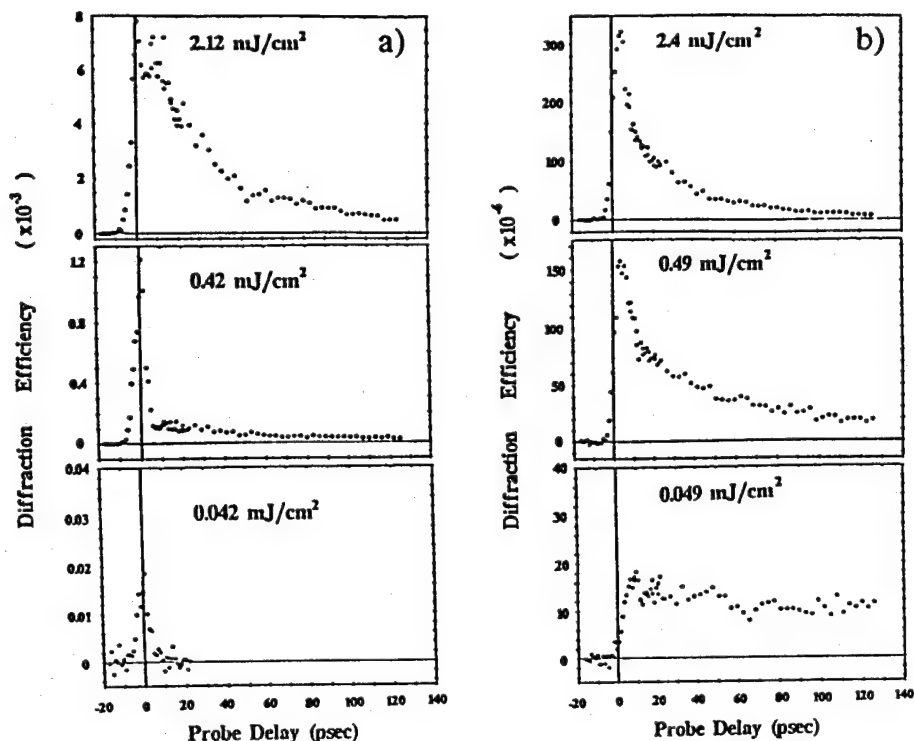


Fig. 2 a) Non-photorefractive (bound-electronic and free-carrier) and b) photorefractive grating diffraction efficiencies versus probe delay.

than 100 ps. The photorefractive signal, which was measured by detecting the p-polarized component of the diffracted probe, is also characterized by three distinct features. At fluences above  $\sim 0.2 \text{ mJ/cm}^2$ , there is an initial transient response (the origin of which is still under investigation), which has a rise time determined by the temporal integration of the probe pulse and a decay shorter than our temporal resolution. This is followed by a signal that is consistent with diffraction from a photorefractive grating associated with the space charge field between electron-hole pairs (i.e. the Demmer field), since it decays with a time constant determined by ambipolar diffusion. At longer delays and lower fluences, we observe a weaker persistent signal associated with the space charge field between free electrons and ionized EL2 donors. We emphasize that no p-polarized signal was observed when the crystal was oriented with the (100) axis parallel to the grating wave vector. Similar results have been obtained for CdTe:V.

This work was supported by DARPA and the Office of Naval Research.

## **Appendix G**

### **Picosecond Separation and Measurement of Coexisting Photorefractive, Bound-Electronic, and Free-Carrier Grating Dynamics in GaAs**

Optics Letters, Vol.16, pp.159-161 (1991)

# Picosecond separation and measurement of coexisting photorefractive, bound-electronic, and free-carrier grating dynamics in GaAs

W. Andreas Schroeder, Thomas S. Stark, Martin D. Dawson, Thomas F. Boggess, and Arthur L. Smirl

Center for Laser Science and Engineering, University of Iowa, Iowa City, Iowa 52242

G. C. Valley

Hughes Research Laboratories, 3011 Malibu Canyon Road, Malibu, California 90265

Received August 8, 1990; accepted October 25, 1990; manuscript in hand November 30, 1990

A novel transient-grating geometry, which is nondegenerate, copropagating, phase matched, and polarization sensitive, is used to isolate and measure independently the ultrafast dynamics of multiple coexisting gratings in GaAs:EL2 with a temporal resolution of  $<5$  psec. This technique permits the measurement of the evolution of the photorefractive grating in materials with zinc blende symmetry, where the photorefractive grating is usually obscured by the stronger free-carrier and instantaneous bound-electronic gratings.

The photorefractive effect in undoped semi-insulating gallium arsenide containing the defect EL2 (GaAs:EL2) has been studied extensively at a wavelength of  $1\ \mu\text{m}$  under steady-state<sup>1</sup> and picosecond transient<sup>2-4</sup> excitation conditions. In previous studies, the two-beam coupling technique was chosen, almost exclusively, as the diagnostic for investigating the photorefractive nonlinearity, primarily because it can be used to discriminate between shifted and unshifted gratings. Even when one is using pulse durations shorter than the carrier lifetime, the competing free-carrier and nonlinear absorption effects, which do not depend on crystal orientation, can be eliminated by measuring the two-beam coupling gain for two selected crystal orientations.<sup>2</sup> One limitation of the two-beam coupling technique, however, is that it provides limited information about the evolution of the photorefractive grating, since the two pulses must be temporally overlapped for the grating to be written. In principle, further temporal information can be obtained by using a third, time-delayed, pulse to probe the grating dynamics; however, since the probe will be diffracted by both shifted and unshifted gratings, the instantaneous bound-electronic and cumulative free-carrier gratings normally obscure the weaker photorefractive gratings in GaAs.<sup>3</sup> Here we describe a novel nondegenerate, polarization-sensitive, transient-grating technique, which we use to separate, to probe the symmetry of, and to time resolve (with a resolution of  $<5$  psec) the individual dynamics of the several coexisting gratings written in zinc blende semiconductors. Specifically, an optically induced anisotropy in the crystal index of refraction is used to isolate the photorefractive grating and, for the first time to our knowledge, to resolve its dynamics temporally on picosecond time scales. The measurements identify various contributions to the photorefractive space-charge field, including that arising from the Demmer field associated with the ambipolar diffusion of free electrons and holes. The tech-

nique also allows the instantaneous electronic and the cumulative free-carrier gratings to be monitored simultaneously.

The experimental technique is illustrated schematically in Fig. 1. A copropagating geometry was chosen to provide enhanced temporal resolution over the conventional counterpropagating four-wave mixing geometry, in which the temporal resolution is limited by the transit time through the sample rather than by the optical pulse duration. A frequency-shifted probe pulse incident at the Bragg angle was used to allow the weak diffracted signal to be separated from the transmitted pump beams in both wavelength and propagation direction. The addition of an analyzer to monitor the polarization of the diffracted probe light and a judicious choice of crystal orientation permitted the separation of photorefractive and nonphotorefractive contributions.

The gratings were written by two temporally and spatially coincident, bandwidth-limited, 1-psec pulses at 960 nm, each with a fluence between  $6\ \mu\text{J}/\text{cm}^2$  and  $3\ \text{mJ}/\text{cm}^2$ . The writing beams were *s* polarized and had equal fluences to eliminate transient energy transfer between the two beams.<sup>5</sup> The external angle between the two beams was chosen as  $32.8^\circ$  to establish the same  $1.7\text{-}\mu\text{m}$  grating period used in our previous investigations.<sup>2-4,6</sup> The pulses, which had a Gaussian spatial profile with a radius of  $0.5\ \text{mm}$  (HW  $1/e$ ), were obtained from an amplified Styryl 13 dye-laser system<sup>7</sup> that consisted of a Styryl 13 dye laser (synchronously pumped by the frequency-doubled, fiber-grating-compressed output of a mode-locked Nd:YAG laser) followed by a three-stage dye amplifier (synchronously pumped by the frequency-doubled output from a 10-Hz Nd:YAG regenerative amplifier<sup>8</sup>). A fraction of the 960-nm radiation was Raman shifted in a 5-cm benzene cell to produce an *s*-polarized  $1.06\text{-}\mu\text{m}$  readout pulse with a measured duration of less than 5 psec and a spot size less than half that of

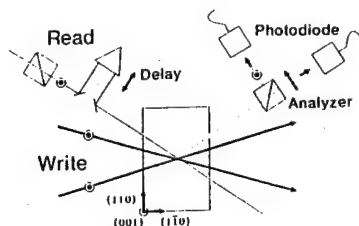


Fig. 1. Experimental configuration.

the writing beams. The readout beam was phase matched to the  $1.7\text{-}\mu\text{m}$  grating period by increasing its external angle of incidence by  $1.76^\circ$  relative to one of the writing beams. The duration and the temporal synchronization of the readout pulse were calibrated by performing a time-resolved, nondegenerate two-photon-induced absorption measurement with one of the writing pulses.

The photorefractive and nonphotorefractive contributions to the diffracted signal were separated by exploiting the zinc blende symmetry of GaAs. Specifically, when a photorefractive-cut ( $\langle 110 \rangle$ ,  $\langle 1\bar{1}0 \rangle$ , and  $\langle 001 \rangle$  crystal faces) sample is oriented with the  $\langle 001 \rangle$  crystallographic axis orthogonal to the grating wave vector (as shown in Fig. 1), the space-charge field produced by the diffusion of the optically generated carriers will induce two new principal axes in the semiconductor at  $\pm 45^\circ$  to the  $\langle 001 \rangle$  crystal axis.<sup>9-11</sup> The index of refraction along one axis will be increased by  $\Delta n = n_b^3 r_{\text{eff}} E_{\text{sc}} / 2$ , where  $n_b$  is the background index of refraction,  $r_{\text{eff}}$  is the effective electro-optic coefficient, and  $E_{\text{sc}}$  is the space-charge field associated with the photorefractive effect.<sup>9,10</sup> The index along the other axis will be decreased by the same amount. Consequently, since the space-charge field is spatially periodic, light polarized along one of these axes will be diffracted by a grating that is spatially shifted by one-half period with respect to that experienced by the orthogonal polarization. If the readout pulse is *s* or *p* polarized, the signal diffracted by these two photorefractive gratings will be *p* or *s* polarized, respectively. By contrast, the nonphotorefractive gratings discussed here (e.g., free-carrier and electronic) are isotropic in GaAs on picosecond time scales; hence the signal diffracted from these gratings will have the same polarization as the incident readout pulse. Therefore the photorefractive and the nonphotorefractive contributions to the grating nonlinearities can be separated by placing an analyzer in the path of the diffracted readout signal.

The measured diffraction efficiency of the nonphotorefractive grating versus probe delay is displayed in Fig. 2 for three different fluences. These measurements, which were obtained by monitoring the unrotated *s*-polarized component of the diffracted probe, show three distinct features, all of which were independent of crystal orientation. The first of these is a peak, symmetric about zero delay, which exhibits a third-order power law dependence ( $\chi^3$  nonlinearity) and has a duration comparable with the readout pulse width. We ascribe this feature, which is dominant at the lower fluences, to the instantaneous bound-electronic index change ( $n_2$ ).<sup>12</sup> The instantaneous signal

is superposed upon a broader feature arising from the accumulation and partial decay of a free-electron grating produced by single-photon ionization of the mid-gap EL2 donors and of an electron-hole grating produced by two-photon (through virtual transitions) and stepwise two-photon (through the EL2 midgap levels) absorption. This free-carrier index grating is dominated by one-photon-generated electrons at the lower fluences and by two-photon-generated electrons and holes at fluences above  $\sim 0.25 \text{ mJ/cm}^2$ , where two-photon absorption exceeds linear absorption. Consequently, above this fluence this feature has a predominantly fifth-order ( $\chi^1 \chi^3$ ) power law dependence,<sup>12</sup> and it eventually dominates the third-order instantaneous electronic response at fluences above  $\sim 2 \text{ mJ/cm}^2$ . The  $\sim 25\text{-psec}$  decay of this free-carrier feature at the higher fluences is consistent with the decay of an electron-hole grating by diffusion and yields an ambipolar diffusion coefficient<sup>13</sup> of  $\sim 15 \text{ cm}^2 \text{ sec}^{-1}$ . Complete diffusive decay of the free-carrier grating is prevented by the space-charge field that is established between the excess free electrons and the immobile ionized EL2 centers. This is manifested in a much weaker signal, which persists until it is destroyed by recombination of electrons at EL2<sup>+</sup> sites [ $\sim 30 \text{ nsec}$  (Ref. 14)].

In contrast, the photorefractive signal was isolated by selecting the *p*-polarized component of the diffracted beam, which was orthogonal to the *s*-polarized readout beam. To confirm that the signal observed in this case was photorefractive in origin, we also measured the *p*-polarized component of the diffracted beam with the crystal rotated by  $90^\circ$  [so that the  $\langle 001 \rangle$  crystallographic axis was parallel to the grating wave vector]. No signal was observed, as expected from the symmetry of GaAs.

The diffraction efficiency of the photorefractive grating measured in this way is shown in Fig. 3 as a function of probe time delay for approximately the same three fluences. At the lowest fluence, an initial rapid increase in diffraction efficiency is observed, which reaches a persistent plateau at a small positive

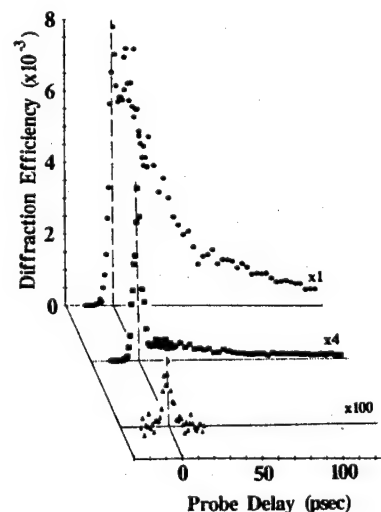


Fig. 2. Nonphotorefractive (bound-electronic and free-carrier) grating diffraction efficiencies versus probe delay for writing fluences of  $2.12 \text{ mJ/cm}^2$  (circles),  $0.42 \text{ mJ/cm}^2$  (squares), and  $0.042 \text{ mJ/cm}^2$  (triangles).

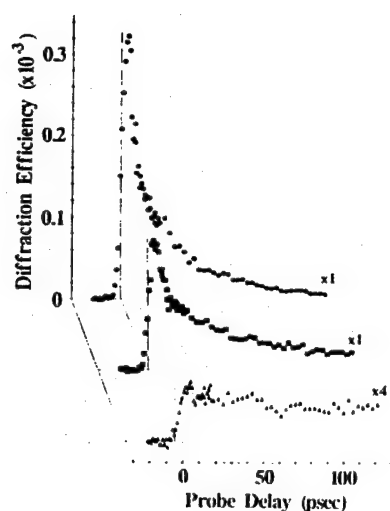


Fig. 3. Photorefractive grating diffraction efficiencies versus probe delay for writing fluences of  $2.4 \text{ mJ/cm}^2$  (circles),  $0.49 \text{ mJ/cm}^2$  (squares), and  $0.049 \text{ mJ/cm}^2$  (triangles).

delay. The initial rise is consistent with the cumulative formation of a space-charge field during the write process by single-photon ionization of EL2 and by the partial decay of the associated free-electron grating by diffusion. The quasi-steady-state region is a reflection of the equilibrium established between the diffusion current and the drift current associated with the space-charge field established between the mobile free electrons and immobile ionized EL2 donors. This equilibrium, which prevents the complete decay of the free-electron grating, is established in  $\approx 5 \text{ psec}$  for a grating spacing of  $1.7 \mu\text{m}$ . This balance will persist until the free-electron population decays by recombination to produce a more conventional steady-state photorefractive grating associated with a modulation of the excess ionized donor and acceptor populations, which will eventually decay by dark conductivity. Thus, once formed, the photorefractive response at low fluences is essentially constant on picosecond time scales.

At higher fluences (again, above  $\sim 0.2 \text{ mJ/cm}^2$ ), two-photon absorption becomes important, and an electron-hole grating is produced in addition to the electron-ionized-donor grating. Even so, as at lower fluences, an initial rise, which peaks at a small positive delay, is observed. It is now followed by a rapid decay lasting tens of picoseconds. The initial portion of this decay occurs on the order of, or shorter than, our 5-psec temporal resolution and is not understood at present. For times longer than our probe pulse width, however, this signal decays with a time constant determined by the same ambipolar diffusion coefficient that was measured for the electron-hole free-carrier grating. This behavior is consistent with that expected for diffracted signals from a photorefractive grating associated with the Dember space-charge field between electron-hole pairs. This Dember field is responsible for establishing ambipolar diffusion, it forms in a time determined by the dielectric relaxation of the material (which is shorter than the experimental temporal resolution for fluences  $\geq 50 \mu\text{J/cm}^2$ ), and it will decay completely as the electron-hole grating de-

cays by ambipolar diffusion. This provides evidence of a Dember field contribution to the photorefractive nonlinearity, and it corroborates our modeling of previous two-beam coupling experiments with 30-psec pulses at  $1.064 \mu\text{m}$ , which invoked both the Dember field and the conventional space-charge field between the electrons and ionized donors.<sup>2-4,14</sup>

In summary, we have demonstrated a novel copropagating, nondegenerate, phase-matched, polarization-sensitive, transient-grating geometry and have used that geometry to separate unambiguously and investigate independently the dynamics of coexisting photorefractive, free-carrier, and bound-electronic gratings in GaAs with a temporal resolution of  $< 5 \text{ psec}$ . The technique provides better temporal resolution than backward readout geometries in thick crystals, is background free, and is particularly well suited for monitoring weak nonlinearities with high temporal resolution over long interaction lengths (i.e., in the Bragg regime). It can be used to interrogate and exploit the sample symmetry and, thus, to isolate the various contributions to the diffracted signal. Most importantly, we have used this technique to provide what is to our knowledge the first temporal resolution of the ultrafast dynamics of photorefractive gratings in a material with zinc blende symmetry, where they are usually obscured by the stronger free-carrier or bound-electronic gratings when more conventional geometries are used.<sup>3</sup>

This research was supported in part by the U.S. Office of Naval Research and by the Defense Advanced Research Projects Agency.

## References

1. See, for example, M. B. Klein, *Opt. Lett.* **9**, 350 (1984).
2. G. C. Valley, A. L. Smirl, M. B. Klein, K. M. Bohnert, and T. F. Boggess, *Opt. Lett.* **11**, 647 (1986).
3. A. L. Smirl, G. C. Valley, K. M. Bohnert, and T. F. Boggess, *IEEE J. Quantum Electron.* **24**, 289 (1988).
4. G. C. Valley, J. Dubard, A. L. Smirl, and A. M. Glass, *Opt. Lett.* **14**, 961 (1989).
5. V. L. Vinetskii, N. V. Kukhtarev, and M. S. Soskin, *Sov. J. Quantum Electron.* **7**, 230 (1977).
6. A. L. Smirl, W. A. Schroeder, M. D. Dawson, D. P. Norwood, and G. C. Valley, in *OSA Annual Meeting*, Vol. 11 of 1989 OSA Technical Digest Series (Optical Society of America, Washington, D.C., 1989), paper MCC2.
7. M. D. Dawson, W. A. Schroeder, D. P. Norwood, and A. L. Smirl, *Opt. Lett.* **14**, 364 (1989).
8. M. D. Dawson, W. A. Schroeder, D. P. Norwood, A. L. Smirl, J. Weston, R. N. Ettelbrick, and R. Aubert, *Opt. Lett.* **13**, 990 (1988).
9. P. Yeh, *J. Opt. Soc. Am. B* **4**, 1382 (1987).
10. L.-J. Cheng, G. Gheen, T.-H. Chao, H.-K. Liu, A. Par-tovi, J. Katz, and E. M. Garmire, *Opt. Lett.* **12**, 705 (1987).
11. A. L. Smirl, J. Dubard, A. G. Cui, T. F. Boggess, and G. C. Valley, *Opt. Lett.* **14**, 242 (1989).
12. M. Sheik-Bahae, A. A. Said, T.-H. Wei, D. J. Hagan, and E. W. Van Stryland, *IEEE J. Quantum Electron.* **26**, 760 (1990).
13. J. S. Blakemore, *J. Appl. Phys.* **53**, R123 (1982).
14. G. C. Valley and A. L. Smirl, *IEEE J. Quantum Electron.* **24**, 304 (1988).

## **Appendix H**

### **Photorefractive Nonlinearities Caused by the Dember Space-Charge Field in Undoped CdTe**

Optics Letters, Vol. 16, pp. 799-801 (1991)



# Photorefractive nonlinearities caused by the Dember space-charge field in undoped CdTe

W. Andreas Schroeder, Thomas S. Stark, Thomas F. Boggess, and Arthur L. Smirl

Center for Laser Science and Engineering, University of Iowa, Iowa City, Iowa 52242

George C. Valley

Hughes Research Laboratories, 3011 Malibu Canyon Road, Malibu, California 90265

Received January 11, 1991

The photorefractive nonlinearity associated with the Dember space-charge field between electrons and holes produced by two-photon absorption is unambiguously isolated and studied in undoped CdTe by using a nondegenerate, forward-probing, polarization-sensitive, transient-grating technique with a temporal resolution of <5 ps.

Recently we demonstrated that a unique combination of conventional transient grating techniques could be used to exploit the symmetry of zinc-blende semiconductors to permit the separation of photorefractive gratings from the stronger, coexisting bound-electronic and free-carrier (or Drude-Lorentz) index gratings in thick samples with picosecond time resolution.<sup>1</sup> Here we use this technique to isolate unambiguously and resolve temporally the decay of photorefractive gratings associated with the Dember space-charge field. The undoped CdTe sample used in our studies has negligible linear absorption at the laser wavelength of 960 nm. Consequently, charged carriers are produced by two-photon band-to-band absorption, and the space-charge field responsible for the photorefractive effect is the Dember field associated with the separation between the mobile electrons and mobile holes (caused by their different mobilities). In this case the photorefractive field will form in either the dielectric relaxation or electronic diffusion time (whichever is faster), decay by ambipolar (or hole) diffusion, and the material will completely recover in the carrier recombination time. For typical conditions reported here, the photorefractive grating forms in ~1 ps or less, decays in ~100 ps, and the material completely recovers in ~1 ns. This is in contrast to the more conventional photorefractive effect, where the charged carriers are produced by single photon ionization of dopants or defects and the space-charge field is subsequently formed by the diffusion of the mobile carrier species away from the stationary dopants or defects. In the latter case, the photorefractive grating is still formed in the dielectric relaxation or diffusion time, but it can decay and the material can fully recover only by recombination and dark decay, which is typically of the order of a millisecond or longer.

Recent two-beam coupling experiments in GaAs and CdTe with ~30-ps pulses at 1.06  $\mu\text{m}$  have provided preliminary evidence of the contribution of the Dember field to the photorefractive response,<sup>2-6</sup> but two-beam coupling provides no temporal resolution.

Thus a key signature of the Dember contribution (the rapid diffusive decay) could not be obtained. By comparison, our recent temporally resolved measurements<sup>1</sup> of the photorefractive grating dynamics in GaAs:EL2 provided further evidence for the presence of the Dember field, but extraction of information was complicated by the presence of the conventional space-charge field between the electrons and the ionized EL2 defects.

The experimental technique<sup>1</sup> is illustrated schematically in Fig. 1. Two temporally and spatially coincident, *s*-polarized, bandwidth-limited 1-ps (FWHM) pulses at 960 nm wrote a grating with a period of 1.7  $\mu\text{m}$  in the photorefractive-cut ((110),  $\bar{1}\bar{1}0$ ), and (001) crystal faces) CdTe sample. The pulses, which were produced by a synchronously amplified Styryl 13 dye-laser system,<sup>7,8</sup> had equal fluences (of as much as 3 mJ/cm<sup>2</sup>) in order to eliminate transient energy transfer between the two beams.<sup>9</sup> A fraction of the 960-nm radiation was Raman shifted in benzene to produce an *s*-polarized 1.06- $\mu\text{m}$  readout pulse with a measured duration of less than 5 ps. The probe pulse had a fluence of <5  $\mu\text{J}/\text{cm}^2$  and a diameter of less than half the 1.0-mm diameter of the writing beams and was phase matched to the grating period. The use of a forward-traveling readout enables this technique to maintain a high temporal resolution over long interaction lengths, while the frequency shift and phase

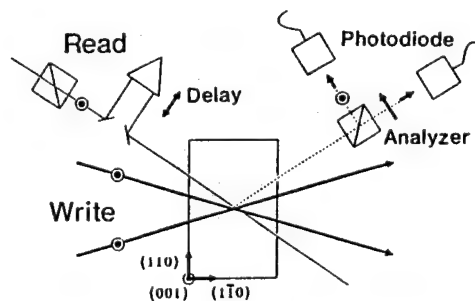


Fig. 1. Experimental configuration.



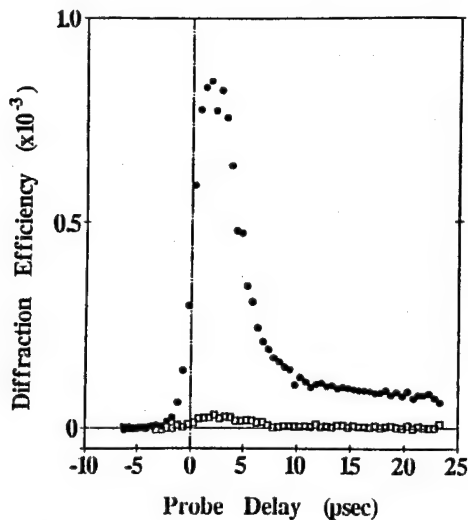


Fig. 2. Diffraction efficiency of the rotated *p*-polarized signal at a fluence of  $1.4 \text{ mJ/cm}^2$  for two crystal orientations: the (001) crystallographic axis parallel (open squares) and perpendicular (circles) to the grating wave vector.

matching ensure that the diffracted signal will be separated from the transmitted writing beams in both wavelength and propagation direction.

The signal diffracted from the anisotropic photorefractive grating was isolated from that of the stronger but isotropic nonphotorefractive (bound-electronic and free-carrier) gratings by exploiting the zinc-blende symmetry of CdTe (as described in more detail elsewhere<sup>1</sup>). With the 1-mm-thick CdTe sample oriented as shown in Fig. 1 [with its (001) crystallographic axis orthogonal to the grating wave vector], the periodic photorefractive space-charge field induces an anisotropy in the index of refraction that results in the *s*-polarized readout pulse's being diffracted to produce a signal that is purely *p* polarized, i.e., rotated by exactly  $90^\circ$  with respect to the incident polarization.<sup>10-12</sup> By contrast, the free-carrier and bound-electronic gratings are isotropic in CdTe on picosecond time scales, and hence the signal diffracted from these nonphotorefractive gratings will have the same polarization as the incident *s*-polarized readout pulse. This allows the photorefractive and nonphotorefractive contributions to be separated by placing an analyzer in the path of the diffracted readout signal.

The photorefractive origin of the rotated *p*-polarized signal was verified by measuring this component of the diffracted signal with the sample oriented so that the grating wave vector was perpendicular to the (001) axis (as shown in Fig. 1) and with the sample rotated by  $90^\circ$  so that the wave vector was parallel to the (001) axis. The result is shown in Fig. 2. As expected from the zinc-blende symmetry of CdTe, the rotated *p*-polarized component of the diffracted signal disappeared when the wave vector was parallel to the (001) axis. The residual signal in the parallel case can easily be attributed to inaccuracies in the alignment of the CdTe sample, polarizer leakage, and tolerances on the cut of the crystal.

The diffraction efficiency of the photorefractive grating, measured up to a probe delay of  $\sim 120$  ps, is displayed on a semilogarithmic plot in Fig. 3 for three

different writing fluences. Since there are no measurable optically active mid-gap levels in this undoped sample, the only source of charge is the generation of free carriers by direct band-to-band two-photon absorption. Thus the mere presence of a diffracted signal provides direct evidence of a photorefractive index change associated with a Dember space-charge field. The buildup of the Dember field is determined by the dielectric relaxation time for the carrier densities produced by the fluences shown in Fig. 3, and it is not resolved since this time is less than the 5-ps experimental resolution. The formation of this field on a time scale less than the  $\sim 30$ -ps electronic diffusion time dictates that the electron-hole grating (and the Dember field) will decay by ambipolar diffusion, since it is the Dember field that is responsible for establishing ambipolar diffusion.

Three features can be distinguished on each curve shown in Fig. 3. The first is a rapid rise that roughly follows the convolution of the probe pulse profile with the accumulation of carriers during the two-photon excitation process. This peak is followed by a two-component decay: an initial fast decay ( $\leq 5$ -ps experimental resolution) followed by a slower decay that is the same for each fluence. An understanding of the origin of the initial, rapidly decaying transient response, which represents more than an order-of-magnitude enhancement in the photorefractive effect over the slower decaying signal for fluences  $> 1 \text{ mJ/cm}^2$ , will require better time resolution and is the subject of a continuing investigation. The slower 55-ps decay is consistent with the expected destruction of the Dember grating by ambipolar diffusion and is a definitive signature of the Dember photorefractive effect.

The ambipolar nature of the decaying Dember field contribution to the photorefractive space-charge field was corroborated by measuring the diffraction efficiency of the nonphotorefractive grating as a function of probe delay in the same undoped CdTe sample. The results, which were obtained by monitoring the

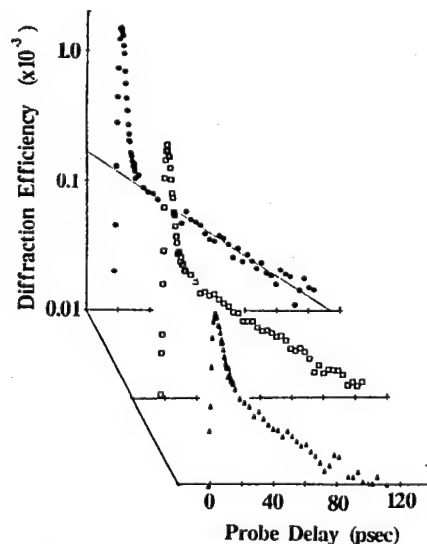


Fig. 3. Diffraction efficiency of the photorefractive grating versus the probe delay for writing fluences of  $2.33 \text{ mJ/cm}^2$  (circles),  $1.26 \text{ mJ/cm}^2$  (open squares), and  $0.50 \text{ mJ/cm}^2$  (triangles), showing a 55-ps decay of the longer-lived signal.

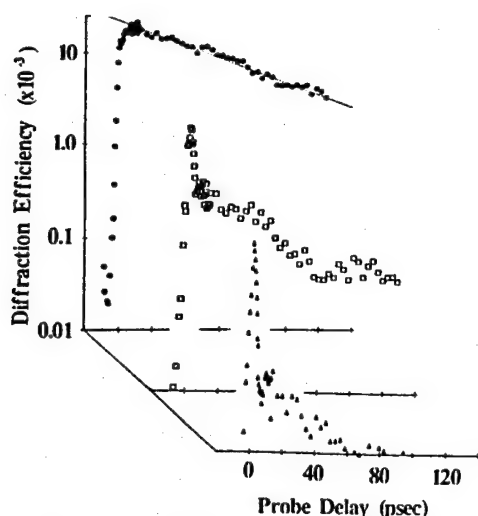


Fig. 4. Diffraction efficiency of the nonphotorefractive (bound-electronic and Drude-Lorentz free-carrier) grating versus the probe delay for writing fluences of  $2.33 \text{ mJ/cm}^2$  (circles),  $1.12 \text{ mJ/cm}^2$  (open squares), and  $0.47 \text{ mJ/cm}^2$  (triangles), illustrating the 65-ps decay of the signal diffracted from the Drude-Lorentz electron-hole grating.

unrotated *s*-polarized component of the diffracted signal, are shown in Fig. 4 for approximately the same three fluences displayed for the photorefractive grating. The data show an instantaneous signal, dominant at low fluences, with a measured third-order power-law dependence, which we attribute to the bound-electronic  $\chi^3$  nonlinearity.<sup>13</sup> More importantly, this instantaneous signal is superimposed onto a feature that is associated with the accumulation of the free-carrier grating produced by two-photon absorption and with its subsequent decay by ambipolar diffusion. The measured decay time of 65 ps for our  $1.7\text{-}\mu\text{m}$  grating period yields an ambipolar diffusion coefficient of  $\sim 5 \text{ cm}^2/\text{s}$ , which is in relatively good agreement with previously measured values in CdTe.<sup>14</sup> The similarity in the two decay rates, therefore, confirms that the photorefractive signal in Fig. 3 is indeed due to a Dember space-charge field.

To summarize, we have isolated and temporally resolved the decay of a photorefractive grating in undoped CdTe produced by sub-band-gap picosecond excitation. This photorefractive grating is observed

to decay completely at the same rate as the free-carrier grating—a rate consistent with the decay of a  $1.7\text{-}\mu\text{m}$ -period grating by ambipolar diffusion. This provides convincing evidence that the source of the photorefractive grating is the Dember space-charge field that is established between electron-hole pairs created by band-to-band two-photon absorption. This establishes the Dember field as a source for the photorefractive space-charge field that can be turned on in the dielectric relaxation time ( $\leq 1 \text{ ps}$ ) and turned off in the ambipolar (or hole) diffusion time ( $\sim 100 \text{ ps}$ ). It also allows the material to recover fully in the recombination lifetime ( $\sim 1 \text{ ns}$ ), which can be adjusted by doping or damaging the material.

This research was supported in part by the U.S. Office of Naval Research and by the Defense Advanced Research Projects Agency.

## References

1. W. A. Schroeder, T. S. Stark, M. D. Dawson, T. F. Boggess, A. L. Smirl, and G. C. Valley, *Opt. Lett.* **16**, 159 (1991).
2. G. C. Valley, A. L. Smirl, M. B. Klein, K. M. Bohnert, and T. F. Boggess, *Opt. Lett.* **11**, 647 (1986).
3. A. L. Smirl, G. C. Valley, K. M. Bohnert, and T. F. Boggess, *IEEE J. Quantum Electron.* **24**, 289 (1988).
4. G. C. Valley, J. Dubard, A. L. Smirl, and A. M. Glass, *Opt. Lett.* **14**, 961 (1989).
5. G. C. Valley and A. L. Smirl, *IEEE J. Quantum Electron.* **24**, 304 (1988).
6. M. S. Petrovic, A. Suchocki, R. C. Powell, G. C. Valley, and G. Cantwell, *Phys. Rev. B* **43**, 2228 (1991).
7. M. D. Dawson, W. A. Schroeder, D. P. Norwood, and A. L. Smirl, *Opt. Lett.* **14**, 364 (1989).
8. M. D. Dawson, W. A. Schroeder, D. P. Norwood, A. L. Smirl, J. Weston, R. N. Ettelbrick, and R. Aubert, *Opt. Lett.* **13**, 990 (1988).
9. V. L. Vinetskii, N. V. Kukhtarev, and M. S. Soskin, *Sov. J. Quantum Electron.* **7**, 230 (1977).
10. P. Yeh, *J. Opt. Soc. Am. B* **4**, 1382 (1987).
11. L.-J. Cheng, G. Gheen, T.-H. Chao, H.-K. Liu, A. Pärtovi, J. Katz, and E. M. Garmire, *Opt. Lett.* **12**, 705 (1987).
12. A. L. Smirl, J. Dubard, A. G. Cui, T. F. Boggess, and G. C. Valley, *Opt. Lett.* **14**, 242 (1989).
13. M. Sheik-Bahae, D. J. Hagan, and E. W. Van Stryland, *Phys. Rev. Lett.* **65**, 96 (1990).
14. M. S. Petrovic, A. Suchocki, and R. C. Powell, *J. Appl. Phys.* **66**, 1359 (1989).

## **Appendix I**

### **Observation of Fundamental Dark Spatial Solitons in Semiconductors Using Picosecond Pulses**

Optics Letters, Vol. 16, pp. 156-158 (1991)

# Observation of fundamental dark spatial solitons in semiconductors using picosecond pulses

G. R. Allan, S. R. Skinner, D. R. Andersen, and A. L. Smirl

Center for Laser Science and Engineering, Department of Electrical and Computer Engineering, The University of Iowa, Iowa City, Iowa 52242

Received July 6, 1990; accepted October 25, 1990

We report what is to our knowledge the first observation of fundamental dark spatial solitons. The solitons are launched in bulk semiconductors using an initial condition with odd symmetry. In order to form the initial condition, a glass platelet is positioned in one half of an incident 30-psec pulse, creating a  $\pi$  phase shift in the spatial profile. Several propagation parameters for the solitons are measured experimentally, and good agreement with theory is obtained.

Spatial solitons have been extensively investigated recently, in large part because of the potential use of these phenomena for optical switching and processing applications. Pairs of dark spatial solitons generated by even initial conditions have previously been observed in Na vapor and various thermally nonlinear liquids,<sup>1</sup> materials of limited technological importance at this time. Bright spatial solitons have been observed in CS<sub>2</sub> (Ref. 2) and glass<sup>3</sup> waveguides. In this Letter we report what is to our knowledge the first observation of the fundamental dark spatial soliton. These experiments were performed in a technologically relevant bulk semiconductor (ZnSe) and on picosecond time scales. The material ZnSe was chosen because it is known to have an instantaneous defocusing component of the nonlinear refractive index at  $\lambda = 532$  nm, owing to the dispersive change associated with two-photon absorption.<sup>4</sup> Our experimental results are consistent with theoretical predictions of various propagation parameters for dark solitons, which supports our interpretation of the observations.

Mathematically, dark spatial solitons are particular solutions of the two-dimensional nonlinear Schrödinger equation for a defocusing nonlinearity that manifest physically as localized irradiance minima existing on a bright optical background. Associated with the irradiance minimum is a phase shift in the electric field centered on the minimum of the soliton. The fundamental (black) dark soliton is a soliton that has an irradiance minimum of zero and an abrupt  $\pi$  phase shift in the electric field centered on the minimum. Single dark spatial solitons can be generated in bulk material by retarding one half of the transverse spatial profile by  $\pi$  before illuminating the nonlinear sample. This can be achieved by passing half of the transverse spatial profile of the beam through a phase-retarding medium, such as glass, arranged to induce the desired phase shift. The resulting nonlinear diffraction pattern evolves into an odd number of dark spatial solitons, as first predicted by Zakharov and Shabat.<sup>5</sup>

To confirm the observation of dark spatial solitons experimentally, it is necessary to measure a number of propagation parameters for the irradiance minima of

interest and compare these results with theoretical predictions. A dark-soliton solution to the integrable nonlinear Schrödinger equation possesses an infinite number of constants of motion; however, in any real physical system, losses and higher dimensionality (two transverse dimensions instead of one) result in a model equation that is not known to be integrable. Despite this equation's apparent nonintegrability, its solitary solutions possess a large number of characteristics in common with the soliton solutions to the integrable nonlinear Schrödinger equation. These solutions have been widely identified as solitons in experimental research despite certain adiabatic relaxation characteristics that they may possess, and we continue to make that identification in this Letter. Characteristics of dark spatial solitons that exist and may be measured experimentally include the phase profile of the electric field near the irradiance minimum, propagation direction, conservation of the product of the square of the width and the peak dark irradiance (soliton constant), and conservation of the total number of dark structures. These four tests will be used to determine the existence of dark spatial solitons experimentally. To observe dark solitons a sufficient propagation distance in the nonlinear medium must exist in order for our initial condition to evolve into the fundamental dark soliton by radiation. This evolution will take place on a length scale that is small with respect to half the soliton period ( $z_{\text{prop}} < z_0 = \pi/4n_2I_p k_0 \approx 9$  mm for our experimental parameters). Our three-dimensional numerical simulations indicate that for our experiment the fundamental dark spatial soliton is well formed at a propagation distance of less than 2 mm, which indicates that sample lengths in excess of 2 mm will be sufficient to permit the formation and observation of dark spatial solitons.

The experimental configuration used here is shown in Fig. 1. The collimated output of a frequency-doubled Nd:YAG laser ( $\lambda = 532$  nm) of near-Gaussian spatial and temporal profile illuminates a phase mask positioned directly in front of a sample of single-crystal ZnSe (5 mm  $\times$  5 mm  $\times$  2 mm). The phase mask is a 150- $\mu$ m-thick glass platelet that is inserted into half of

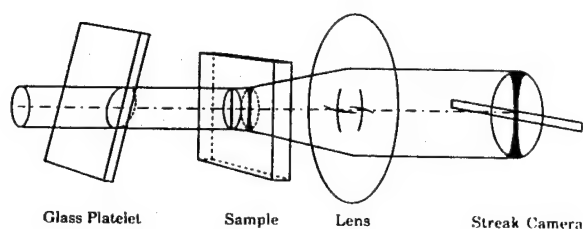


Fig. 1. Experimental configuration for the observation of dark spatial solitons. The incident optical pulse passes through a phase mask (the glass platelet), illuminates the sample, and then is imaged onto the entrance slit of a streak camera.

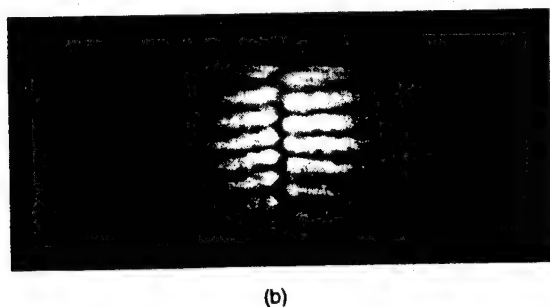
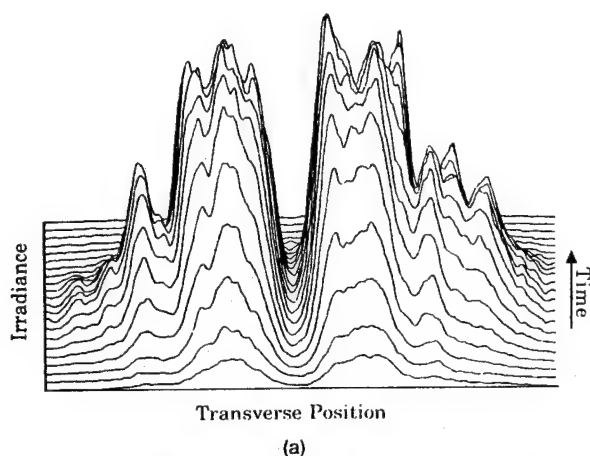


Fig. 2. Experimental results for bulk ZnSe at  $\lambda = 532$  nm, depicting (a) the temporal evolution of the output field for an odd initial condition and (b) the corresponding interferogram.

the beam path. The platelet is rotated to provide a variable phase delay between the two transverse spatial halves of the pulse. The odd initial condition requires a  $\pi$  phase delay between the two spatial halves of the pulse. The correct delay was confirmed by examining the interference pattern formed by the confluence of the initial condition and a reference beam split from the original laser pulse. The spot size of the  $\sim 30$ -psec pulse (FWHM) laser beam at the input face of the sample is  $220 \mu\text{m}$  ( $1/e$ ) in diameter. The electric field distribution at the rear face of the sample is imaged directly onto the entrance slit of a streak camera, which records the temporal evolution of the central horizontal strips of the irradiance pattern in the plane perpendicular to the edge of the mask. A streak camera is necessary to resolve the

formation of solitons that occurs during the temporal center of the pulse. The resolution of the imaging system that records the output of the streak camera is finite in its spatial extent owing to the pixel size of the detector array elements. Thus the experimental data shown are convolved with a detector response function of approximately  $3\text{-}\mu\text{m}$  spatial FWHM.

A series of experiments was performed in order to investigate the propagation of the fundamental dark spatial soliton. Figure 2(a) shows the temporal evolution of the fundamental dark spatial soliton within the pulse (all experimental results in this Letter were obtained with a nonlinear sample propagation length of 5 mm). The transverse spatial profile is plotted horizontally, and the irradiance is plotted vertically, with the time axis on the side. Each trace is separated by  $\sim 7$  psec, with  $t = 0$  at the front of the figure. Figure 2(b) is a photograph of the irradiance pattern produced by interfering the pulse that is traversing the sample with the reference pulse in a manner similar to that described above for the initial condition. The horizontal bright lines evident in the interferogram are equiphase contours. The phase discontinuity in the transverse profile manifests itself as a discontinuity in the horizontal stripes. The central irradiance minimum maintains its  $\pi$  phase shift, propagates parallel to the propagation axis of the incident optical pulse, and has a width that is approximately constant as a function of propagation distance, and the number of such irradiance minima is conserved. A slight broadening of the width is observed with increasing propagation distance (sample thickness), owing to the

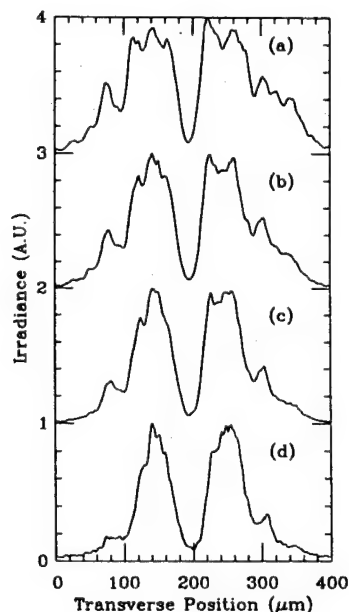


Fig. 3. Experimental results showing the spatial irradiance profile after propagation through a 5-mm sample thickness for four incident pulse irradiances: (a)  $1.6 \text{ GW/cm}^2$ , (b)  $1.4 \text{ GW/cm}^2$ , (c)  $1.0 \text{ GW/cm}^2$ , and (d) linear diffraction. As the bright background irradiance is increased, a narrowing of the spatial width of the dark feature can be observed, a behavior consistent with that expected theoretically for dark spatial solitons.



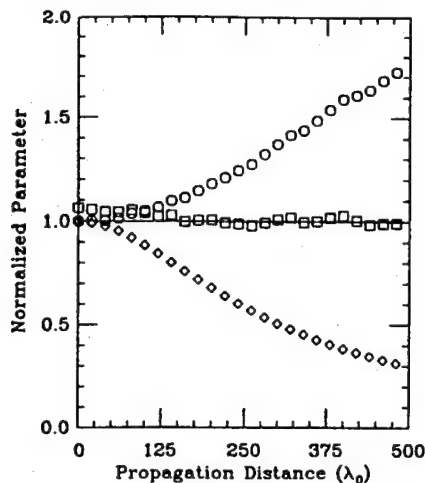


Fig. 4. Results of a numerical simulation for the propagation of the fundamental dark spatial soliton on a bright Gaussian pulse background: the peak dark irradiance (diamonds), the full width at half-maximum (circles), and the width squared times peak dark irradiance product as a function of propagation distance (squares). It can be noted that the product is a constant of motion and is equal to the soliton constant (solid line).

adiabatic relaxation of the bright background irradiance from linear diffraction and nonlinear defocusing processes. Within the accuracy of our measurement technique the irradiance minimum of the fundamental soliton is zero. These results agree with theoretical predictions for fundamental dark solitons and are consistent with previous observations of fundamental dark temporal solitons propagating in optical fibers.<sup>6</sup>

To confirm our interpretation of the experimental results further, a second series of experiments was performed, for which a summary is presented in Fig. 3. Shown are four instantaneous irradiance profiles recorded at the output face of the sample by the streak camera, plotted for increasing initial irradiances from top to bottom. As the incident irradiance is increased, two distinct changes become apparent in the irradiance profiles. First, the width of the entire bright background increases, owing to spatial defocusing of the optical pulse. Second, the spatial width of the intensity minimum narrows. At the largest irradiance shown ( $\sim 1.6 \text{ GW/cm}^2$ ) the feature width is approximately  $30 \mu\text{m}$ . With the theoretical value previously obtained for  $n_2$  ( $-7 \times 10^{-15} \text{ cm}^2/\text{W}$ ) in ZnSe at  $\lambda = 532 \text{ nm}$  (see Ref. 4), the soliton constant ( $1.76^2/n_0 n_2 k_0^2$ ) (Ref. 7) for this system is predicted to be  $1.18 \times 10^4 \text{ W}$ . Experimentally measured values for the product of the width squared times the peak dark irradiance from the data in Fig. 3 range from  $1.1 \times 10^4$  to  $1.3 \times 10^4 \text{ W}$ , in good agreement with the soliton constant theoretically predicted. This result represents quantitative evidence of the fact that the irradiance minimum observed propagates as a dark spatial soliton.

Finally, a series of numerical simulations was performed, with the technique reported in Ref. 8, in order to understand the particular nonlinear diffraction

processes that give rise to the soliton phenomena identified in the experiments described above. With parameters identical to the experimental ones, the nonlinear Schrödinger equation was solved numerically for the case of a three-spatial-dimension (two transverse, one longitudinal) optical pulse. The simulation results captured all the essential features of the experiment, including the characteristic  $\pi$  phase shift associated with the fundamental dark spatial soliton, the propagation direction, conservation of the product of the square of the width and the peak dark irradiance, and conservation of the number of dark structures. A simulation result illustrating conservation of the soliton constant is shown in Fig. 4. Plotted are the spatial FWHM of the dark feature, the peak dark irradiance, and the product of the width squared and the peak dark irradiance. It should be noted that the product is a constant of motion: after a small initial transient due to the initial condition, the product oscillates slightly about the soliton constant in a manner entirely consistent with that of a soliton propagating in the presence of various radiation modes. A series of collision studies was also performed and indicates that these dark structures are sufficiently robust that they survive collisions with large external perturbations, including collisions with other dark spatial solitons.

In summary, this Letter has described an experimental investigation of the propagation of fundamental dark spatial solitons in bulk ZnSe by using picosecond optical pulses. To our knowledge this is the first observation of fundamental dark spatial solitons in a semiconductor and the first dark spatial solitons to be produced by picosecond pulses.

This research was supported in part by the National Science Foundation, the Office of Naval Research, and the Defense Advanced Research Projects Agency.

## References

1. G. A. Swartzlander, Jr., D. R. Andersen, J. J. Regan, and A. E. Kaplan, in *Digest of Annual Meeting of the Optical Society of America* (Optical Society of America, Washington, D.C., 1989), paper PD-7; D. R. Andersen, D. E. Hooton, G. A. Swartzlander, and A. E. Kaplan, *Opt. Lett.* **15**, 783 (1990).
2. A. Barthelemy, S. Maneuf, and C. Froehly, *Opt. Commun.* **55**, 201 (1985); Ph. Emplit, J. P. Hamaide, and R. Tremblay, *Opt. Commun.* **62**, 374 (1987).
3. J. S. Aitchison, A. M. Weiner, Y. Silberberg, M. K. Oliver, J. L. Jackel, D. E. Leaird, E. M. Vogel, and P. W. E. Smith, *Opt. Lett.* **15**, 471 (1990).
4. M. Sheik-bahae, D. J. Hagan, and E. W. VanStryland, in *International Quantum Electronics Conference*, Vol. 8 of 1990 OSA Technical Digest Series (Optical Society of America, Washington, D.C., 1990), paper QTUM3.
5. V. E. Zakharov and A. B. Shabat, *Sov. Phys. JETP* **37**, 823 (1973).
6. A. M. Weiner, J. P. Heritage, R. J. Hawkins, R. N. Thurston, E. M. Kirshner, D. E. Leaird, and W. J. Tomlinson, *Phys. Rev. Lett.* **61**, 2445 (1988).
7. W. J. Tomlinson, R. J. Hawkins, A. M. Weiner, J. P. Heritage, and R. N. Thurston, *J. Opt. Soc. Am. B* **6**, 329 (1989).
8. D. R. Andersen and J. J. Regan, *J. Opt. Soc. Am. A* **6**, 1484 (1989).

## **Appendix J**

### **Stationary Fundamental Dark Surface Waves**

**Journal of the Optical Society of America B, Vol. 8, pp. 759-764 (1991)**

# Stationary fundamental dark surface waves

Steven R. Skinner and David R. Andersen

*Department of Electrical and Computer Engineering, University of Iowa, Iowa City, Iowa 52242*

Received April 19, 1990; accepted September 24, 1990

We present analytic solutions obtained for the case of a stationary TE fundamental dark surface wave propagating at the interface between two dissimilar defocusing Kerr media. Expressions describing the wave are obtained, and certain characteristics of the solutions are discussed.

## 1. INTRODUCTION

The field of nonlinear integrated optics has attracted much attention recently.<sup>1</sup> Of particular interest are planar, quasi-two-dimensional waveguide structures, which offer the potential for implementing various optical switching and coupler geometries. These planar structures can be fabricated by various epitaxial growth procedures, because they consist of one or more thin layers. Their associated interfaces confine the optical field in the direction normal to the plane of the substrate. Lateral confinement may be provided by the imposition of an inhomogeneous effective refractive-index profile in the plane of the substrate by, e.g., rib waveguide techniques.

The problem of light coupling to one or more interfaces between linear and nonlinear self-focusing media has been examined in great detail. The earliest researchers reported an analytic result for the propagation of TE light at the interface between a linear medium and a nonlinear self-focusing one.<sup>2,3</sup> Afterward, multilayered structures,<sup>4</sup> TM polarization,<sup>5</sup> and coupling between TE and TM modes<sup>6</sup> were considered. Most recently an investigation of the propagation of bright surface waves at the interface between nonlocal self-focusing media was reported.<sup>7</sup> In addition to stationary surface-wave modes, various reports were published regarding the oblique incidence of light onto the interface. Plane-wave,<sup>8</sup> two-dimensional (local<sup>9</sup> and nonlocal<sup>10</sup> nonlinearities), and three-dimensional<sup>11</sup> (3D) solutions were obtained. Besides the theoretical surface-wave studies summarized above, bright spatial soliton propagation was investigated experimentally in several different material systems.<sup>12,13</sup> Such spatial solitons consist of light that is guided by a balance between the existing nonlinear focusing and linear diffraction processes. These experiments were performed with quasi-two-dimensional geometries in order to avoid the well-known instability inherent in the propagation of light in 3D self-focusing media. All the studies referenced here were motivated primarily by the potential for device applications that these problem geometries possess.

One significant problem with the structures discussed above is that, although the confinement in the direction normal to the substrate may result in a quasi-two-dimensional mode, the structure is still 3D (two transverse, one longitudinal). Thus for a self-focusing nonlinearity the modes will be unstable, collapsing to a singularity, for mode powers above a certain critical power.

Such instabilities have been known in 3D bulk self-focusing media for a long time.<sup>14,15</sup> A second problem with nonlinear integrated-optical devices that use self-focusing nonlinearities is that the modes in such guides contain peak intensities that are substantially above the average intensity of the guide. Such large peak intensities can result in the onset of substantial multiphoton absorption processes, even when the guide possesses a relatively small average intensity, which will deleteriously affect the performance of such devices. In fact, for one of the integrated bright spatial soliton experiments, two-photon absorption dominated the nonlinear process for a large range of the experimental parameter space,<sup>13</sup> complicating the interpretation of the experimental results to a substantial degree. Because one of the rationales for using integrated optics is that it is possible to concentrate large optical powers into small guides, these limitations may be severe.

In an attempt to surmount these problems with nonlinear integrated waveguide devices, it is interesting to examine the behavior of modes guided by layers that consist of one or more self-defocusing materials. For the self-defocusing case, the guided modes do not develop singularities at any power level (even in the 3D bulk case), nor do the eigenmodes of the defocusing problem exhibit sharply peaked structures for which the maximum intensity is substantially larger than the average intensity.<sup>16,17</sup> Such eigenmode profiles permit the concentration of larger total powers in a waveguide mode before the onset of the multiphoton processes that can degrade performance of the integrated-optics devices. The present work is motivated in part by the recent experimental demonstration of the propagation of dark spatial solitons (the eigenmodes from which the new dark surface waves are constructed) in bulk defocusing media. The initial experiments were done in the cw regime and took advantage of the defocusing nonlinearity associated with the D<sub>2</sub> resonance in Na vapor<sup>18</sup> and thermal nonlinearities in various liquids.<sup>19</sup> After these studies, a set of dark spatial soliton experiments were performed in bulk ZnSe in the picosecond temporal regime,<sup>20</sup> taking advantage of the bound electronic nonlinearity in that material at 532 nm.<sup>21</sup> The relaxation time of the bound electronic nonlinearity in ZnSe is ~1 psec, indicating that this nonlinearity may be useful in device applications requiring rapid switching times.

It is the purpose of this paper to examine analytically the simplest guide-wave geometry possible for a self-



defocusing nonlinearity. This geometry is an interface between two self-defocusing media. We obtain solutions for the guided wave in terms of the fundamental eigenmodes ( $|E| = 0$  at the intensity minimum) of the two respective media and then match boundary conditions at the interface in order to obtain the propagation parameters governing the total solution. The solutions obtained represent fundamental dark surface waves (FDSW's) at the interface between two dissimilar defocusing media. Although the FDSW solutions may not be useful for implementing nonlinear-optical waveguides alone because of the infinite power requirements necessary to establish the mode, the analysis suggests a technique for obtaining modes based on layered self-defocusing geometries that do have a finite power and retain the advantages discussed above with regard to mode collapse and multiphoton absorption processes.

At this point it is appropriate to make an important distinction between the FDSW and the possible existence of more general dark surface waves comprising nonfundamental or gray eigenmodes. Such surface waves would be characterized by a nonzero-intensity minimum. A key feature of the gray eigenmodes of defocusing Kerr media is that they do not propagate perpendicular to the phase front of the bright background but instead have an associated component of transverse velocity.<sup>16</sup> Thus, for a nonfundamental surface wave to exist (propagating parallel to the interface), the bright background must be obliquely incident. Such oblique incidence complicates the surface-wave problem enormously because of the reflection of light, which must occur in general at the interface. The nonfundamental case is therefore not considered here, and we limit ourselves in this paper strictly to the fundamental surface wave, which does propagate perpendicular to the phase front of the bright background.

The propagation of stationary dark surface waves at defocusing nonlinear interface geometries has not been considered in the past. One related study considered the case of a plane wave obliquely incident from a linear medium onto a defocusing one.<sup>22</sup> In that study a surface wave was identified that was essentially the evanescent tail in the defocusing medium associated with the total internal reflection of light back into the linear medium. Such an evanescent tail was found to exist in that study only for the linear dielectric constant offset between the linear and nonlinear media negative ( $\Delta\epsilon < 0$ ), in contrast with the new dark surface-wave solutions presented here, which are valid for  $\Delta\epsilon > 0$ . Additionally, the solutions obtained in our analysis are guided dark-wave solutions in which the phase front of the bright background is perpendicular to the interface, and radiation from the interface does not occur.

Below we present an analysis (based on Ref. 2) of the single defocusing nonlinear interface geometry that gives rise to FDSW solutions. Section 4 contains a discussion of the characteristics of the FDSW's, and, finally, in Section 5 the paper is summarized.

## 2. NONLINEAR-NONLINEAR INTERFACE

The propagation of TE light through a general two-dimensional medium can be described by the wave equation

$$\nabla^2 E + \epsilon \frac{\omega^2}{c^2} E = 0. \quad (1)$$

The dielectric function for the two dissimilar Kerr media considered first can be written as

$$\begin{aligned} \epsilon(x, y, z) &= \epsilon_0 - \epsilon_1 |E(x, y, z)|^2 & (x < 0), \\ \epsilon(x, y, z) &= \epsilon_0 + \Delta\epsilon - \epsilon_2 |E(x, y, z)|^2 & (x > 0). \end{aligned} \quad (2)$$

Here  $\epsilon_1$ ,  $\epsilon_2$ , and  $\Delta\epsilon$  are taken to be greater than zero. The stationary electric-field eigenmodes of the respective nonlinear media are well known<sup>16,17</sup> and are given by

$$\begin{aligned} E(x, y, z) &= E_1 \tanh[k_1(x - x_1)] \exp(ik_z z) & (x < 0), \\ E(x, y, z) &= E_2 \tanh[k_2(x - x_2)] \exp(ik_z z) & (x > 0). \end{aligned} \quad (3)$$

The fact that the minimum field amplitude for this function is zero implies that the solutions are fundamental dark surface waves. Substituting Eqs. (2) and (3) into Eq. (1) for  $x < 0$ , we obtain

$$-k_z^2 - 2k_1^2 + k_0^2 + \left( \frac{2k_1^2}{E_1^2} - k_0^2 \frac{\epsilon_1}{\epsilon_0} \right) |E|^2 = 0,$$

where  $k_0^2 = \epsilon_0 \omega^2 / c^2$ . By requiring a solution for all powers of  $|E|^2$ , we obtain two separate equations, with

$$k_z^2 = k_0^2 - 2k_1^2 \quad (4)$$

and

$$k_1^2 = k_0^2 E_1^2 \frac{\epsilon_1}{2\Delta\epsilon} \Psi_c^2, \quad (5)$$

where  $\Psi_c^2 = \Delta\epsilon / \epsilon_0$  and  $\sin^{-1} \Psi_c$  is the critical glancing angle for total internal reflection. Substituting Eqs. (2) and (3) into Eq. (1) for  $x > 0$ , we obtain

$$-k_z^2 - 2k_2^2 + k_0^2 + k_0^2 \Psi_c^2 + \left( \frac{2k_2^2}{E_2^2} - k_0^2 \frac{\epsilon_2}{\epsilon_0} \right) |E|^2 = 0.$$

This equation also can be separated into two equations, with

$$k_z^2 = k_0^2 (1 + \Psi_c^2) - 2k_2^2 \quad (6)$$

and

$$k_2^2 = k_0^2 \Psi_c^2 E_2^2 \frac{\epsilon_2}{2\Delta\epsilon}. \quad (7)$$

From Eqs. (4) and (6),

$$k_1^2 = k_2^2 - \frac{k_0^2 \Psi_c^2}{2}. \quad (8)$$

Therefore the eigenmodes of the respective media must take on different  $k$  values. From Eqs. (5), (7), and (8) we obtain

$$\epsilon_1 E_1^2 = \epsilon_2 E_2^2 - \Delta\epsilon. \quad (9)$$

Equation (9) shows that the wings of the dark eigenmodes must propagate at the same velocity. This condition is necessary to maintain a constant  $\pi$  phase shift between

the wings of the FDSW. Additionally, Eq. (9) tells us that  $E_1$  and  $E_2$  cannot be chosen independently for given interface parameters and also that the linear dielectric constant offset between the two materials must be of the order of the total nonlinear dielectric constant change.

Imposing appropriate TE boundary conditions by requiring  $E$  and  $\partial E/\partial x$  to be continuous at the interface yields the following two relations:

$$E_1 \tanh(k_1 x_1) = E_2 \tanh(k_2 x_2) \quad (10)$$

and

$$k_1 E_1 \operatorname{sech}^2(k_1 x_1) = k_2 E_2 \operatorname{sech}^2(k_2 x_2). \quad (11)$$

We now have a solution with six equations and seven unknowns. One independent parameter can thus be set and the other unknowns calculated with respect to it. In a manner similar to that of Ref. 2 we choose to set  $D$ , where  $D$  is defined as

$$E_2^2 = \frac{2\Delta\epsilon}{\epsilon_2} \left( D + \frac{1}{2} \right). \quad (12)$$

Therefore, from Eqs. (6)–(9) and (12),

$$k_2 = k_0 \Psi_c \left( D + \frac{1}{2} \right)^{1/2}, \quad (13)$$

$$k_1 = k_0 \Psi_c D^{1/2}, \quad (14)$$

$$k_z = k_0 \Psi_c (\Psi_c^{-2} - 2D)^{1/2}, \quad (15)$$

and

$$E_1^2 = \frac{2\Delta\epsilon D}{\epsilon_1}. \quad (16)$$

Because we require real propagation constants for the FDSW to exist, limits on  $D$  are  $D > 0$  and  $D < \Psi_c^{-2}/2$ . The boundary equations are used to find  $x_1$  and  $x_2$ :

$$\begin{aligned} \tanh(k_1 x_1) &= \pm \frac{k_1 E_1 - k_2 E_2}{k_1 E_1 - k_2 \frac{E_1^2}{E_2}} \\ &= \pm \frac{\left[ \frac{D + 0.5 \left( \frac{\epsilon_2}{\epsilon_1} \right)^{1/2} - 1}{D} \right]^{1/2}}{\left( \frac{\epsilon_2}{\epsilon_1} \right)^{1/2} - 1} \equiv \pm \beta_1 \end{aligned} \quad (17)$$

and

$$\begin{aligned} \tanh(k_2 x_2) &= \pm \frac{k_2 E_2 - k_1 E_1}{k_2 E_2 - k_1 \frac{E_2^2}{E_1}} \\ &= \pm \frac{\left[ \frac{D}{D + 0.5 \left( \frac{\epsilon_2}{\epsilon_1} \right)^{1/2} - 1} \right]^{1/2}}{\left( \frac{\epsilon_1}{\epsilon_2} \right)^{1/2} - 1} \equiv \pm \beta_2. \end{aligned} \quad (18)$$

Because  $\beta_1$  and  $\beta_2$  must be real and their magnitude less than unity, limits on  $\epsilon_1$  and  $\epsilon_2$  and additional limits on  $D$

are found to be

$$\frac{\epsilon_2}{\epsilon_1} > 1, \quad D < \frac{1}{2} \left[ \left( \frac{\epsilon_2}{\epsilon_1} \right)^{1/2} - 1 \right]^{-1}, \quad D > \frac{1}{2} \left( \frac{\epsilon_2}{\epsilon_1} - 1 \right)^{-1}. \quad (19)$$

Solving for  $x_1$  and  $x_2$ , from Eqs. (17) and (18), we obtain

$$x_1 = \frac{\pm 1}{2k_1} \ln \left( \frac{1 + \beta_1}{1 - \beta_1} \right) \quad (20)$$

and

$$x_2 = \frac{\pm 1}{2k_2} \ln \left( \frac{1 + \beta_2}{1 - \beta_2} \right). \quad (21)$$

Note that  $x_1$  and  $x_2$  must have the same sign to ensure continuity at the interface. Also note that neither the propagation constants nor the peak electric-field magnitudes change if the + or - sign is taken; however, the location of the intensity minimum will be shifted to one region or the other by changing the sign. Both  $k_1$  and  $k_2$  or  $E_1$  and  $E_2$  could also have been chosen to be negative, but this option would only lead to a constant phase shift in the solution and thus will be ignored.

### 3. LINEAR-NONLINEAR INTERFACE

If  $\epsilon_1$  goes to zero, a new eigenmode emerges for  $x < 0$ . The electric-field eigenmode for this medium is

$$E(x, y, z) = E_3 \exp(k_3 x) \exp(ik_z z) \quad (x < 0). \quad (22)$$

Solving the scalar wave equation for  $x < 0$ , we find that

$$k_3 = k_0 \Psi_c (-2D)^{1/2}. \quad (23)$$

The boundary conditions at the interface give a new relation for  $x_2$  and  $E_3$ :

$$E_3^2 = \frac{\Delta\epsilon}{\epsilon_2} \{ 1 - 2[-D(D+1)]^{1/2} \} \quad (24)$$

and

$$x_2 = \frac{-1}{2k_2} \ln \left( \frac{E_2 + E_3}{E_2 - E_3} \right). \quad (25)$$

Equations (12), (13), and (15) are still valid. Equations (13), (23), and (24) now limit  $D$  to  $-1/2 < D < 0$ , and, as expected, Eq. (25) requires  $E_2$  to be greater than  $E_3$ .

### 4. SURFACE-WAVE CHARACTERISTICS

In this section we investigate the behavior of the solutions obtained above for a particular set of material parameters. The parameters chosen are  $\epsilon_0 = 2.25$  and  $\Delta\epsilon = 0.00225$ , with the total nonlinear change in the dielectric constant of the same order as  $\Delta\epsilon$  (specific numbers are given in Figs. 1 and 2). This parameter set results in a maximum nonlinear change in the dielectric constant of  $\sim 0.1\%$ . Materials possessing a nonlinear dielectric constant of this order are readily available. It should be noted, however, that it is possible to obtain FDSW solutions for a large variety of system parameters as long as

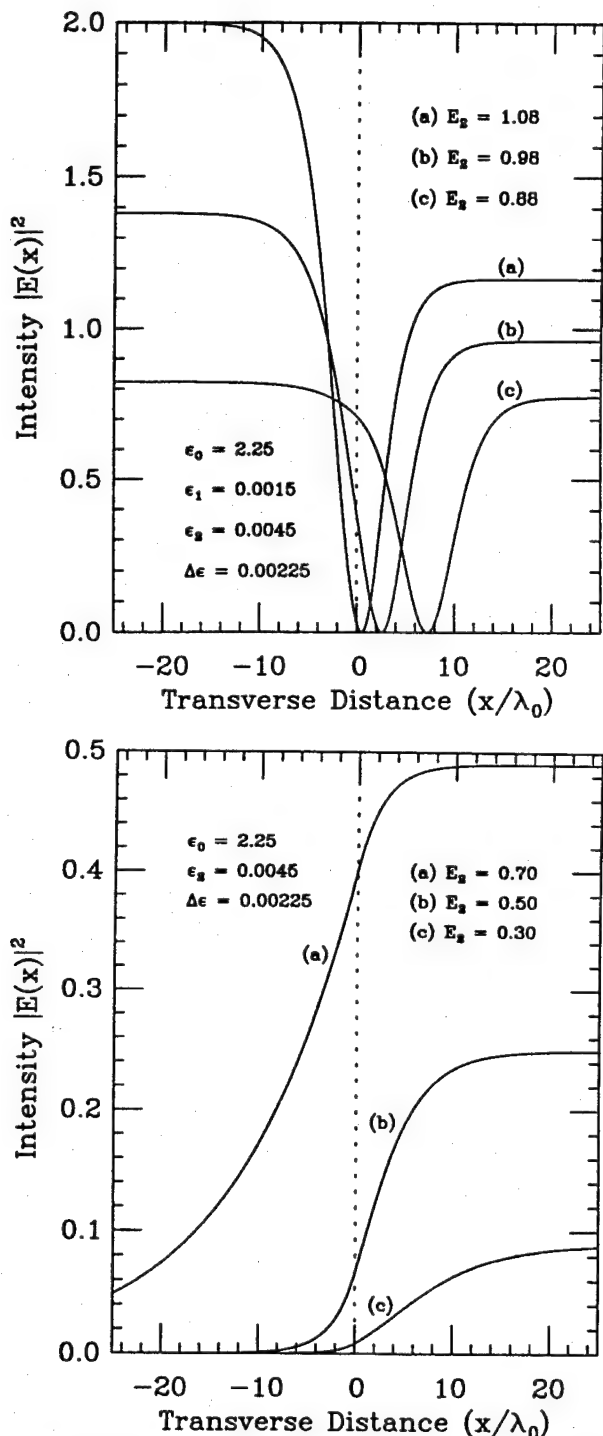


Fig. 1. Nature of the intensity profile for the FDSW solution as  $E_2$  is varied from near the minimum value to near the maximum value for (top) a nonlinear-nonlinear interface and (bottom) a linear-nonlinear interface.

the maximum nonlinear change in the dielectric constant is of the order of or greater than the linear-offset parameter  $\Delta\epsilon$ . The particular point in the parameter space chosen here is by no means unique but is used simply to illustrate the nature of the FDSW solutions obtained in Section 3. We show that, for the given set of parameters, an existence criterion in the form of bounds on  $D$  can be obtained. For example, the location of the minimum of the electric field variable is found to approach asymptoti-

cally  $x = 0$  (the location of the interface) or  $x = \pm\infty$  as  $D$  approaches its maximum or minimum value, respectively. A set of plots of the transverse intensity profiles for the FDSW is also included, indicating graphically the evolution of the solution as certain parameters are varied.

For the case of the nonlinear-nonlinear interface, the conditions that  $D > \frac{1}{2}[(\epsilon_2/\epsilon_1) - 1]^{-1}$ , from relations (19), and  $D < \frac{1}{2}\Psi_c^{-2}$ , from Eq. (15), provide an additional

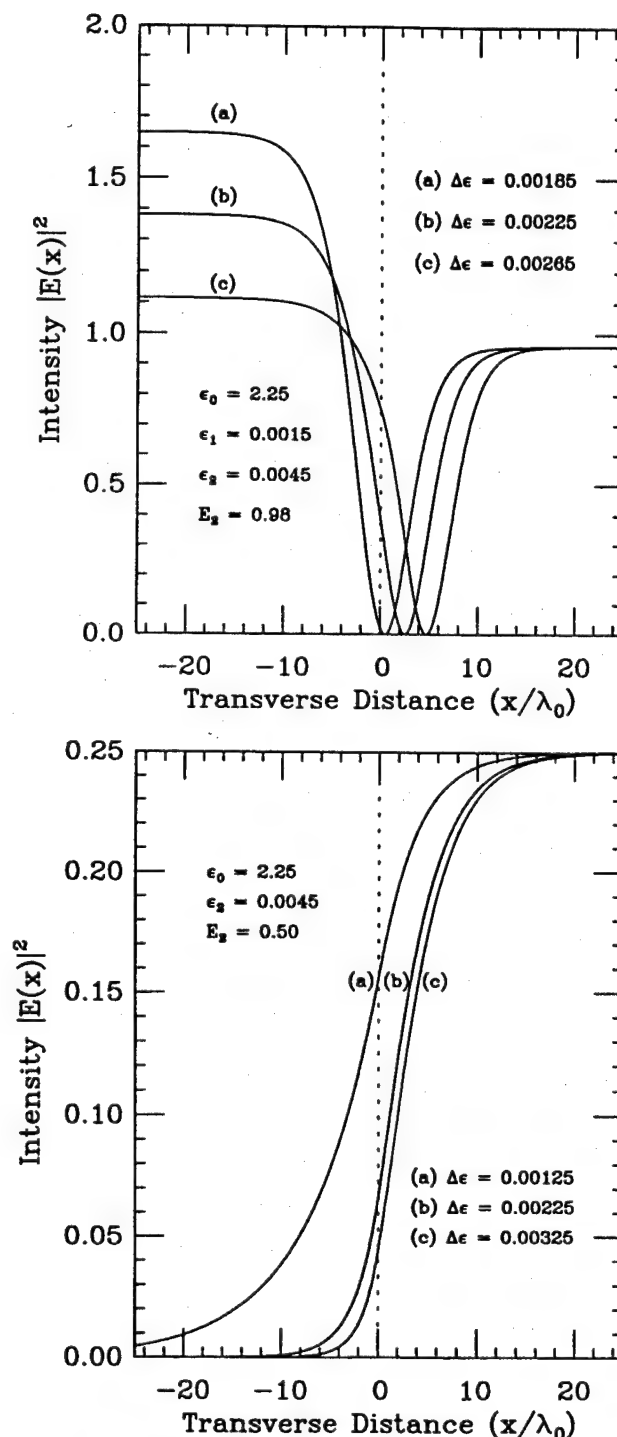


Fig. 2. Nature of the intensity profile for the FDSW solution as  $\Delta\epsilon$  is varied from near the minimum value to near the maximum value for (top) a nonlinear-nonlinear interface and (bottom) a linear-nonlinear interface.

parameter limit of the form

$$\frac{\varepsilon_2}{\varepsilon_1} > \frac{\Delta\varepsilon}{\varepsilon_0} + 1. \quad (26)$$

Given the interface parameters  $\varepsilon_2$ ,  $\varepsilon_1$ ,  $\Delta\varepsilon$ , and  $\varepsilon_0$  for which FDSW solutions can be obtained, minimum and maximum peak intensities are found from Eqs. (12) and (16) and relations (19) to be

$$E_{2\min}^2 = E_{1\min}^2 = \frac{\Delta\varepsilon}{\varepsilon_2 - \varepsilon_1} \quad (\text{i.e., } D = D_{\min}) \quad (27)$$

and

$$E_{2\max}^2 = \left(\frac{\varepsilon_1}{\varepsilon_2}\right)^{1/2} E_{1\max}^2 = \frac{\Delta\varepsilon}{\varepsilon_2 - (\varepsilon_2\varepsilon_1)^{1/2}} \quad (\text{i.e., } D = D_{\max}). \quad (28)$$

Therefore we find from Eq. (9) that  $\varepsilon_1 E_1^2 < \varepsilon_2 E_2^2$  but from relation (26) and Eq. (28) that  $E_1^2 \geq E_2^2$ . Taking the limit as  $D$  approaches  $D_{\min}$ ,  $x_1$  and  $x_2$  asymptotically approach  $\pm\infty$ . If  $D$  goes to  $D_{\max}$ ,  $x_1$  and  $x_2$  asymptotically approach zero. We thus expect the intensity minimum in the FDSW to approach  $x = 0$  as the background intensity is increased. For the linear-nonlinear case,  $E_2^2$  can range from a minimum of zero to a maximum of  $\Delta\varepsilon/\varepsilon_2$  as  $D$  ranges over the allowed values. Also note that as  $D$  goes from the minimum value of  $-1/2$  to the maximum value of zero,  $x_2$  ranges from  $-1/(k_0\Psi_c)$  to  $-\infty$ . A set of transverse intensity profiles illustrating the behavior of the FDSW as  $E_2$  is varied from near the minimum value to near the maximum value for the set of material parameters given above is shown in Fig. 1 (top) for the nonlinear-nonlinear interface and in Fig. 1 (bottom) for the linear-nonlinear interface. It can be seen in Fig. 1 that for the nonlinear-nonlinear interface the intensity minimum in the FDSW solution moves toward the interface as the input background intensity is increased. Similarly, for the linear-nonlinear problem  $x_2$  becomes larger as the background intensity is increased.

Note that, from Eq. (12), (16), or (24),  $D$  can range from its minimum to its maximum value when  $E_2$  or  $E_1(E_3)$  is held constant and one of the interface parameters is varied. For example, by varying  $\Delta\varepsilon$  while keeping  $E_2$  constant, we can produce a new set of curves showing the intensity profile of the FDSW. A set of these curves is shown in Fig. 2 for both the nonlinear-nonlinear interface (top) and the linear-nonlinear interface (bottom). Note that in Figs. 1 (top) and 2 (top)  $x_1$  and  $x_2$  are taken to be positive, although they could have both been negative, resulting in the FDSW minimum's being located in the  $x < 0$  portion of the problem space with  $E_1$  and  $E_2$  remaining the same.

## 5. SUMMARY

In this paper we obtain solutions for FDSW's that exist at the interface between two dissimilar defocusing Kerr media. The FDSW solutions are built from eigenmodes of the respective media with the propagation parameters obtained by applying appropriate boundary conditions at the interface. The analytic results obtained provide an existence criterion that indicates the relationship between

the FDSW propagation parameters and the material parameters of the two Kerr media. Characteristics of the FDSW solutions are then discussed in the context of this existence criterion. Finally, a set of mode profiles are presented. The profiles are calculated with material parameters characteristic of those currently available in bulk nonlinear-optical materials.

## ACKNOWLEDGMENTS

This study was supported in part by National Science Foundation grant EET-88-13464 and Defense Advanced Research Project Agency contract DAAB07-89-F412.

## REFERENCES

1. For a recent survey of this field see, e.g., *Integrated Photonics Research*, Vol. 5 of 1990 OSA Technical Digest Series (Optical Society of America, Washington, D.C., 1990), and references therein.
2. W. J. Tomlinson, "Surface waves at a nonlinear interface," *Opt. Lett.* **5**, 323-325 (1980).
3. A. A. Maradudin, "s-polarized nonlinear surface polaritons," *Z. Phys. B* **41**, 341-344 (1981).
4. A. D. Boardman and P. Egan, "Optically nonlinear waves in thin films," *IEEE J. Quantum Electron.* **QE-22**, 319-324 (1986).
5. A. D. Boardman, A. A. Maradudin, G. I. Stegeman, T. Twardowski, and E. M. Wright, "Exact theory of nonlinear p-polarized optical waves," *Phys. Rev. A* **35**, 1159-1164 (1987); D. Mihalache, G. I. Stegeman, C. T. Seaton, E. M. Wright, R. Zanon, A. D. Boardman, and T. Twardowski, "Exact dispersion relations for transverse magnetic polarized guided waves at a nonlinear interface," *Opt. Lett.* **12**, 187-189 (1987).
6. A. D. Boardman and T. Twardowski, "Transverse-electric and transverse-magnetic waves in nonlinear isotropic waveguides," *Phys. Rev. A* **39**, 2481-2492 (1989).
7. A. B. Aceves, P. Varatharajah, A. C. Newell, E. M. Wright, G. I. Stegeman, D. R. Heatley, J. V. Moloney, and H. Adachi-hara, "Particle aspects of collimated light channel propagation at nonlinear interfaces and in waveguides," *J. Opt. Soc. Am. B* **7**, 963-974 (1990).
8. A. E. Kaplan, "Hysteresis reflection and refraction of light by a nonlinear boundary—a new class of effects in nonlinear optics," *JETP Lett.* **24**, 114-119 (1976); A. E. Kaplan, "Theory of hysteresis reflection and refraction of light by a boundary of a nonlinear medium," *Sov. Phys. JETP* **45**, 896-905 (1977).
9. W. J. Tomlinson, J. P. Gordon, P. W. Smith, and A. E. Kaplan, "Reflection of a Gaussian beam at a nonlinear interface," *Appl. Opt.* **21**, 2041-2051 (1982).
10. D. R. Andersen, "Surface wave excitation at the interface between Kerr-like nonlinear and linear media," *Phys. Rev. A* **37**, 189-193 (1988).
11. D. R. Andersen and J. J. Regan, "Reflection and refraction of a three-dimensional Gaussian beam at a nonlinear interface," *J. Opt. Soc. Am. A* **6**, 1484-1492 (1989).
12. A. Barthelemy, S. Maneuf, and C. Froehly, "Propagation soliton et auto-confinement de faisceaux laser par non linearite optique de Kerr," *Opt. Commun.* **55**, 201-206 (1985).
13. J. S. Aitchison, A. M. Weiner, Y. Silberberg, M. K. Oliver, J. L. Jackel, D. E. Leaird, E. M. Vogel, and P. W. E. Smith, "Observation of spatial optical solitons in a nonlinear glass waveguide," *Opt. Lett.* **15**, 471-473 (1990).
14. P. L. Kelley, "Self-focusing of optical beams," *Phys. Rev. Lett.* **15**, 1005-1007 (1964).
15. R. Y. Chiao, E. Garmire, and C. H. Townes, "Self-trapping of optical beams," *Phys. Rev. Lett.* **15**, 479-482 (1964).
16. V. E. Zakharov and A. B. Shabat, "Interaction between solitons in a stable medium," *Sov. Phys. JETP* **37**, 823-828 (1973).
17. A. Hasegawa and F. Tappert, "Transmission of stationary nonlinear optical pulses in dispersive dielectric fibers,

- II. Normal dispersion," *Appl. Phys. Lett.* **23**, 171-172 (1973).
18. G. A. Swartzlander, D. R. Andersen, J. J. Regan, and A. E. Kaplan, "Observation of spatial dark waves and solitons," in *OSA Annual Meeting*, Vol. 18 of 1989 OSA Technical Digest Series (Optical Society of America, Washington, D.C., 1989), p. 272.
19. D. R. Andersen, D. E. Hooton, G. A. Swartzlander, and A. E. Kaplan, "Direct measurement of the transverse velocity of dark spatial solitons," *Opt. Lett.* **15**, 783-785 (1990).
20. G. R. Allan, S. R. Skinner, D. R. Andersen, and A. L. Smirl, "Observation of fundamental dark spatial solitons in semiconductors using picosecond pulses," *Opt. Lett.* **16**, 156-158 (1991).
21. M. Sheik-bahae, D. J. Hagan, and E. W. VanStryland, "Dispersion and bandgap scaling of the electronic Kerr effect in solids associated with two-photon absorption," *Phys. Rev. Lett.* **65**, 96-99 (1990).
22. A. E. Kaplan, "Conditions of excitation of new waves (LITW) at nonlinear interface and diagram of wave states of the system," *IEEE J. Quantum Electron.* **QE-17**, 336-340 (1981).

## **Appendix K**

### **Dark Spatial Soliton Propagation in Bulk ZnSe**

IEEE Journal of Quantum Electronics, Vol. 27, pp. 2211-2219 (1991)

# Dark Spatial Soliton Propagation in Bulk ZnSe

Steven R. Skinner, Graham R. Allan, David R. Andersen, and Arthur L. Smirl, *Senior Member, IEEE*

**Abstract**—The propagation of dark spatial solitons is experimentally demonstrated in bulk ZnSe at  $\lambda = 532$  nm using a picosecond laser system. Several propagation and collision parameters are measured and compared with analytic and numerical predictions.

## I. INTRODUCTION

**D**ARK solitons have been the subject of much interest, mainly due to possible applications they possess in optical switching and communications. Dark solitons were first theoretically predicted to exist in defocussing materials [1], [2] and then experimentally demonstrated, both temporally and spatially, in various media [3]–[6]. The purpose of this paper is to report important new experimental evidence for the propagation of nonfundamental dark spatial soliton (DSS) pairs in bulk ZnSe.

In a previous paper [3], we have reported the observation of the fundamental dark spatial soliton (FDSS) in this material system. The FDSS is experimentally generated from an initial condition consisting of an irradiance minimum in the center of a transverse spatial profile of an optical pulse, along with a  $\pi$  phase delay between the two sidelobes. The result is a spatial field profile possessing odd symmetry. However, a rigorous experimental demonstration of the soliton character of such an irradiance minimum as it propagates through the nonlinear sample is difficult due to the relative lack of accurately measurable quantities for which a comparison to analytic theory can be made. A far richer experiment, also with an analytic solution in two dimensions, is to launch pairs of DSS's by using even initial conditions. Such initial conditions consist of an irradiance minimum in the center of the transverse spatial profile of the pulse with a zero phase delay between the two sidelobes. In addition to the quantities that were measured experimentally for the fundamental soliton, DSS's excited with even initial conditions exhibit a transverse velocity and initial repulsive shift, each of which may also be measured and compared with analytic theory. The analytic background necessary for comparison with experimental results will be summarized in the next section.

Manuscript received January 14, 1991; revised April 23, 1991. This work was supported in part by DARPA and ONR. Computation was performed at the National Center for Supercomputing Applications and the San Diego Supercomputer Center.

The authors are with the Department of Electrical and Computer Engineering, Center for Laser Science and Engineering, University of Iowa, Iowa City, IA 52242.

IEEE Log Number 9101809.

The important result of this work is that it is possible to create pronounced dark features (dark spatial solitons) on a bright optical pulse which do not disappear due to the self-defocussing and diffraction processes operating in the media of interest. For example, Fig. 1 shows the temporal evolution of the transverse profile for three different intense optical pulses after they have been occluded by a stripe beam block of width  $x_w = 5 \mu\text{m}$  and propagated through a 2-mm-thick sample of ZnSe. This data were taken using the apparatus and techniques described in the experimental details section of the paper.

The peak irradiances of the incident pulses are 0.12, 0.37, and 1.1  $\text{GW}/\text{cm}^2$  for parts (a), (b), and (c) of Fig. 1, respectively. It can be noted that the center irradiance maxima and the spacing between the irradiance minima increase with increasing nonlinearity ( $|n_2|u_0^2$  where  $u_0^2$  is proportional to the peak irradiance of the incident pulse). This is a result of the fact that as the nonlinearity increases, the width of the dark solitons generated decreases (see (3c)) and their transverse velocity increases (see (6)). Thus at the output face of a fixed-length sample, narrower dark solitons with greater separation would be expected as the nonlinearity is increased. Such behavior is exactly what is observed in Fig. 1(a)–(c). Fig. 1(d) is a numerical solution to the three-dimensional nonlinear Schrödinger (NLS) equation [for parameters equivalent to that of Fig. 1(c)] which captures the important aspects of this experiment.

## II. ANALYTIC BACKGROUND

The propagation of high-irradiance monochromatic light, where  $E(x, z)$  is the optical field in two dimensions and  $E(x, z) = u(x, z) \exp(-ik_z z)$ , in a Kerr-type nonlinear material can be described by the NLS equation

$$2ik_z \frac{\partial u(x, z)}{\partial z} = \frac{\partial^2 u(x, z)}{\partial x^2} + (n_0^2 k_0^2 + 2n_0 n_2 |u|^2 k_0^2 - k_z^2) u(x, z) \quad (1)$$

where  $k_0$  is the free space wavenumber,  $n_0$  is the linear index of refraction,  $k_z$  is the propagation constant of the bright background, and  $n_2$  is the Kerr nonlinear index of refraction of the material. Here it is assumed that the response of the material is instantaneous, the material loss is zero, and that we need only consider a two-dimensional problem space (one longitudinal and one transverse axis). For a defocussing nonlinearity ( $n_2 < 0$ ), (1) admits a general dark soliton solution of the form [2]



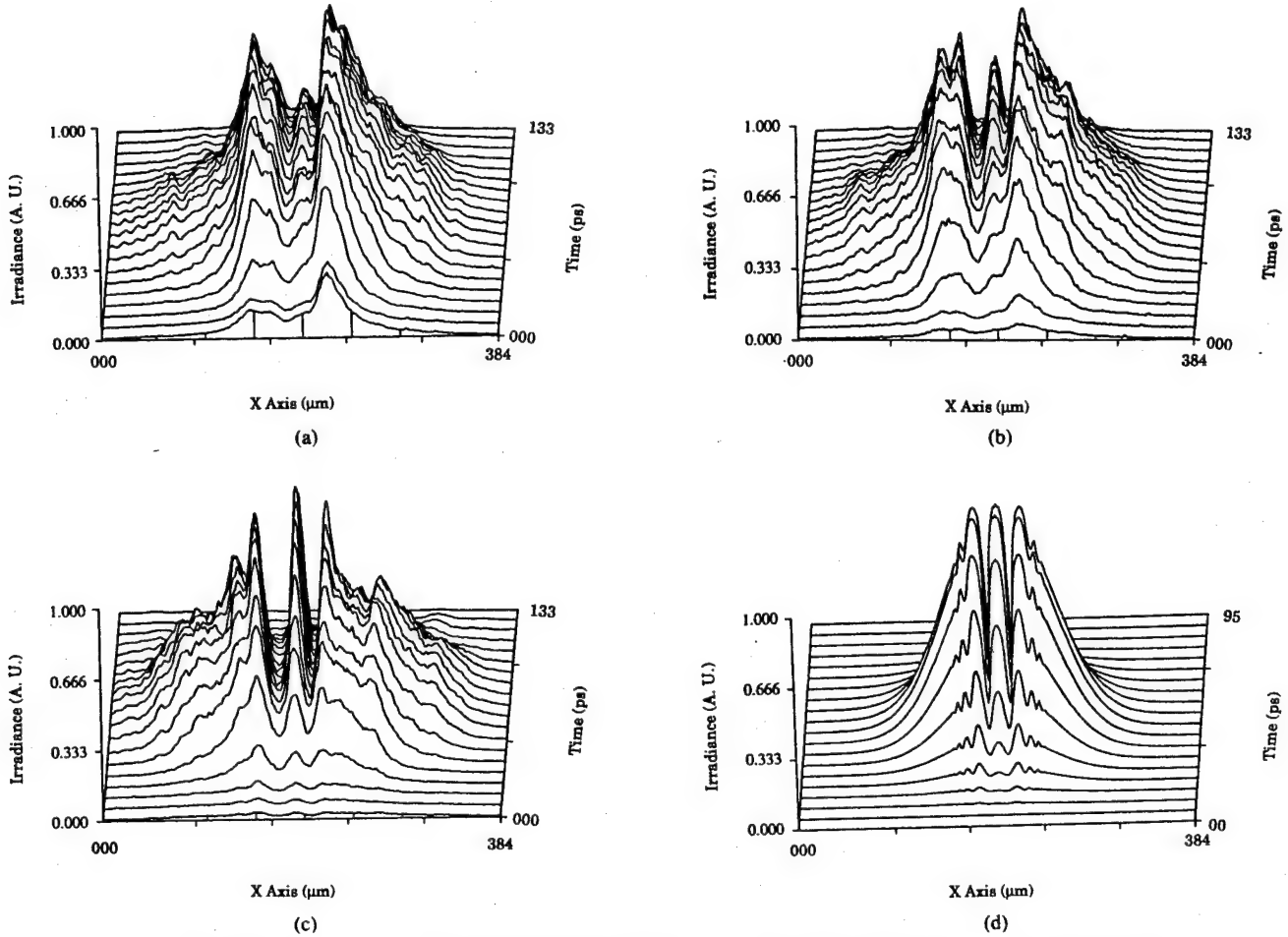


Fig. 1. Temporal evolution of a pulse propagating through a defocusing nonlinear medium after passing through an amplitude mask consisting of a dark band of  $5 \mu\text{m}$  thickness. Parts (a)–(c) show experimental results. The peak irradiance of the incident pulses are  $0.12$ ,  $0.37$ , and  $1.1 \text{ GW/cm}^2$  for (a), (b), and (c), respectively. (d) shows numerical simulation results for the same parameters as the experimental result of (c). In all cases, the dark, even initial condition breaks up into a single pair of transversely counterpropagating dark spatial solitons. The apparent temporal lengthening of the experimental pulse is due to jitter in the streak camera triggering apparatus.

$$u(x, z) = u_0 [1 - B^2 \text{sech}^2(\xi)]^{1/2} \exp[i(\pm\phi(\xi) - k_x x)] \quad (2)$$

where

$$\phi(\xi) = \sin^{-1} \left( \frac{B \tanh(\xi)}{[1 - B^2 \text{sech}^2(\xi)]^{1/2}} \right)$$

and  $\xi = \kappa(x - x_0 - vz)$ . Here,  $B$  is a measure of the “blackness” of the dark soliton solution and can take on a value between 0 and 1 [7],  $x_0$  is the location of the soliton minimum at  $z = 0$ ,  $v$  is the dimensionless transverse velocity of the dark soliton center with respect to the  $z$  axis, and  $k_x$  is the wavevector of the bright optical background in the  $x$  direction. The dark irradiance ( $I_d$ ) of the dark soliton (i.e., the depth of the irradiance minimum) is represented by  $B^2 u_0^2$ , and the soliton width ( $\Delta_{\text{FWHM}}$ ) is related to the soliton shape factor ( $\kappa$ ) by

$$\Delta_{\text{FWHM}} = \frac{1.76}{\kappa}$$

Representative plots of the background irradiance ( $|u|^2$ )

and phase factor ( $\phi(\xi)$ ) for the case  $B = 0.8$  are shown in Fig. 2(a) and (b), respectively.

The propagation parameters are found by substituting (2) into (1) and equating the real and imaginary parts and also all powers of  $|u|$ . Three equations are thus obtained

$$(k_z v - k_x) = \pm \frac{\kappa}{B} (1 - B^2)^{1/2} \quad (3a)$$

• (+ when  $+\phi(\xi)$  is taken,  $-$  with  $-\phi(\xi)$ )

$$k_z^2 = n_0^2 k_0^2 - \frac{2\kappa^2}{B^2} \quad (3b)$$

and

$$\kappa^2 = n_0 |n_2| k_0^2 B^2 u_0^2 \quad (3c)$$

Given  $u_0$  and  $B$ , we are left with a solution with three equations and four unknowns ( $k_x$ ,  $k_z$ ,  $\kappa$ , and  $v$ ), providing an independent parameter or degree of freedom. This degree of freedom is the choice of the  $z$  direction of our coordinate system. For example, Fig. 3 demonstrates two



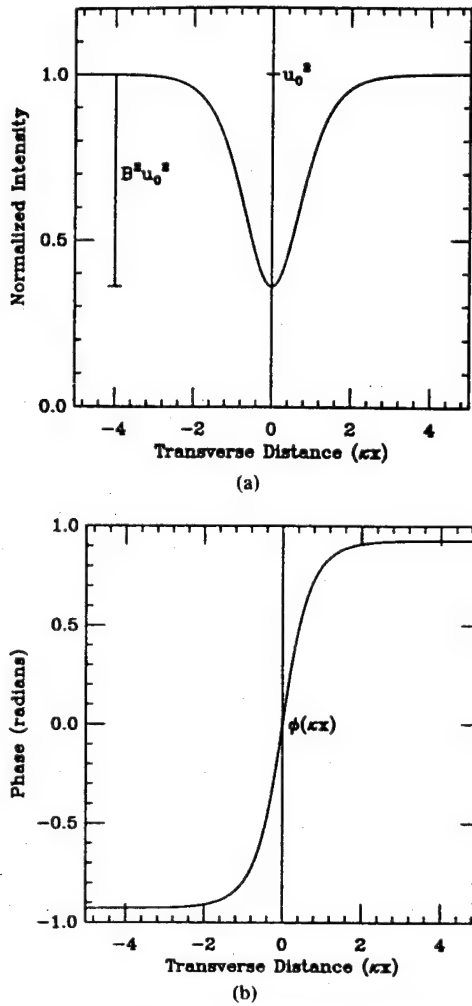


Fig. 2. Representative plots of (a) the background irradiance  $|u|^2$ , and (b) the phase factor  $\phi$ .

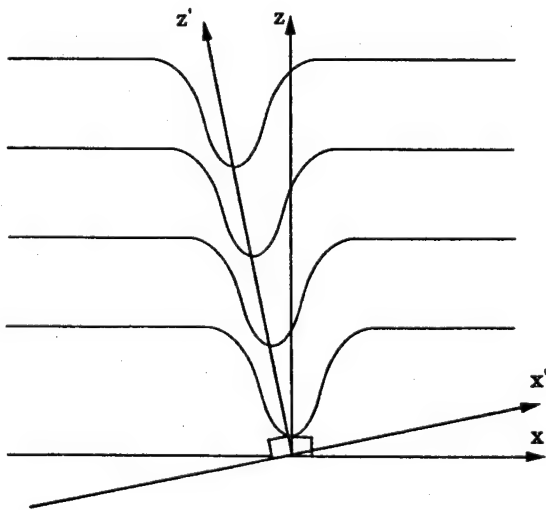


Fig. 3. Two possible choices for coordinate systems. The  $(x', z')$  axis provides a stationary soliton solution in the  $z'$  direction, and the  $(x, z)$  axis is a coordinate system where the  $z$  direction is normal to the phasefront of the bright optical field.

possible choices for coordinate systems. One choice,  $(x', z')$  axis, provides a stationary soliton solution in the  $z'$  direction (i.e.,  $v = 0$  and  $u(x', z') = u(x')$ ). The  $(x, z)$  axis is a coordinate system where the  $z$  direction is normal to the phase front of the bright optical field (i.e.,  $k_x = 0$ ). It is important to note that from (3),  $k_x$  and  $v$  cannot both be chosen to be zero except for the special case where  $B = 1$  (fundamental dark soliton). Hence for  $B < 1$  the soliton will travel at some angle to the phasefront normal of the bright background.

In order to analyze the experimental results presented here, we will use the  $(x, z)$  coordinate system, where the  $z$  direction is normal to the phasefront ( $k_x = 0$ ). This will allow us to measure the transverse velocity  $v$  and compare it to analytic predictions. From (3) the propagation parameters become ( $|n_2|u_0^2 \ll n_0$ )

$$k_z^2 = n_0^2 k_0^2 - 2n_0 |n_2| k_0^2 u_0^2 \cong n_0^2 k_0^2 \quad (4a)$$

$$\kappa^2 = n_0 |n_2| k_0^2 B^2 u_0^2 \quad (4b)$$

and

$$v = \pm (1 - B^2)^{1/2} \left( \frac{n_2 u_0^2}{n_0 - 2|n_2|u_0^2} \right)^{1/2} \cong \pm (1 - B^2)^{1/2} \left( \frac{|n_2|u_0^2}{n_0} \right)^{1/2} \quad (4c)$$

Note that when  $B = 1$ , the dark soliton solution propagates normal to the phasefront of the bright background ( $v = 0$ ) and the irradiance minimum is zero. This is the well-known fundamental dark soliton solution.

An important observation to make at this point is that for a DSS the product of the peak dark irradiance ( $I_d$ ) and the soliton width squared ( $\Delta_{FWHM}^2$ ) is a constant irrespective of  $B$ , and dependent only on the material parameters and the vacuum wavenumber of the optical beam [7]. This soliton constant has the value

$$I_d \Delta_{FWHM}^2 = B^2 u_0^2 \frac{(1.76)^2}{\kappa^2} = \frac{(1.76)^2}{n_0 |n_2| k_0^2} \quad (5)$$

The quantity  $I_d \Delta_{FWHM}^2$ , known as the soliton parameter, can be experimentally measured for any arbitrary irradiance minimum and compared to the theoretical value. We have shown in [3] that for the FDSS, the soliton parameter is conserved, and equal to the soliton constant, even in the presence of a finite width optical background, optical losses, and two transverse dimensions. The soliton parameter can be used in this fashion to verify soliton propagation.

Experimentally launching a single nonfundamental soliton is a difficult task, as it requires generating the proper irradiance and phase profile. However, Zakharov and Shabat [1] have shown that pairs of nonfundamental dark solitons can be generated in a defocussing medium by forming a band of zero irradiance and width  $x_w$  in the bright background of the initial condition. The analytic result obtained by Zakharov and Shabat indicates that each

soliton pair excited by this dark band consists of two transversely counterpropagating nonfundamental DSS's with equal and opposite transverse velocities (eigenvalues). The transverse velocities of each pair were calculated by Zakharov and Shabat [1] and are given in (6). The minimum number of pairs which may be excited in this fashion is one, with an unlimited maximum. The interdependence of the width of the initial condition ( $x_w$ ), material and optical parameters, and the transverse velocity of the DSS is described by the following eigenequation [1]:

$$v = \pm \left( \frac{|n_2| u_0^2}{n_0} \right)^{1/2} \cos(n_0 k_0 v x_w). \quad (6)$$

In addition to the pairs of solitons generated by this dark band, a small fraction of the dark energy is radiated away as a nonsoliton component. This radiation does not effect the eigenvalues of the soliton pairs, however.

Such a dark band can be created experimentally by occluding the front surface of a nonlinear medium illuminated by an intense optical beam or pulse with, e.g., a wire. One of the solitons will have a transverse velocity of  $-v$  and a phase factor of  $+\phi(\xi)$  while the other soliton will have a transverse velocity of  $+v$  and a phase factor of  $-\phi(\xi)$ . The two solitons maintain a kink-antikink symmetry so that the phase of the  $E$  field in the wings of the optical beam will be the same (maintaining the even character of the initial condition as required by the conservation properties of the NLS equation).

This dark-band initial condition can be interpreted as a nonlinear superposition of all of the colliding pairs of nonfundamental DSS's which emanate from it, plus any radiation components. It should be possible to measure the shift associated with the collisional interaction of the DSS pairs at the initial condition. If the dark band is chosen to be centered around  $x = 0$ , and located at  $z = 0$ , then the initial shift from center ( $x_0$ ) for each of the solitons can be calculated as one-half the repulsive shift associated with the collision of the two like solitons traveling with opposite transverse velocities. The shift associated with each soliton is then [1]

$$x_0 = \pm \left( \frac{n_0}{|n_2| u_0^2} \right)^{1/2} \frac{1}{4k_0 n_0 B} \ln \left( \frac{1}{1 - B^2} \right) \\ \cdot (+ \text{ when } v > 0, - \text{ when } v < 0). \quad (7)$$

Equation (7) is strictly valid only for the single-pair case investigated experimentally below. A general expression would include the shifts resulting from collisions with other solitons and pairs as well. A numerical investigation of dark soliton collisional properties for a single transverse direction is presented in [8].

The separation between a pair of solitons produced by the band after propagating a distance of  $L$  in the  $z$  direction is the sum of the contributions to the separation from the transverse velocity and collisional shift and is expressed as

$$\Delta x = 2(L|v| + |x_0|) \quad (8)$$

where  $\Delta x$  is the soliton spacing at the rear face of the sample.

All of the analytic solutions in this section have been obtained for the case of a two-dimensional problem space. The dark soliton solution to the two-dimensional  $(1 + 1)$  NLS equation possesses an infinite number of constants of motion; however, in the real physical system, loss and higher dimensionality (two transverse dimensions instead of one) result in a model equation which is not known to be integrable. Numerical simulations of DSS propagation governed by the three-dimensional NLS equation have been performed which demonstrate that these basic features of the two-dimensional theory are reproduced in three dimensions. An example of these results is given in Fig. 1(d).

### III. EXPERIMENTAL DETAILS

The experimental configuration used in this work is shown schematically in Fig. 4. The experiments were performed with a well-characterized active-passive mode-locked Nd:YAG laser. The output of the laser system is a single linearly polarized pulse of  $\sim 33$  ps (FWHM) duration at  $1.064 \mu\text{m}$  in a  $\text{TEM}_{00}$  mode with a 5 Hz repetition rate. Each pulse is selected from the generated pulse train by an electrooptic shutter and then amplified by two single-pass amplifiers. The amplifiers are operated well below gain saturation, giving a pulse of near-Gaussian temporal and spatial profile ( $< 5\%$ ) with a maximum energy of  $\sim 10$  mJ. A portion of the preamplified pulse is interrogated by a calibrated pulse monitoring system which measures the pulse duration on a shot-to-shot basis. After the second amplifier the infrared pulse is frequency doubled to  $\lambda = 532$  nm using a type II K\*DP crystal. The green light then follows a long optical path, which is necessary in the optical circuit to match the inherent delay times of the electronics in the streak camera with the time of flight of the pulse, is collimated, and also illuminates the mask placed immediately in front of the sample. Due to the presence of  $\sim 10$  ps of jitter in the triggering electronics of the streak camera, all data presented in this paper except those presented in Fig. 1(a)–(c) were taken in the camera's single-shot mode. This prevents quantitative dark soliton effects from becoming smeared out due to averaging. The nonlinear material is a  $5 \times 5 \times 2$  mm single crystal of ZnSe, chosen because of its relatively large defocussing Kerr coefficient at 532 nm [9] (supplied commercially by Eagle Pitcher). The nonlinearity of this material is bound electronic in nature, with a relaxation time of less than 100 fs, indicating that it may be useful in device applications requiring rapid switching times. The irradiance incident on the sample is measured for each laser pulse by a calibrated detector and monitored by the data acquisition computer. The computer is programmed to reject pulses for data acquisition that are outside a pre-

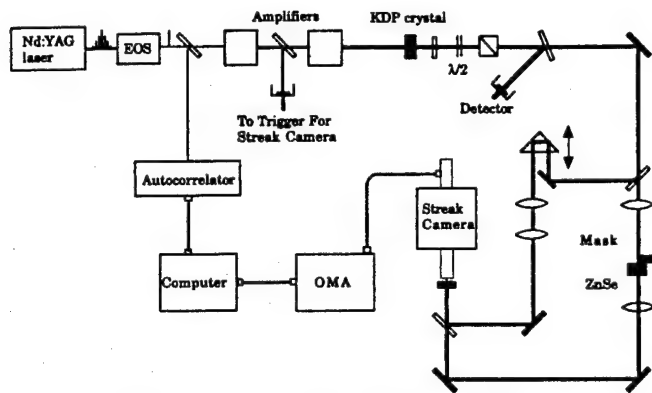


Fig. 4. Schematic of the experimental configuration used to generate dark spatial solitons in ZnSe.

set noise limit. The incident irradiance is continuously varied via a half-wave plate and Glan-Foucault prism placed after the frequency doubling crystal. The irradiance necessary to achieve the required nonlinearity in these experiments is of the order of a gigawatt per square centimeter and can be achieved over a reasonable spot size for modest powers in our system.

Two different masks are used depending on the nature of the dark solitons to be investigated. A phase mask is used to provide an odd number of dark solitons, including the fundamental dark soliton, and an amplitude mask is used to provide dark soliton pairs. The phase mask, shown in Fig. 5(a), is a 150  $\mu\text{m}$  glass platelet which is inserted into one-half of the spatial beam path. The platelet is rotated to provide a variable phase delay between the two transverse spatial halves of the pulse. An odd initial condition is formed when the two spatial halves of the bright background are  $180^\circ$  out of phase. The amplitude mask, shown in Fig. 5(b), is a glass plate with photolithographically deposited metallic stripes (wires) of various widths, which can be accurately positioned so as to occlude the central vertical portion of the beam path. This has the effect of creating a region of zero irradiance in the form of a vertical shadow, or dark band, on the front surface of the sample. This is the even initial condition, because the electric fields in the two spatial halves of the bright background, separated by the dark band, are in phase.

To record the dark spatial solitons, the output face of the sample is imaged directly onto the entrance slit of a streak camera which records the temporal evolution of the optical field in the plane perpendicular to the wire, horizontally across the diameter of the laser beam. The entrance slit permits the central 20  $\mu\text{m}$  of the pulse's vertical transverse dimension to be streaked and recorded. This value is small with respect to the waist parameter. The streak camera is necessary for the temporal resolution of the DSS's within the pulse. The confluence of a reference beam, split off before the mask, and the image of the sample output face were used to measure the relative phase interferometrically of the bright background of the pulse. The phase profile of the initial condition was also monitored by this technique.

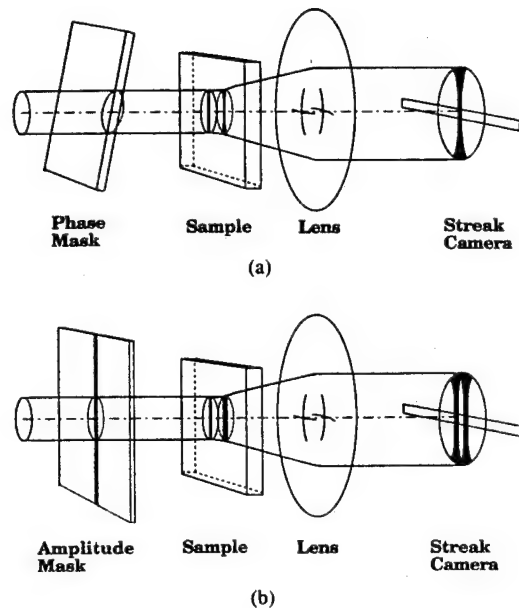


Fig. 5. Experimental configuration for the observation of dark spatial solitons. The incident optical pulse passes through (a) a phase or (b) an amplitude mask, illuminates the sample, and then is imaged onto the entrance slit of a streak camera.

#### IV. EXPERIMENTAL RESULTS

The first reported observation of the FDSS [3], employed a phase mask to create the odd initial condition necessary to generate a single dark soliton. A detailed view of this arrangement is shown in Fig. 4(a). In that paper it was shown that the fundamental dark spatial soliton maintained a  $\pi$  phase shift across its irradiance minimum, propagated parallel to the propagation axis of the incident optical pulse, had a width which was approximately constant as a function of propagation distance (modified only by the adiabatic relaxation of the bright background), and that the number of such irradiance minima was conserved. Within the accuracy of the measurement technique, the irradiance minimum of the fundamental soliton was zero and the soliton parameter was conserved over a variety of irradiances. These results agreed with theoretical predictions for fundamental dark solitons and were consistent with previous observations of fundamental dark temporal solitons propagating in optical fibers [5], [6].

In order to qualitatively illustrate the different experimental results which were obtained depending upon the symmetry of the initial condition, a set of irradiance profiles measured at the output face of the sample is presented in Fig. 6. The figure contains a set of instantaneous, transverse cross sections of the irradiance profile through the temporal center of the pulse, Fig. 6(a) for the odd, and Fig. 6(b) for the even initial conditions. The even condition was created by rotating the glass platelet so as to provide an even phase profile. Fig. 6 clearly shows that simply by altering the phase of the initial condition, one obtains startlingly dissimilar results. As seen, the odd initial condition produces a single irradiance minimum (fundamental dark soliton) whereas the even initial con-

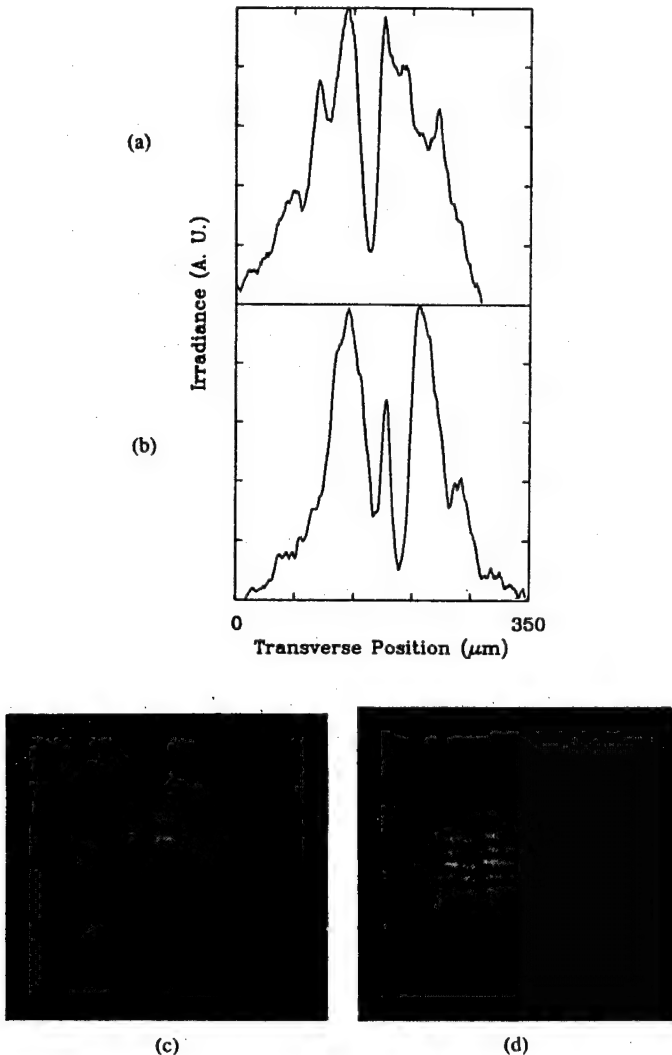


Fig. 6. Measured irradiance profiles along the transverse direction through the temporal center of the pulse, (a) for the odd and (b) for the even initial condition, along with corresponding interferograms, (c) for the odd, and (d) for the even initial condition.

dition exhibits two irradiance minima (nonfundamental dark soliton pairs). Further differences can be seen when we look at the phase profile of the optical background. Also shown in Fig. 6 is a set of photographs of the irradiance pattern produced by interfering the pulse traversing the sample with the reference pulse for (c) the odd initial condition, and (d) the even initial condition. The horizontal bright lines evident in the interferogram are equi-phase contours. The phase discontinuity in the transverse profile manifests itself as a discontinuity in the bright lines. The photographs show for the odd initial condition a  $\pi$  phase shift exists across the irradiance minimum whereas for the even initial condition, the phase shift across each irradiance minimum is less than  $\pi$ . These results are in good qualitative agreement with the predictions of [1].

Such results indicate that we have observed the propagation of DSS's experimentally. Nevertheless, these sim-

ple tests provide only limited evidence of soliton formation. A far richer experiment is to launch pairs of nonfundamental DSS's by using even initial conditions consisting of a black band of zero irradiance surrounded by an equiphase bright background, as shown in Fig. 5(b). Such an experimental configuration permits the measurement of several soliton propagation parameters. These new measurements include the transverse velocity, and repulsive shift of two like dark solitons.

To gain an understanding of the differences between linear diffraction and nonlinear diffraction resulting in the formation of DSS's, a comparison between theory and experiment was performed. Shown in Fig. 7(a) and (b) are three-dimensional numerical simulations showing the linear [Fig. 7(a)] and nonlinear [Fig. 7(b)] diffraction by a 10  $\mu\text{m}$  wire as a function of the propagation distance in the nonlinear medium. Plotted are the spatially transverse irradiance profiles at the temporal center of the pulse, taken in the direction normal to the wire, as the beam propagates through a 5 mm sample. The differences between the evolution of the irradiance profile from the case of linear diffraction to the case of nonlinear propagation of DSS's is clearly observed. For the nonlinear case, a pair of high-contrast, distinct dark features form, which are the DSS's. The separation between the two features is a manifestation of the transverse velocity and repulsive shift associated with them. Shown in Fig. 7(c) and (d) are the corresponding experimental results showing the low irradiance ( $\sim$  linear) [Fig. 7(c)] and high irradiance (1.1  $\text{GW}/\text{cm}^2$ , nonlinear) [Fig. 7(d)] diffraction. The low irradiance data were taken at a pulse energy approximately two orders of magnitude less than the high irradiance data. The profiles shown are the initial condition and for sample lengths of 2 and 5 mm. Note that the numerical simulations evolve in the same manner as the experimental linear and nonlinear diffraction. For the nonlinear case, nonfundamental DSS's form and the soliton separation increases as the sample thickness is increased, as is expected. The conservation laws governing the number of DSS's can be noted as well. Fig. 7(d) represents a study of the propagation over a substantial fraction of a soliton period.

To further quantify our experimental understanding of the relationship between the geometric parameters of the even initial condition and the resulting soliton propagation parameters, a study was performed using pulses of 1.1  $\text{GW}/\text{cm}^2$  peak irradiance which were occluded by dark bands of various thicknesses ruled onto a chrome mask. The resulting initial condition was immediately incident onto the input face of the 5 mm thick ZnSe sample. The irradiance distribution at the output face of the sample was then measured and recorded by a streak camera in a manner similar to that described above.

Shown in Fig. 8 are typical results for the experiment. Instantaneous spatially transverse irradiance profiles, taken in the direction normal to the dark band used to create the initial condition, at the temporal center of the

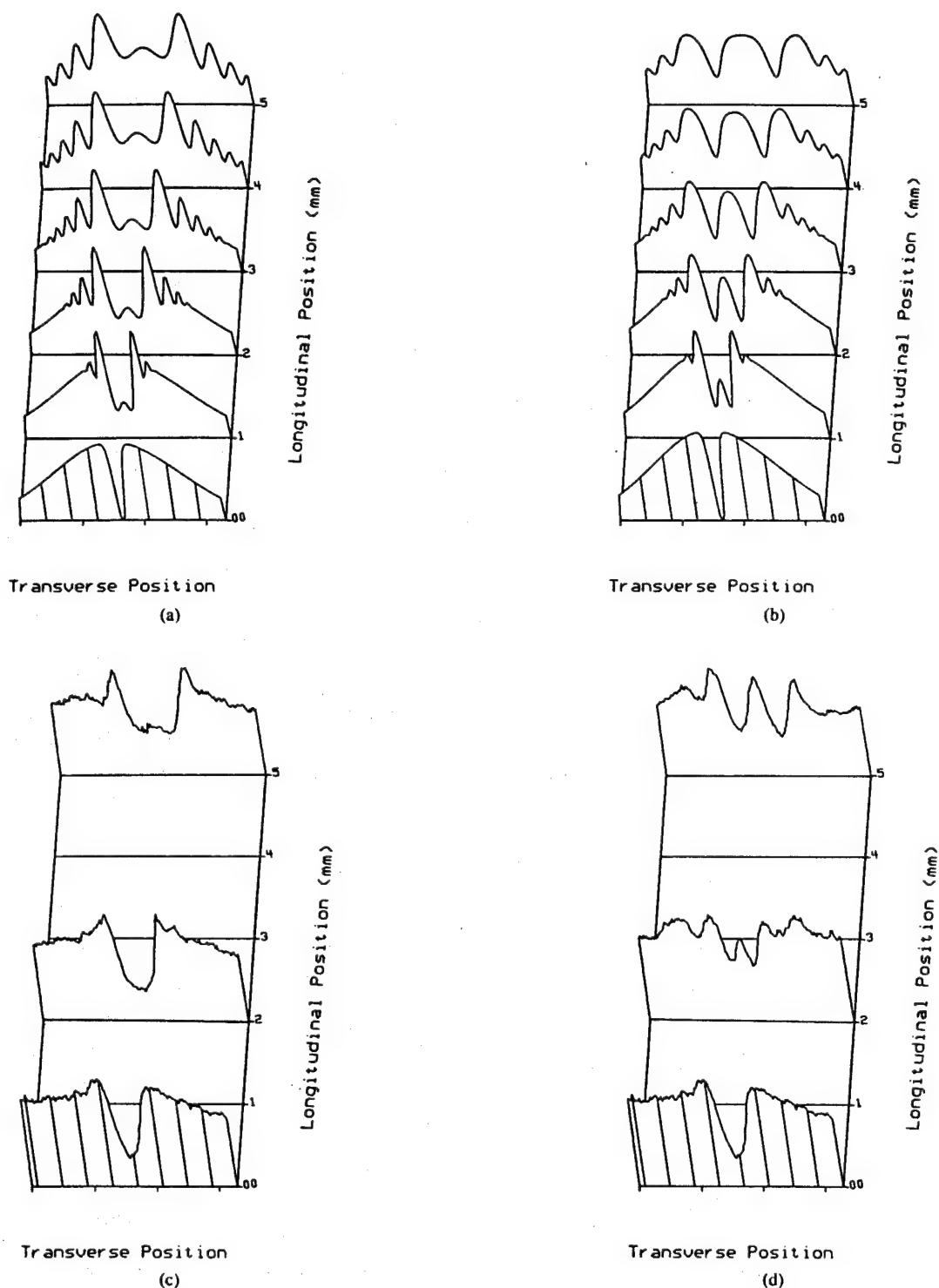


Fig. 7. A comparison between theory and experiment for linear and nonlinear diffraction. Shown are three-dimensional numerical simulations showing the linear (a) and nonlinear (b) diffraction of a  $10\text{ }\mu\text{m}$  wire along with linear (c) and nonlinear (d) experimental results. Note that the nonlinear diffraction results in the formation of two counterpropagating nonfundamental dark spatial solitons in both the theoretical and experimental cases.

pulse are shown for four different widths. The dark band widths used in the figure are, respectively: Fig. 8(a)  $2\text{ }\mu\text{m}$ , Fig. 8(b)  $5\text{ }\mu\text{m}$ , Fig. 8(c)  $10\text{ }\mu\text{m}$ , and Fig. 8(d)  $20\text{ }\mu\text{m}$ . The inverse relationship between the initial condition wire width, and the soliton spacing and dark irradiance,

both characteristics of the propagation of dark spatial solitons, can be readily noted. A quantitative comparison between the experimental results and those predicted theoretically by the Zakharov and Shabat two-dimensional theory is shown in Fig. 9.



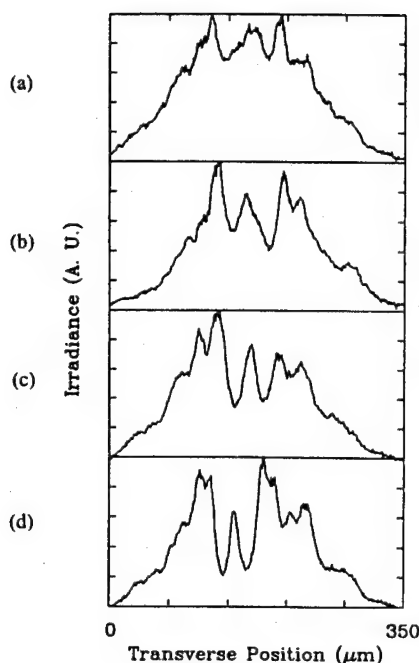


Fig. 8. Spatially transverse irradiance profiles, taken in the direction normal to the wire used to create the initial condition, at the temporal center of the pulse are shown for wire widths of (a) 2  $\mu\text{m}$ , (b) 5  $\mu\text{m}$ , (c) 10  $\mu\text{m}$ , and (d) 20  $\mu\text{m}$ . The incident peak irradiance for this data was 1.1 GW/cm<sup>2</sup> in all cases.

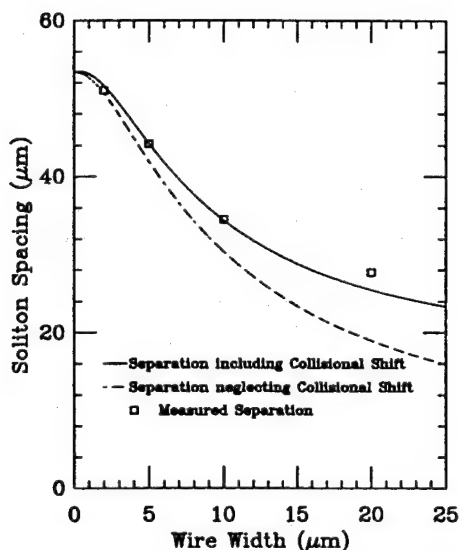


Fig. 9. A quantitative comparison between the experimental results, of the soliton separation as a function of wire width, and those predicted theoretically by [1]. The dashed line is the theoretical contribution from the transverse velocity associated with each of the DSS generated by the initial condition, and the solid line is the spacing predicted when both the contribution from the transverse velocity, as well as the collision shift are included.

In order to interpret this figure, recall that there are two primary contributions to the soliton spacing arising from the geometry of the initial condition, as given in (4). The first contribution comes from the transverse velocity associated with each of the DSS's generated by the initial condition, and is indicated by the dashed curve in Fig. 9. The second contribution is from the shift associated with

the collision interaction which occurs at the initial condition plane. Such a shift is characteristic of the collision interaction of DSS's. The solid curve of Fig. 9 indicates the spacing predicted when both the contribution from the transverse velocity, as well as the collision shift are included. As can be seen, there is good quantitative agreement between experiment and theory. This result is the first experimental evidence for a collision interaction occurring for the propagation of DSS's, and such evidence further supports the interpretation of these experiments as the propagation of dark spatial solitons.

## V. DISCUSSION

In this section we will endeavor to identify the essential features of dark spatial soliton propagation, comment on the differences between the observed experimental solitons and their mathematical counterparts, and differentiate the propagation of dark spatial solitons from the general propagation of optical beams in Kerr media.

In general, all optical beams and pulses, for which propagation is governed by the nonlinear Schrödinger equation, are subject to diffraction. The nature of the diffraction is strongly dependent upon the nature of the medium through which the light energy travels. For example, in a two-dimensional (one transverse, one longitudinal) self-focusing medium, a single behavior is observed, corresponding to the formation of bright spatial solitons. Any initial condition will evolve into a set of solitons, which propagate as localized excitations where the diffraction is balanced by the self-focusing of the medium [note that, in general, these solitons are not stationary, i.e.,  $N = 2$  solitons], plus a radiation component, the amplitude of which decays asymptotically to zero as the propagation axis goes to infinity. If the number of transverse degrees of freedom is permitted to increase to two (a three-dimensional medium), the so-called soliton solution can become unstable [10]. A critical power can be defined which bounds two regions of the parameter space governing this instability. This low-power region is the one where diffraction dominates over self-focusing and the amplitude of the light approaches zero in the infinite limit of the longitudinal variable. For the case of the high-power region, the self-focusing dominates over the diffraction and the beam collapses, theoretically to a point singularity. This result immediately leads to the observation that plane waves are not stable solutions of the NLS equation in three-dimensional self-focusing media. For the case of self-defocusing Kerr media, the situation is substantially different. A straightforward linear stability analysis shows that for this case, two- and three-dimensional plane-wave solutions are stable. This fundamental difference between the self-focusing and defocusing problems is responsible for much of the interesting behavior observed in the experiments presented in this paper. Because the plane-wave modes of the two- and three-dimensional problems are subject to the same general stability criterion, it is possible to observe in the three-dimensional

physical systems behavior which is described quite accurately by two-dimensional mathematics. For example, numerical solutions of the three-dimensional NLS equation show that the analytic two-dimensional analysis provides a good model for the case of dark spatial solitons riding on beams of the order of one wavelength diameter in both transverse dimensions where the adiabatic relaxation of the bright background irradiance due to diffraction and defocusing is included. The similarity between the two- and three-dimensional problems identified above permits experimental investigation of an ostensibly two-dimensional object in a three-dimensional problem space for which the dark soliton solution obtained in [1] by Zakharov and Shabat generalizes to a fundamental dark stripe soliton. Also, the nonlinear diffraction past a dark band discussed in the last section of that work generalizes to the problem experimentally investigated in this paper, that of nonlinear diffraction of a beam or pulse past a single dark band in a self-defocusing medium. In the latter case, the nonlinear diffraction results in the formation of non fundamental dark spatial solitons in pairs, in exactly the same manner as that predicted by Zakharov and Shabat.

Finally, it should be noted that dark spatial soliton-related phenomena have been proposed as an explanation for certain experiments in  $\text{LiNbO}_3$  [11], [12].

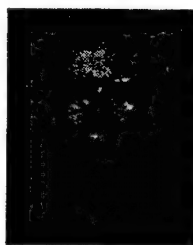
## VI. SUMMARY

In this paper we have experimentally demonstrated the propagation of dark spatial solitons in ZnSe. We have shown that the propagation parameters behave in a manner consistent with two-dimensional analytic and three-dimensional numerical predictions and have also presented the first evidence regarding the collisional shift inherent in the interaction of dark spatial solitons.

## REFERENCES

- [1] V. E. Zakharov and A. B. Shabat, "Interaction between solitons in a stable medium," *Sov. Phys. JETP*, vol. 27, pp. 823-828, 1973.
- [2] A. Hasegawa and F. Tappert, "Transmission of stationary nonlinear optical pulses in dispersive dielectric fibers, II: Normal dispersion," *Appl. Phys. Lett.*, vol. 23, pp. 171-172, 1973.
- [3] G. R. Allan, S. R. Skinner, D. R. Andersen, and A. L. Smirl, "Observation of picosecond fundamental dark spatial solitons in semiconductors," *Opt. Lett.*, vol. 16, pp. 156-158, 1991.
- [4] D. R. Andersen, D. E. Hooton, G. A. Swartzlander, and A. E. Kaplan, "Direct measurement of the transverse velocities of dark spatial solitons," *Opt. Lett.*, vol. 15, pp. 783-785, 1990.
- G. A. Swartzlander, Jr., D. R. Andersen, J. J. Regan, H. Yin, and A. E. Kaplan, "Spatial dark soliton stripes and grids in self-defocusing materials," *Phys. Rev. Lett.*, vol. 66, pp. 1583-1586, 1991.
- [5] A. M. Weiner, J. P. Heritage, R. J. Hawkins, R. N. Thurston, E. M. Kirshner, D. E. Leaird, and W. J. Tomlinson, "Experimental observation of the fundamental dark soliton in fibers," *Phys. Rev. Lett.*, vol. 61, pp. 2445-2558, 1988.
- [6] D. Krokel, N. J. Halas, G. Giuliani, and D. Grishkowsky, "Dark pulse propagation in optical fibers," *Phys. Rev. Lett.*, vol. 60, pp. 29-31, 1988.

- [7] W. J. Tomlinson, R. J. Hawkins, A. M. Weiner, J. P. Heritage, and R. N. Thurston, "Dark optical solitons with finite-width background pulses," *J. Opt. Soc. Amer.*, vol. B6, pp. 329-334, 1989.
- [8] R. N. Thurston and A. M. Weiner, "Collision of dark solitons in optical fibers," *J. Opt. Soc. Amer.*, vol. B8, pp. 471-477, 1991.
- [9] M. Sheik-Bahae, D. J. Hagan, and E. W. VanStryland, "Dispersion and bandgap scaling of the electronic Kerr effect in solids associated with two-photon absorption," *Phys. Rev. Lett.*, vol. 65, pp. 96-99, 1990.
- [10] P. L. Kelley, "Self-focussing of optical beams," *Phys. Rev. Lett.*, vol. 15, pp. 1005-1007, 1964.
- [11] H. Jerominek, C. Delisle, and R. Tremblay, "Optical branching effect in  $\text{Ti:LiNbO}_3$  waveguides: Near-field pattern studies," *Appl. Opt.*, vol. 25, pp. 732-736, 1986.
- [12] P. A. Belanger and P. Mathieu, "Dark soliton in a Kerr defocussing medium," *Appl. Opt.*, vol. 26, pp. 111-113, 1987.



Steven R. Skinner, was born in Des Moines, IA, in 1962. He received the B.S., M.S., and Ph.D. degrees from the University of Iowa, Iowa City, in 1985, 1989, and 1991, respectively. His Ph.D. dissertation is entitled "Ultrafast Dark Spatial Solitary Wave Propagation Phenomena."

He has recently joined the faculty of Electrical and Computer Engineering at Wichita State University, Wichita, KS, where his research interests include nonlinear waveguides and solitary wave propagation.



Graham R. Allan was born on March 21, 1959 in Largs, Scotland. He received the B.S. and Ph.D. degrees in 1981 and 1985, respectively, from Heriot-Watt University, Edinburgh, Scotland. His Ph.D. dissertation is entitled "Nonlinear Far Infrared Magneto-Optical Spectroscopy of III-V Semiconductors." This work concerned the dynamics of the electron scattering processes, including the effects of doping, in bulk and 2-D materials.

From 1985 to 1987 he developed a photo-Hall technique to measure nonlinear optical parameters in InSb in order to gain a more fundamental understanding of nonlinear optical absorption and refraction. In 1988 he joined the Service National des Champ Intense, of the C.N.R.S., Grenoble, France where his work involved magnetotransport at high pressures and very low temperatures in heterostructures and superlattices. He is currently a Visiting Research Scientist with the University of Iowa, Iowa City, where he is working on nonlinear optical propagation phenomena and optical limiting.

Dr. Allan is a member of the Optical Society of America.



David R. Andersen, was born in Iowa Falls, IA, on February 28, 1959. He received the B.S.E.E. degree in 1981 from Iowa State University, Ames, and the M.S.E.E. and Ph.D. degrees in 1982 and 1986, respectively, from Purdue University, West Lafayette, IN.

Since 1986, he has been an Assistant Professor of electrical and computer engineering at the University of Iowa.

Dr. Andersen is a member of the Optical Society of America and the American Physical Society.

Arthur L. Smirl (S'65-S'73-M'75-SM'84), photograph and biography not available at the time of publication.

## **Appendix L**

### **Picosecond Measurements of Optical Nonlinearities in King's Complex and Synthesized Analogues**

**SPIE, Vol. 1692, pp. 170-176 (1992)**



# PROCEEDINGS REPRINT



SPIE—The International Society for Optical Engineering

*Reprinted from*

## ***Nonlinear and Electro-Optic Materials for Optical Switching***

23–24 April 1992  
Orlando, Florida



**Volume 1692**

# Picosecond measurements of optical nonlinearities in King's complex and synthesized analogues

G. R. Allan, S.J. Rychnovsky, Arthur L. Smirl, and Thomas F. Boggess

Center for Laser Science and Engineering, The University of Iowa,  
124 A.M.R.F. Oakdale Campus, Iowa City, Iowa 52240

&

Lee Tutt, Alan. Kost, and M. B. Klein

Hughes Research Laboratories, 3011 Malibu Canyon Road, Malibu, California 90265

## ABSTRACT

We have measured the photodynamics of reverse saturable absorption (RSA) in solutions of cyclopentadienyliron carbonyl tetramer (King's complex) using picosecond pump-probe techniques. Similar preliminary measurements in solutions of synthesized variations of the King's complex indicate that the excited state transition responsible for the observed RSA is most likely a second d-d transition within the metal core of the molecule. On time scales of hundreds of picoseconds, the observed RSA in the King's complex is well characterized by a three-level rate-equation, singlet-state absorption model, where the excited-state cross section is greater than that of the ground state. On nanosecond timescales and at fluences above  $200 \text{ mJ.cm}^{-2}$ , however, we observe the onset of a response that is consistent with a thermally induced scattering process. Further evidence of this scattering is provided by angularly-resolved measurements of the transmitted and back-scattered signals for nanosecond excitation. When the King's complex is incorporated in a solid host negligible scatter was observed and the response is completely described by the singlet parameters extracted from the picosecond measurements. The observation of, scatter from solution, together with a time-resolved decay to the ground state that is rapid ( $\sim 120 \text{ ps}$ ) and largely nonradiative in this molecule, indicate that solutions of King's complex may provide a mechanism for efficiently generating thermal nonlinearities on a subnanosecond timescale.

## I. INTRODUCTION

In this paper, we discuss picosecond photodynamics and optical limiting in the organometallic compound cyclopentadienyliron carbonyl tetramer  $[(C_5H_5)Fe(CO)]_4$ , commonly referred to as King's Complex<sup>1</sup>. Solutions of this compound in methylene chloride have been previously shown to exhibit optical limiting properties on nanosecond time scales<sup>2</sup>. The nonlinearity responsible for the limiting was initially attributed to triplet-triplet excited-state absorption with an excited-state cross section larger than that of the ground state (i.e., reverse saturable absorption, RSA). As we have reported<sup>3</sup>, such RSA also occurs in this molecule on picosecond time scales, indicating that singlet-singlet transitions must also be considered. In order to quantify the photodynamics that determine the RSA, we have performed time-resolved nonlinear spectroscopy on King's complex in methylene chloride solution as well as in other solvents. Specifically, by comparing the results of pump-probe transmission measurements performed with 532 nm picosecond pulses to a five-level rate-equation model, we have extracted values for the singlet lifetime and the excited singlet-state absorption cross section, and we have determined bounds on the lifetime of the second excited singlet state and the product of the singlet-triplet crossing rate with the triplet-triplet absorption cross section. Here, we briefly review these results and then discuss preliminary measurements on synthesized analogues of the King's Complex that indicate that the excited-state absorption is most likely not a charge-transfer transition involving the ligands of the molecule but a second d-d transition involving the metal core. We further demonstrate that the parameters extracted from the picosecond measurements cannot describe the observed limiting behavior for nanosecond excitation conditions. Moreover, from picosecond pump-probe data obtained at high fluences and at nanosecond probe delays, from angularly-resolved transmission and reflection measurements with nanosecond excitation, and from nonlinear transmission data obtained from samples of King's complex embedded in a solid host, we conclude that the discrepancy between the picosecond and nanosecond results can be attributed to

optically induced scattering that is initiated on a nanosecond timescale.

## II. EXPERIMENTAL

The King's complex used in these experiments was prepared from cyclopentadienyliron dicarbonyl dimer, which was purchased from Strem Chemicals and was used as received. The cyclopentadienyliron carbonyl tetramer, King's complex, was synthesized from the cyclopentadienyliron dicarbonyl dimer by the method of White and Cunningham<sup>4</sup> and recrystallized twice from methylene chloride/hexane. All measurements reported here were performed on solutions of King's complex dissolved in one of three solvents, methylene chloride, THF, or toluene. The solvents were all oxygen degassed with nitrogen by a vigorous bubbling purge for at least 2 hours prior to use. This precaution avoids possible quenching of triplet state population by oxygen contamination. All solutions were subsequently handled anaerobically.

The photodynamics were measured using time-resolved pump-probe transmission techniques with an excitation wavelength of 532 nm and a pulse duration of 25 ps (FWHM intensity). The picosecond pulses were produced by a frequency-doubled, actively and passively mode-locked, Nd:YAG laser. The laser operates in the TEM<sub>00</sub> transverse mode and produces temporally near-Gaussian pulses. The actual pulse width was determined on a shot-by-shot basis using second harmonic techniques.

The nanosecond data were taken using the frequency doubled output of an injection-seeded, single-longitudinal-mode, Q-switched Nd:YAG laser. The output of a gain-saturated amplifier was imaged into the samples to provide a near-top-hat spatial profile and, hence, near uniform excitation.

## III. RESULTS AND DISCUSSION

King's complex in methylene chloride has been shown to exhibit RSA on picosecond timescales. This is clearly shown in figure 1 which is a plot of the differential transmission of a picosecond probe for four different pump fluences in a  $7 \times 10^{-4}$  molar solution of King's complex in methylene chloride. The solid lines are the numerical fits to the data based on a rate equation model (discussed in detail in reference 3), where the significant fitting parameters are the excited singlet state absorption cross-section,  $\sigma_{12}$ , and the excited singlet state relaxation time,  $\tau_{10}$ . The numerical fits agree with the experimental results over a wide range of fluence. The measured parameters are  $\tau_{10} = 120$  ps,  $\sigma_{12} = 8 \times 10^{-18} \text{cm}^2$  compared to the ground state absorption cross section  $\sigma_{01}$  of  $4.1 \times 10^{-18} \text{cm}^2$  and the lifetime of the upper excited singlet state is estimated to be  $\tau_{21} \leq 1$  ps. The observed response of King's complex dissolved in the other solvents (THF and toluene) to picosecond pulses at 532 nm was similar at these fluences. The excited state cross-section and recovery times that were extracted by the numerical fits were unchanged. Only at the very highest fluences ( $> 200 \text{mJ.cm}^{-2}$ ) in the picosecond experiments were any solvent related effects observed and then only near zero delay. These will be subject to further investigation and discussed in a future publication.

Previous nanosecond measurements<sup>2</sup> of the excited-state absorption of King's complex suggest that for nanosecond optical excitations a long lived induced absorption is present. This residual absorption was tentatively attributed to a build up of population in the triplet state. The overall contribution of the triplet state to the absorption of the pump and probe in the picosecond experiments reported here is difficult to quantify, but it has to be extremely weak. Clearly, if a long lived triplet absorption is present, its maximum value is less than our minimum detectable  $\Delta T/T$ . This allows us to estimate an upper bound on the intersystem crossing and the triplet's photon absorption cross section quotient ( $\sigma_{34}/\tau_{13}$ ). The upper bound is found to be  $3 \times 10^{-9} \text{cm}^2 \text{s}^{-1}$ . If we assume  $\sigma_{34} = \sigma_{12}$ , this indicates that for both the picosecond and nanosecond experiments the majority of photoexcited molecules relax directly back to the ground state from the first excited singlet state.

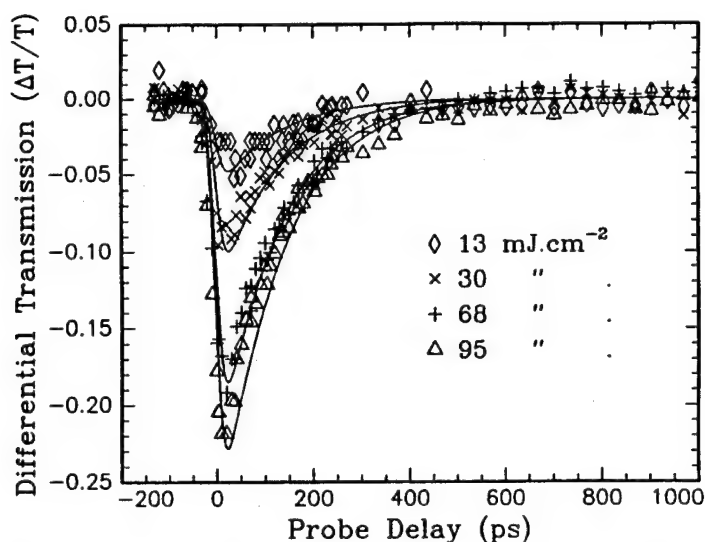


Fig. 1. Time resolved differential transmission measurements of King's complex in methylene chloride using pulses of 532 nm with a FWHM of 25 ps. The linear transmission is ~35%. A negative value for differential transmission indicates increased absorption. The solid lines are the numerical fits for a single set of parameters at the indicated fluence.

To help develop a more complete understanding of the photodynamics involved within this molecule and possibly isolate the excited state transition responsible for RSA in King's complex we have identified three possible excited-state transitions by examining the molecular orbital diagram for this molecule as derived by Trinh-Toan et al<sup>6</sup>. The three possibilities for the excited state transition are: (i.) charge transfer from the cyclopentadienyl ligand to the metal, (ii.) charge transfer to the carbonyl ligand from the metal or (iii.) a second d-d transition within the metal core. To test which of these transitions may be involved in the RSA we have selectively altered the molecule by replacing either the cyclopentadienyl ligand or the carbonyl ligand. If the synthesized molecule contains an altered ligand that is involved in the excited state transition then this should affect the observed excited state absorption cross section. We note that the ground state absorption is attributed to a d-d transition involving primarily the metal core<sup>5</sup>, and ligand substitution should, therefore, not strongly influence the ground-state absorption cross section. Specifically, we have synthesized a version of the King's complex (referred to as methyl-King's) in which a methyl group has been substituted for one of the hydrogen atoms in each of the cyclopentadienyl ligands and a version (referred to as tri-ethyl King's) in which a tri-ethyl aluminum group is bonded to each of the carbonyl ligands. The former molecule allows us to isolate a charge-transfer transition from the cyclopentadienyl ligand to the metal, while the second molecule allows us to isolate a charge-transfer from the metal to the carbonyl ligand. These substitutions alter the bonding strength of the ligand and hence the energy levels, however, they have very little effect on the tetrahedral iron core of the molecule. Linear spectra of the molecules in solution confirm that little change has resulted in the ground state absorption. Preliminary pump-probe measurements in solutions of these compounds also suggests that the excited state absorption and recovery are unaltered. The implication of these results is that the most likely source of the excited state absorption is a second d-d transition involving primarily the metal core.

The picosecond pump-probe measurements have allowed us to quantify the photodynamics of this molecule and tentatively identify the possible excited state transition. However, on trying to model the nanosecond experimental results we consistently fail to predict the limiting response of the system except at the very lowest fluences. This is illustrated in figure 2, where we plot the nanosecond limiting data for King's complex dissolved in methylene chloride along with the numerical fit based on the measured parameters from the picosecond experiments. As discussed above, we have measured an upper bound on  $\sigma_{34}/\tau_{13}$  and it is found to be at least several orders of magnitude too small to explain the nanosecond result.

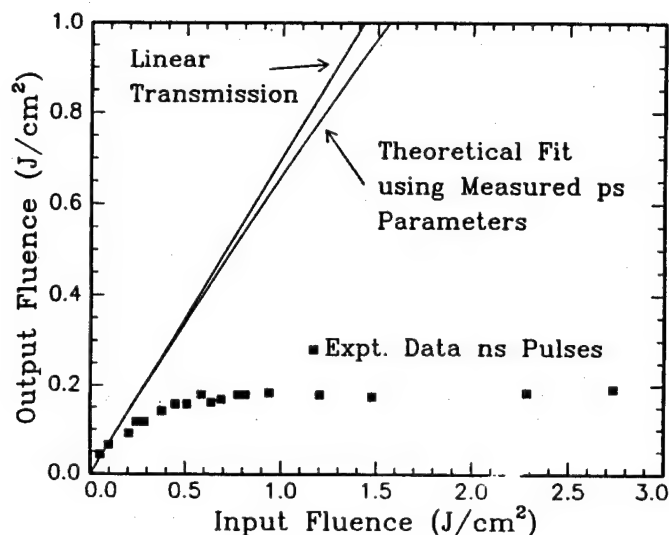


Fig. 2. The observed limiting of nanosecond pulses in a solution of King's complex and methylene chloride is plotted (squares). The linear transmission and the predicted response of King's complex using the parameters obtained from the picosecond measurements is also shown.

To resolve the discrepancy between the nanosecond experimental data and the numerical fits, we have performed a series of picosecond time-resolved pump-probe experiments at higher fluences and longer delays. Figure 3 is a plot of the differential transmission of the probe through King's complex in THF at 200 and 277  $\text{mJ}\cdot\text{cm}^{-2}$  with up to 2 ns delay between the pump and probe. At 200  $\text{mJ}\cdot\text{cm}^{-2}$ , we observe prompt RSA that

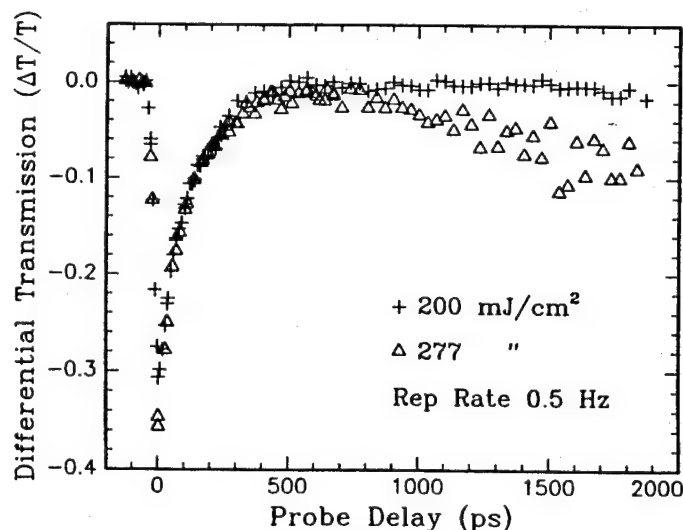


Fig. 3. Differential probe transmission as a function of probe delay for pump fluences of 200  $\text{mJ}\cdot\text{cm}^{-2}$  and 277  $\text{mJ}\cdot\text{cm}^{-2}$  in a solution of King's complex and THF.

recovers completely within a few hundred picoseconds. This is completely consistent with the results shown in figure 1 for lower fluences. At the higher fluence, however, after the predictable initial response of the system, a renewed reduction in the differential transmission appears. This feature continues to increase in magnitude, even up to our maximum delay of  $\sim 2$  ns, with a corresponding increase in scatter in the data. We

further note that at the higher fluence bubbles were observed rising from the interaction volume. The data in figure 3 were taken at a repetition rate of 0.5 Hz. We repeated the higher fluence data at a repetition rate of

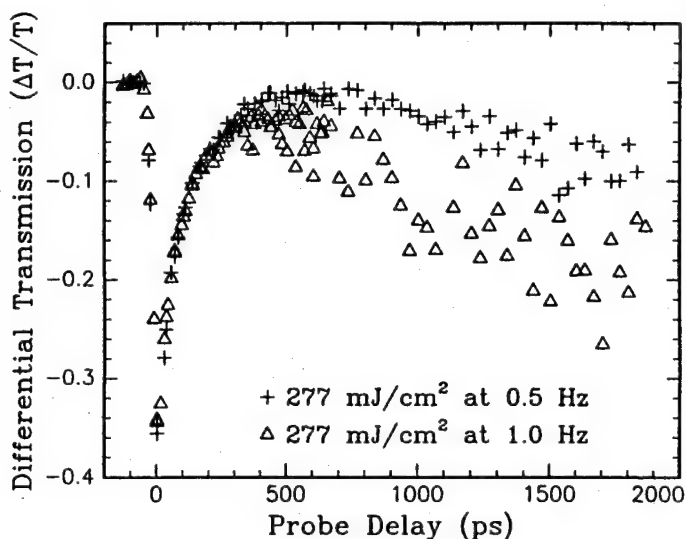


Fig. 4. Differential probe transmission for a pump fluence of 277 mJ/cm<sup>2</sup> and repetition rates of 0.5 and 1 Hz. The increase in scatter is evident at the higher repetition rate.

1 Hz, and we compare these results with the 0.5 Hz data in figure 4. The signal at ns delays is clearly much more pronounced and the scatter in the data is more severe at the higher repetition rate, indicating that the effect is not intrinsic to the King's complex. We believe that all of the signatures of the reduction in transmission at nanosecond delays are consistent with a thermally induced scattering process that develops within a nanosecond of excitation. We emphasize that this scatter occurs only for fluences in excess of 200 mJ.cm<sup>-2</sup> and develops on a nanosecond time scale. Hence, this process does not influence the system parameters extracted from the picosecond pump-probe data at lower fluences.

The strong limiting response of King's complex in methylene chloride for nanosecond optical pulses, the inability of our numerical model to predict this behaviour, and the presence of a fast thermally induced scattering process suggest that the latter mechanism may be contributing to the observed optical limiting of nanosecond pulses. An angularly resolved measurement of the transmission and reflection of nanosecond pulses in the solutions of King's complex confirmed that significant amounts of energy were being scattered from the beam.

To eliminate the possibility of thermally induced scattering within the solvent, King's complex has been incorporated into a solid host, poly-methyl-methylacrylate (PMMA). The optical limiting of nanosecond pulses by King's complex in PMMA is plotted in figure 5 (squares). Clearly, the optical limiting observed for this solid sample is much weaker than that observed in solutions (compare to figure 2). The solid curve in figure 5 represents the results of a numerical calculation based on the system parameters determined from the picosecond experiments on King's complex in methylene chloride solutions. To emphasize the weak dependence on triplet absorption, we have numerically "switched off" the intersystem crossing for this calculation. We found that the curve was only slightly altered when we used our experimentally determined upper bound on the product of the intersystem crossing rate with the triplet cross section. This is consistent with the rapid (120 ps) recovery of the singlet RSA. The agreement between the data and theory suggests that the observed weak limiting in the King's complex/PMMA can be completely described by intrinsic properties of the King's complex and that the stronger limiting in solutions of King's complex observed for nanosecond excitation appears to be a fast thermally induced scattering process. Furthermore, the excellent fit obtained using only singlet system parameters suggests that the triplet system plays little, if any, role in the nanosecond optical response of the molecule.

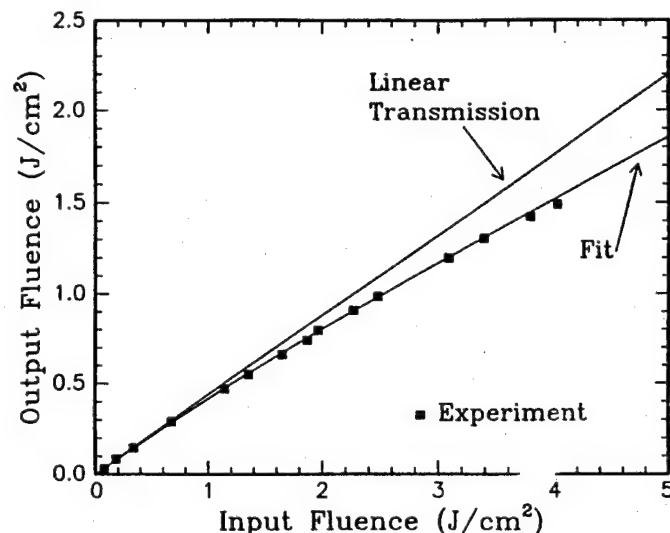


Fig. 5. The limiting response of King's complex in PMMA to nanosecond pulses is plotted (squares) and superimposed is the numerical fit generated by the three level model using the parameters measured by picosecond techniques.

#### IV CONCLUSIONS

We have measured and numerically modelled the picosecond photodynamics of RSA in King's complex and synthesized variations. The photodynamics of the system are well described by a three level rate equation model. Only the singlet states need be considered to obtain a good fit to the picosecond experimental data over a wide range of fluence. By including the triplet system in our model (five-level model) we have placed an upper limit on the product of the intersystem crossing rate and the triplet absorption cross section. From picosecond pump-probe experiments in synthesized variations of King's complex we have tentatively identified the excited state transition responsible for RSA. The observed RSA on picosecond times may be attributed to a second d-d transition within the metal core of the tetramer.

We have been able to accurately model the optical limiting of nanosecond pulses on transmission through King's complex in PMMA using only the singlet system parameters. On the other hand, the nanosecond limiting data obtained for methylene chloride solutions of King's complex could not be fit even with the five level model. This indicates that an additional mechanism is beneficially contributing to the optical limiting of nanosecond pulses in solutions of King's complex and methylene chloride.

In the picosecond pump-probe experiments, evidence of a fast (sub-nanosecond) thermally related scatter was observed. This scatter appears to be connected with the recovery of the differential transmission. As the molecules relax back to the ground state the optically absorbed energy is evidently very efficiently transferred to the solvent. We note that, in preliminary attempts, we have observed no fluorescence from these molecules. This suggests that relaxation back to the ground state involves significant nonradiative pathways. This rapid transfer of energy to the solvent apparently results in a very effective thermal nonlinearity that could be applied to optical limiting of nanosecond pulses.

#### V REFERENCES

1. R.B. King, *Inorg. Chem.*, Vol 5, No12, pp. 2227-2230, December 1966.

2. Lee Tutt, S.W. McCahon and M.B. Klein, "Nonlinear Optical Properties of Organometallic Compounds in Solids and Solutions." Proc of NLO90, pp. 57-58, Hawaii 1990.
3. G.R. Allan, D.R. Laberge, S.J. Rychnovsky, T.F. Boggess, and A.L. Smirl, To be published *J.Phys.Chem.* July 2, 1992.
4. A.J. White and A.J. Cunningham, *J. Chem. Ed.*, Vol. 57, No4, (1980).
5. Trinh-Toan, W.P. Fehlhammer and Lawrence F. Dhal, *J. Am. Chem. Soc.*, 94:10, pp 3389-3396, May 1972.



## **Appendix M**

### **Picosecond Reverse Saturable Absorption in King's Complex $[(C_5H_5)Fe(CO)]_4$**

Journal of Physical Chemistry, Vol. 96, pp.6313-6317 (1992)

Reprinted from The Journal of Physical Chemistry, 1992, 96.  
Copyright © 1992 by the American Chemical Society and reprinted by permission of the copyright owner.

## Picosecond Reverse Saturable Absorption in King's Complex $[(C_5H_5)Fe(CO)]_4$

G. R. Allan, D. R. Laberge, S. J. Rychnovsky, Thomas F. Boggess, Arthur L. Smirl,  
and Lee Tutt

## Picosecond Reverse Saturable Absorption in King's Complex $[(C_5H_5)Fe(CO)]_4$

G. R. Allan,\* D. R. Laberge, S. J. Rychnovsky, Thomas F. Boggess, Arthur L. Smirl,

*Center for Laser Science and Engineering, 124 AMRF, Oakdale Campus, The University of Iowa, Iowa City, Iowa 52240*

and Lee Tutt

*Hughes Research Laboratories, 3011 Malibu Canyon Road, Malibu, California 90265*

*(Received: February 10, 1992)*

We have demonstrated reverse saturable absorption of picosecond pulses at 532 nm using the organometallic tetramer cyclopentadienyliron carbonyl  $[(C_5H_5)Fe(CO)]_4$  dissolved in methylene chloride. Time-resolved pump-probe measurements and numerical simulations based on a five-level model indicate that reverse saturable absorption of ultrafast optical pulses is due to excited singlet absorption in this tetramer. We have determined the lifetime of the first excited singlet state to be 120 ps, and have measured a singlet excited-state capture cross-section of  $8 \times 10^{-18} \text{ cm}^2$ , twice that of the ground-state cross-section. In addition, we have placed bounds on the lifetime of the second excited singlet state and the branching ratio between the singlet and triplet systems.

### I. Introduction

The phenomena of reverse saturable absorption (RSA), as reported in 1967 by Giuliano and Hess,<sup>1</sup> was observed while dyes for saturable absorption were being investigated. Giuliano et al. reported that, in contrast to saturable absorption, some compounds, such as sudanschwarz-B and indanthrone, exhibit an absorption that increases with increasing intensity (RSA). Physically, the process can occur when the absorption cross-section of an excited molecular state exceeds that of the ground state. As the optical excitation rate increases, more molecules are promoted to the excited state, thus causing the absorption to increase with fluence. Because this process involves electronic transitions, materials that exhibit RSA generally have an extremely fast response, unlike the photochromic materials used in commercial sunglasses which depend on slow geometric rearrangements. Although RSA has not been extensively studied since the early work of Giuliano and Hess, recent interest in the potential application of RSA to optical limiting<sup>2-5</sup> and mode locking of solid-state lasers<sup>6</sup> has renewed study in such materials.

In this paper, we examine the picosecond photodynamics of the organometallic compound cyclopentadienyliron carbonyl tetramer

$[(C_5H_5)Fe(CO)]_4$ . This compound was first synthesized by R. B. King<sup>7</sup> in 1966 and commonly bears his name. The compound possesses high photostability, thermal (160 °C) stability, and chemical stability and has been previously shown to exhibit RSA on nanosecond time scales.<sup>8</sup> In this case the RSA was attributed to triplet-triplet excited-state absorption. As we report below, RSA also occurs in this molecule on picosecond time scales, indicating that singlet-singlet transitions are also involved. In order to quantify the photodynamics that determine the RSA, we have performed time-resolved nonlinear spectroscopy on King's complex in methylene chloride solution. Specifically, by comparing the results of pump-probe transmission measurements performed with 532-nm picosecond pulses to a five-level rate-equation model, we extract values for the singlet lifetime and the excited singlet-state absorption cross-section, and we determine bounds on the lifetime of the second excited singlet state and the product of the singlet-triplet crossing rate with the triplet-triplet absorption cross-section.

In the following section we describe the preparation of King's complex and the experimental arrangements for the picosecond measurements. In section III, we describe the results of single

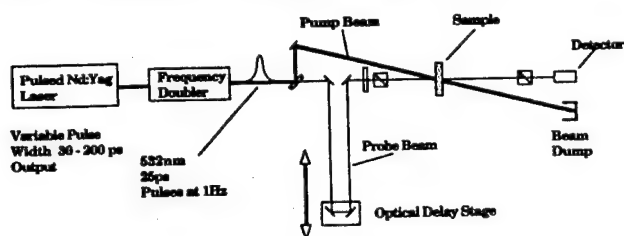


Figure 1. Schematic of the experimental setup used for the time-resolved pump-probe and nonlinear transmission measurements.

pulse transmission (induced absorption) and time-resolved pump-probe transmission measurements. We then discuss the possible optically-induced transitions in King's complex that give rise to the RSA and develop a five-level model used to analyze our results in section IV. Finally, our concluding remarks are presented in section V.

## II. Experimental Section

The King's complex used in these experiments was prepared from cyclopentadienyliron dicarbonyl dimer, which was purchased from Strem Chemicals and was used as received. The cyclopentadienyliron carbonyl tetramer, King's complex, was synthesized from the cyclopentadienyliron dicarbonyl dimer by the method of White and Cunningham<sup>9</sup> and recrystallized twice from methylene chloride/hexane. All measurements reported here were performed on solutions of King's complex dissolved in methylene chloride. The methylene chloride was oxygen degassed with nitrogen by a vigorous bubbling purge for at least 2 h prior to use. This precaution avoids possible quenching of triplet-state population by oxygen contamination. All solutions were subsequently handled anaerobically.

The nonlinear optical properties were measured using an excitation wavelength of 532 nm and a pulse duration of 25 ps (fwhm intensity) in two distinctly different types of experiments: single-pulse transmission and time-resolved pump-probe measurements. The picosecond pulses were produced by a frequency-doubled, actively and passively mode-locked, Nd:YAG laser. The laser operates in the TEM<sub>00</sub> transverse mode and produces temporally near-Gaussian pulses of nominally 30-ps duration (fwhm) at 1.064  $\mu\text{m}$ . The actual pulse width was determined on a shot-by-shot basis using second harmonic techniques.

The picosecond pump-probe and transmission experimental arrangement is shown schematically in Figure 1. A single pulse is split into two (an intense pump and a much weaker probe), a variable delay is introduced into the probe path, and the two pulses are recombined at the sample cell at a small angle (1.2°). The pump was collimated, and the probe was focused to measured Gaussian spots of radii 280 and 30  $\mu\text{m}$ , respectively, at the sample. Considerable care was taken to ensure accurate overlap within the sample. The small angle between the beams and the fact that the probe spot size is considerably smaller than the pump ensure that the probe interrogates a radially uniform region of material in the 2-mm cell. The probe polarization, which was controlled by a half-wave plate and polarizer, was for most measurements selected to be perpendicular to the polarization of the pump. Absolute timing between the pump and probe (i.e., zero delay) was determined by translating a thin wafer of ZnSe, which is a two-photon absorber at 532 nm, into the beam interaction volume and measuring the probe transmission as a function of the relative delay between the pump and probe. The instantaneous two-photon-induced absorption of the probe is negligible except when the pump and probe are temporally and spatially coincident, and it is maximized at zero delay. Zero delay is, therefore, the delay at which the probe transmission is a minimum. We characterize the nonlinear absorption in King's complex by measuring the transmitted probe energy as a function of pump fluence and relative delay between the pump and probe. The single-pulse nonlinear transmission measurements were conducted by simply blocking single-pulse nonlinear transmission measurements were conducted by simply blocking the incident probe and measuring

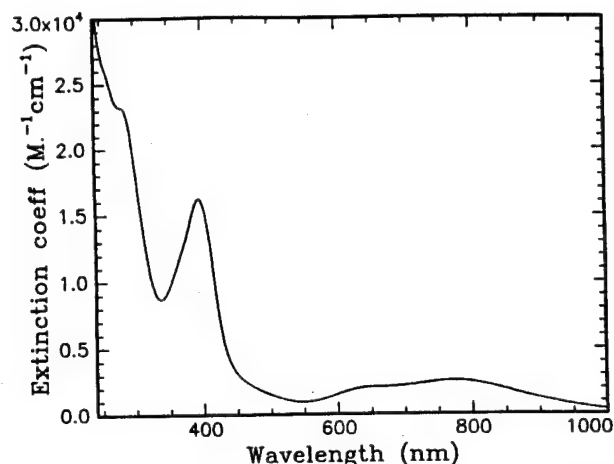


Figure 2. Linear absorption spectrum of a  $7 \times 10^{-3}$  M solution of King's complex in methylene chloride with solvent background subtracted. The extinction coefficient is  $1035 \text{ cm}^{-1} \text{ M}^{-1}$  at 532 nm.

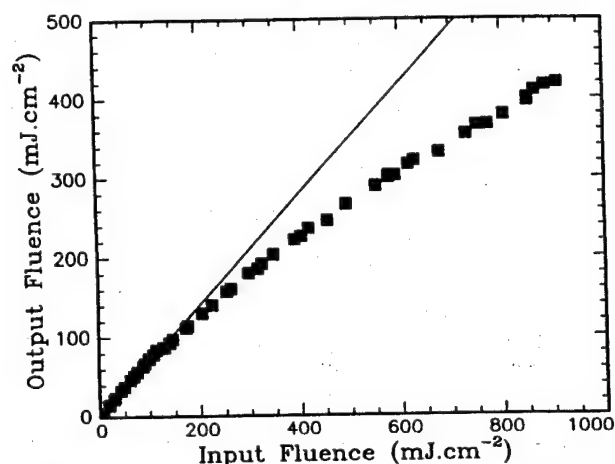


Figure 3. Transmitted fluence as a function of input fluence in King's complex for picosecond pulses. The solid line represents linear transmission of  $\sim 70\%$ ; the squares are the experimental points which clearly show the onset of reverse saturable absorption, i.e., increasing absorption with fluence.

the pump transmission as a function.

## III. Results and Discussion

The ground-state absorption spectrum of a  $\sim 7 \times 10^{-4}$  M methylene chloride solution of the cyclopentadienyliron carbonyl tetramer was measured in a 1-cm-optical-path quartz cell using a standard UV/visible spectrometer and is shown in Figure 2. This spectrum is background corrected, i.e., the absorption due to the solvent alone has been removed, and it is consistent with those reported in the literature.<sup>10</sup> For wavelengths between approximately 550 and 1000 nm, the spectrum consists of a broad, relatively weak absorption band. Upon close inspection this feature is seen to be composed of two separate peaks, one centered near 650 nm and one centered near 775 nm. These peaks have been assigned to metal-metal core transitions.<sup>12</sup> The 532-nm excitation used for the present experiments lies on the high energy side of these resonances and below the strong charge-transfer transitions that dominate the spectrum in the blue. The extinction coefficient at 532 nm is  $1035 \text{ cm}^{-1} \text{ M}^{-1}$  corresponding to an optical absorption cross-section,  $\sigma_{01}$ , of  $4.1 \times 10^{-18} \text{ cm}^2$ .

The results of the single-pulse picosecond transmission measurement are shown in Figure 3, where we plot the transmitted fluence as a function of input fluence. For this measurement, the concentration of the solution was set such that the 2-mm cell had a small signal transmission of  $\sim 70\%$  at 532 nm, corresponding to a molarity of  $\sim 9 \times 10^{-4}$  M. The solid line represents the linear response of the system. Comparison of the data with this line clearly shows the onset of RSA for input fluences in excess of 200

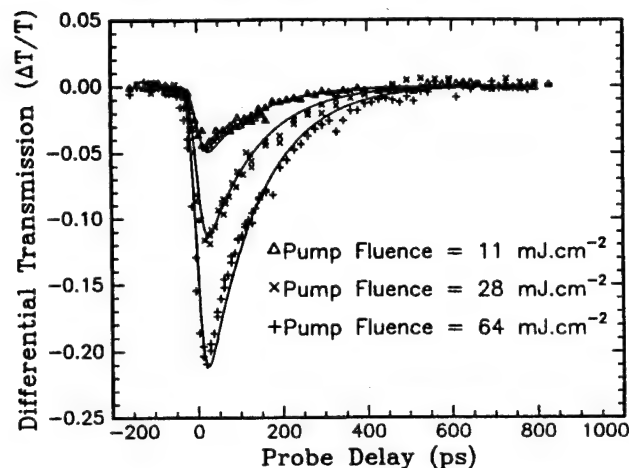


**Figure 4.** Time-resolved differential transmission measurements of King's complex in methylene chloride using pulses of 532 nm with a fwhm of 25 ps. The linear transmission is  $\sim 35\%$ . A negative value for differential transmission indicates increased absorption. The solid lines are the numerical fits for a single set of parameters at the indicated fluence; see section IV and Table I.

$mJ/cm^2$ . Inspection of the transmitted beam profile showed that no significant self-lensing occurred as the beam passed through the cell, indicating that the system response was due to induced absorption. We emphasize that this optically-induced absorption occurs during the 25-ps optical pulse. Since we expect no significant intersystem crossing to occur on such time scales, we attribute the observed picosecond RSA to excited-state absorption within the singlet system. If the lifetime of the excited singlet state is on the order of or shorter than the optical pulse duration, this singlet excited-state absorption will depend on both the singlet lifetime,  $\tau_{10}$ , and the absorption cross-section,  $\sigma_{12}$ . In such a case, we cannot isolate and separately measure these two quantities from the single-pulse transmission results. This problem can be overcome by picosecond time-resolved measurement (i.e., pump-probe) techniques, where we can resolve the induced absorption and its recovery.

The picosecond, time-resolved, pump-probe measurements were performed over a range of relatively low pump fluences ( $11\text{--}64\text{ mJ/cm}^2$ ) in a 2-mm sample with a linear transmission of  $\sim 35\%$ . A higher sample concentration,  $\sim 2 \times 10^{-3}\text{ M}$ , for the pump-probe experiments relative to the single-pulse measurements was chosen to improve the signal to noise ratio. The differential transmission, i.e., the change in the probe transmission normalized by the linear transmission ( $\Delta T/T$ ), is shown as a function of probe delay in Figure 4 for three pump fluences. At each fluence, we observe reverse saturable absorption. Initially the absorption of the solution increases as a function of time in a manner consistent with the temporal integration of the pump pulse. Once the pump pulse has passed through the sample, this initial response is followed by a decay to the original transmission within a few hundred picoseconds. This behavior is consistent with induced absorption in the first excited singlet state that increases as the excited state is populated and then diminishes as the population in that state relaxes to the ground state. Quantitatively, we find that the measured dynamics of the tetramer solution on picosecond time scales are consistent with the physical model described below. Comparison of the experimental results with this model has allowed us to extract values for several system parameters.

#### IV. Theory and Modeling

Figure 5 shows the molecular structure of the King's complex as determined from X-ray crystallography by Neuman et al.<sup>11</sup> The four iron atoms are equivalent and form a tetrahedron. Each cyclopentadienyl ligand bonds through the five  $\pi$ -orbitals of the carbons to an iron atom. Each carbonyl is  $\mu$ -bonded (triply bonding) to three iron atoms on a face of the metal tetrahedron core. This cage-like structure contributes greatly to the molecule's robust nature.

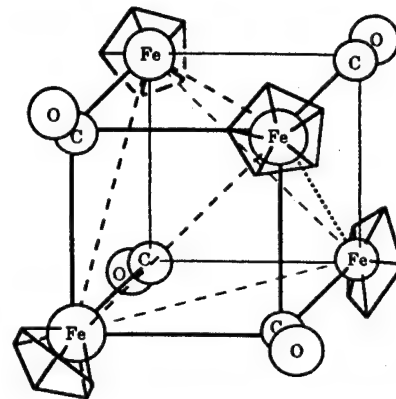


**Figure 5.** Atomic structure of cyclopentadienyliron carbonyl tetramer after ref 8.

The molecular orbital levels of cyclopentadienyliron carbonyl tetramer were originally determined by Trinh-Toan and co-workers.<sup>12</sup> The highest occupied molecular orbital (HOMO) is predominately composed of essentially nonbonding iron atomic orbitals. The orbital is fully occupied, giving rise to the diamagnetic character of the compound. The lowest unoccupied molecular orbital (LUMO) is formed from six strongly antibonding tetrairon orbitals. The lowest energy transition, the HOMO to the LUMO, is from a nonbonding predominately d-orbital of the irons to an antibonding orbital. This d-d transition should primarily involve the metal core of the cluster and cause a general bond weakening within the tetragonal structure. The ground state is a singlet, and an allowed transition will conserve spin to an excited singlet state. Intersystem crossing will allow a spin change of the excited unpaired electron to give a triplet state. The triplet state will possess a longer lifetime than the excited singlet, since relaxation back to the ground state requires another spin flip transition.

Large absorption cross-sections are due to spin-allowed transitions (spin conserved); hence, the excited-state transitions will be either singlet-singlet transitions or triplet-triplet transitions. The nature of these excited-state transitions is difficult to predict or to experimentally determine. The molecular orbital diagram suggests three major possibilities. First, the transition could involve promotion of another electron out of the nonbonding metal orbitals to the strongly antibonding metal orbitals. Although this possibility is difficult to exclude, one would expect significant cluster fragmentation from this process, which was not observed. A second possibility for the transition is an excitation from a low-lying fully occupied cyclopentadienyl  $\pi$ -bonding orbital into the now partially occupied metal nonbonding orbital. This transition involves movement of charge from the cyclopentadienyl ligand to an iron atom. This type of transition, referred to as a ligand to metal charge transfer, possesses a large absorption cross-section due to the induced dipole occurring from the charge separation. The final possibility is that the transition is from the newly occupied metal antibonding orbital to a low-lying carbonyl  $\pi$ -orbital. This involves movement of charge from the metal core to a carbonyl, resulting in a metal to ligand charge-transfer transition. This transition would also possess a strong absorption cross-section.

It is likely that either charge-transfer transition, discussed above, will have a larger absorption cross-section than the d-d ground-state transition. Thus, the presence of such transitions is consistent with an excited state that is more strongly absorbing than the ground state and the observation of RSA. It is not necessary, however, to determine the exact assignment of the excited-state transition for the purpose of modeling our results. It is sufficient only to include these levels in the model. We will attempt to experimentally determine the excited-state transition in future work.

The above discussion leads to a simplified five-level model (shown in Figure 6) consisting of three singlet and two triplet states. In this model, level 0 corresponds to the HOMO, while level 1 corresponds to the LUMO, and the ground-state absorption

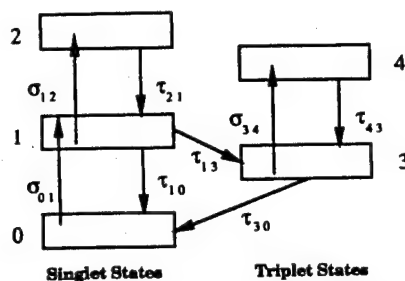


Figure 6. Proposed five-level model for reverse saturable absorption in King's complex. The symbols are defined in the text of section IV.

is associated with 0-to-1 transitions. Intersystem crossing is associated with the 1-to-3 transition, and excited-state absorption may occur in either the singlet system (1-to-2 transition) or the triplet system (3-to-4 transition).

By inspection of Figure 6, we obtain the coupled differential equations describing the photodynamics of this system:

$$dN_1/dt = \sigma_{01}IN_0 + N_2/\tau_{21} - N_1\left(\frac{1}{\tau_{10}} + \frac{1}{\tau_{13}}\right) - \sigma_{12}IN_1 \quad (1)$$

$$dN_2/dt = \sigma_{12}IN_1 - N_2/\tau_{21} \quad (2)$$

$$dN_3/dt = -\sigma_{34}IN_3 - N_3/\tau_{30} + N_4/\tau_{43} + N_1/\tau_{13} \quad (3)$$

and

$$dN_4/dt = \sigma_{34}IN_3 - N_4/\tau_{43} \quad (4)$$

Here,  $I$  is the incident photon flux ( $\text{cm}^{-2} \text{s}^{-1}$ ),  $N_i$  is the density of molecules in level  $i$ , and  $\sigma$  and  $\tau$  are the respective cross-sections and decay times. The branching ratio  $\text{Br} = \tau_{13}/\tau_{10}$  is the ratio of molecules that relax to the ground state versus intersystem crossing to the triplet state. In addition conservation of molecules gives

$$N = N_0 + N_1 + N_2 + N_3 + N_4 \quad (5)$$

The propagation of the pulse is determined from the wave equation, which assuming a slowly varying envelope approximation can be written as

$$dI/dz = -\sigma_{01}IN_0 - \sigma_{12}IN_1 - \sigma_{34}IN_3 \quad (6)$$

From the above equations we generate numerical fits to the experimental data and consequently extract the relevant cross-sections and decay times. The procedure we follow is to first fit the low fluence data where the population in level 2 may be neglected. We can also neglect  $N_3$  and  $N_4$  as the experimentally measured induced absorption recovers on time scales too short for triplet-state transitions. For these conditions, the system is completely specified by the ground-state cross-section,  $\sigma_{01}$ , the singlet excited-state cross-section,  $\sigma_{12}$ , and the lifetime of the first excited singlet state,  $\tau_{10}$ . Moreover,  $\sigma_{12}$  and  $\tau_{10}$  are largely decoupled parameters for pulse durations shorter than  $\tau_{10}$ ; the peak  $\Delta T/T$  near zero delay is primarily sensitive to  $\sigma_{12}$ , while the decay of  $\Delta T/T$  determines  $\tau_{10}$ . The linear absorption measurements provide  $\sigma_{01}$ , and fitting to the data allows us to uniquely extract  $\tau_{10}$  and  $\sigma_{12}$ . The theoretical curves superposed on the data in Figure 4 were obtained using a single set of parameters,  $\sigma_{12} = 8.0 \times 10^{-18} \text{ cm}^2$  and  $\tau_{10} = 120 \text{ ps}$  and are in good agreement with the data over the fluence range 11–64  $\text{mJ}/\text{cm}^2$ . At the higher fluences, the induced absorption becomes more sensitive to the upper excited singlet decay time,  $\tau_{21}$ , due to the greater number of excited-state transitions. The numerical fits to the data indicate that the upper excited-state recombination time is considerably shorter than the pulse duration, and we estimate  $\tau_{21} \leq 1 \text{ ps}$ . The excellent agreement between the numerical simulations and the data reported here indicates that RSA of picosecond pulses in cyclopentadienyliron carbonyl tetramer is predominantly due to optical transitions within the singlet system.

To determine whether the pump-probe results were sensitive in any way to induced anisotropy and reorientational diffusion

TABLE I: Measured Parameters for King's Complex

capture cross-section	recombination time
$\sigma_{01} = 4.1 \times 10^{-18} \text{ cm}^2$	$\tau_{10} = 120 \text{ ps}$
$\sigma_{12} = 8 \times 10^{-18} \text{ cm}^2$	$\tau_{21} < 1 \text{ ps}$
branching ratio $\tau_{13}/\tau_{10} > 23$	

in the molecular system, we repeated our measurements with the probe polarized at the "magic angle"<sup>13</sup> of  $54.7^\circ$  to the pump, at which the probe transmission should be insensitive to reorientational dynamics. We found that both the peak value and the measured decay of  $\Delta T/T$  in this configuration were indistinguishable from that measured with the probe and pump orthogonally polarized. This is consistent with the anticipated highly symmetrical nature of the excited molecules.

Previous nanosecond measurements<sup>8</sup> of the excited-state absorption of the King's complex suggest that for nanosecond optical excitations a long-lived ( $\tau_{30} \approx 60 \text{ ns}$ ) induced absorption is present. This residual absorption was tentatively attributed to a buildup of population in the triplet state. The overall contribution of the triplet state to the absorption of the pump and probe in the picosecond experiments reported here is difficult to quantify, but it has to be extremely weak. Clearly, if triplet absorption is present, its maximum value is less than our minimum detectable  $\Delta T/T$ . This allows us to place an upper limit for the product of the triplet absorption cross-section with the intersystem crossing rate. For times  $t$  in the domain  $\tau_{30} > t > t_{10} > \tau_{\text{pulse}}$ , we can rewrite the branching ratio as

$$\sigma_{34}/\tau_{13} \leq \Delta\alpha/\tau_{10}N_1(\text{max}) \quad (7)$$

where  $\Delta\alpha = N_3\sigma_{34}$  is the estimated induced absorption coefficient at time  $t$  and  $N_1(\text{max})$  is the excited singlet population immediately after illumination. We estimate the excited singlet population  $N_1(\text{max}) \approx 1.5 \times 10^{17} \text{ cm}^{-3}$  for a fluence of 64  $\text{mJ}/\text{cm}^2$  from the maximum measured induced absorption near zero delay. At delays  $\sim 600 \text{ ps}$ , the measured  $\Delta T/T (\approx \Delta\alpha L)$  is less than 0.01, and for our  $L = 2 \text{ mm}$  cell, the induced absorption,  $\Delta\alpha$ , is less than 0.05  $\text{cm}^{-1}$ . For these values, eq 7 gives  $\sigma_{34}/\tau_{13} < 2.8 \times 10^{-9} \text{ cm}^2/\text{s}$ . If we assume that the cross-section for triplet and singlet excited-state absorption are approximately equal, i.e.,  $\sigma_{34} \approx \sigma_{12}$ , this gives an intersystem crossing time  $\tau_{13} > 2.8 \text{ ns}$  and a branching ratio  $> 23$ .

## V. Conclusions

We have demonstrated that the cyclopentadienyliron carbonyl tetramer in solution with methylene chloride exhibits reverse saturable absorption on picosecond time scales. The dynamics of the optically-excited molecules have been measured using picosecond time-resolved absorption at 532 nm and are consistent with a five-level model with the parameters indicated in Table I. We emphasize that the measured singlet excited-state absorption cross-section is only a factor of 2 larger than that of the ground state. This value is too small to explain the nonlinear transmission behavior previously reported<sup>8</sup> for nanosecond excitation of nominally identical solutions. Furthermore, our estimate of the product of the intersystem crossing rate and the triplet absorption cross-section indicates that it is unlikely that triplet absorption could fully account for the nanosecond-excitation response. The implication of these results is that the nanosecond measurements are influenced by additional nonlinear mechanisms not accounted for in the present model.

A number of areas of investigation are necessary for a complete description of the picosecond photodynamics of reverse saturable absorption of this tetramer. The assignment of the specific transition associated with the singlet excited-state absorption remains to be determined. To this end, we are currently synthesizing various King's complex derivatives. These derivatives have different ligands substituted and will allow us to determine whether the excited-state absorption involves charge transfer from the iron to the carbonyl ligands or from the cyclopentadienyl ligands to the iron atoms. Furthermore, we have not yet unambiguously measured the intersystem crossing rate and the triplet

absorption cross-section. We anticipate that the triplet population can be enhanced by optical excitation of an equivalent fluence but longer duration compared to the measurements reported here. Under such conditions there is more opportunity for the molecules to undergo intersystem crossing, since molecules that relax back to the ground state can be reexcited during the excitation pulse. This results in an increased population in the triplet. With the singlet parameters known from the present picosecond measurements, time-resolved studies of the triplet absorption for different optical excitation pulse widths should allow direct measurements of the triplet system parameters  $\sigma_{34}$ ,  $N_3$ , and  $\tau_{13}$ . Such measurements should help to clarify the current discrepancy between the nanosecond and picosecond responses of the King's complex.

**Acknowledgment.** The work performed at Hughes Research Laboratories was supported by the Naval Air Development Center under Contract 62269-90-C-0239. The research at The University of Iowa was supported by the Defense Advanced Research Projects Agency and the Center for Night Vision and Electro-Optics.

Registry No.  $[(C_5H_5)Fe(CO)]_4$ , 12203-87-1.

## References and Notes

- (1) Giuliano, C. R.; Hess, L. D. *IEEE J. Quantum Electron.* **1967**, *3* (8, Aug), 358-367.
- (2) Harter, D. J.; Shand, M. L.; Band, Y. B. *J. Appl. Phys.* **1984**, *56* (3, Aug 1).
- (3) Hoffman, R. C.; Stetyick, K. A.; Potember, R. S.; McLean, D. G. *J. Opt. Soc. Am. B* **1989**, *6* (4, Apr).
- (4) Guha, S.; Frazier, C. C.; Chen, W. P.; Porter, P.; Kang, K.; Finberg, S. E. *Proc. SPIE-Int. Soc. Opt. Eng.* **1989**, *1105*, 14-19.
- (5) Coulter, D. R.; Miskowski, V. M.; Perry, J. W.; Wei, T.-H.; Van Stryland, E. W.; Hagan, D. J. *Proc. SPIE-Int. Soc. Opt. Eng.* **1989**, *1105*, 42-51.
- (6) Harter, D. J.; Band, Y. B.; Ippen, E. P. *IEEE J. Quantum Electron.* **1985**, *21* (8, Aug).
- (7) King, R. B. *Inorg. Chem.* **1966**, *5* (12, Dec), 2227-2230.
- (8) Tutt, L.; McCahon, S. W.; Klein, M. B. *Proceedings of NLO90*, Hawaii, 1990.
- (9) White, A. J.; Cunningham, A. J. *J. Chem. Educ.* **1980**, *57* (4).
- (10) Bock, C. R.; Wrighton, M. S. *Inorg. Chem.* **1977**, *16*, 1309.
- (11) Neuman, M. A.; Trinh-Toan; Dahl, L. F. *J. Am. Chem. Soc.* **1972**, *94* (10, May 17), 3383-3388.
- (12) Trinh-Toan; Fehlhammer, W. P.; Dahl, L. F. *J. Am. Chem. Soc.* **1972**, *94* (10, May), 3389-3396.
- (13) von Jena, A.; Lessing, H. E. *Berichte der Bunsen-Gesellschaft fuer Physikalische Chemie*; Verlag Chemie: D-6940 Weinheim, 1979; Vol. 83, pp 181-191.

**Appendix N**

**Picosecond Investigations of Optical Limiting Mechanisms in King's  
Complex**

Optical Engineering, Vol. 32, pp. 1063-1067 (1993)



# Picosecond investigations of optical limiting mechanisms in King's complex

Thomas F. Boggess  
Graham R. Allan  
Steven J. Rychnovsky  
D. R. Laberge  
Clark H. Venzke, MEMBER SPIE  
Arthur L. Smirl, MEMBER SPIE  
University of Iowa  
Center for Laser Science and Engineering  
124 AMRF Oakdale Campus  
Iowa City, Iowa 52242

Lee W. Tutt\*  
Alan R. Kost, MEMBER SPIE  
Stephen W. McCahon  
Marvin B. Klein  
Hughes Research Laboratories  
3011 Malibu Canyon Road  
Malibu, California 90265

**Abstract.** We have investigated the nonlinear optical mechanisms responsible for optical limiting of both picosecond and nanosecond 532-nm optical pulses in the organometallic compound cyclopentadienyliron carbonyl tetramer (King's complex). For fluences below  $\sim 200 \text{ mJ/cm}^2$ , picosecond pump-probe measurements in solutions of the King's complex reveal a prompt reverse saturable absorption (RSA) that recovers with a time constant of 120 ps. We attribute this RSA to excited-state absorption within the singlet system of the King's complex, and we demonstrate that the RSA is completely characterized by a simple three-level model. We find, however, that the material parameters extracted from these picosecond measurements cannot account for the strong optical limiting previously observed in identical solutions of this compound using nanosecond excitation at higher fluences. Picosecond measurements at fluences greater than  $200 \text{ mJ/cm}^2$  reveal the onset of an additional loss mechanism that appears  $\sim 1 \text{ ns}$  after excitation. The magnitude of this loss depends on both the laser repetition rate and the solvent, indicating that the loss is not directly related to the intrinsic properties of the King's complex but is most likely thermal in origin. Using nanosecond excitation pulses, we have performed angularly resolved transmission and reflection measurements, which reveal strong forward- and backward-induced scattering at these fluences. Furthermore, when the King's complex is incorporated in a solid host, we observe negligible induced scatter and the response is completely described by the singlet parameters extracted from the picosecond measurements. These observations indicate that the nanosecond optical limiter response of solutions of King's complex is dominated by thermally induced scattering.

**Subject terms:** organometallics; cyclopentadienyliron carbonyl tetramer; King's complex; optical limiting; reverse saturable absorption; thermally induced scattering; picoseconds.

*Optical Engineering* 32(5), 1063–1067 (May 1993).

## 1 Introduction

Rapid advances in the development of tunable solid state and high-power frequency-agile lasers have led to a pressing demand for broadband nonlinear optical devices designed to protect sensitive optical sensors, including the human eye, from intense optical radiation. These "optical limiters,"<sup>1</sup> which can rely on gas, liquid, and/or solid state nonlinear optical materials, must be highly transparent under ambient conditions but must become essentially opaque when exposed to high levels of optical radiation. Since potential threat lasers may have pulse durations of nanoseconds or even picoseconds, these devices must switch from the trans-

parent to the opaque state on an equivalent time scale. On the other hand, the very fact that the pulse duration of the threat may be unknown requires the optical limiter response to be relatively insensitive to pulse width. Furthermore, practical considerations of the sensor performance, e.g., field of view, dynamic range, etc., typically place further restrictions on the physical characteristics of the limiter.

The stringent requirements on sensitivity, response time, bandwidth, insertion loss, etc., have to date precluded the development and demonstration of a practical optical limiter that will protect a given sensor from all potential threats. The problem is ultimately traced to limitations on the nonlinear optical properties of available materials. Nevertheless, many material systems show promise for at least partially satisfying the requirements for a practical optical limiter, and continued research into the material properties, and perhaps materials engineering, may lead to the successful development of a practical device.

One particularly promising group of materials that has recently been studied<sup>2–7</sup> for optical limiting applications is

\*Present address: Eastman Kodak, Rochester, New York 14650.

Paper 10102 received Oct. 5, 1992; accepted for publication Nov. 5, 1992. This paper is a revision of a paper presented at the SPIE conference on Nonlinear and Electro-Optic Materials for Optical Switching, April 1992, Orlando, Florida. The paper presented there appears (unrefereed) in SPIE Proceedings Vol. 1692.  
© 1993 Society of Photo-Optical Instrumentation Engineers. 0091-3286/93/\$2.00.

the organometallics. Many of these molecules exhibit broad-band and relatively low linear absorption features at visible wavelengths but display reverse saturable absorption<sup>8</sup> (RSA) under conditions of intense optical excitation. The RSA in these materials, which is a consequence of the excited-state absorption cross sections being larger than that of the ground state, can occur in the singlet or the triplet system (or both). RSA in the triplet system is particularly attractive, since the long lifetime typically associated with the triplet state ensures that the material response is relatively pulse-width insensitive over a wide range of pulse durations. In addition, many of these molecules can be chemically engineered<sup>2</sup> to tailor their optical properties to specific applications. Such molecular engineering may also produce new materials that ultimately lead to practical optical limiting devices.

In this paper, we discuss picosecond photodynamics and optical limiting in the organometallic compound cyclopentadienyliron carbonyl tetramer  $[(C_5H_5)Fe(CO)]_4$ , commonly referred to as King's complex.<sup>9</sup> This molecule displays a relatively weak (extinction coefficient less than  $5 \times 10^3 \text{ M}^{-1} \text{ cm}^{-1}$ ) linear absorption over nearly the entire visible spectrum, and it has high photo-, chemical, and thermal stability. Solutions of this compound in methylene chloride have been previously shown to exhibit optical limiting properties on nanosecond time scales.<sup>6</sup> The nonlinearity responsible for the limiting was initially tentatively attributed to RSA in the triplet state. As we have previously reported,<sup>7</sup> RSA also occurs in this molecule on picosecond time scales, indicating that singlet-singlet transitions must also be considered. To quantify the photodynamics that determine the RSA, we have performed time-resolved nonlinear spectroscopy on King's complex in methylene chloride solution as well as in other solvents. Specifically, using picosecond pump-probe transmission measurements performed at 532 nm together with a simple rate-equation model, we have extracted values for the singlet lifetime and the excited singlet-state absorption cross section. Furthermore, these measurements have allowed us to determine an upper bound on the lifetime of the second excited singlet state and on the product of the intersystem crossing rate with the triplet-triplet absorption cross section. We find, however, that the parameters extracted from the picosecond measurements cannot describe the observed limiting behavior for nanosecond excitation conditions. Moreover, from picosecond pump-probe data obtained at high fluences and at nanosecond probe delays, angularly resolved transmission and reflection measurements with nanosecond excitation, and nonlinear transmission data obtained from samples of King's complex embedded in a solid host, we conclude that the discrepancy between the picosecond and nanosecond results can be attributed to optically induced scattering that is initiated on a subnanosecond time scale.

## 2 Experimental Details

The King's complex used in these experiments was prepared from cyclopentadienyliron dicarbonyl dimer, which was purchased from Strem Chemicals and used as received. The cyclopentadienyliron carbonyl tetramer, or King's complex, was synthesized from the cyclopentadienyliron dicarbonyl dimer using the method of White and Cunningham<sup>10</sup> and recrystallized twice from methylene chloride/hexane. All measurements reported here were performed on solutions

of King's complex dissolved in one of three solvents: methylene chloride, distilled tetrahydrofuran (THF), or toluene. All solvents were oxygen degassed with nitrogen by a vigorous bubbling purge for at least 2 h prior to use. This precaution avoids possible quenching of the triplet-state population by oxygen contamination. All solutions were subsequently handled anaerobically.

The photodynamics were measured using time-resolved pump-probe transmission techniques with an excitation wavelength of 532 nm and a pulse duration of 25 ps [full-width at half-maximum (FWHM) intensity]. The picosecond pulses were produced by a frequency-doubled, actively and passively mode-locked Nd:YAG laser. The laser operates in the TEM<sub>00</sub> mode and produces temporally near-Gaussian pulses. The actual pulse width was determined on a shot-by-shot basis using second harmonic techniques. A single pulse from this laser was split into two, a weak probe and an intense pump, and the two pulses were recombined at a small angle ( $\sim 1.2^\circ$ ) in the cell containing the King's complex solution. The pump and probe were orthogonally polarized, and the probe diameter was a factor of  $\sim 9$  smaller than the pump to ensure that the probe interrogated a uniformly excited volume of material. The linear transmission of the King's complex solution was  $\sim 35\%$  for the 2-mm-thick optical cell used for these studies.

The nanosecond optical limiting and angularly resolved scattering data were taken using the frequency-doubled output of an injection-seeded single-longitudinal-mode Q-switched Nd:YAG laser. The pulses produced by this system were typically 8 ns (FWHM intensity) in duration. The output of a gain-saturated amplifier was imaged into the samples to provide a near-top-hat spatial profile and, hence, near-uniform excitation. The linear transmission of the King's complex solutions for these measurements ranged from  $\sim 40\%$  to  $70\%$ .

## 3 Results and Discussion

We have previously demonstrated<sup>7</sup> that solutions of King's complex in methylene chloride exhibit RSA on picosecond time scales. This is clearly illustrated in Fig. 1, where we plot the differential transmission  $\Delta T/T$  of a picosecond probe for pump fluences ranging from 13 to 95 mJ/cm<sup>2</sup> in a  $7 \times 10^{-4}$  molar solution of King's complex in methylene chloride. The solid curves are the numerical fits to the data based on a rate-equation model (discussed in detail in Ref. 7), where the significant fitting parameters are the excited singlet-state absorption cross section  $\sigma_{12}$  and the excited singlet-state relaxation time  $\tau_{10}$ . The numerical fits agree with the experimental results over this entire range of fluences using a single set of parameters:  $\tau_{10} = 120$  ps and  $\sigma_{12} = 8 \times 10^{-18} \text{ cm}^2$ . The latter should be compared to the ground-state absorption cross section  $\sigma_{01}$  of  $4.1 \times 10^{-18} \text{ cm}^2$ . The fluence dependence of the data allows us to place an upper bound on the second excited singlet-state lifetime of  $\tau_{21} \leq 1$  ps. The observed picosecond response of King's complex dissolved in THF and toluene was similar at these fluences, and the excited-state cross sections and recovery times that were extracted by the numerical fits were essentially unchanged from those extracted from the methylene chloride solutions.

Previous measurements<sup>6</sup> of the excited-state absorption of King's complex suggest that, for nanosecond optical excitation, a long-lived induced absorption is present. This

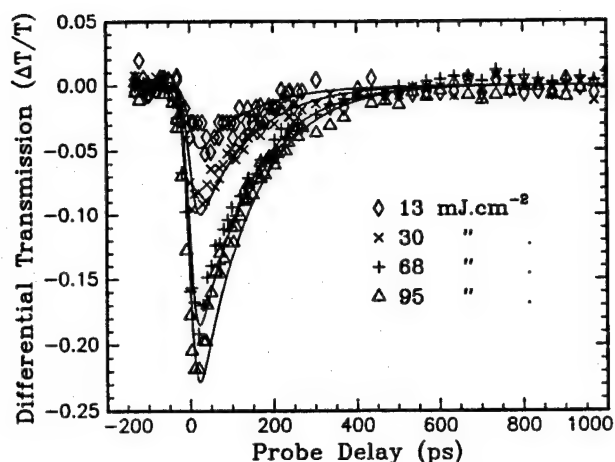


**Fig. 1** Time-resolved differential transmission for King's complex in methylene chloride using 25-ps pulses at 532 nm. The linear transmission is  $\sim 35\%$ . The solid lines are the numerical fits for a single set of parameters at the indicated fluence.

was tentatively attributed to excited-state absorption associated with a buildup of population in the triplet state. The overall contribution of the triplet state to the absorption of the pump and probe in the picosecond experiments reported here is difficult to quantify, but it is evidently extremely weak. Clearly, if a long-lived triplet absorption is present, its maximum value is less than our minimum-detectable  $\Delta T/T$ . This consideration allows us to place an upper bound of  $3 \times 10^{-9} \text{ cm}^2/\text{s}$  on the product of the intersystem crossing rate ( $1/\tau_{13}$ ) and the triplet absorption cross section ( $\sigma_{34}$ ). If we assume  $\sigma_{34} \approx \sigma_{12}$ , i.e., if the triplet and singlet excited-state absorption cross sections are comparable, this upper bound indicates that for both the picosecond and nanosecond experiments the majority of photoexcited molecules relax directly back to the ground state from the first excited singlet state, and no significant population accumulates in the triplet state. This seems to indicate that the long-lived reduction in transmission observed for nanosecond excitation may not be associated with triplet excited-state absorption.

Using the singlet and triplet parameters obtained from the picosecond pump-probe measurements, we have attempted to model the optical limiting response obtained using nanosecond excitation. This is illustrated in Fig. 2, where we plot the nanosecond limiting data for King's complex dissolved in methylene chloride along with the results of a numerical calculation based on the measured parameters and a five-level (three singlet and two triplet levels) rate-equation model. Clearly, the optical limiting obtained with nanosecond excitation is far too strong to be described by the excited-state parameters extracted from the picosecond absorption measurements. The weak optical limiting predicted by the model is not surprising given the 120-ps singlet-state decay time and the fact that the excited-state absorption cross section is only a factor of 2 larger than that of the ground state.

To resolve the discrepancy between the nanosecond experimental data and the numerical results, we have performed a series of picosecond time-resolved pump-probe experiments at higher fluences and for longer probe delays. Figure 3 is a plot of the differential transmission of the probe

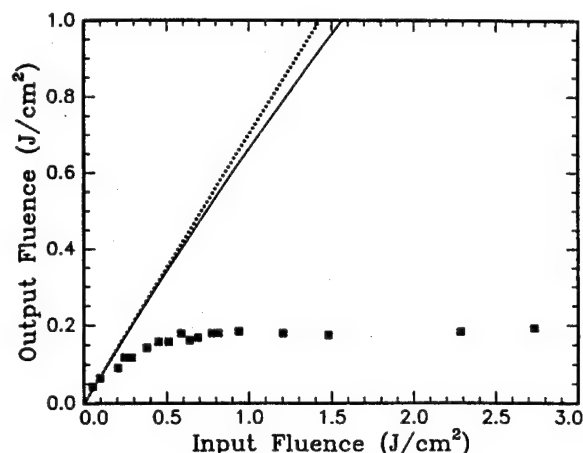


**Fig. 2** The observed limiting of 8-ns pulses at 532 nm in a solution of King's complex and methylene chloride is plotted (squares). The linear transmission (dotted line) and the predicted response (solid curve) of King's complex using the parameters obtained from the picosecond measurements is also shown.

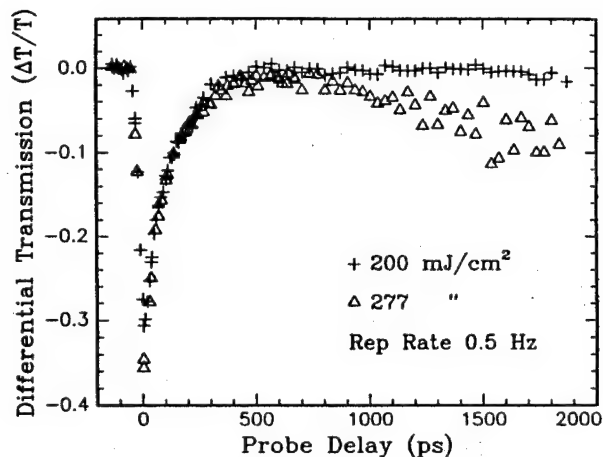


**Fig. 3** Differential probe transmission as a function of probe delay for a 0.5-Hz repetition rate and pump fluences of 200 and 277  $\text{mJ}/\text{cm}^2$  in a solution of King's complex and THF.

through a solution of King's complex in THF at 200 and 277  $\text{mJ}/\text{cm}^2$  with up to 2-ns delay between the pump and probe. At 200  $\text{mJ}/\text{cm}^2$ , we observe prompt RSA that recovers completely within a few hundred picoseconds. This is completely consistent with results shown in Fig. 1 for lower fluences. At a fluence of 277  $\text{mJ}/\text{cm}^2$ , however, after the predictable initial response of the system, a renewed reduction in the differential transmission appears. This feature continues to increase in magnitude up to our maximum delay of  $\sim 2$  ns. We further note that at the higher fluence, bubbles were observed rising from the interaction volume, indicating that sufficient energy was deposited in the solvent to induce boiling. The data in Fig. 3 were taken at a repetition rate of 0.5 Hz. We repeated the higher fluence data at a repetition rate of 1 Hz, and in Fig. 4 we compare these results with the 0.5-Hz data. While the RSA feature near-zero delay is independent of repetition rate, the signal at nanosecond delays is clearly much more pronounced at the

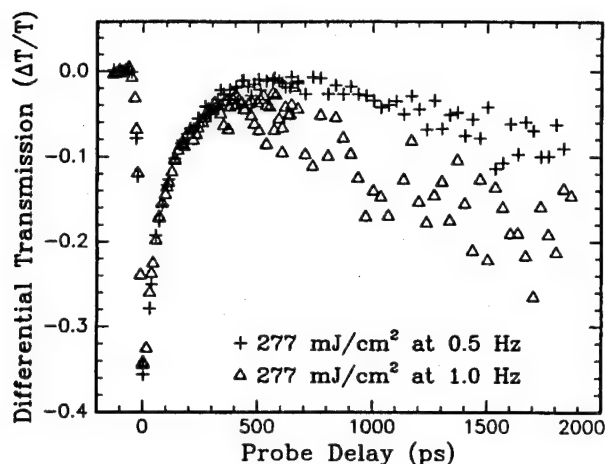


Fig. 4 Differential probe transmission as a function of probe delay for a pump fluence of 277 mJ/cm<sup>2</sup> and repetition rates of 0.5 and 1 Hz in a solution of King's complex and THF.

higher repetition rate. This behavior indicates that the reduced transmission at nanosecond delays is not intrinsic to the King's complex but is most likely thermally induced. The higher repetition rate results in a higher average temperature in the interaction volume, thereby assisting the development of a thermal nonlinearity. We note that the reduced transmission at nanosecond delays in the picosecond experiments also appears to be solvent dependent. Preliminary experimental evidence indicates that the threshold fluence for the observation of the induced scattering scales with the relative boiling points of the three solvents used (methylene chloride, THF, and toluene). For solutions of similar concentration, the lower the boiling point, the lower the threshold fluence for induced scattering. This, while not conclusive, is further evidence that the induced scattering is thermal in origin.

Although the precise nature of the signal observed at nanosecond delays in the pump-probe transmission measurements is unclear, we have gained some insight into the origin of this response by performing angularly resolved measurements of the transmission and reflection using nanosecond excitation. These measurements demonstrate that, for fluences at which strong optical limiting is observed, significant energy is scattered from the beam in both the forward and backward directions. This is illustrated in Fig. 5, where the back-scattered signal (measured at an angle of 30 deg with respect to the input axis) divided by the input fluence is plotted as a function of input fluence. These data were taken at a laser repetition rate of 10 Hz using a 70% transmitting solution of King's complex in methylene chloride. A deviation from linearity is clearly observed for input fluences as low as 40 mJ/cm<sup>2</sup> (note that a linear response corresponds to a constant ratio, i.e., a horizontal line, on this plot). From these observations and those discussed previously, we conclude that thermally induced scattering is strongly influencing the optical limiting of nanosecond pulses in solutions of King's complex. We emphasize, however, that in the picosecond measurements performed at 0.5 Hz, the optically induced scatter occurs only for fluences in excess of 200 mJ/cm<sup>2</sup> and requires hundreds of picoseconds to develop (see Fig. 3). Hence, this process does not influ-

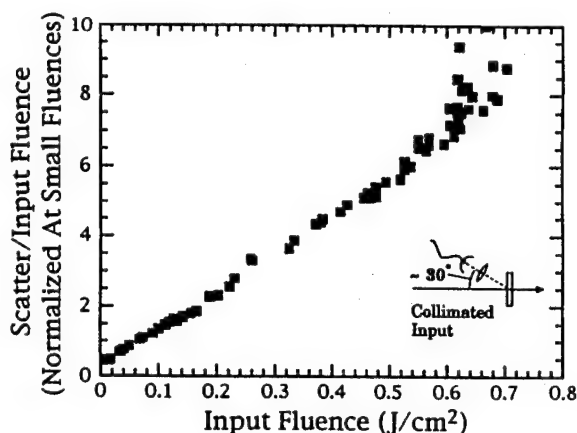


Fig. 5 Ratio of back-scattered signal to input fluence plotted as a function of input fluence for a solution of King's complex and methylene chloride. The scattered signal was measured at an angle of 30 deg with respect to the input axis, and the ratio has been normalized to unity at the lowest input fluence. The data were taken at 10 Hz using 8-ns excitation.

ence the system parameters extracted from the picosecond pump-probe data obtained at lower fluences and repetition rates. The lower 40 mJ/cm<sup>2</sup> threshold for the nanosecond scattering data in Fig. 5 is consistent with the higher repetition rate used for these measurements and the thermal origin of the nonlinearity.

To eliminate the possibility of thermally induced scattering within the solvent, we have embedded the King's complex into a solid host, specifically polymethylmethacrylate (PMMA), and have examined the optical nonlinearities of this solid sample using the nanosecond output of the Q-switched laser. We note that for these measurements, the laser was not injection seeded, and hence did not operate on a single longitudinal mode. We do not believe that this significantly influences our results or conclusions. In Fig. 6 we plot the measured optical response (squares) of King's complex in PMMA to 8-ns 532-nm excitation. Clearly, the optical limiting observed for this solid sample is much weaker than that observed in solutions (compare to Fig. 2). We also show in Fig. 6 (dashed curve) the results of a numerical calculation based on a five-level model and the system parameters determined from the picosecond experiments on King's complex in methylene chloride solutions. We attribute the small discrepancy between the data and the theory to the upper bound used in the model for the product of the intersystem crossing rate and the triplet cross section. It is evident, and not surprising, that the upper limit on this product, which was extracted from the picosecond pump-probe measurements and was used for the curve shown in Fig. 6, is too large to describe the data. What is surprising, however, is that we can fit these data well by neglecting triplet absorption all together. This is illustrated by the solid curve in Fig. 6, which is the result of considering only singlet-state absorption using the singlet parameters extracted from the picosecond studies. The agreement between the data and theory suggests that triplet absorption plays little, if any, role in the nonlinear optical response of King's complex at 532 nm. Furthermore, the fact that the observed weak limiting in the King's complex/PMMA can be completely described by intrinsic properties of the King's com-

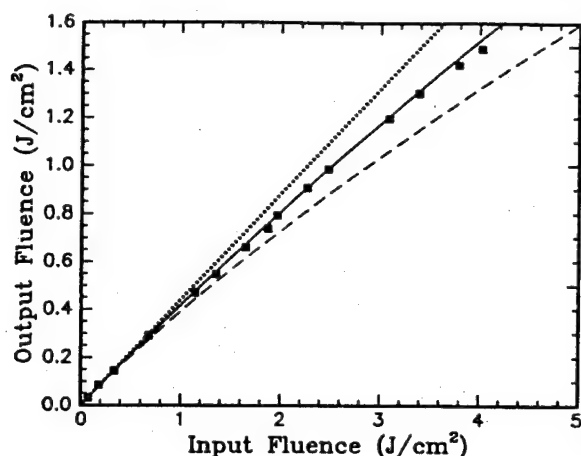


Fig. 6 The limiting response of King's complex in PMMA for 8-ns pulses at 532 nm. The squares represent the data, the dashed and solid curves represent numerical results based on a five-level and a three-level model, respectively, and the dotted line indicates a linear response.

plex is further evidence that the stronger limiting observed for nanosecond excitation in solutions of this molecule appears to be a consequence of the fast thermally induced scattering process discussed previously.

#### 4 Conclusions

We have measured and numerically modeled the picosecond photodynamics of RSA in King's complex, and we find that these photodynamics are described well by a three-level rate-equation model that incorporates only absorption and relaxation within the singlet system. By including the triplet system in our model (five-level model) we have placed an upper limit on the product of the intersystem crossing rate and the triplet absorption cross section. We have accurately modeled the optical limiting of nanosecond pulses on transmission through King's complex in PMMA using only the singlet-system parameters. On the other hand, the nanosecond limiting data obtained for methylene chloride solutions of King's complex could not be fit even with the five-level model, indicating that an additional mechanism is contributing to the optical limiting for these experimental conditions. This mechanism was initially identified from picosecond pump-probe experiments at high fluences and nanosecond delays. In addition to the expected RSA associated with the singlet excited-state absorption, these measurements demonstrated a fluence and repetition-rate dependent loss process that appeared hundreds of picoseconds after excitation. Subsequent angularly resolved transmission and reflection measurements indicated that this signal arose from optically induced scattering, and the repetition-rate dependence of this scattering indicated that it is most likely thermal in origin. This scatter appears to be connected with

the recovery of the singlet RSA. As the molecules relax back to the ground state, the optically absorbed energy is evidently very efficiently transferred to the solvent. We note that, in preliminary attempts, we have detected no visible fluorescence from these optically excited molecules. This suggests that relaxation back to the ground state, which again occurs with a time constant of 120 ps, involves significant nonradiative pathways. This rapid transfer of energy to the solvent apparently results in a very effective thermal nonlinearity that can be applied to optical limiting of nanosecond pulses.

#### Acknowledgments

The research at the University of Iowa was supported in part by the Defense Advance Research Projects Agency and the U.S. Army Night Vision and Electro-Optics Directorate. The work performed at Hughes Research Laboratories was sponsored by the Naval Air Warfare Center. We gratefully acknowledge Kirk Dougherty and Bill Elias at Hughes Electro-Optic Systems for preparation of the King's complex in PMMA.

#### References

1. See, e.g., R. C. C. Leite, S. P. S. Porto, and T. C. Damen, "The thermal lens effect as a power-limiting device," *Appl. Phys. Lett.* **10**, 100-101 (1967); M. J. Soileau, W. E. Williams, and E. W. Van Stryland, "Optical power limiter with picosecond response time," *IEEE J. Quantum Electron.* **QE-19**, 731-735 (1983).
2. D. R. Coulter, V. M. Miskowski, J. W. Perry, T. H. Wei, E. W. Van Stryland, and D. J. Hagan, "Optical limiting in solutions of metallo-phthalocyanines and naphthalocyanines," *Proc. SPIE* **1105**, 42-51 (1989).
3. L. W. Tutt and S. W. McCahon, "Reverse saturable absorption in metal cluster compounds," *Opt. Lett.* **15**, 700-702 (1990).
4. J. W. Perry, L. R. Khundkar, D. R. Coulter, D. Alvarez, Jr., S. R. Marder, T. H. Wei, M. J. Sence, E. W. Van Stryland, and D. J. Hagan, "Excited state absorption and optical limiting in solutions of metallophthalocyanines," in *Organic Molecules for Nonlinear Optics and Photonics*, J. Messier, F. Kajzar, and P. Prasad, Eds., pp. 369-382, Kluwer Academic Publishers, Netherlands (1991).
5. T. H. Wei, D. J. Hagan, M. J. Sence, E. W. Van Stryland, J. W. Perry, and D. R. Coulter, "Direct measurements of nonlinear absorption and refraction in solutions of phthalocyanines," *J. Appl. Phys.* **B54**, 46-51 (1992).
6. L. Tutt, S. W. McCahon, and M. B. Klein, "Nonlinear optical properties of organometallic compounds in solids and solutions," *Proc. of NLO90*, sponsored by IEEE Laser and Electro-Optics Society in cooperation with the Optical Society of America, pp. 57-58 (1990).
7. G. R. Allan, D. R. Labergerie, S. J. Rychnovsky, T. F. Boggess, A. L. Smirl, and L. W. Tutt, "Picosecond reverse saturable absorption in King's complex  $[(C_5H_5)_2Fe(CO)]_4$ ," *J. Phys. Chem.* **96**, 6313-6317 (1992).
8. C. R. Giuliano and L. D. Hess, "Nonlinear absorption of light: optical saturation of electronic transitions in organic molecules with high intensity laser radiation," *IEEE J. Quantum Electron.* **QE-3**, 358-367 (1967).
9. R. B. King, "Organometallic chemistry of the transition metals. XVI. Polynuclear cyclopentadienyl carbonyls of iron and cobalt," *Inorg. Chem.* **5**, 2227-2230 (1966).
10. A. J. White and A. J. Cunningham, "Synthesis and electrochemistry of cyclopentadienylcarbonyliron tetramer," *J. Chem. Ed.* **57**, 317-319 (1980).

Biographies and photographs of authors not available.

## **Appendix O**

### **Picosecond Investigations of the Excited-State Transition at 532 nm in King's Complex $[(C_5H_5)Fe(CO)]_4$ and Synthesized Analogs**

**Journal of Physical Chemistry, Vol. 98, pp. 216-221 (1994)**



## Picosecond Investigations of the Excited-State Transition at 532 nm in King's Complex $[(C_5H_5)Fe(CO)]_4$ and Synthesized Analogs

G. R. Allan, S. J. Rychnovsky, C. H. Venzke, and Thomas F. Boggess\*

Center for Laser Science and Engineering and Department of Physics and Astronomy, 100 IATL,  
The University of Iowa, Iowa City, Iowa 52242

Lee Tutt†

Hughes Research Laboratories, 3011 Malibu Canyon Road, Malibu, California 90265

Received: September 20, 1993\*

Variations of the organometallic cluster known as King's complex,  $[(C_5H_5)Fe(CO)]_4$ , have been synthesized to study the excited-state transition responsible for reverse saturable absorption observed at 532 nm in this molecule. Picosecond pump-probe measurements have been used to measure the excited-state cross sections and lifetimes in King's complex and the analogs methyl-King's complex,  $[CH_3(C_5H_4)Fe(CO)]_4$ , and triethylaluminum King's complex,  $[(C_5H_5)Fe(COAl(C_2H_5)_3)]_4$ . Within experimental error, the excited-state parameters are unaffected by alterations to either the carbonyl or the cyclopentadienyl ligand of the King's complex. These results are consistent with an excited-state absorption resulting from a second d to d transition within the singlet states of the metal core.

### I. Introduction

Ultrafast optical techniques have recently been used<sup>1,2</sup> to measure the fundamental nonlinear optical properties of organometallic compounds that exhibit reverse saturable absorption (RSA).<sup>3</sup> Reverse saturable absorption is a nonlinear optical process that results in an increase in optical absorption upon intense illumination, and it is indicative of a system in which the excited-state absorption cross section exceeds that of the ground state. Potential uses for reverse saturable absorbers have been suggested in several areas, including modelocking lasers,<sup>4</sup> pulse compression,<sup>5</sup> and optical limiting.<sup>6</sup> The strength of the RSA depends not only on the ratio of the absorption cross sections but also on the lifetime of the excited state. Characterization of RSA, therefore, requires time-resolved measurements of the excited-state dynamics.

In a previous paper,<sup>2</sup> we reported RSA at 532 nm in King's complex (cyclopentadienyliron carbonyl tetramer,  $[(C_5H_5)Fe(CO)]_4$ ),<sup>7</sup> on picosecond time scales, measured the salient nonlinear parameters, and also specified three possible transitions which could be responsible for the excited-state absorption. If one can identify the excited-state transition, it may be possible, on the molecular level, to engineer an enhanced nonlinear optical absorber or tailor the response of the molecule to a specific application. In this paper, we apply picosecond pump-probe techniques to measure the absorption cross sections and excited-state lifetimes in King's complex and in synthesized variations of this molecular cluster in order to investigate the origin of the excited-state transition responsible for reverse saturable absorption.

### II. Background and Theory

From a study of the energy level diagram<sup>8</sup> of King's complex, three optical transitions have been identified as the possible origin of the excited-state absorption. We will show below that ligand substitution combined with picosecond time-resolved absorption measurements allows us to individually test two of the three options. The identification of the excited-state transition from measurements in these synthesized variations critically depends on our knowledge of the excited-state cross section and lifetime

in King's complex and on our understanding of the possible optical transitions in this molecule. To this end, we will first discuss the molecular structure of King's complex, the possible optical transitions given this structure, and the numerical model used to describe RSA.

The molecular structure of cyclopentadienyliron carbonyl tetramer was first determined from X-ray crystallography by Neuman et al.<sup>9</sup> and is shown in Figure 1. It was found to consist of an inner metal tetrahedron with an iron at each apex. Each iron atom of the tetragonal core is equivalent and has an attached cyclopentadienyl,  $(C_5H_5)$ , ligand. This "Cp" ligand bonds to the iron atom via the  $5\pi$  electron orbitals of the carbon ring. Each of the four carbonyl ligands, CO, is triply bonded to three adjacent iron atoms.

The molecular orbital levels of cyclopentadienyliron carbonyl tetramer were originally determined by Trinh-Toan and co-workers<sup>8</sup> and are shown in Figure 2. The highest occupied molecular orbital (HOMO), predominately composed of essentially nonbonding iron atomic orbitals, is fully occupied, giving rise to the diamagnetic character of the compound. The lowest unoccupied molecular orbital (LUMO) is formed from six antibonding tetrairon orbitals. The lowest energy transition, the HOMO to the LUMO, is from a nonbonding predominately d-orbital of the irons to an antibonding orbital (transition A in Figure 2). This d-d transition primarily involves the metal core of the cluster and causes a general bond weakening within the tetragonal structure. The ground state is a singlet and, since optically allowed transitions conserve spin, so are the initial excited states. Intersystem crossing can result from a spin change of the excited unpaired electron to give a triplet state. The triplet state will possess a longer lifetime than the excited singlet, since relaxation back to the ground state requires another spin flip transition.

While the ground-state absorption is well understood, the nature of the excited-state transition is difficult to predict or to experimentally determine. We have previously shown<sup>2</sup> that the excited-state cross section at 532 nm in King's complex is  $\sim 8 \times 10^{-18} \text{ cm}^2$ , which is approximately twice the ground-state cross section. Generally, large absorption cross sections are due to spin-allowed transitions (spin conserved). Hence the excited-state transition is expected to be a singlet-singlet or a triplet-triplet transition. We have also shown that the excited-state

\* Present address: Eastman Kodak, Rochester, NY 14650.

• Abstract published in *Advance ACS Abstracts*, December 1, 1993.

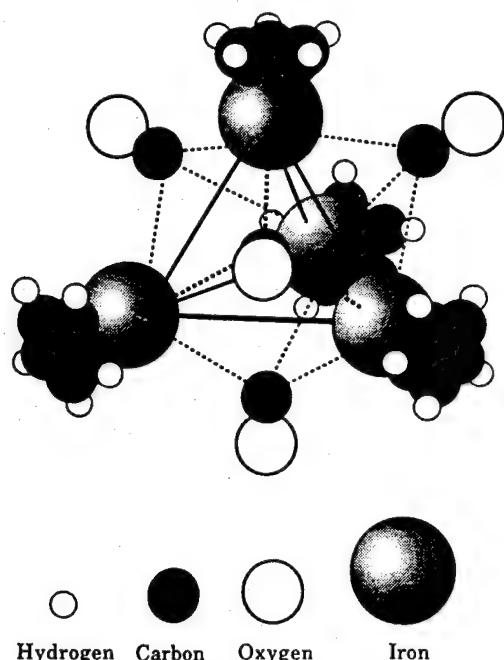


Figure 1. Schematic representation of the molecular structure of cyclopentadienyliron carbonyl tetramer, more commonly known as King's complex, after ref 9. This diagram is not to scale.

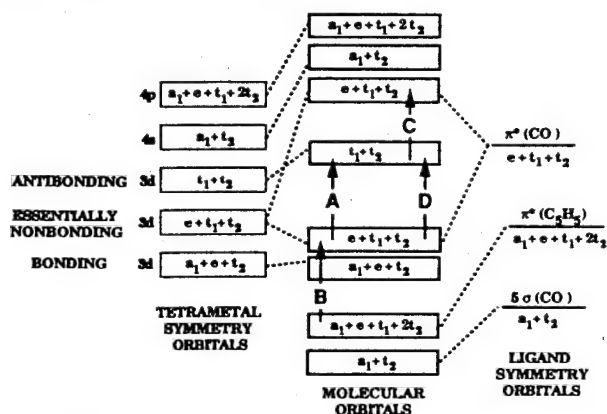


Figure 2. Molecular orbital levels of cyclopentadienyliron carbonyl tetramer showing the ground-state transition and the possible excited-state transitions (vertical arrows). Transition (A) represents ground-state absorption, the lowest energy transition within the metal core; (B) is the ( $C_5H_5$ ) ligand-to-metal excited-state transition; (C) is the metal-to-CO ligand excited-state transition; and (D) is another metal-to-metal transition.

absorption decays with a single time constant of  $\sim 120$  ps, which corresponds to the lifetime of the excited state. Lifetimes of spin-forbidden triplet-singlet transitions in organo iron complexes are typically on the order of a nanosecond. One of the shortest reported lifetimes<sup>10</sup> of 430 ps occurs in the compound  $Fe(4,7-(SO_3C_6H_5)_2 \text{ phenanthroline})_3$ . Our measured lifetime of 120 ps is significantly shorter than this. Furthermore, if one were to argue that the excited-state absorption was occurring in the triplet manifold, then the single exponential decay of this absorption would imply that either (a) intersystem crossing is occurring on a time scale that is much faster than the 25-ps excitation pulse duration and substantially faster than the singlet state lifetime in order to populate the triplet state or (b) the excited-state absorption cross sections and lifetimes of the singlet and triplet states are essentially identical. In either case, the spin-forbidden triplet transition would be characterized by a single measured lifetime of 120 ps, significantly shorter than that observed in other organo iron compounds, with no discernable deviation near  $t = 0$  (during the excitation pulse) and, as discussed below, independent of solvent. Although these scenarios are not

impossible, we believe that these considerations strongly suggest that the excited-state absorption is occurring within the singlet system.

The molecular orbital diagram suggests three possibilities for the excited-state transition. The first possibility is an excitation from a low lying fully occupied Cp  $\pi$ -bonding orbital into the now partially occupied metal nonbonding orbital (transition B in Figure 2). This transition involves movement of charge from the Cp ligand to an iron atom. This type of transition, referred to as a ligand-to-metal charge transfer, can possess a large absorption cross section due to the induced dipole occurring from the charge separation. A second possibility for the transition is from the newly occupied metal antibonding orbital to a low lying  $\pi$  carbonyl orbital (transition C). This involves movement of charge from the metal core to the CO ligand resulting in a metal-to-ligand charge-transfer transition. This transition can also possess a large absorption cross section. It is likely that either charge-transfer transition will have a larger absorption cross section than the d-d ground-state transition. Thus, the presence of such transitions is consistent with an excited state that is more strongly absorbing than the ground state. The final possibility for excited-state absorption is that the transition could involve promotion of another electron out of the nonbonding metal orbitals to the strongly antibonding metal orbitals, labeled D in Figure 2. All three of these excited-state transitions occur between distinct regions of the molecular cluster.

We have the ability to alter, on the molecular level, any particular one of these identified regions, i.e., the Cp ligand, the CO ligand, or the metal core, and we take advantage of this ability in attempting to identify the excited-state transition. The two ligands are not directly involved in the ground-state absorption process, and thus replacement of these ligands is not expected to significantly modify the ground-state absorption cross section. On the other hand, the strength of the ligand to metal bonds would be altered by such a modification, thereby changing the separation of the states in question. If either of these ligands is involved in the excited-state transition, ligand substitution would influence the excited-state cross section. Hence, by measuring the excited-state parameters for the ligand-substituted molecules and comparing them with those in King's complex, we can investigate the role of these ligands in the excited-state absorption. In principle, metal core substitution could be used to identify a metal-to-metal excited-state transition, but it is difficult to extract information from such a substitution, since the ground-state absorption is also strongly modified.

The optical parameters relevant to RSA are obtained from fitting picosecond pump-probe transmission data using a rate equation analysis of the molecular dynamics. It is not necessary to determine the exact assignment of the excited-state transition for the purpose of modeling RSA in these systems. It is sufficient to only include an excited-state transition in the model. The dismissal of the triplet states from the excited-state dynamics leads to a simplified model that includes three broadened energy levels as shown in Figure 3. In this model, level 0 corresponds to the HOMO, while level 1 corresponds to the LUMO and the ground-state absorption is associated with singlet transitions from level 0 to 1. We assume that electrons relax from the optically-coupled vibrational states of electronic level 1 to the bottom of the level 1 manifold on a time scale that is short compared to the excitation pulse duration of  $\sim 25$  ps. Excited-state absorption corresponds to transitions from level 1 to level 2. From the model we define a parameter set which completely describes RSA within the measured range of fluences. These parameters are the ground-state absorption cross section  $\sigma_{01}$ , the excited-state absorption cross section  $\sigma_{12}$ , the first-excited-state lifetime  $\tau_{10}$ , and the second-excited-state lifetime  $\tau_{12}$ . A more complete description of this model is given in ref 2.



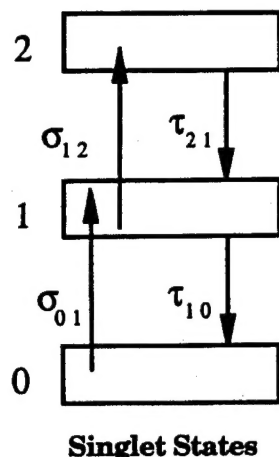


Figure 3. Three-level model used to describe reverse saturable absorption in King's complex and synthesized variations. The symbols are defined in the text of section II.

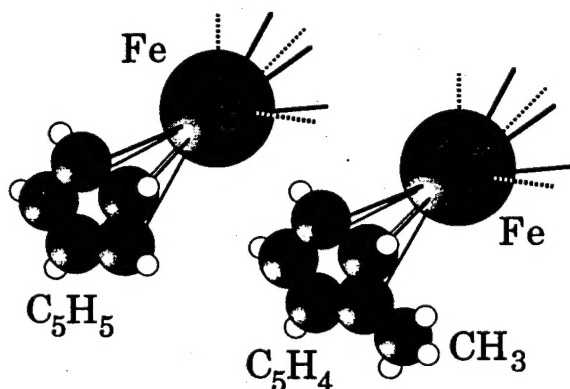


Figure 4. View of an apex of the tetragonal core of King's complex showing the cyclopentadienyl ligand and the modified molecule of methyl-King's complex, where methylcyclopentadienyl ( $\text{CH}_3\text{C}_5\text{H}_4$ ) is substituted for the cyclopentadienyl ( $\text{C}_5\text{H}_5$ ) ligand. Described in the text, this molecule is used in optical measurements to test the Cp's role in RSA.

### III. Material Synthesis and Experimental Technique

In addition to King's complex, for these experiments we have synthesized two versions of this organometallic cluster, each of which, through ligand substitution, specifically targets one of the possible excited-state transitions. To test for the ligand-to-metal charge-transfer transition, methylcyclopentadienyl ( $\text{CH}_3\text{C}_5\text{H}_4$ ) is substituted for the Cp ligand, as shown in Figure 4. To test for the metal-to-ligand charge transfer, triethylaluminum carbonyl,  $[(\text{C}_2\text{H}_5)_3\text{AlCO}]$ , is substituted for the CO ligand, as illustrated in Figure 5. The following is a brief description of the synthesis of each organometallic cluster.

King's complex,  $[\text{CpFe}(\text{CO})_4]$ , was prepared from cyclopentadienyliron dicarbonyl dimer, which was purchased from Strem Chemicals and was used as received. The cyclopentadienyliron carbonyl tetramer was synthesized from the cyclopentadienyliron dicarbonyl dimer by the method of White and Cunningham<sup>11</sup> and recrystallized twice from methylene chloride/hexane. The crystals of the tetramer when dissolved in methylene chloride produced an emerald green solution.

The methyl-King's complex,  $[\text{CH}_3\text{CpFe}(\text{CO})_4]$ , was synthesized in a manner analogous to King's complex<sup>11</sup> where, under an argon atmosphere, 7 g of triphenylphosphine and 8 g of the dimer  $[\text{CH}_3\text{CpFe}(\text{CO})_2]_2$  were added to 300 mL of degassed xylene. The reddish brown solution was heated to reflux with stirring for 7 h. The solution evolved gas during this period. Upon cooling to room temperature, 300 mL of hexane was added and the solution cooled to 0 °C for 2 days. Dark-green crystals were collected by filtration and recrystallized from methylene chloride/hexane to yield 0.58 g of methyl-King's complex. The

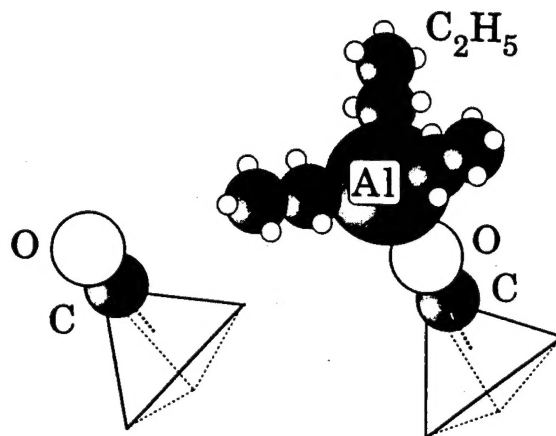


Figure 5. View of a carbonyl ligand of King's complex. The metal core is represented as the tetragon, and all other ligands are removed for clarity in this figure. The modified molecule, triethylaluminum King's complex, is shown on the right, where  $[(\text{C}_2\text{H}_5)_3\text{AlCO}]$  is substituted for the carbonyl ligand. This modified molecule is used in optical measurements to test the carbonyl's role in RSA.

compound gave an apple green color in methylene chloride, indicating a slight red shift in the ground-state absorption. The IR spectrum showed the one carbonyl stretch at  $1626\text{ cm}^{-1}$ , compared to  $1620\text{ cm}^{-1}$  for King's complex.

The triethylaluminum King's complex,  $[\text{CpFe}(\text{COAlEt}_3)_4]$ , was synthesized in a manner similar to Alich et al.<sup>12</sup> and was started from 0.54 g of  $[\text{CpFe}(\text{CO})_4]$ , which was dissolved in 145 mL of sodium-dried, degassed benzene in a glove box. A small volume of triethylaluminum,  $\text{AlEt}_3$  (1.08 mL) was added dropwise and the solution stirred for 2 h. To this solution was added 145 mL of sodium-dried, degassed heptane, and the solution was then reduced under vacuum to about 15 mL. The green precipitate, which is extremely air sensitive, was separated by vacuum filtration to yield 200 mg of triethylaluminum King's complex. For optical measurements, while still under an inert atmosphere in a glove box, the compound was dissolved in methylene chloride, placed in a glass cell with a 1-mm optical path and the cell torch sealed. For this compound, the IR spectrum showed that the carbonyl stretching resonance was red shifted by nearly  $100\text{ cm}^{-1}$  relative to that measured in King's complex.

Both the linear and nonlinear optical measurements reported here were performed on solutions of King's complex or the synthesized variations dissolved in methylene chloride. The solvent was oxygen degassed with nitrogen by a vigorous bubbling purge for at least 2 h prior to use. This precaution avoids possible quenching of any triplet-state population by oxygen contamination and also, in the case of triethylaluminum King's complex, an exothermic reaction with oxygen. All solutions were subsequently handled anaerobically.

The linear absorption spectra of  $\sim 7 \times 10^{-4}\text{ M}$  solutions of the cyclopentadienyliron carbonyl tetramer and the synthesized variations were measured separately in a 1-cm optical path quartz cell using a standard spectrophotometer. All spectra are background corrected, i.e., the absorption due to the solvent alone has been removed. The visible-near-IR spectra of the ligand-substituted compounds are similar to those of King's complex, as seen in Figure 6, indicating that the core of the molecule, which gives rise to the ground-state absorption, is largely unaltered. For wavelengths between approximately 550 and 1000 nm, the spectra of King's complex, methyl-King's complex, and triethylaluminum King's complex consist of a broad, relatively weak absorption band. Upon closer inspection, this feature is seen to be composed of two separate peaks. In King's complex and methyl-King's complex, one is centered near 650 and the second is centered near 775 nm. In triethylaluminum King's complex, the corresponding peaks are at 625 nm and 750 nm. These peaks

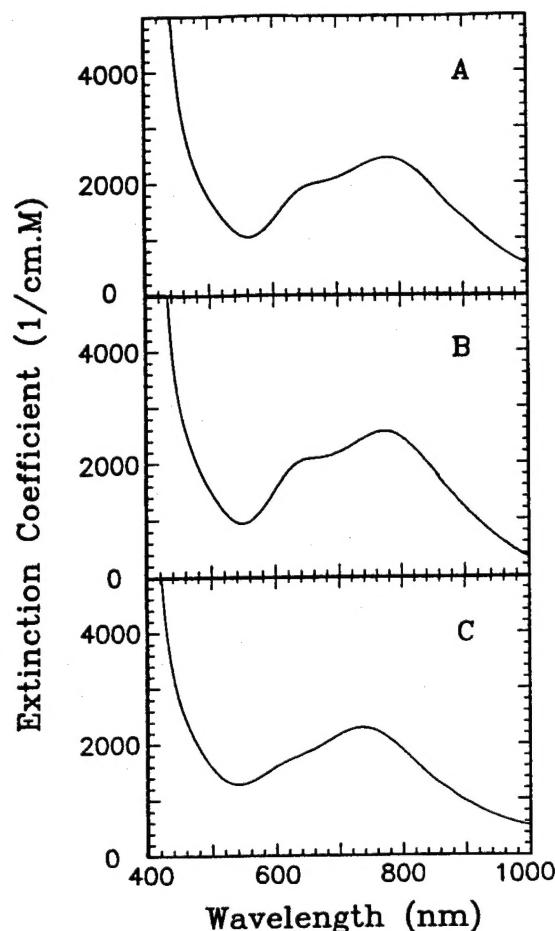


Figure 6. Linear absorption spectra of  $\sim 7 \times 10^{-4}$  M solutions of King's complex and synthesized variations dissolved in methylene chloride with the solvent backgrounds subtracted are shown. The labels correspond to methyl-King's complex, A; King's complex, B; and triethylaluminum King's complex, C.

in King's complex have been assigned to metal-metal, d to d, core transitions,<sup>8</sup> and it is likely that they are of the same origin in the ligand-substituted compounds. The 532-nm excitation wavelength used in the nonlinear measurement lies on the high-energy side of these resonances but below the strong charge-transfer transitions that dominate the spectra in the blue. The methyl-King's complex spectrum is slightly displaced to lower energies with respect to King's complex. This small shift in the ground-state absorption spectrum is a second-order effect resulting from the methyl substitution in the Cp ligand. Here the methyl group acts as an electron donor to the ring, decreasing the need for the bonding electrons from the iron. This overall effect lowers the energy of the tetragonal core, resulting in the observed red shift. The minor spectral shift to the blue in the spectrum of the triethylaluminum King's complex is also a second-order effect that results from the substitution of the carbonyl group. The triethylaluminum carbonyl is a net electron attractor. This ligand "pulls" electrons away from the iron core, increasing the binding energy of the ground state and resulting in the slight blue shift.

To measure the nonlinear optical properties of King's complex and the synthesized variations, we used a picosecond, time-resolved pump-probe technique. The optical source for these experiments was a frequency-doubled Nd:YAG laser that operates in TEM<sub>00</sub> mode and produces temporally near-Gaussian pulses of 25-ps (FWHM intensity) duration at 532 nm. A standard pump-probe setup was used with up to 2 ns of variable delay in the probe path. The probe was cross-polarized and then recombined with the pump at the sample cell at a small angle ( $\sim 1.2^\circ$ ). The pump was collimated, and the probe was focused to measured Gaussian spots of radii 280 and 30  $\mu\text{m}$ , respectively, at the sample.

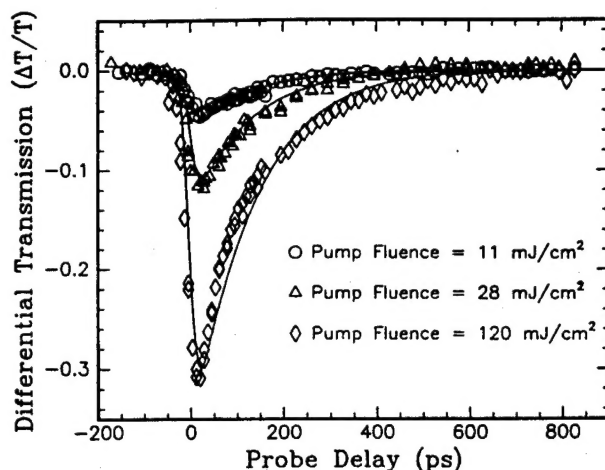


Figure 7. Time-resolved differential transmission measurements of King's complex in methylene chloride using pulses of 25-ps FWHM intensity, at 532 nm. The linear transmission is  $\sim 35\%$ . A negative value for differential transmission indicates increased absorption. The solid lines are the numerical fits for a single set of parameters, recorded in Table I, at the indicated fluence.

Considerable care was taken to ensure accurate overlap within the sample. The small angle between the beams and the fact that the probe spot size was considerably smaller than the pump ensured that the probe interrogated a radially uniform region of material in the optical cell. Absolute timing between the pump and probe (i.e., zero delay) was determined unambiguously from two-photon absorption in a wafer of ZnSe. The instantaneous two-photon-induced absorption of the probe is negligible except when the pump and probe are temporally and spatially coincident. Zero delay is, therefore, the delay at which the probe transmission is a minimum with a certainty of better than  $\pm 2.5$  ps. All of the experiments were performed over a range of pump fluences (10–100  $\text{mJ}/\text{cm}^2$ ) in either a 1- or 2-mm-thick optical cell containing  $\sim 2 \times 10^{-3}$  M solution of the organometallic compound and methylene chloride giving a linear transmission of either  $\sim 70\%$  or  $\sim 35\%$ , respectively.

#### IV. Results and Discussion

To investigate the nature of the excited-state transition, we have measured the nonlinear parameters of each of the synthesized analogs and compared these values with those of King's complex. Although we have previously reported<sup>2</sup> the measurement of the optical cross sections and lifetimes of King's complex, the experimental parameters, analysis, and results are pertinent to the present discussion and will be described here for completeness. The differential transmission of King's complex, i.e., the change in the probe transmission normalized by the linear transmission ( $\Delta T/T$ ), was recorded as a function of probe delay for a range of pump fluences and is shown in Figure 7. At each fluence, we observed RSA. Initially the absorption of the solution increases as a function of time in a manner consistent with the temporal integration of the pump pulse. Once the pump pulse has passed through the sample, this initial response is followed by a complete recovery in the probe transmission within a few hundred picoseconds. This behavior is consistent with an induced absorption in the first excited singlet state that increases as the excited state is populated and then diminishes as the population in that state relaxes to the ground state.

To extract the nonlinear parameters from the differential transmission data, we first fit the low-fluence data where the population in level 2 may be neglected. For these conditions, the system is completely specified by the ground-state cross section  $\sigma_{01}$ , the singlet excited-state cross section  $\sigma_{12}$ , and the lifetime of the first excited singlet state  $\tau_{10}$ . Moreover,  $\sigma_{12}$  and  $\tau_{10}$  are largely decoupled parameters for pulse durations shorter than the excited-

TABLE 1: Fit Parameters

synthesized variation of King's complex	absorption cross section		recombination time $\tau_{10}$ , ps
	ground state $\sigma_{01}$ ( $1 \times 10^{-18}$ cm $^2$ )	excited state $\sigma_{12}$ ( $1 \times 10^{-18}$ cm $^2$ )	
King's complex [(C <sub>5</sub> H <sub>5</sub> )Fe(CO)] <sub>4</sub>	4.1	$7.8 \pm 0.8$	$120 \pm 5$
methyl-King's complex [CH <sub>3</sub> (C <sub>5</sub> H <sub>4</sub> )Fe(CO)] <sub>4</sub>	4.7	$9.1 \pm 0.9$	$120 \pm 5$
triethylaluminum King's complex [(C <sub>5</sub> H <sub>5</sub> )Fe[COAl(C <sub>2</sub> H <sub>5</sub> ) <sub>3</sub> ]] <sub>4</sub>	4.9	$7.3 \pm 1.4$	$120 \pm 5$

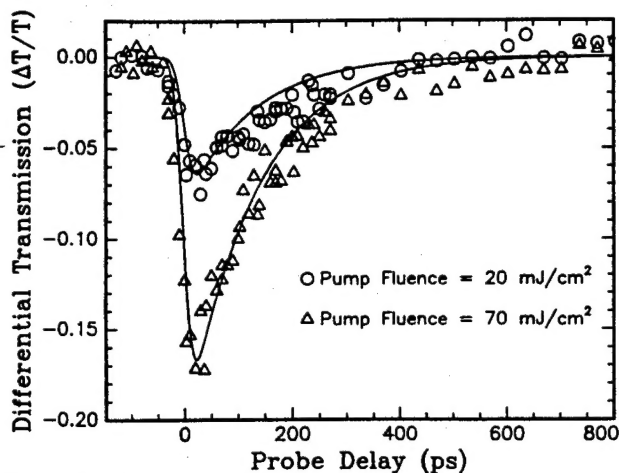


Figure 8. Time-resolved differential transmission measurements of methyl-King's complex. The linear transmission is  $\sim 35\%$ . The solid lines are the numerical fits for a single set of parameters, recorded in Table I, at the indicated fluence.

state lifetime,  $\tau_{10}$ ; the peak  $\Delta T/T$  near zero delay is primarily sensitive to  $\sigma_{12}$ , while the decay of  $\Delta T/T$  determines  $\tau_{10}$ . The linear absorption measurements provide  $\sigma_{01}$ , and fitting to the data allows us to uniquely extract  $\tau_{10}$  and  $\sigma_{12}$ . The theoretical curves superposed on the low-fluence data in Figure 7 were obtained using  $\sigma_{12} = (7.8 \pm 0.8) \times 10^{-18}$  cm $^2$ ,  $\tau_{10} = 120 \pm 5$  ps. At the higher fluences, the induced absorption becomes more sensitive to the upper excited singlet decay time,  $\tau_{21}$ , due to the greater number of excited-state transitions. The numerical fits to the data indicate that  $\tau_{21}$  is considerably shorter than the pulse duration and is estimated to be  $< 1$  ps. With this estimate and the values of  $\sigma_{12}$  and  $\tau_{10}$  obtained from the fit to the low-fluence data, we obtain excellent agreement with data obtained at the higher fluences, as seen in Figure 7. The fit parameters are recorded in Table 1. The excellent fit to the data at all fluences supports our assertion that the observed RSA in King's complex can be described completely within the singlet manifold.

Having established the experimental technique, numerical model, and results for King's complex, we now discuss the results obtained for the synthesized analogs. Methyl-King's complex was synthesized to test for the ligand-to-metal charge-transfer transition between the Cp ligand and the iron core. The results of the differential probe transmission through methyl-King's complex are plotted as a function of pump-probe delay in Figure 8. It can be seen that the material's response is similar to that of King's complex, but only from fitting the data can one compare the excited-state optical absorption cross section and excited-state lifetime. This is due to a slightly different ground-state absorption cross section, molarity, linear transmission, and fluence used in the different experiments. The parameter set used to produce the numerical fits to the data in Figure 8 is recorded in Table I. The excited-state absorption cross section and lifetime for methyl-King's complex are  $(9.1 \pm 0.9) \times 10^{-18}$  cm $^2$  and  $120 \pm 5$  ps, essentially identical to the values determined for King's complex. Since the measured parameters appear to be largely unaffected by such a major alteration to the Cp ligand, it is unlikely

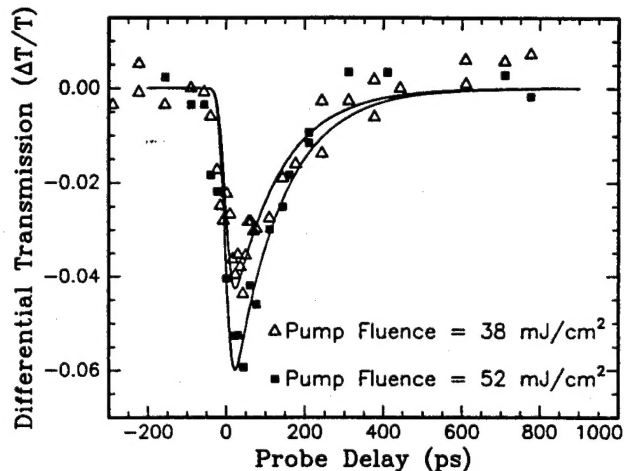


Figure 9. Time-resolved differential transmission measurements of triethylaluminum King's complex. The linear transmission is  $\sim 70\%$ . The solid lines are the numerical fits for a single set of parameters, recorded in Table I, at the indicated fluence.

that the ligand-to-metal charge transfer is involved in the excited-state absorption observed in King's complex.

To test for the metal-to-ligand charge-transfer transition involving the carbonyl ligand, the methyl-King's complex was replaced with triethylaluminum King's complex and the experiment repeated. The triethylaluminum King's complex also exhibits RSA as illustrated in Figure 9, where we again show the time-resolved differential probe transmission. The smaller peak absorption, compared to that observed for the King's complex and methyl-King's complex, is attributed to the thinner optical cell used for this measurement. The solid curves are the numerical fits using the parameters listed in Table I, and again good agreement between the experimental data and theory is obtained. The values of  $\sigma_{12} = (7.3 \pm 1.4) \times 10^{-18}$  cm $^2$  and  $\tau_{10} = 120 \pm 5$  ps are again, within the experimental error, indistinguishable from the values determined for King's complex. These data are consistent with an excited-state transition that is independent of the carbonyl ligand.

Since the above measurements provide strong evidence that the excited-state absorption in King's complex is not a charge-transfer transition, we conclude that the most likely source for the observed RSA is another nonbonding to strongly antibonding transition within the iron core. In principle, this could be verified by repeating our measurements on a compound in which the metal core atoms have been substituted. The problem with this, however, is that the ground-state absorption is associated with transitions within the metal core. Hence, any alteration of the metal core strongly influences the ground-state absorption, making a direct comparison with King's complex difficult.

We note that, from the measurements discussed above, we cannot *absolutely* rule out the possibility that the excited-state absorption in King's complex is associated with a charge-transfer transition. It is conceivable that the ligand substitutions that we have made have not sufficiently shifted the charge-transfer resonance to allow us to detect a significant change in absorption.

An even more pathological (and less likely) possibility exists that any shift in such a resonance was accompanied by a corresponding change in transition strength resulting in a constant excited-state cross section. In spite of these caveats, we emphasize that our measurements do indicate that the excited-state cross sections of the King's complex and methyl-King's complex are indistinguishable within  $\pm 10\%$  and that the cross section for the triethylaluminum King's complex is, within the  $\pm 20\%$  error, the same as that measured in the King's complex. The larger error in the measurement of the triethylaluminum King's cross section is less worrisome in view of the dramatic change in the CO bonding evidenced by the large shift ( $\sim 100\text{ cm}^{-1}$ ) in the CO stretching mode relative to that in King's complex. We would expect that such a significant change in bond strength would strongly impact any charge-transfer transition involving this ligand. We further note that, in addition to the measurements discussed above in which the compounds were dissolved in methylene chloride, we have performed identical measurements on King's complex and methyl-King's complex with the compounds dissolved in either toluene or THF. We find that the excited-state cross section and lifetime are independent of solvent. Since charge-transfer transition energies are typically strongly sensitive to environmental changes, these results also support our conclusion that the excited-state transition is not a charge-transfer transition.

#### IV. Conclusions

We have used picosecond pump-probe transmission measurements at 532 nm to investigate the excited-state dynamics in King's complex and synthesized analogs. Since the nonlinear optical response of methyl-King's complex, triethylaluminum King's complex, and King's complex are virtually indistinguishable, we have rejected both the ligand-to-metal charge-transfer and the metal-to-ligand charge-transfer transitions as the source of the excited-state absorption. The only remaining possibility for the excited-state transition is a second d-d transition within the metal core, corresponding to promotion of an electron out of the nonbonding to the strongly antibonding metal orbitals, and

we conclude that this is the most likely source of the excited-state absorption in King's complex. We note that the measured excited-state cross section in both King's complex and methyl King's complex was independent of whether methylene chloride, toluene, or THF was used as a solvent. This provides additional evidence that the ligands are not involved in the excited-state transition. All three of the compounds studied exhibited a recovery of the induced absorption with a characteristic time constant of 120 ps. This time scale is believed to be too fast for intersystem conversion followed by spin-forbidden relaxation back to the ground state, indicating that the excited-state absorption occurs in the singlet system.

#### V. Acknowledgements

The research at The University of Iowa was supported in part by the Advanced Research Projects Agency and the U.S. Army Night Vision and Electronic Sensors Directorate.

#### References and Notes

- (1) Coulter, D. R.; Miskowski, V. M.; Perry, J. W.; Wei, T.-H.; Van Stryland, E. W.; Hagan, D. J. *Proc. SPIE-int Soc. Opt. Eng.* **1989**, *1105*, 42-51. Wei, T. H.; Hagan, D. J.; Sence, M. J.; Van Stryland, E. W.; Perry, J. W.; Coulter, D. R. *Appl. Phys.* **1992**, *B54*, 46-51.
- (2) Allan, G. R.; Laberge, D. R.; Rychnovsky, S. J.; Boggess, T. F.; Smirl, A. L. *J. Phys. Chem.* **1992**, *96*, 6313-6317.
- (3) Giuliano, C. R.; Hess, L. D. *IEEE J. Quantum Electron.* **1967**, *3* (8, Aug), 358-367.
- (4) Harter, D. J.; Band, Y. B.; Ippen, E. P. *IEEE J. Quantum Electron.* **1985**, *21* (8, Aug).
- (5) Band, Y. B.; Harter, D. J.; Bavli, R. *Chem. Phys. Lett.* **1986**, *126*(3-4), 280-284.
- (6) Harter, D. J.; Shand, M. L.; Band, Y. B. *J. Appl. Phys.* **1984**, *56* (3, Aug 1).
- (7) King, R. B. *Inorg. Chem.* **1966**, *5* (12, Dec), 2227-2230.
- (8) Trinh-Toan; Fehlhammer, W. P.; Dhal, L. F. *J. Am. Chem. Soc.* **1972**, *94* (10, May), 3389-3396.
- (9) Neuman, M. A.; Trinh-Toan; Dhal, L. F. *J. Am. Chem. Soc.* **1972**, *94* (10, May), 3383-3388.
- (10) Creutz, C.; Mei Chou; Netzel, T. L.; Okumura, M.; Sutin, N. *J. Am. Chem. Soc.* **1980**, *102*, 1309.
- (11) White, A. J.; Cunningham, A. J. *J. Chem. Educ.* **1980**, *47* (4).
- (12) Alich, A.; Nelson, N. J.; Strobe, D.; Shriver, D. F. *Inorg. Chem.* **1972**, *11*, 2976.